

Chapter 3-7. Geochemistry of U and Pb in secondary minerals from Yucca Mountain and interpretation of the results of the U-Pb dating

By S.E. Pashenko and Y.V. Dublyansky

Table of contents

Chapter 3-7. Geochemistry of U and Pb in secondary minerals from Yucca Mountain and interpretation of the results of the U-Pb dating	355
3.7.1. Introduction	355
3.7.1.1. The USGS physicochemical model	356
3.7.1.2. Enhanced physicochemical model	357
3.7.1.2.1. Conflict between the U-Pb dates and the paleotemperatures	358
3.7.1.2.2. Growth rates obtained from U-Pb ages appear to be physically impossible	359
3.7.2. A formal mathematical definition of the problem of the migration of isotopes from the decay series of U and Th from the rock into aqueous fluid	363
3.7.3. Migration of Rn and the accumulation of Pb_{Rn} in cavities and fractures	364
3.7.3.1. Radon in rocks	364
3.7.3.2. A model of case 1: A spherical cavity filled with stagnant water	365
3.7.3.2.1. Fluxes and resulting concentrations of isotopes in a cavity	365
3.7.3.2.2. Direct ejection of isotopes into the cavity by the alpha-recoil mechanism	365
3.7.3.2.3. Normalized differential equations for ^{222}Rn	367
3.7.3.2.4. Distribution of Rn in a cavity	368
3.7.3.2.5. Diffusion mobility of the daughters of Rn	370
3.7.3.2.6. Concentrations of Pb isotopes in a cavity	373
3.7.3.2.7. A model: generation and accumulation of Pb-isotopes in a cavity filled with stagnant water	374
3.7.3.2.8. Comparison between the theoretical estimates and the experimental data	377
3.7.3.3. Model case 2: Thin fracture	381

3.7.3.3.1. Distribution of isotopes in narrow fractures and the time required to reach steady state	381
3.7.3.4. Model case 3: Distribution of Rn- and Pb-isotopes in a cavity with moving water	385
3.7.3.4.1. Distribution of isotopes in a channel	385
3.7.3.4.2. Calculations for the model geometry: channel-cone	385
3.7.4. Accumulation of Pb_{Rn} on micelles	390
3.7.4.1. Assessment of the role of colloids in accumulation of Pb_{Rn}	390
3.7.4.2. Nucleation and growth of micelles	391
3.7.4.3. Growth of micelles: condensation and coagulation mechanisms	392
3.7.4.3.1. Qualitative analysis of the processes	392
3.7.4.3.2. Possible change in the ionic composition of water due to coagulation of micelles	393
3.7.4.4. Accumulation of lead on micelles of silica in cavities and fractures	395
3.7.4.4.1. Flux of isotopes on a sphere	395
3.7.5. Uptake of lead in opal	396
3.7.5.1. Uptake of lead during the diffusion-controlled growth of minerals	396
3.7.5.2. Coagulation/sedimentation supply of Pb on the surface of growing minerals	398
3.7.5.2.1. Processes involved	398
3.7.5.2.2. Coagulation/sedimentation: Comparison of the theoretical predictions with the actual Pb isotope abundances in opals	400
3.7.6. Pb_{Rn} and the "conventional" U-Pb age dates	403
3.7.6.1. Evolution of lead isotope composition during the opal "lifetime"	403
3.7.6.2. The "common lead" and Pb_{Rn} corrections in computing the U-Pb radiometric ages	406
3.7.6.4. Variability and evolution trends of the Pb_{Rn}	407
3.7.7. Summary and conclusions	410
3.7.7.1. The model	410
3.7.7.1.1. Assumptions	410
3.7.7.1.2. Limitations of the model	410
3.7.7.2. The most important results	411
Appendix 3-7-1: Distributions of elements and isotopes in samples from the ESF	413
The database	413
Distribution of total U, Pb, Th and ^{204}Pb across the crusts	414
Distribution of elements and isotopes in the ESF	425
Abundances of U along the ESF	425

Abundances of Th along the ESF _____	427
Abundances of Pb along the ESF _____	428
Abundances of ^{204}Pb along the ESF _____	429
Abundances of ^{206}Pb along the ESF _____	430
Abundances of ^{207}Pb along the ESF _____	431
Abundances of ^{208}Pb along the ESF _____	432
Summary on the lead isotope database _____	433
The U/Th ratios in silica minerals along the ESF and in individual crusts	433
Concentrations of Pb isotopes in the upper parts of crusts _____	436
Concentrations of U in the upper parts of crusts _____	437
Concentrations of Th in the upper parts of crusts _____	439
Appendix 3-7-2: Statistical analysis of the elemental abundances and isotope ratios _____	440
Distribution of U- and Pb-abundances along the ESF _____	440
Pb in chalcedony and opal _____	441
Concentrations of U in different silica minerals _____	445
$^{234}\text{U}/^{238}\text{U}$ (concentration) ratios _____	450
Radiogenic Pb-isotopes vs. ^{204}Pb _____	450
Elements and isotopes in quartz and calcite _____	453
Appendix 3-7-3: The theory of formation of micelles through condensation and coagulation _____	456
Algorithms for solving Smolukhovski's equations for fast coagulation__	456
Using the MPV algorithm for calculating the "self-sustaining" spectra of particle size distribution _____	458
Approximation formulae for different stages of the coagulation process	459

Chapter 3-7. Geochemistry of U and Pb in secondary minerals from Yucca Mountain and interpretation of the results of the U-Pb dating

By S.E. Pashenko and Y.V. Dublyansky

3.7.1. Introduction

Beginning in 1996, the U.S. Geological Survey has pursued an aggressive uranium-lead age dating program for silica minerals (primarily opals but chalcedony and quartz, as well) from the Yucca Mountain vadose zone. In the course of the USGS studies, many samples from the secondary mineral crusts were subjected to U-Pb age dating analysis and more than 80 age determinations were reported (USGS, 1997; Fabryka-Martin et al., 2000; Neymark et al., 2001; Neymark et al., 2002). The reported radiometric ages span the time period from approximately 10 Ma to essentially the present. The data have led the USGS researchers to two conclusions that have influenced their models for the characterization of the Yucca Mountain geologic and hydrologic systems: (a) secondary mineral crusts in the Yucca Mountain vadose zone appear to have been forming continuously during the last ~10 Ma; and (b) the calculated growth rate of minerals, based on the radiometric ages, ranged between 0.035 and 1.8 mm·Ma⁻¹ (Neymark et al., 1998; 2000).

We have developed a physical model, which we believe demonstrates that the U-Pb method cannot be used for dating minerals that: (a) crystallize in large (~1 cm) open cavities; (b) crystallize from, or in the presence of colloidal solutions, and (c) are young (Miocene or younger). The model is described in detail in this chapter. Calculations derived from the model show that if the “conventional” equations of the U-Pb dating are applied to the foregoing minerals that are constrained, as noted, the resulting ages will appear excessively older. For example, minerals formed 1000 years ago may produce “conventional” U-Pb radiometric ages of several million years.

We are convinced that minerals growing in an open cavity are exposed to a flux of additional radiogenic Pb isotopes, which are not accounted for by the “common lead” correction. The parents for these isotopes are U and Pb, which reside in the surrounding rock. The decay chains of U and Pb contain radon. Being a gas, the radon readily diffuses into the cavity (“radon emanation”). After several decays, radon produces stable isotopes of Pb, which take up residence in the fluid filling the cavity. Our modeling shows that concentrations of this Rn-derived radiogenic Pb in relatively large cavities will be substantially higher than in thin fractures.

The Pb residing in the fluid moves via diffusion and becomes adsorbed on the surface of the growing mineral. We calculated the characteristic diffusion fluxes of Pb on the surface of the opal, assuming the rock contains 5 ppm of U and 14 ppm of Th (typical values for Yucca Mountain rhyolitic tuffs), and found that this mechanism alone could produce over a period of time on the order of 1 Ma, amounts of radiogenic Pb comparable to the amounts of Pb present in opal specimens from Yucca Mountain.

Opals are commonly formed through the coagulation of colloids. This process is considered responsible for the formation of the uraniferous opals (Yucca Mountain opals with 200+ ppm of U fall into this category). If colloidal solutions are present in the cavity, the accumulation of Rn-derived isotopes occurs on the micelles, which possess a very large surface area. Upon coagulation and sedimentation, the micelles become incorporated in the opal. The mechanism of concentration of the “excess” radiogenic Pb on the micelles is orders of magnitude more efficient than the net diffusion mechanism referred to above. Our calculations show that concentrations of Pb on the order of hundreds of ppb, typical of the Yucca Mountain opals, may be acquired by micelles of silica over a period of several days. Controlled by the velocity of water exchange in the cavities, the absolute quantities of Pb contained in the Yucca Mountain opals from individual cavities could accumulate within 100 to 1000 years.

We have concluded, after a detailed analysis, that the numeric data reported by the USGS researchers are of a high quality, but in both the USGS and UNLV age dating efforts the use of “conventional” equations for the U-Pb dating without first having been determined to be applicable in the specific setting (i.e., the deposition of opals in cavities from colloidal solutions) was inappropriate. The tuffs at Yucca Mountain do contain U and Th and the emanation of Rn does occur, and therefore, additional Rn-derived Pb must be present in the system. Therefore, the ages calculated without accounting for the additional Rn-derived lead cannot be accurate.

It is important to note that the Rn derived Pb is in addition to the contribution of Pb and other daughters of U carried by the mineral depositing fluids described in Chapter 2.5.6.3 and 2.5.6.4.

3.7.1.1. The USGS physicochemical model

In order to apply the technique of U-Pb dating to the Yucca Mountain minerals, the USGS researchers necessarily had to adopt the “conventional” model that limits to two sets the “pool” of lead isotopes that are present in minerals. One set is allogenic lead, incorporated in growing minerals from the mineral-forming fluid; it includes the radiogenic isotopes, ^{206}Pb , ^{207}Pb and ^{208}Pb , as well as the stable ^{204}Pb isotope. The other set is in situ produced lead isotopes, formed during the decay of ^{238}U , ^{235}U and ^{232}Th in the minerals. The latter set contains only radiogenic lead isotopes in amounts that are time-dependent

products of the radioactive decay process. After subtracting the allogenic lead (the so-called "common lead correction") isotope component from the pool the second set can be used for calculating the ages of the minerals.

3.7.1.2. Enhanced physicochemical model

We introduce a physicochemical model, in which we complement the USGS model's two sources of radiogenic lead present in samples with a third source – bedrock-derived radon (Pashenko and Dublyansky, 2002). Our enhanced model recognizes that the rhyolites of Yucca Mountain contain, on an average, about 4 ppm of U and 18 ppm of Th (Marshall et al., 1996). The decay chains of these radioactive elements contain intermediate daughter Rn isotopes. Being a gas, radon can migrate from the bedrock into open cavities, such as fractures and lithophysae, and concentrate in the fluid filling the cavities. Isotopes of radon then undergo further decay to finally yield stable Pb isotopes.

As demonstrated below, the concentrations of Rn-derived radiogenic lead (hereinafter denoted Pb_{Rn}), are significantly different in large open cavities (0.1 to 10 cm) as compared to thin fractures (less than 0.1 mm). Minerals depositing in open cavities uptake "excess" Pb isotopes according to water-mineral distribution coefficients. The uptake may be particularly efficient if mineral growth involves colloidal solutions, as is commonly the case with uraniferous opals (see section 3.4.6.4.7. "Uranium in the silica minerals" in Chapter 3-4). Micelles of silica suspended in solution, adsorb Pb_{Rn} . After coagulation of the micelles and sedimentation of the particles the adsorbed Pb_{Rn} becomes incorporated in the opal. Being unbalanced by U and Th isotopes in the mineral, the excess lead distorts the true ages derived from the "conventional" U-Pb radiometric age dating calculations by overestimating them.

In our enhanced model we recognize that: (a) growing minerals are surrounded by open space (lithophysal cavities or open fractures) filled with aqueous solutions; (b) the volume of the fluid passing through the cavity in the course of mineral deposition was much greater than the volume of the deposited materials; and (c) the precipitation of opals at Yucca Mountain occurred through or in the presence of colloidal solutions (see discussion in section 3.4.5.5. "Colloids in the Yucca Mountain mineral forming system" in Chapter 3-4).

As we stated above, our enhanced model predicts that there is a substantial difference in the behavior of U and Pb isotopes in thin fractures and in open cavities such as lithophysae. Preliminary analysis of the data published by Neymark et al. (2002) confirms our expectations. Figure 3-7-1 shows that secondary silica minerals deposited in lithophysal cavities exhibit the greatest maximum values of both U and Pb abundances. These samples also show the greatest variability of U and Pb abundances in

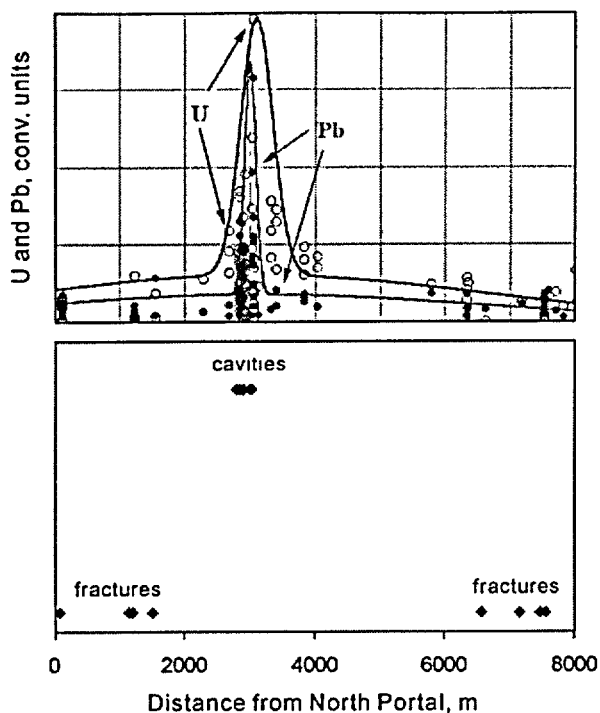


Figure 3-7-1. Distribution of U and Pb abundances in silica minerals along the ESF and settings in which minerals occur (fractures or lithophysal cavities). For more details see Appendices 3-7-1 and 3-7-2.

in Appendices 3-7-1 and 3-7-2 to this Chapter).

We begin our discussion of the models with a brief description of reasons, which convinced us that enhancement of the basic USGS physicochemical model and a critical reevaluation of the U-Pb age dates, are both warranted and necessary.

3.7.1.2.1. Conflict between the U-Pb dates and the paleotemperatures

Two data sets were obtained independently from the ESF mineral samples: radiometric ages and paleotemperatures of fluids (fluid inclusion method; see Chapter 3-6). The acceptance of both data sets leads to the inevitable conclusion that temperatures as high as 40-60 °C must have persisted in the shallow vadose zone of Yucca Mountain (at a depth of 30 to 300 m from land surface) during the several million year-long period (approximately between 10 and 6 Ma, and probably longer). It may be demonstrated that these temperatures would translate into heat flow values as great as 150 to 2600 mWt m⁻² (or 3.5 to 62 HFU), which is roughly 3 to 50 times the average heat flow in the western United States (Sass et al., 1971). Such extreme values of heat flow are possible only in association with short-lived events, such as

individual mineral crusts (sometimes up to three orders of magnitude). Samples from fractures generally show smaller abundances of U and Pb, and a lesser variability of their values.

In subsequent sections of this chapter we develop a series of mathematical models, which explore the processes of production and migration of Rn, the uptake of the radon-derived lead (Pb_{Rn}) by depositing minerals, and the processes of coagulation of the colloids of silica. Finally, we attempted to combine these “partial” components into one comprehensive model.

The predictions of the mathematical models were tested against numeric data reported by USGS scientists. The data used for this evaluation were published by Neymark et al. (2000 and 2002) and Paces et al. (1996 and 2001). A detailed analysis of the data is provided

the cooling of the freshly deposited layers of the pyroclastic rock (maximum duration on the order of the few thousand years) or in association with active geothermal systems (see Chapter 3-6 for discussion). It is physically impossible to maintain the requisite temperatures in the vadose zone, where the heat is transferred primarily by conductance, for millions of years.

The combined paleotemperature and radiometric age data also present conflicts with the hydrothermal model of deposition of the Yucca Mountain secondary minerals based on rainwater percolating through a hot mountain. In this case, the hot or warm water must have resided at and above the planned repository horizon for millions of years. The geological record indicates that this definitely did not happen. Over such long times heated water would necessarily de-vitrify non-welded ash-fall tuffs, which is not observed.

Thus, neither of the competing models seems to be compatible with the coupled paleotemperature – radiometric age data set, which led us to the conclusion that one subset of the data must be in error. The paleotemperature data, however, are quite robust. This stems from the inherent reliability of the fluid inclusion method, *per se*, as well as from the substantial effort of the researchers in obtaining sets of technically unassailable data. Thousands of measurements of paleotemperatures were carried out in recent years by as many as three independent groups of researchers (e.g., Dublyansky et al., 2001; Whelan et al., 2001; and Wilson and Cline, 2001) and at least two groups concurred in the opinion that the quality of the thermal record is exceptional. Thus, the probability that this data set is erroneous is negligible.

3.7.1.2.2. Growth rates obtained from U-Pb ages appear to be physically impossible

The average growth rates for mineral crusts at Yucca Mountain were calculated by the USGS researchers based on the results of the U-Pb and ^{230}Th -U dating: "*... secondary minerals are assumed to have been deposited continuously at a rate of 1×10^{-6} mm/yr over 10 million year period resulting in 10 mm-thick coating.*" (Paces et al., 1996) and "*... thin sheets sampled from mineral surfaces commonly were 0.1 - 0.3-mm-thick. In these cases, deposition rates between about 0.035 and 1.8 mm/m.y. are obtained by dividing the thickness by the total duration of deposition These values are in general agreement with long-term rates of mineral deposition during the past 10 m.y. based on direct U-Pb dating of sequential inner layers of opal from calcite-silica fracture and cavity coatings at Yucca Mountain (Neymark et al , 1998).*" (Neymark et al., 2000).

Intuitively, such extraordinary low rates of growth are questionable. It is instructive, in this regard, to assess the physicochemical parameters that must be maintained around the growing crystal to evaluate the postulated growth rates.

Consider the growth of a typical bladed shaped crystal, like those found in Yucca Mountain, with dimensions of approximately $1 \times 0.5 \times 0.005$ cm. The crystal is oriented perpendicularly to the substratum,

and the vector of the fastest growth is oriented along the longest axis of the blade (i.e., the growth is strongly anisotropic). Measurements of the thickness of the growth zones along the longest and the shortest axes of several typical crystals yield an estimate of the maximum rate of growth anisotropy of 19.6 (i.e., calcite grew 19.6 times faster along the blade than across it; Smirnov and Dublyansky, 2001). To simplify calculations, we assumed that the growth velocity along one of the two shortest dimensions is zero. The velocity of deposition of the matter on the crystal surface, then, is expressed as:

$$Q = \frac{n}{S \cdot t}, \quad (3-7-1)$$

$$n = M v_1 \rho \quad (3-7-2)$$

where Q is the net growth velocity [$\text{mmole} \cdot \text{m}^{-2} \cdot \text{hr}^{-1}$]; n is the amount of deposited matter [mmole]; S is the surface area on which deposition occurs [m^2]; t is the time [hr]; M is the mole mass of the calcite; ρ is the density of calcite [$\text{kg} \cdot \text{m}^{-3}$]; and v_1 is the volume of the depositing layer of calcite [m^3].

Assuming the growth occurs at $T = 25^\circ\text{C}$, and a layer of 1.8 mm formed over a period of 1 million years, with a given crystal morphology and calculated growth anisotropy, the net growth velocity is $Q = 2.8 \cdot 10^{-15} \text{ mmole} \cdot \text{m}^{-2} \cdot \text{hr}^{-1}$.

It is well known that the major parameter controlling the velocity of crystal growth is the supersaturation of the solution. The chemical affinity method developed by Morse (1983) is the most widely used method for assessment of the interrelationships between the supersaturation and the velocity of growth:

$$Q = K(\Omega - 1)^n \quad (3-7-3)$$

where Q is the velocity of growth, K is the growth rate constant and n is the reaction order (both values are determined experimentally; Morse, 1983; Mucci and Morse, 1983). In Morse's equation, Ω defines the degree of the supersaturation:

$$\Omega = \frac{|Ca^{2+}| \cdot |CO_3^{2-}|}{K_{sp}}, \quad (3-7-4)$$

where the numerator is the activity product for dissolved ions, and K_{sp} is the solubility product for calcite.

Neither K nor n are known for the Yucca Mountain system; therefore, we used values obtained elsewhere for crystallization of calcite at 25°C . By analyzing the influence of surface reactions on the kinetics of calcite growth, Nillson and Sternberg (1999) demonstrated that at low supersaturations ($\Omega <$

1.49), $n \equiv 2$, and the velocity of the calcite crystal growth may be approximated by Eq. 3-7-3. The best approximation of the growth rate constant for our calculations is the value of $K = 0.4 \text{ mmole}\cdot\text{m}^{-2}\cdot\text{hr}^{-1}$ given by Lee and Morse (1999), since the conditions of their experiments approximate the hypothetical setting of calcite growth from films of waters as proposed in the "rainwater" model. For the purpose of the bounding calculations, we also used the greatest reported value for calcite: $K = 1.37 \text{ mmole}\cdot\text{m}^{-2}\cdot\text{hr}^{-1}$ (Nillson and Sternberg, 1999).

Our calculations demonstrate that in order to obtain the net growth velocity $Q = 2.8\cdot 10^{-15} \text{ mmole}\cdot\text{m}^{-2}\cdot\text{hr}^{-1}$, the supersaturation Ω must range between 1.000000083 and 1.000000045 (for $K = 0.4$ and 1.37 , respectively). Obviously, it does not seem to be physically possible to maintain such a minute deviation from exact equilibrium ($\Omega = 1$) for any extended period of time. It is to be noted here that such a hypothetical ultra-stable environment would have to be maintained for millions of years within the vadose zone (at a depth of 30 to 300 m from land surface), which by its very nature is an open and dynamic system.

The chemical affinity approach used above to assess the possible growth rates adequately portrays the real crystal growth only if the latter occurs through the dislocation mechanism. We reiterate here that at Yucca Mountain crystals commonly grow along a selected direction (hence the bladed morphology), which make them genetically similar to skeleton crystals. It is known that skeleton growth requires the predominance of the two-dimensional nucleation growth mechanism (Sunagawa, 1984). The latter mechanism is associated with growth rates substantially higher than the dislocation growth mechanism (see Chapter 3-4 for details).

Variation of the temperature at the crystallization site may disrupt the equilibrium in the system. We had to consider, therefore, variations of the temperature expected within the shallow vadose zone at a depth of 30 to 300 m due to the changing climate. The temperature depth profile is controlled by the attenuation of the harmonic fluctuations:

$$\Delta T_z = 2\Delta T_s \exp\left(-h\sqrt{\frac{\pi}{a\tau}}\right) \quad (3-7-5)$$

where ΔT_z is the change of the temperature at depth z , ΔT_s is the amplitude of the temperature change at the surface, a is the temperature diffusivity, and τ is the period of the temperature fluctuation (Eckert and Drake, 1959; Frolov, 1976). Assuming the long-term climate-related change in the mean annual temperature at the Earth's surface was 2°C over the last 1000 years, the calculation of the variation in temperature at a depth of 30 and 300 m is 1.5 and 0.11°C , respectively.

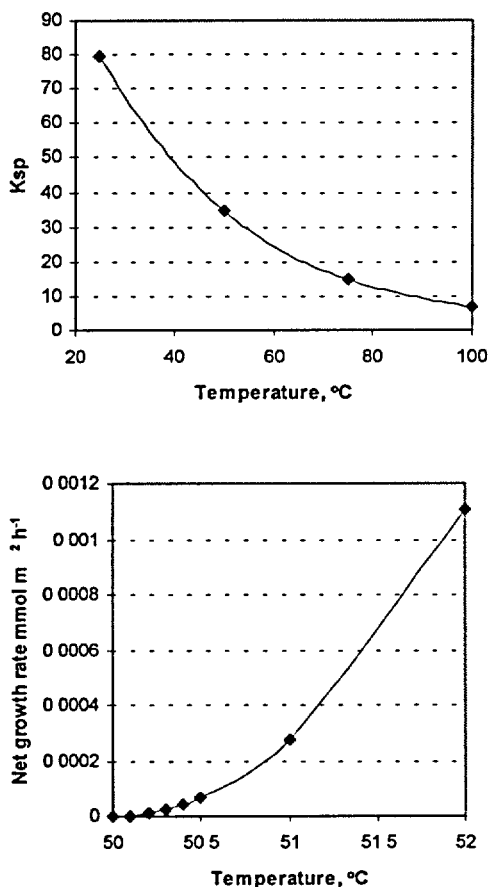


Figure 3-7-2. The K_{sp} and the net growth rate of calcite as a function of the temperature.

The net growth velocity of the model crystal where $K = 0.4 \text{ mmole}\cdot\text{m}^{-2}\cdot\text{hr}^{-1}$, and $n = 2$ may be calculated for a change in the temperature of crystallization from 0.1 to 2.0°C. Assume, at $T = 50^\circ\text{C}$ the $K_{sp} \cong 34.7$ and the solution is in equilibrium with calcite ($\Omega = 1$, no growth, no dissolution). An increase of temperature by only 0.1 °C in such a system (Figure 3-7-2) would lead to a calcite net growth velocity of $Q = n \cdot 10^{-6} \text{ mmole}\cdot\text{m}^{-2}\cdot\text{hr}^{-1}$, which is 9 orders of magnitude faster than the growth velocities inferred from U-Pb radiometric dating ($Q = 2.8 \cdot 10^{-15} \text{ mmole}\cdot\text{m}^{-2}\cdot\text{hr}^{-1}$, see above).

We have demonstrated, thus, that even minute climate-related temperature variations would destabilize a hypothetical crystallization system and would make the maintenance of ultra-low supersaturation rates impossible. In reality, however, the crystals growing in the vadose zone of Yucca Mountain have witnessed much greater temperature variations. Fluid inclusion data demonstrate that the temperature

changes during crystal growth ranged from a maximum of 85-90 °C to less than 35-50 °C (Dublyansky et al., 2001; Whelan et al., 2001; Wilson and Cline, 2001; see also Chapter 3-6).

Summarizing the foregoing evaluation, it is apparent that the growth rates inferred on the basis of the radiometric dating of secondary minerals at Yucca Mountain require an exceptionally small deviation from equilibrium; a deviation which must be maintained over millions of years. From either a physical or geological perspective, this does not appear to be possible.

3.7.2. A formal mathematical definition of the problem of the migration of isotopes from the decay series of U and Th from the rock into aqueous fluid

The tuff of Yucca Mountain may be considered for analytical purposes as a system of micro channels through which water flows. Considering it in this manner, key terms may be defined. The vector velocity of the water flow through the unity of surface area is \vec{V} . The flow velocity in each micro channel is V_i and its direction corresponds to the direction of the channel. Concentrations of isotopes in solution flowing through these channels is denoted by a lower index $_{mi}$. For water the isotopes being considered are:

$${}^{23N}U_{water_mi}(t), {}^{23N}Th_{water_mi}(t), \text{ and } {}^{20M}Pb_{water_mi}(t) \quad (3-7-6)$$

and for the tuff matrix:

$${}^{23N}U_{tuff_mi}(t), {}^{23N}Th_{tuff_mi}(t), \text{ and } {}^{20M}Pb_{tuff_mi}(t) \quad (3-7-7)$$

Using ${}^{238}U$, for example, an equation describing the change of the U concentration is as follows:

$$\frac{\partial {}^{238}U(\vec{r}, t)}{\partial t} = D\Delta {}^{238}U + \nabla_r(\vec{V} \cdot {}^{238}U) - \lambda_{238} \cdot {}^{238}U(\vec{r}, t) + I_+ {}^{238}(\vec{r}, t) + I_- {}^{238}(\vec{r}, t) \quad (3-7-8)$$

where the first term of the equation (Laplace operator Δ) describes diffusion (D) of uranium within the channel, the second term describes the gradient (∇) input of uranium at the given point in space, the third term describes the decay of uranium, and the fourth and the fifth terms account for the flux of uranium from water on the tuff surface and from the tuff surface into the water, respectively. A definition of the last two terms requires detailed information on the concentrations of fluids and the structure of the flow velocities at the water-rock interface with the water-crystal boundaries.

Eq. 3-7-8 does not have an analytical solution and must, therefore, be solved numerically. Assuming that the system has reached a quasi-equilibrium state, Eq. 3-7-8 may be rewritten as:

$$D\Delta {}^{238}U + \nabla_r(\vec{V} \cdot {}^{238}U) - \lambda_{238} \cdot {}^{238}U(\vec{r}) + I_+ {}^{238}(\vec{r}) + I_- {}^{238}(\vec{r}) = 0 \quad (3-7-9)$$

which, as rewritten, depends only on spatial coordinates.

3.7.3. Migration of Rn and the accumulation of Pb_{Rn} in cavities and fractures

Below we develop a series of qualitative and quantitative physicochemical models and compare the predictive results of these models with experimental data reported by Neymark et al. (2000 and 2002) and USGS (1997) (see Appendices 1 and 2 to this chapter). We start from simplified models and gradually increase the level of sophistication. Our starting premise is that crystal growth occurs in an aqueous phase (i.e., the cavities in which crystals grow are filled with water). Justification of this premise may be found in Chapter 3-4. The mathematical models we develop in subsequent sections of this chapter may be adjusted for cases where cavities are filled with water only during certain period(s) of mineral "life".

3.7.3.1. Radon in rocks

A knowledge of the emanation and concentrations of radon in the underground vadose zone atmosphere of Yucca Mountain is necessary to set quantitative boundary conditions in the model. Surprisingly, a search of the Yucca Mountain Project publication database failed to disclose numeric data on radon concentrations in rhyolitic tuffs or radon emanation from the tuffs and groundwater at Yucca Mountain.

Liu et al. (1995) reported results of the continuous monitoring of Rn concentrations at two stations within the 16 km radius of the North Portal of the ESF. Measurements recorded Rn concentrations of about 2-5 Bk·l⁻¹ having pronounced diurnal patterns, which are strongly affected by meteorological conditions. Sullivan and Pescatore (1994) considered the theoretical aspects of modeling the buoyancy driven Rn flow, and in the process touched on aspects of the barometric and topographic controls. The closest location for which samples of the air removed from the rocks were studied was Rainier Mesa on the Nevada Test Site. There, Fauver (1987) reported Rn contents of 25 to 200 pCi·l⁻¹.

Indirect information exists, however, suggesting that concentrations of Rn in the Yucca Mountain tuffs might be quite high. The NEA/IAEA (2001) report states: "*Analysis of ²²⁶Ra is also suggested to provide analogue data and understanding of radium mobility as well as to indicate the likely source of radon gas which occurs in high concentrations in the Exploratory Studies Facility (ESF) and Cross Drift tunnels in the absence of ventilation.*" (p. 24; emphasis added). The high concentrations of Rn are not surprising. Extensive research carried out in natural karst caves in the United States and elsewhere over the last several decades (Atkinson et al., 1983; Bottrell, 1991; Cunningham and LaRock, 1991; Gunn et al., 1990; Yarborough, 1980; Klimchuk and Nasedkin, 1992) have demonstrated that high levels of Rn is an attributive property of the underground space. The Rn contents measured in natural caves range from n-

10^2 to $n \cdot 10^4$ Bk·m⁻³. It was shown that the contents are lower in well-ventilated parts of caves and high where ventilation is suppressed. It should be expected, therefore, that Rn concentrations in poorly ventilated lithophysal cavities in the rhyolitic tuffs (the rock characterized by relatively high contents of U and Th) must be quite high.

The paucity of radon related data for Yucca Mountain is astonishing, taking into account the amount of research invested in Yucca Mountain over the last two decades. Due to this apparent gap in the dataset, we had to use the average characteristics obtained from the literature for similar types of rocks in our model calculations. It must be realized, however, that there exists a significant scatter of values reported for similar types of rocks and similar geologic settings (e.g., Baranov, 1955), which indicates a high sensitivity of radon emanation and migration processes with regard to the state of the rock matrix and the character of occurrence of isotopes of Ra in it.

3.7.3.2. A model of case 1: A spherical cavity filled with stagnant water

3.7.3.2.1. Fluxes and resulting concentrations of isotopes in a cavity

In a water-filled sphere with radius R , various isotope components from, for example, the ²³⁵U-decay chain (²³⁵U resides in the bedrock) are introduced into the water. We define the flux of the k -th component as I_k , its coefficient of diffusion in water as D_k , and the initial concentration in water as $N_k(0)$. Taking into account the chain of radioactive decays, a system of equations describing the process may be written as:

$$\frac{dN_k}{dt} = D_k \cdot \Delta N_k + N_{k+1} \cdot \exp(-\lambda_{k+1}) - N_k \cdot \exp(-\lambda_k) \quad (3-7-10)$$

with the boundary condition:

$$\left. \frac{dN_k}{dR} \right|_S = I_k \quad (3-7-11)$$

(It is to be noted that the surface area S from which Rn may enter the cavity may change in time due to the "screening" of the tuff surface by the deposition of calcite and silica minerals).

The most difficult task is to define the fluxes of components at the sphere's surface. The flux I_k , indiscriminately lumps together a number of mechanisms. These are: the "common" chemical dissolution (I_{diss_k}), preferential leaching due to the damage of the crystal lattice (formation of channels) due to alpha-recoil (I_{chan_k}), and the direct ejection of the daughter elements into the water from the rock surface (I_{eject_k}).

3.7.3.2.2. Direct ejection of isotopes into the cavity by the alpha-recoil mechanism

The direct ejection flux of elements into the cavity by alpha-recoil may be described as:

$$I_{\text{eject}_k} = \frac{1}{2} \int_0^{\frac{\pi}{2}} \int_0^{\infty} 2\pi\lambda_{k+1}C_{k+1} \exp\left[-\frac{h}{L_k \cos\theta}\right] d\theta dh \quad (3-7-12)$$

where $C_{k+1}(h)$ is the concentration of the parent isotope in the host rock; h is the depth from the cavity surface; L_k is the average free length path of the daughter that forms during the decay of the $k+1$ element.

Different publications cite different mechanisms for the ejection of ^{231}Th into ground water in the course of the decay of ^{235}U (e.g., Fleischer, 1988; Sun and Semkow, 1998). Our evaluation assumes that the ^{235}U -to- ^{238}U ratio corresponds to its "normal" natural value. The solution to Eq. 3-7-12 yields an ejection flux of approximately $6U \cdot 10^{-10}$ atoms of ^{231}Th into the water per cm^2 per second (where U is the concentration of uranium in the rock in ppm).

The equation was solved for two cases. In the first case we assumed that the decay constant is 0, which approximates the case of the long-lived isotope and its complete adsorption upon contact with the cavity wall. In the second case we used the actual decay constant for ^{231}Th .

For the first case, the concentration inside a sphere monotonically increases, which is to be expected because no "sinks" for the isotopes inside the sphere are considered. In the second case, the concentration of ^{231}Th across the cavity increases asymptotically. The function for a cavity with $R = 10$ cm may be presented as:

$$^{231}\text{Th}(R) = ^{231}\text{Th}(0) \cdot \exp\left[-\left(1.378 \cdot \frac{\lambda}{D}\right)^{0.5} \cdot R\right] \quad (3-7-13)$$

The equation is accurate within several percent over the range of concentrations of two orders of magnitude. It shows that the concentration of ^{231}Th decreases by 2.8 times in 1 cm from cavity walls, and by 6.9 times in 2 cm. The sharp dependency of the concentration upon cavity size and the half-life of isotopes will be discussed later for other isotopes.

The maximum concentration of ^{231}Th will be reached at a distance of L_k from the cavity wall after a certain time has elapsed:

$$^{231}\text{Th}(\text{max}) = \frac{A \cdot I_{\text{eject}_Th} \cdot L_{Th}}{D_{Th}} \quad (3-7-14)$$

where A is the coefficient ($\cong 1$) determined numerically. Quantitatively, for ^{231}Th this concentration is estimated as $n \cdot 10^{-9}$ to $n \cdot 10^{-10}$ atom $\cdot \text{cm}^3$. This value corresponds to the precipitation of 2 atoms of ^{231}Th (or, more strictly speaking, its daughters) onto the surface of a sphere with a diameter of 1 cm per million

years. The value is very small for two reasons. First, the length of the recoil of an atom of Th (formed by the decay of U) in water is only several hundredths of a micrometer. Second, an atom of Th may only be ejected from a very thin near-surface layer of rock.

Calculations for all three parents (^{235}U , ^{238}U , and ^{232}Th) yielded numerically similar results. Thus, the direct ejection of daughter isotopes into the cavity filled with stagnant water does not provide, at this level of approximation, a plausible mechanism for the accumulation of substantial amounts of radiogenic lead. Our calculations, however, did not take into account the fact that each decay chain contains the gaseous member, Rn.

3.7.3.2.3. Normalized differential equations for ^{222}Rn

We now consider an equation describing the generation of ^{222}Rn in bedrock tuff due to the decay of Ra. The decay rate may be obtained from the conditions of secular equilibrium in the ^{238}U decay chain:

$$\frac{d^{222}\text{Rn}}{dt} = D_{\text{Rn_tuff}} \frac{d^2 222 \text{Rn}}{dx^2} + \lambda_{238} \cdot {}^{238}\text{U} - \lambda_{222} \cdot {}^{222}\text{Rn} \quad (3-7-15)$$

where t is the time, x is the coordinate, $D_{\text{Rn_tuff}}$ is the coefficient of diffusion of radon in tuff, λ is the decay constant, and ^{238}U and ^{222}Rn are concentrations of the isotopes. Assume for simplicity that water does not contain dissolved uranium:

$$\frac{d^{222}\text{Rn}}{dt} = D_{\text{Rn_water}} \frac{d^2 222 \text{Rn}}{dx^2} - \lambda_{222} \cdot {}^{222}\text{Rn} \quad (3-7-16)$$

An equilibrium concentration in the rock far from the cavity (∞) may be expressed as:

$${}^{222}\text{Rn}(\infty) = \frac{\lambda_{238}}{\lambda_{222}} {}^{238}\text{U}(\infty) \quad (3-7-17)$$

We introduce a new variable, the normalized concentration of radon:

$$\eta = \frac{{}^{222}\text{Rn}}{{}^{222}\text{Rn}(\infty)} = \frac{{}^{222}\text{Rn}}{{}^{238}\text{U}(\infty)} \frac{\lambda_{222}}{\lambda_{238}} \quad (3-7-18)$$

Then Eqs. 3-7-15 and 3-7-16 may be re-written as:

$$\frac{d\eta}{dt} = D_{\text{Rn_tuff}} \frac{d^2 \eta}{dx^2} + \lambda_{222} (1 - \eta) \quad (3-7-19)$$

$$\frac{d\eta}{dt} = D_{\text{Rn_water}} \frac{d^2 \eta}{dx^2} - \lambda_{222} \cdot \eta \quad (3-7-20)$$

Defining $R_{eff_water} = \sqrt{D_{Rn_water} / \lambda_{222}}$ and $R_{eff_tuff} = \sqrt{D_{Rn_tuff} / \lambda_{222}}$, Eqs. 3-7-19 and 3-7-20 may be re-written as:

$$\frac{d^2\eta}{dx^2} = -\frac{1-\eta}{R_{eff_tuff}^2} \quad (3-7-21)$$

and

$$\frac{d^2\eta}{dx^2} = -\frac{\eta}{R_{eff_water}^2} \quad (3-7-22)$$

It is apparent that the concentration of Rn in both water and rock, normalized to the U-content in tuff, is controlled by only one parameter: the effective radii of diffusion (R_{eff_water} and R_{eff_tuff}) of Rn.

3.7.3.2.4. Distribution of Rn in a cavity

Let us consider the concentration of radon inside a sphere, taking into account the generation of Rn in the surrounding rock and its diffusion into the water that fills the sphere. We assume radon is not adsorbed when it contacts the cavity wall (since Rn is a gas), whereas its daughters are adsorbed with the efficiency coefficient $\alpha \cong 1$.

Eq. 3-7-10 may be solved numerically in the manner of Eq. 3-7-13 for all three isotopes of radon. We assume that in the rock, all isotopes in the three decay chains are in secular equilibrium. The solution of Eq. 3-7-10 for radon is:

$${}^{222}\text{Rn} = \frac{{}^{238}\text{U} \cdot \lambda_{238}}{\lambda_{222}} \cdot \exp\left[-B \cdot (R_0, 222) \cdot \left[\frac{\lambda_{222}}{D_{Rn}}\right]^{0.5}\right] \cdot R \quad (3-7-23)$$

The coefficient, B , depends on the specific geometry of the problem. It may readily be found numerically, and is close to 1. Taking into account the difference in the coefficients of diffusion for Rn in the rock (D_{Rn_rock}) and in water (D_{Rn_water}), a more complete solution for the area near the cavity wall (within 2-3 cm) may be written as:

$${}^{222}\text{Rn} = \frac{{}^{238}\text{U} \cdot \lambda_{238}}{\lambda_{222}} \cdot (A1 + A2) \quad (3-7-24)$$

where

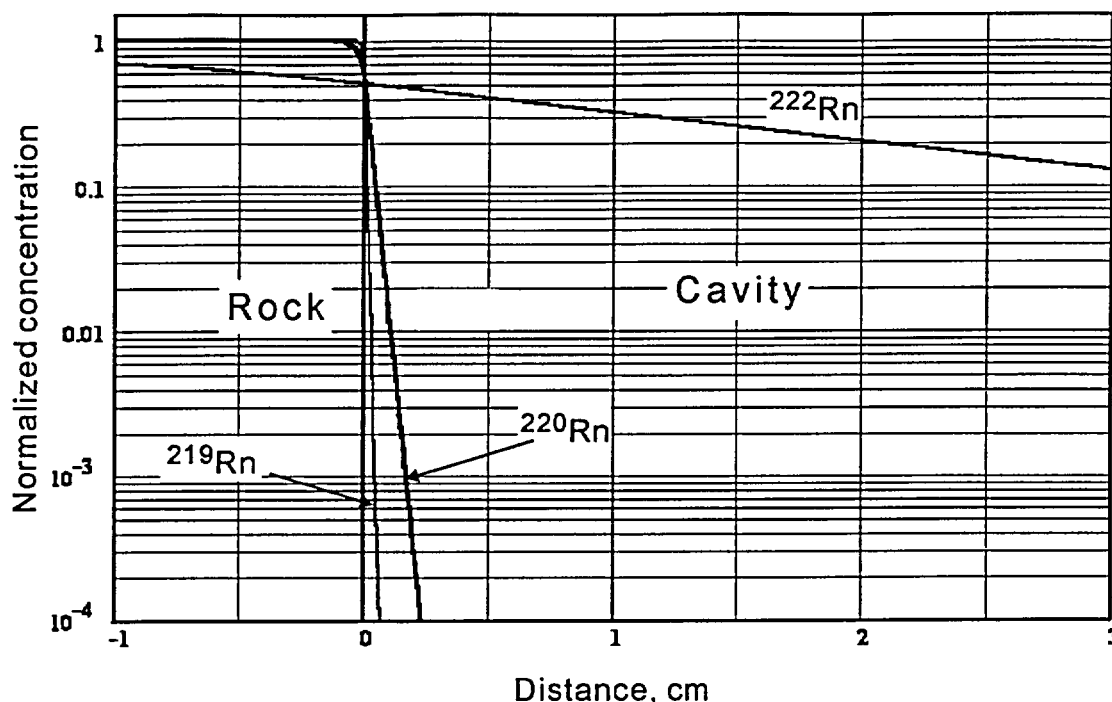


Figure 3-7-3. Concentration profiles for three Rn isotopes, produced in the course of the radioactive decay of ^{238}U , ^{235}U , and ^{232}Th in the bedrock, near the wall of the water-filled cavity. All values are normalized to the equilibrium content of Rn isotopes in the rock. 0 on the X-axis corresponds to the cavity wall; positive values are inside the cavity.

$$A1 = \left[1 - \frac{\left[\frac{D_{Rn_rock}}{D_{Rn_water}} \right]^{0.5}}{1 + \left[\frac{D_{Rn_rock}}{D_{Rn_water}} \right]^{0.5}} \exp \left[B1(R_0, 2nn) \cdot \left[\frac{\lambda_{2nn}}{D_{Rn_rock}} \right]^{0.5} \cdot X \right] \right] \text{ at } X < 0 \quad (3-7-25)$$

and where

$$A2 = \left[\frac{1}{1 + \left[\frac{D_{Rn_rock}}{D_{Rn_water}} \right]^{0.5}} \exp \left[-B2(R_0, 2nn) \cdot \left[\frac{\lambda_{2nn}}{D_{Rn_water}} \right]^{0.5} \cdot X \right] \right] \text{ at } X > 0 \quad (3-7-26)$$

In Figure 3-7-3 we show the calculated equilibrium distributions of radon from different decay chains, normalized to the equilibrium contents of these Rn isotopes in the rock (within 10 cm from the cavity).

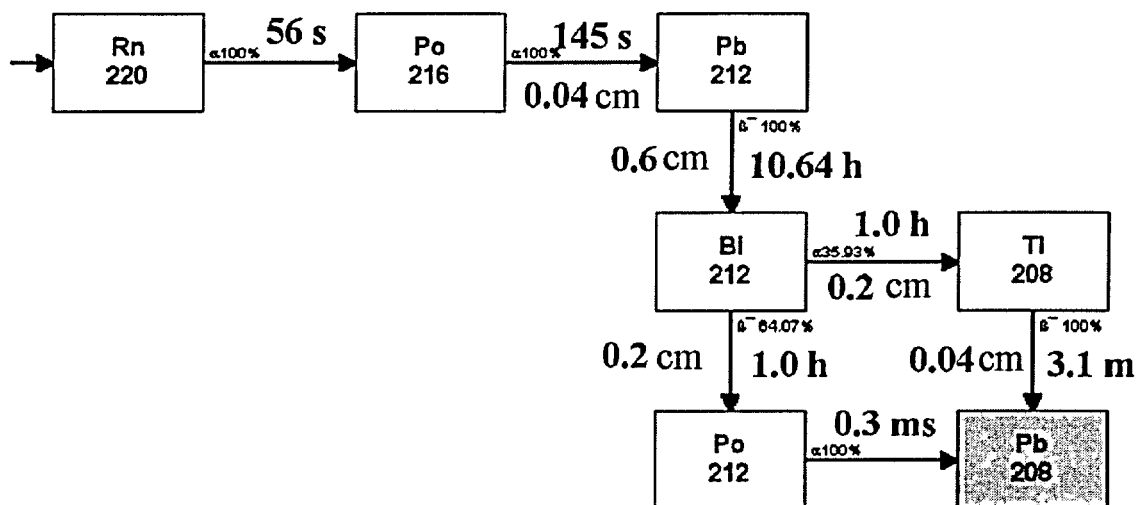


Figure 3-7-4. Chart showing decay chain from ^{220}Rn to stable ^{208}Pb . Also shown are half-lives of isotopes, probabilities of the specific decay path (in %), as well as effective displacement radii (R_{eff}) – distances, on which an isotope can move in water via diffusion before it decays into the next in chain.

3.7.3.2.5. Diffusion mobility of the daughters of Rn

The isotopes of radon are chemically inert and their distributions in the rock matrix and in water are controlled primarily by the coefficients of diffusion in the respective mediums. In the decay chain from the respective radon parents to stable ^{206}Pb , ^{207}Pb and ^{208}Pb there is a number of daughters. Below we analyze them from the standpoint of the model of diffusion migration.

The presence of intermediate daughters complicates the calculation of concentrations of radiogenic lead isotopes in the model cavity for two reasons. First, the intermediate daughters (e.g., Po and Bi) have chemical properties, which differ from those of Pb; therefore their adsorption on and desorption from the surface of growing minerals may occur at different rates than Pb. Second, the daughters of the intermediate daughters adsorbed on the surface of the cavity, mineral or colloidal particle, have a substantial probability, in the case of their parent's decay, to be ejected back into the solution. For example, the probability that an atom, which originated by decay of an alpha-emitting parent atom absorbed on the surface of a $0.1\ \mu\text{m}$ -sized colloidal particle, will return to the solution is approximately 50 %.

We evaluate, from this point of view, the specifics of migration of the three radon isotopes and their daughters.

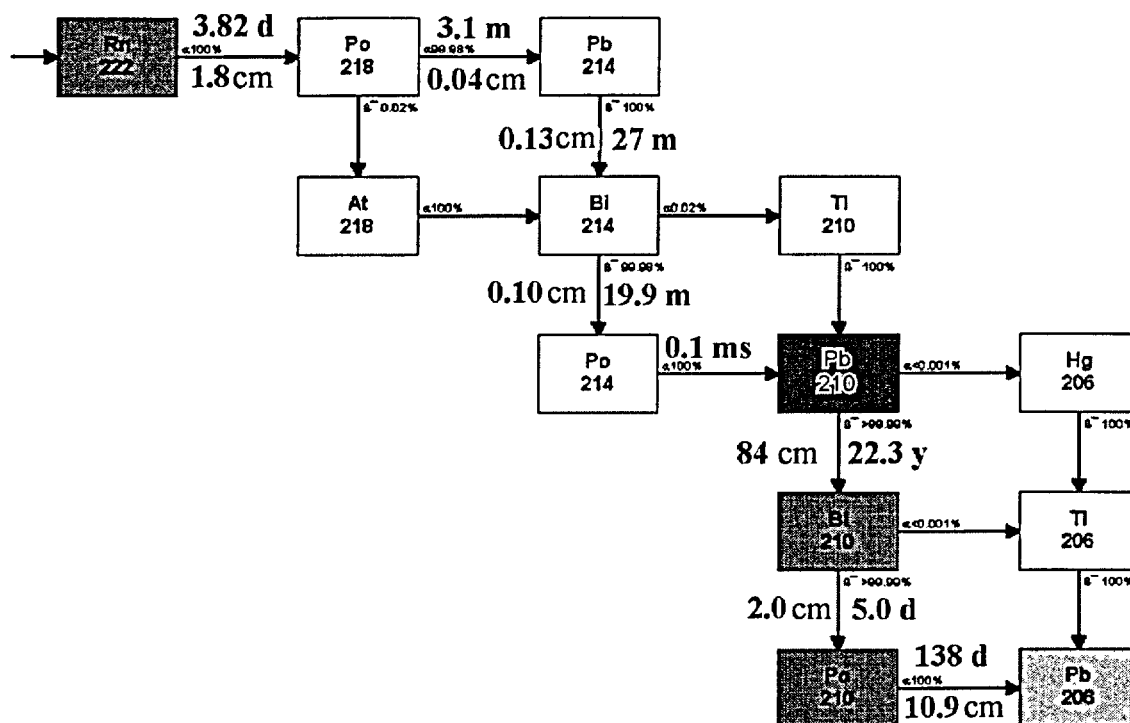


Figure 3-7-5. Chart showing decay chain from ^{222}Rn to stable ^{206}Pb . Also shown are half-lives of isotopes, probabilities of the specific decay path (in %), as well as effective displacement radii (R_{eff}) – distances, on which an isotope can move in water via diffusion before it decays into the next in chain.

Diffusion migration in the decay chain $^{232}\text{Th} - ^{220}\text{Rn} - ^{208}\text{Pb}$

The half-life of ^{220}Rn , $T_{1/2} = 56$ s, and its immediate daughter is ^{216}Po ($T_{1/2} = 145$ s; Figure 3-7-4). Assuming the coefficient of diffusion of atoms in water is 10^{-5} $\text{cm}^2\cdot\text{s}^{-1}$, an average radius of displacement for ^{216}Po (i.e., average distance over which an atom of daughter isotope may migrate via diffusion from the place where the parent isotope had decayed) may be evaluated as:

$$R_{\text{eff}}(^{216}\text{Po}) \cong [D \cdot T_{1/2}(^{216}\text{Po})]^{0.5} \cong 400 \mu\text{m} \quad (3-7-27)$$

In this equation we equalize the time of diffusion to the half-life of the daughter element, because at greater times the concentrations of these elements decrease significantly due to decay. Unlike "normal" diffusion problems, the distribution of radioactive atoms may be defined with reasonable accuracy by diffusion over the time $T_{1/2}$ or $2T_{1/2}$.

Next in the decay chain is ^{212}Pb , for which $T_{1/2} = 10.64$ hours, which yields $R_{\text{eff}}(^{212}\text{Pb}) \cong 0.6$ cm. Then follows ^{212}Bi ($T_{1/2} = 1$ hour, $R_{\text{eff}}(^{212}\text{Bi}) \cong 0.2$ cm). In 64% of the cases, ^{208}Pb forms at or near the same spot as ^{212}Bi (because the only intermediate isotope, ^{212}Po , has $T_{1/2} = 0.3$ ms). In 36% of the cases,

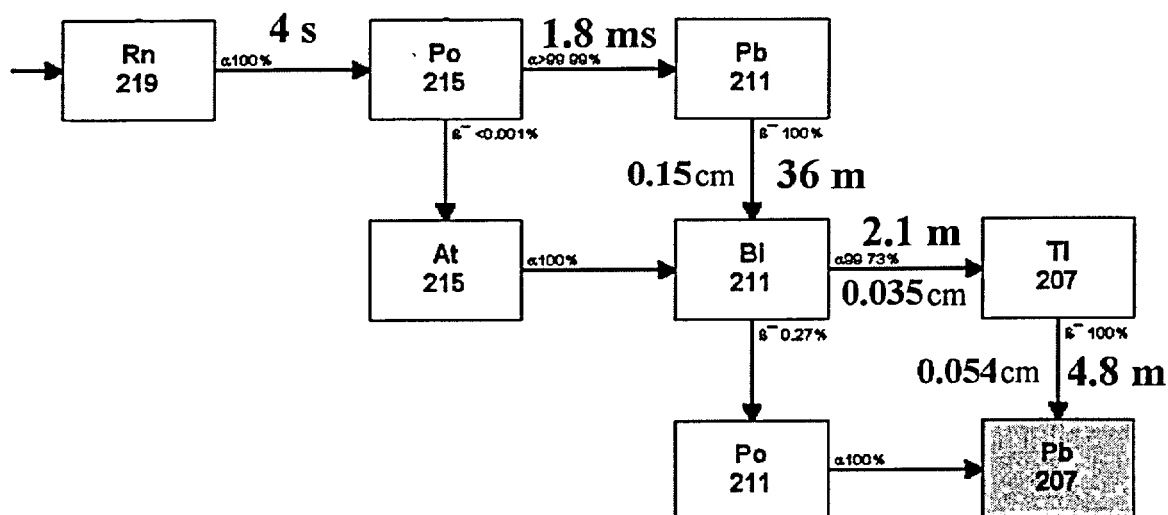


Figure 3-7-6. Chart showing decay chain from ^{219}Rn to stable ^{207}Pb . Also shown are half-lives of isotopes, probabilities of the specific decay path (in %), as well as effective displacement radii (R_{eff}) – distances, on which an isotope can move in water via diffusion before it decays into the next in chain.

the intermediate isotope is longer-lived ^{208}Tl ($T_{1/2} = 3.1$ min), so its radius of displacement $R_{eff}(^{208}\text{Tl}) \cong 420$ μm .

The effective displacement radius in the chain $^{220}\text{Rn} \rightarrow ^{208}\text{Pb}$ is found as the square root of the sum of all intermediate displacement radii (R_{eff} 's) and equals 0.64 cm (which means that the displacement is primarily controlled by the longest-lived isotope ^{212}Pb). This conclusion is important, because it allows the selection of realistic boundary conditions for equilibrium and fluxes of Pb isotopes in our models. For example, if it is assumed that the environment in the cavity does not change dramatically over the time of 1 hour (the half-life of ^{212}Bi), diffusion of lead in water may safely be approximated by the simplified decay chain $^{212}\text{Pb} \rightarrow ^{208}\text{Pb}$.

It may be inferred from the discussion above that in a spherical cavity with $R = 10$ cm, the input of $^{208}\text{Pb}_{\text{Rn}}$ (i.e., ^{208}Pb formed from independently migrating radon) is controlled by the flux of ^{220}Rn through the surface of the cavity, and by fluxes of ^{212}Pb that form within the sphere because of the decay of ^{220}Rn .

Diffusion migration in the decay chain $^{238}\text{U} - ^{222}\text{Rn} - ^{210}\text{Pb} - ^{206}\text{Pb}$

The half-life of ^{222}Rn ($T_{1/2}$) is 3.8 days. Its immediate daughter ^{218}Po has a $T_{1/2}$ of 3.1 min and $R_{eff}(^{218}\text{Po}) = 0.04$ cm. The displacement radii for all intermediate daughters in the chain are given in Figure 3-7-5. Unlike the ^{232}Th decay chain, some members of the ^{238}U chain have rather large diffusion

displacement radii (e.g., $R_{eff}(^{210}\text{Pb}) = 84$ cm, $R_{eff}(^{210}\text{Bi}) = 2.0$ cm, and $R_{eff}(^{210}\text{Pa}) = 10.9$ cm). This means that in a model cavity with $R = 10$ cm, such isotopes will inevitably contact cavity walls. Hence, their concentration in water filling the cavity will be controlled not only by kinetic factors, but also by conditions of equilibrium at the water/rock interface.

Diffusion migration in the decay chain $^{235}\text{U} - ^{219}\text{Rn} - ^{207}\text{Pb}$

In this chain, the greatest $R_{eff}(^{211}\text{Pb}) = 0.15$ cm (Figure 3-7-6). Thus, for many problems with characteristic times greater than 1 hour, it may safely be assumed that only the stable ^{207}Pb isotope moves via diffusion.

Characteristic scales: cavities vs. thin fractures

Considering the characteristic average radii of diffusion we assumed characteristic dimensions of the mineralized cavities at Yucca Mountain (i.e., $R = 5$ to 25 cm). It must be realized that the situation will change dramatically if the processes occur in a thin fracture. At fracture widths of about 0.1 cm, for many intermediate decay products the probability to contact the fracture wall and to be adsorbed becomes significant. Thus, the boundary conditions in thin fractures will be different from those in wider fractures and in cavities.

3.7.3.2.6. Concentrations of Pb isotopes in a cavity

In the ^{232}Th and ^{235}U decay series, the Rn isotopes transform into the stable Pb isotopes in less than 1 day. In the ^{238}U decay chain, two intermediate daughters have relatively long half-lives: ^{210}Pb ($T_{1/2} = 23$ years) and ^{210}Po ($T_{1/2} = 138$ days).

We address the following conditions: a concentration of ^{238}U in the rock $^{238}\text{U} = 5$ ppm (which translates into $\sim 2.5 \cdot 10^{16}$ atom $\cdot\text{cm}^{-3}$); $^{235}\text{U} = 0.0075 \cdot ^{238}\text{U}$ (which corresponds to the isotopic ratio in natural U); and $^{232}\text{Th} = 4 \cdot ^{238}\text{U}$. Equations for concentrations of Rn isotopes discussed above yield at the water-rock interface equilibrium concentrations of $^{222}\text{Rn} \cong 30,000$ atom $\cdot\text{cm}^{-3}$, $^{219}\text{Rn} = 0.01$ to 0.03 atom $\cdot\text{cm}^{-3}$, and $^{220}\text{Rn} = 5$ to 10 atom $\cdot\text{cm}^{-3}$. The production rates of the stable Pb isotopes at this interface equal: for ^{207}Pb - 0.004 atom $\cdot\text{cm}^{-3}\text{s}^{-1}$ and for ^{208}Pb - 0.1 atom $\cdot\text{cm}^{-3}\text{s}^{-1}$. For radioactive ^{210}Pb the production rate equals 0.055 atom $\cdot\text{cm}^{-3}\text{s}^{-1}$.

Our system has a number of characteristic time scales, which control the maximum concentrations of Pb that may be created in the cavity. First is the time for reaching equilibrium concentrations of Pb isotopes, provided the surface of a cavity serves as a "sink" for these isotopes. This time is controlled by

the coefficient of diffusion of Pb in water* and the size of the sphere. Assuming $D_{Pb_water} = 10^{-5} \text{ cm}^2 \cdot \text{s}^{-1}$, the time necessary for establishing equilibrium concentrations of Pb isotopes in cavities with $R = 1, 5, \text{ and } 10$ cm will be $t_{eq} = 1\text{-}2$ days, 30 days (1 month), and 120 days (or 4 month), respectively. The most intense removal of Pb isotopes from water onto the cavity surface would be characteristic of the greatest sphere ($R = 10$ cm); the process, however, involves only an approximate, 1 cm-thick, layer of water adjacent to the cavity wall.

3.7.3.2.7. A model: generation and accumulation of Pb-isotopes in a cavity filled with stagnant water

We are interested in the distribution of Pb-isotopes that form due to decay of Rn in a cavity. Formally, the problem may be presented (e.g., for ^{222}Rn) as:

$$\frac{\partial {}^{222}\text{Rn}(\vec{r}, t)}{\partial t} = D\Delta {}^{222}\text{Rn} - \lambda_{222} \cdot {}^{222}\text{Rn}(\vec{r}, t) \quad (3-7-28)$$

$$\frac{\partial {}^{210}\text{Pb}(\vec{r}, t)}{\partial t} = D\Delta {}^{210}\text{Pb} + \lambda_{222} \cdot {}^{222}\text{Rn}(\vec{r}, t) \quad (3-7-29)$$

Boundary conditions. Assume the concentration of Rn on the surface of the cavity ($R = R_{sphere}$) corresponds to the values obtained in the previous section (Eq. 3-7-24).

$${}^{222}\text{Rn}(t, R_{sphere}) = \frac{{}^{226}\text{Ra}(tuff) \cdot \lambda_{226}}{\lambda_{222}} \cdot \left[\frac{2}{1 + \left(\frac{D_{Rn_tuff}}{D_{Rn_water}} \right)^{0.5}} \right] \quad (3-7-30)$$

It can be demonstrated that the equation describing the concentration of Pb-isotopes in the cavity does not have a stationary solution, although it has an asymptotic solution at infinite time ($t = \infty$). This stems from the fact that Pb isotopes accumulate in the cavity and become immobilized (adsorbed) upon contact with cavity walls. Numeric solutions for the accumulation of different Rn and Pb isotopes in cavities with different sizes are discussed below.

Analysis of the $^{222}\text{Rn} - {}^{210}\text{Pb} - {}^{206}\text{Pb}$ system

In this decay chain all intermediate daughters transform quickly (in less than 1 hour) to ^{210}Pb . The half-life of the latter isotope is 22.3 years, and its effective diffusion displacement radius is 84 cm. If the

* In this work we simplify the problem by considering "generic" Pb rather than the specific species of Pb that will be present in water. For our problem these will be PbOH^+ and subordinate Pb^{2+} . Since the diffusion coefficients for these species differ by a factor not exceeding 2, this simplification seems to be justified.

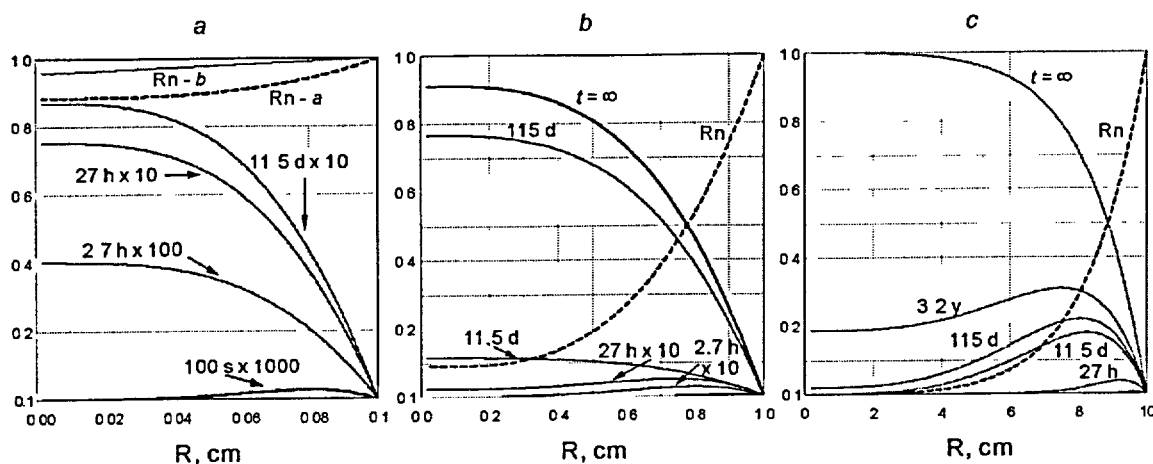


Figure 3-7-7. Dynamics of accumulation of ^{206}Pb (solid lines) and the equilibrium concentration profile of ^{222}Rn (dashed line) in spherical cavity filled with stagnant water. Cavity radii: *a* – 0.1 cm; *b* – 1.0 cm; and *c* – 10 cm. The curve *Rn-a* shows numerical solution for radon; *Rn-b* shows analytical exponential solution. Calculations were carried out for spherical geometry. For the slot geometry (e.g., thin fracture with width $H = 0.1$ cm) distributions of isotopes are similar.

^{210}Pb isotope gets adsorbed at the surface of a growing mineral and the atom gets covered with more than 2 to 4 molecular layers of the mineral during its half-life, its chances to re-dissolve and return to the solution become negligible. This is a likely situation, because the growth rate of 2 molecular layers per 22 years would correspond to the linear growth rate of about 1 mm per 40 Ma, which is so low that it does not seem to be physically plausible; the actual growth rates must be many orders of magnitude greater. The decay chain contains two more members having relatively large diffusion displacement radii (^{210}Bi and ^{210}Po – 2.0 and 10.9 cm respectively). The assumption introduced above allows us to neglect the role of these two isotopes in diffusion migration in the sphere and to treat ^{210}Pb as the proxy for ^{206}Pb . The results of the numeric calculations for the behavior of ^{210}Pb in three spheres ($R = 0.1, 1.0,$ and 10.0 cm) are shown in Figure 3-7-7. All calculations are normalized to the contents of Rn at the cavity wall. It should be noted that calculations for the slot geometry yield similar concentration profiles at a slot width of $H = 0.1$ cm. Thus, the results for spherical cavities with $R = 0.1$ cm are applicable to the fractures with opening of $H = 0.1$ cm.

For a cavity with $R = 0.1$ cm, (Figure 3-7-7-*a*), the concentration of Rn in the central part of the sphere will promptly reach an asymptotic value of 0.9. For the asymptotic solution ($t = \infty$) the following equality must hold:

$$Pb(\infty, X) + Rn(\infty, X) = 1 \quad (3-7-31)$$

For any coordinate X , in the center of the sphere with $R=0.1$ cm, the normalized Pb contents should not exceed 0.1 (note that in the figure the curves show Pb concentrations with different multipliers). It is

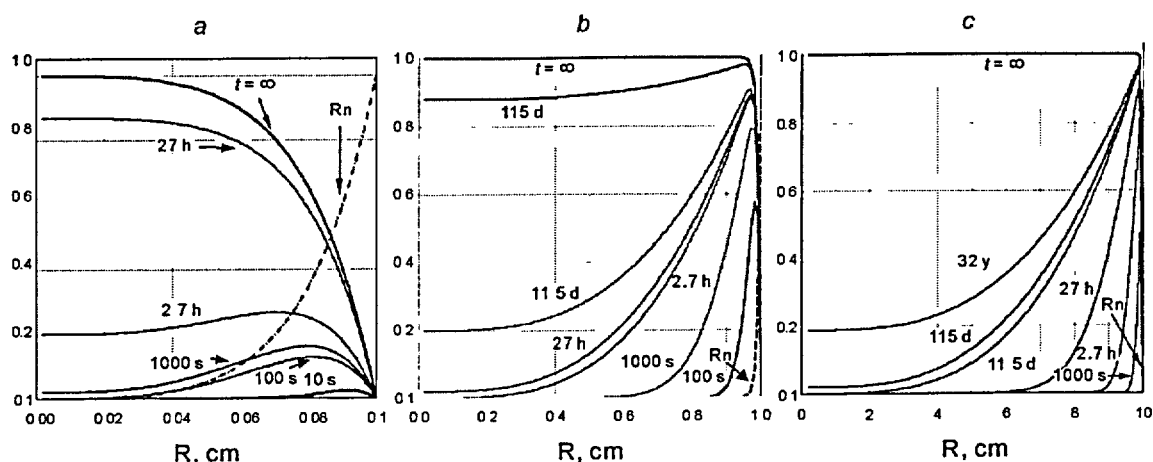


Figure 3-7-8. Dynamics of accumulation of ^{207}Pb (solid lines) and the asymptotic concentration profile of ^{219}Rn (dashed line) in spherical cavity filled with stagnant water. Cavity radii: $a - 0.1$ cm; $b - 1.0$ cm; and $c - 10$ cm. Calculations were carried out for spherical geometry. For the slot geometry (e.g., thin fracture with width $H = 0.1$ cm) distributions of isotopes are similar.

apparent that both ^{222}Rn and ^{210}Pb reach quasi-stationary distributions after approximately 1 day. In a cavity with $R = 1$ cm, the distributions are drastically different. The concentration of Rn in the center of the sphere stabilizes at about 0.1, which means that Pb may accumulate until it reaches a 0.9 value. Accumulation is relatively slow, so that the normalized concentration of 0.77 is reached in approximately 115 days. In a cavity with $R = 10$ cm, the concentration of Rn in the center of the cavity is practically 0, which gives an asymptotic solution for Pb concentrations of 1. The process is slow, however, and more than 3 years are needed to reach a normalized concentration of $\text{Pb} = 0.2$.

Assuming that reasonable characteristic times for the diffusion of Pb-isotopes in a cavity up to $R = 10$ cm range between 1 and 10 days, it is possible to visualize the characteristic distributions of Pb inside a cavity. Importantly, these distributions have maximums between 1 and 2 cm from the cavity wall.

Analysis of the $^{219}\text{Rn} - ^{207}\text{Pb}$ system

In this decay chain there are no elements with substantial diffusion displacement radii. Hence, it may be assumed that the calculations relate directly to ^{207}Pb . The very short half-life of ^{219}Rn ($T_{1/2} = 4$ s) sets this system apart from the $^{222}\text{Rn} - ^{210}\text{Pb} - ^{206}\text{Pb}$ system. This means that radon cannot move more than 0.03 cm from the cavity wall. This, in turn, implies that the dominant process of ^{207}Pb redistribution inside the cavity is diffusion. For example, for a cavity with $R = 0.1$ cm, the asymptotic distribution of ^{207}Pb is reached within tens of hours. For a time of less than 1 hour there is a sharp maximum near the cavity wall (Figure 3-7-8).

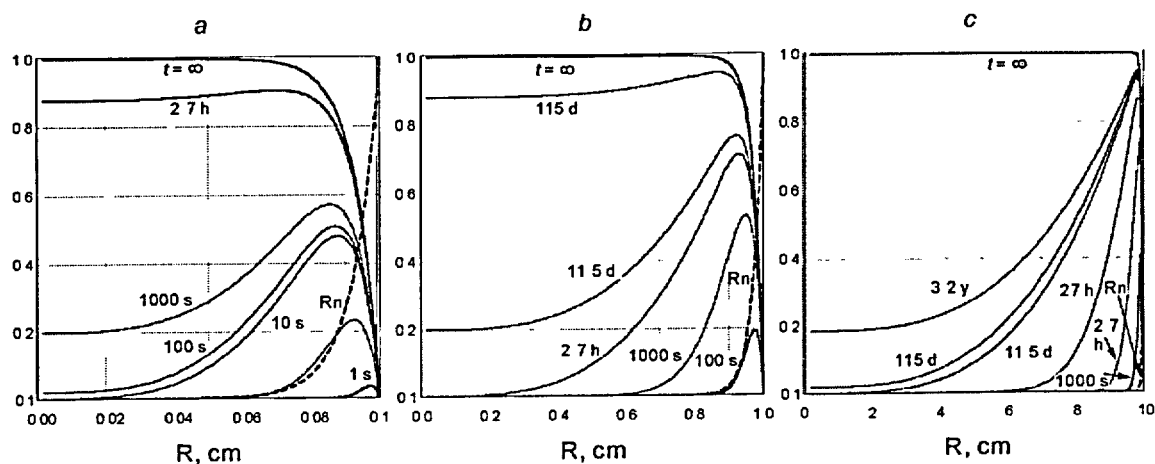


Figure 3-7-9. Dynamics of accumulation of ^{208}Pb (solid lines) and the asymptotic concentration profile of ^{220}Rn (dashed line) in spherical cavity filled with stagnant water. Cavity radii: $a - 0.1$ cm; $b - 1.0$ cm; and $c - 10$ cm. Calculations were carried out for spherical geometry. For the slot geometry (e.g., thin fracture with width $H = 0.1$ cm) distributions of isotopes are similar.

For spheres with $R = 1$ and 10 cm, sharp maximums persist very close to the cavity wall. It might be assumed that the concentration of ^{207}Pb monotonically decreases toward the center of the cavity (which is in sharp contrast to the ^{206}Pb distribution). For a characteristic time of 10 days, substantial concentrations of Pb may be expected within 4 cm from the cavity wall.

Analysis of the $^{220}\text{Rn} - ^{208}\text{Pb}$ system

In this decay chain the intermediate ^{212}Pb has $T_{1/2} = 10.6$ hours. Its daughter, ^{212}Bi , has a half-life of approximately 1 hour. It is thus possible that physicochemical properties of bismuth affect to some extent the kinetics of its uptake into the growing minerals (e.g., possible desorption from the opal surface and its return to the solution). Its influence on the overall system performance, however, is not expected to be significant primarily because of the relatively short half-life. Thus, the results shown in Figure 3-7-9 should be representative of stable ^{208}Pb . As is apparent from the figure, the results are quite similar to those for the ^{219}Rn chain.

3.7.3.2.8. Comparison between the theoretical estimates and the experimental data

It is apparent from the discussion above that the kinetics for the accumulation of Pb-isotopes in a cavity may lead to the appearance of a non-uniform distribution of Pb-isotopes in the water through out the cavity's space. These distributions differ depending on the Rn-isotope (long-lived or short-lived), which is the parent of the Pb isotope of interest.

Using the data from the database described in Appendices 1 and 2 (Neymark et al., 2000 and 2002), we plotted the distribution of Pb isotopes across individual mineral crusts from fractures and lithophysal

cavities. In the series of figures discussed below we compared the distribution of the total abundances of Pb isotopes with the distribution of their abundances corrected for the presence of "common lead" using the correction values suggested by Neymark et al. (2002). For example, for ^{208}Pb (Figure 3-7-10), the equation is: $^{208}\text{Pb}^* = ^{208}\text{Pb} - 38.78 \cdot ^{204}\text{Pb}$ (asterisk denotes calculated radiogenic Pb after subtraction of the common-Pb component).

The equation

$$^{208}\text{Pb}^* = 0.2 \exp\left[-\frac{L}{0.5}\right], \quad (3-7-32)$$

where L is the distance from the cavity wall [cm] approximates the maximum values of the $^{208}\text{Pb}^*$

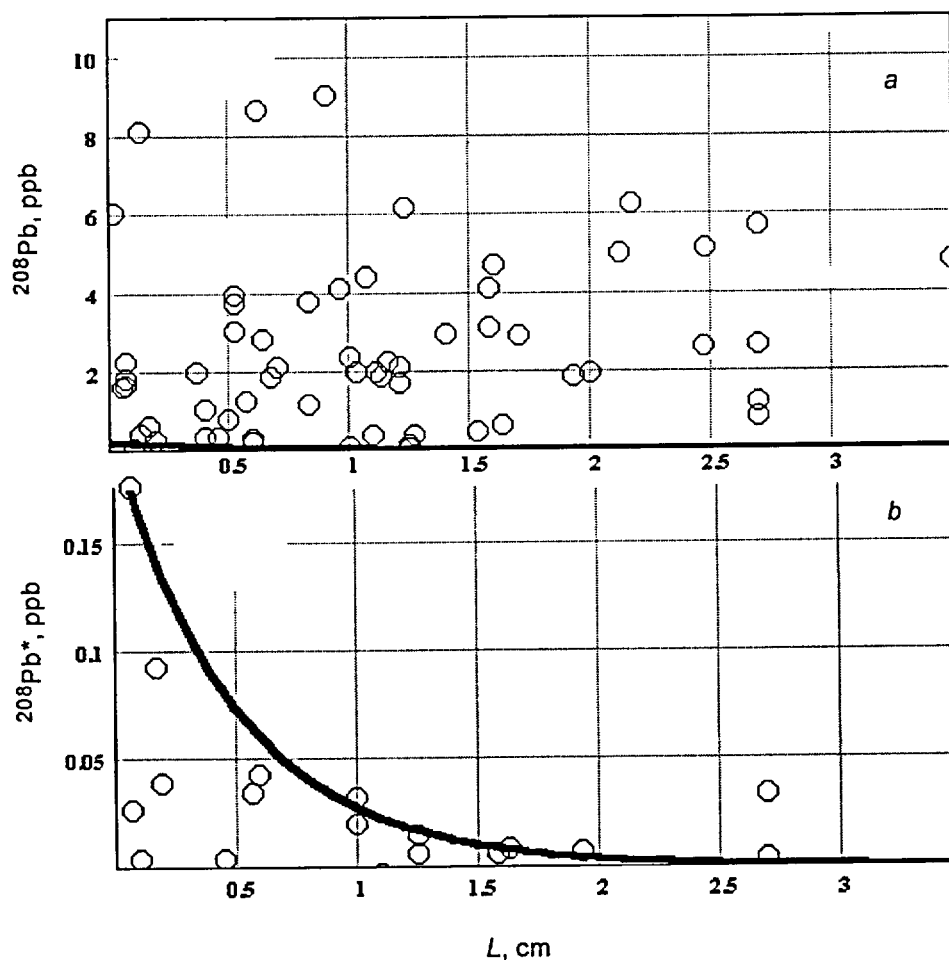


Figure 3-7-10. Distribution of total ^{208}Pb (a) and corrected $^{208}\text{Pb}^*$ (i.e., after subtraction of the common-Pb component; b) as a function of the distance from cavity wall L . It is assumed that minerals are deposited directly on the cavity walls, so that the base of mineral crust corresponds to 0 on the abscissa. Information regarding L was obtained from line drawings and one photograph of samples presented in Neymark et al. (2002; see Appendix 3-7-1).

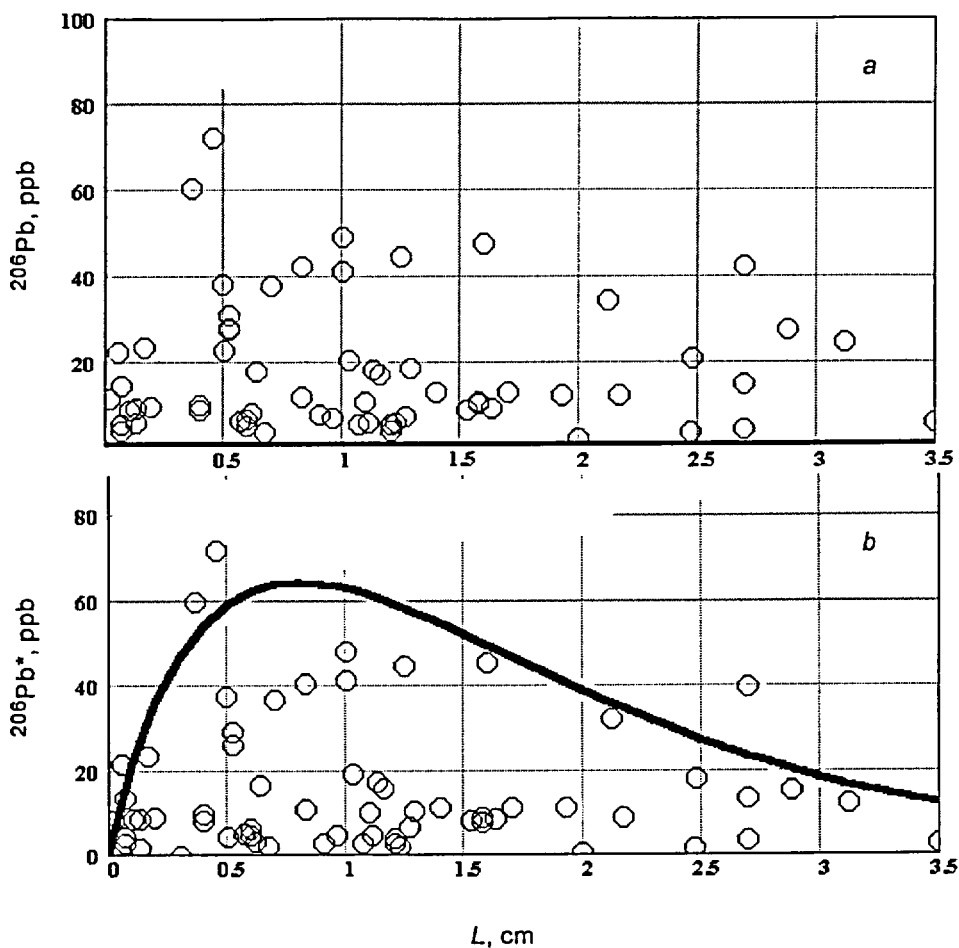


Figure 3-7-11. Distribution of total ^{206}Pb (a) and corrected $^{206}\text{Pb}^*$ (i.e., after subtraction of the common-Pb component; b) as a function of the distance from cavity wall L . It is assumed that minerals are deposited directly on the cavity walls, so that the base of mineral crust corresponds to 0 on the abscissa. Information regarding L was obtained from line drawings and one photograph of samples presented in Neymark et al. (2002; see Appendix 3-7-1).

[ppb]. Even though the contents of "uncorrected" ^{208}Pb are tenfold multiples greater than the obtained values of corrected $^{208}\text{Pb}^*$ (i.e., large values of "common lead" were deducted from large values of total lead), the results obtained do not seem to have a "noisy" character. This demonstrates the high quality of the measurements reported by Neymark et al. (2000 and 2002). By comparing the experimental approximation curve (Eq. 3-7-32) with the theoretical calculations for a sphere with $R = 10$ cm for this isotope (see Figure 3-7-9), it was found that the rate of decay of the ^{208}Pb -concentrations suggests characteristic times of about 10-20 hours.

Figure 3-7-11 shows similar graphs for ^{206}Pb . In this case, the corrected values were calculated by: $^{206}\text{Pb}^* = ^{206}\text{Pb} - 18.83 \cdot ^{204}\text{Pb}$. We used data belonging to the first mode of the concentration

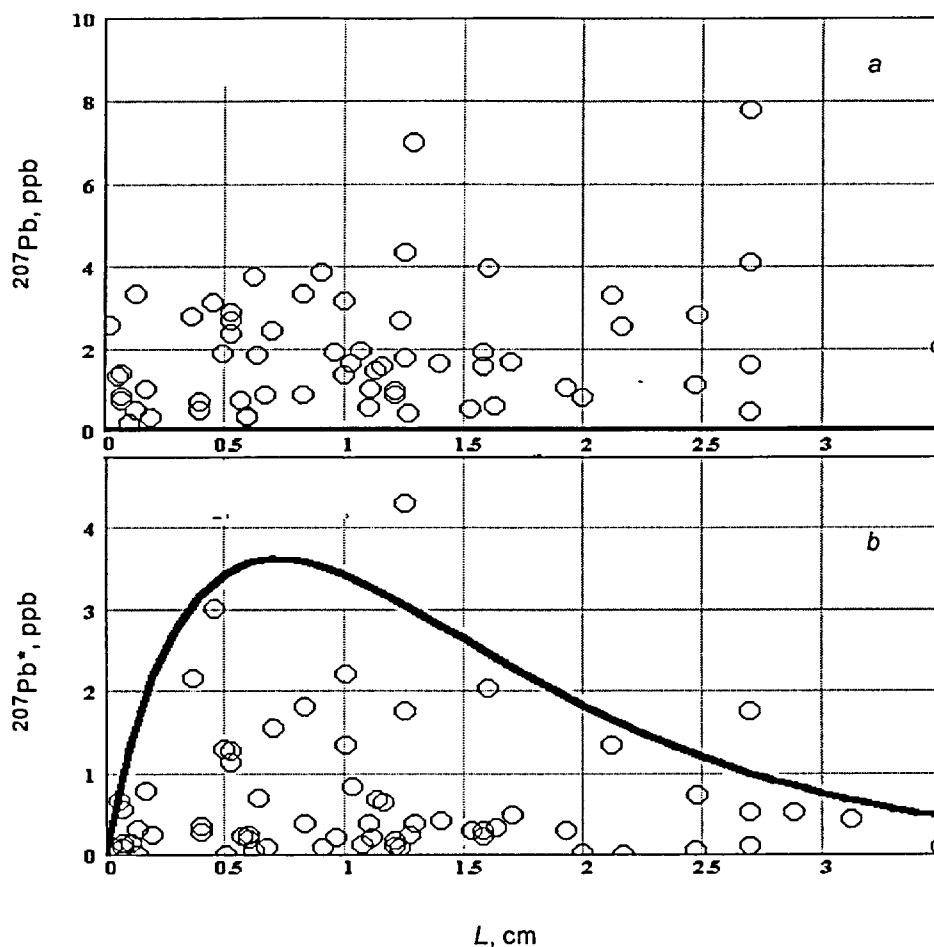


Figure 3-7-12. Distribution of total ^{207}Pb (a) and corrected $^{207}\text{Pb}^*$ (i.e., after subtraction of the common-Pb component; b) as a function of the distance from cavity wall L . It is assumed that minerals are deposited directly on the cavity walls, so that the base of mineral crust corresponds to 0 on the abscissa. Information regarding L was obtained from line drawings and one photograph of samples presented in Neymark et al. (2002; see Appendix 3-7-1).

distributions ($Pb_{total} < 100$ ppb) which means that only a few measurements with Pb concentrations greater than 100 ppb were excluded.

Unlike ^{208}Pb , the distributions shown on the upper and the lower graphs are quite similar. This is understandable, since concentrations of total ^{206}Pb are much greater than concentrations of the "common" ^{206}Pb . The distribution of the maximum values of $^{206}\text{Pb}^*$ may be described by the equation:

$$^{206}\text{Pb}^* = 24 \cdot L^{0.9} \exp\left[-\frac{L}{0.9}\right] \quad (3-7-33)$$

The experimental curve (Eq. 3-7-33) demonstrates reasonable agreement with theoretical curves for a sphere with $R = 10$ cm for ^{206}Pb (see Figure 3-7-7) at characteristic times of 10 to 20 hours.

Figure 3-7-12 shows graphs for ^{207}Pb . The corrected values were calculated by equation $^{207}\text{Pb}^* = ^{207}\text{Pb} - 15.62 \cdot ^{204}\text{Pb}$. It is apparent that values for concentrations on the upper and the lower graphs are different (times). This feature was expected because, for ^{207}Pb , the total contents of the isotope are very similar to the contents of the "common lead" (see Appendix 3-7-2, Figure 3-7-A-32). The behavior of the maximum $^{207}\text{Pb}^*$ values can be approximated by:

$$^{207}\text{Pb}^* = 1.5 \cdot L^{0.9} \exp\left[-\frac{L}{0.8}\right] \quad (3-7-34)$$

The experimental curve (Eq. 3-7-34) is clearly different from all those in the family of curves calculated for a cavity with $R = 10$ cm (see Figure 3-7-8). Owing to the short half-life of ^{219}Rn , the monotonically decreasing curves similar to those calculated for ^{208}Pb would also be expected for ^{207}Pb ; instead, the experimental curves have shapes similar to those obtained for the longer-lived ^{222}Rn and possess a maximum.

It is clear therefore that our simple model, while reasonably explaining the patterns of accumulation of ^{206}Pb and ^{208}Pb , fails to adequately explain the patterns observed for ^{207}Pb . From the standpoint of geology, the model (i.e., accumulation of Pb-isotopes in a cavity filled with stagnant water) is undoubtedly overly simplistic. In order to deposit the quantities of minerals observed in cavities at Yucca Mountain, the water would have to be changing many times, which means, the water must have moved repeatedly through the cavity. In the subsequent sections we shall consider a model that takes into account such water flows.

3.7.3.3. Model case 2: Thin fracture

In previous sections we considered the processes of generation, migration and accumulation of Rn and Pb_{Rn} in cavities. The cavities were considered in isolation from the surrounding rock. This is a simplification, because water entering a cavity will already contain dissolved Pb isotopes acquired in the course of its flow through thin interconnected fractures and pores of the tuff. In this section we examine the processes occurring in thin water-bearing fractures in the bedrock tuff.

3.7.3.3.1. Distribution of isotopes in narrow fractures and the time required to reach steady state

Below we introduce three postulates that serve as a basis of the model.

Postulate 1. Water in fractures contain dissolved Pb-isotopes. The contents of Pb-isotopes in the water reflect an equilibrium with Pb-isotopes residing on the surface of the tuff at the water-rock interface.

Postulate 2. The width of the model fracture $H = 0.1$ cm. Over time $t_D = L^2/D$ (where D is the coefficient of diffusion for Pb atoms or Pb-bearing complexes) the equilibrium profile of Pb will form

across the fracture. Assuming $H = 0.1$ cm, $D = 10^{-5}$ cm²·s⁻¹ we obtain $t_D = 1000$ s. In other words, time on the order of 15 min is sufficient for establishing stationary concentrations of Pb isotopes, which are produced by the decay of Rn.

Postulate 3. The appearance of these additional Pb-isotopes in water does not change the boundary conditions for total Pb at the fracture-water interface. In other words, the concentration of Pb at the interface does not change appreciably due to Rn-decay. We now examine the validity of the later postulate.

Consider the ²²²Rn – ²⁰⁶Pb system. Both varieties of Pb discussed in our model (common Pb and Pb_{Rn}) may reside inside the volume of water (²⁰⁶Pb_{vol} and ²⁰⁶Pb_{Rn_vol}) or they may be adsorbed on the cavity surface (²⁰⁶Pb_{surf} and ²⁰⁶Pb_{Rn_surf}). Assume that at a time t , the surface of the tuff at the fracture-water interface contains ²⁰⁶Pb_{surf} atom·cm⁻² of the ²⁰⁶Pb isotope. The flux of the isotope entering the water (number of atoms per cm² per second) may be defined as $K_{dis} \cdot ^{206}\text{Pb}_{surf}$, where K_{dis} is the constant of dissociation. At equilibrium, the same number of atoms return to the surface: $K_{ads} \cdot ^{206}\text{Pb}_{vol}$, where ²⁰⁶Pb_{vol} is the effective concentration of the isotope near the surface (within a few angstroms) and K_{ads} is the constant of adsorption. (Here K_{dis} and K_{ads} are constants in the most general form).

The condition of equilibrium for the common ²⁰⁶Pb may be written as:

$$K_{dis} \cdot ^{206}\text{Pb}_{surf} = K_{ads} \cdot ^{206}\text{Pb}_{vol} \quad (3-7-35)$$

Now consider the equilibrium for Pb isotopes formed from Rn decaying in the thin fracture (channel). In a cylindrical channel with radius R and length dL , the number of Rn atoms decaying (or, Pb atoms forming) per second is:

$$I(\text{Pb}) = dL \int_0^R \lambda_{222} ^{222}\text{Rn}(R) \cdot 2\pi R dR \quad (3-7-36)$$

The Pb atoms will be adsorbed on the channel surface whose area is:

$$dS = dL \cdot 2\pi R \quad (3-7-37)$$

The equation describing changing concentrations of ²²²Rn-derived ²⁰⁶Pb atoms under these conditions on the channel surface [atom·cm⁻²·s⁻¹] will assume the form:

$$\frac{d^{206}\text{Pb}_{Rn_surf}}{dt} = \frac{dL \int \lambda_{222} ^{222}\text{Rn}(R) \cdot 2\pi R dR}{dL \cdot 2\pi R_0} - K_{dis} \cdot ^{206}\text{Pb}_{Rn_surf} + K_{ads} \cdot ^{206}\text{Pb}_{Rn_vol} \quad (3-7-38)$$

Assuming the derivative in Eq. 3-7-38 is much smaller than all other terms (a condition of equilibrium):

$$\frac{dL \int \lambda_{222}^{222} Rn(R) \cdot 2\pi R dR}{dL \cdot 2\pi R_0} - K_{dis} \cdot {}^{206}Pb_{Rn_surf} + K_{ads} \cdot {}^{206}Pb_{Rn_vol} = 0 \quad (3-7-39)$$

The physicochemical properties of Pb do not depend on its origin (i.e., "common" or Rn-derived). Therefore, the K_{dis} , which accounts for all mechanisms for the dissolution of lead (i.e., in the form of atoms, complexes, compounds, etc.) at the tuff surface can be eliminated by using Eq. 3-7-35:

$$K_{dis} = K_{ads} \cdot \frac{{}^{206}Pb_{vol}}{{}^{206}Pb_{surf}} \quad (3-7-40)$$

Before proceeding further with this discussion, we need to make two observations. First, the dimensions of the surface and volume densities of atoms are different (atom·cm⁻² and atom·cm⁻³ respectively), hence the constants K_{dis} and K_{ads} also have different dimensions. Second, upon reaching stationary conditions (i.e., after about 1000 s), the term $\frac{dL \int \lambda_{222}^{222} Rn(R) \cdot 2\pi R dR}{dL \cdot 2\pi R_0}$ becomes a constant

whose value depends solely on the radius (or, in more general terms, on the geometry) of the channel and the concentration of the parent Rn. Because the decay chain of ²³⁸U in the bedrock tuff is in secular equilibrium, the following equality holds true:

$$\lambda_{222} \cdot {}^{222}Rn = \lambda_{238} \cdot {}^{238}U \quad (3-7-41)$$

and therefore,

$$\frac{dL \int \lambda_{222}^{222} Rn(R) \cdot 2\pi R dR}{dL \cdot 2\pi R_0} = \frac{\lambda_{238}}{\lambda_{222}} \cdot {}^{238}U \cdot \frac{\int {}^{222}Rn(R) \cdot 2\pi R dR}{dL \cdot 2\pi R_0} = \frac{\lambda_{238}}{\lambda_{222}} \cdot {}^{238}U \cdot G \quad (3-7-42)$$

We introduced the parameter G without defining it because in order to define it, it is necessary first to define the specific geometry of the problem, which may be idealized (e.g., sphere, channel, slot, etc.) or measured in the field, and second, based on the geometry it is necessary to numerically calculate the distribution of Rn inside the cavity. For example, for a spherical cavity, the distribution of Rn was calculated in section "A model: generation and accumulation of Pb-isotopes in a cavity filled with stagnant water" (see Figures 3-7-7 through 3-7-9) above.

Based on the considerations presented above and using Eq. 3-7-40, the stationary equation 3-7-39 may be re-written as:

$$\frac{\lambda_{238}}{\lambda_{222}} \cdot {}^{238}\text{U} \cdot G + K_{dis} \cdot {}^{206}\text{Pb}_{surf} \cdot \left[\frac{{}^{206}\text{Pb}_{Rn_vol}}{{}^{206}\text{Pb}_{vol}} - \frac{{}^{206}\text{Pb}_{Rn_surf}}{{}^{206}\text{Pb}_{surf}} \right] = 0 \quad (3-7-43)$$

It follows that the ${}^{206}\text{Pb}_{Rn_vol}$ near the tuff surface is significantly smaller than the maximum value, which may be achieved in this closed volume:

$$\text{Max } {}^{206}\text{Pb}_{Rn_vol} = \frac{\lambda_{238}}{\lambda_{222}} \cdot {}^{238}\text{U} \quad (3-7-44)$$

The numeric assessment of the $\frac{\lambda_{238}}{\lambda_{222}} \cdot {}^{238}\text{U}$ values yields maximum concentrations of the Rn-derived ${}^{206}\text{Pb}$ in water on the order of 10^{-6} ppb (assuming bedrock tuff contains 5 ppm of ${}^{238}\text{U}$). Such minute concentrations allow the simplification of Eq. 3-7-43:

$$\frac{\lambda_{238}}{\lambda_{222}} \cdot {}^{238}\text{U} \cdot G = K_{ads} \cdot {}^{206}\text{Pb}_{vol} \cdot \frac{{}^{206}\text{Pb}_{Rn_surf}}{{}^{206}\text{Pb}_{surf}} \quad (3-7-45)$$

or

$$\frac{\lambda_{238}}{\lambda_{222}} \cdot {}^{238}\text{U} \cdot G \cdot \frac{{}^{206}\text{Pb}_{surf}}{{}^{206}\text{Pb}_{Rn_surf}} = K_{ads} \cdot {}^{206}\text{Pb}_{vol} \quad (3-7-46)$$

Eq. 3-7-46 is now written in the form analogous to that of Eq. 3-7-35. This allows us to define the effective dissociation constant:

$$K_{eff_dis} = \frac{\lambda_{238}}{\lambda_{222}} \cdot {}^{238}\text{U} \cdot D \cdot \frac{1}{{}^{206}\text{Pb}_{Rn_surf}} \quad (3-7-47)$$

It is important to recognize that for Rn-derived Pb, the effective dissociation constant, K_{eff_dis} , depends on the concentration of U in the tuff, as well as on the parameter G, which reflects the geometry of the cavity and the dynamics of the accumulation of Rn in the cavity. This emphasizes the fact that the chemical processes of redistribution of the Pb (accounted for by the last term of Eq. 3-7-47) play only a partial role in the overall redistribution of the Rn-derived Pb in open cavities. The contents of U in the tuffs of Yucca Mountain vary within a relatively narrow range (between 3-7 ppm, NBMG, 2000). The highly consistent values measured for Pb isotopes in opals (reported by Neymark et al., 2000 and 2002) suggests that the adsorptive properties of the surfaces of cavities relative to Pb remain largely constant in the course of mineral growth. The only remaining factor that may change the concentrations of Rn in different areas of the cavities is the geometry. Our qualitative assessments show that geometry-related changes may be as large as up to 4 orders of magnitude.

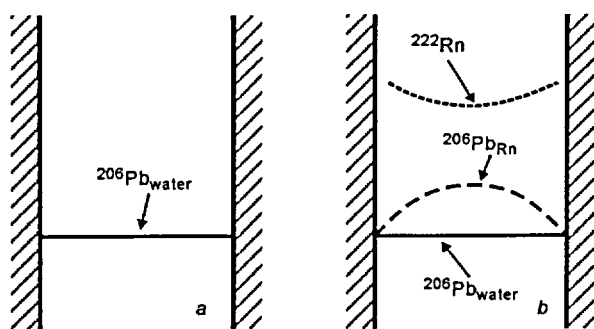


Figure 3-7-13. Schematic presentation of the characteristic concentration profiles for "common" $^{206}\text{Pb}_{\text{water}}$ (a), as well as concentrations of ^{222}Rn and "additional" $^{206}\text{Pb}_{\text{Rn}}$ formed through the decay of ^{238}U in the rock, diffusion and decay of ^{222}Rn (b). Fracture width is 0.1 cm.

3.7.3.4. Model case 3: Distribution of Rn- and Pb-isotopes in a cavity with moving water

In order to obtain semi-quantitative descriptions of the processes occurring in a cavity through which water flows, the following model geometry was used. A channel with radius R_0 enters the top of a cone (an "overturned funnel" geometry). This geometry imitates the intersection of a fracture with a lithophysal cavity. It may be demonstrated that the details of the geometry do not alter the essence of our

conclusions regarding the processes operational inside cavities.

3.7.3.4.1. Distribution of isotopes in a channel

The distribution of the "common" ^{206}Pb is schematically shown in Figure 3-7-13-a. Since generation in water is not considered, the concentration of ^{206}Pb will be constant across the channel. Now consider the supply of ^{222}Rn from wallrock into the fracture. In such a narrow fracture (0.1 cm) its concentration in water will be nearly constant with a slight (5-10%) decrease in the center. The distributions of Rn and Pb in the small sphere of $R = 0.1$ cm presented above (Figures 3-7-7-a through 3-7-9-a) may serve as a reasonable approximation of the steady state in a thin channel. According to the condition discussed above, which requires that the sum of the maximum concentrations of Pb and Rn isotopes equal one, the concentration of ^{210}Pb in the center of the channel may not be greater than a few per cent of the maximum possible concentration. In other words, the concentrations of the ^{210}Pb isotope are significantly smaller than those in wide fractures and cavities.

For the ^{220}Rn and ^{219}Rn decay chains, however, the patterns are virtually the opposite to that of the ^{222}Rn chain (Figure 3-7-14). This is because of the short half-life of these isotopes.

3.7.3.4.2. Calculations for the model geometry: channel-cone

The set of base equations was discussed earlier (Eqs. 3-7-8 through 3-7-10). For the given geometry, the symmetry is one of a cylinder, which greatly simplifies numerical calculations. Equations for ^{222}Rn and ^{210}Pb are:

$$\frac{\partial^{222}\text{Rn}(\vec{r}, t)}{\partial t} = D_{\text{Rn}} \Delta^{222}\text{Rn} + \nabla_r \cdot (\vec{V} \cdot^{222}\text{Rn}) - \lambda_{222} \cdot^{222}\text{Rn}(\vec{r}, t) \quad (3-7-48)$$

and

$$\frac{\partial {}^{210}\text{Pb}(\vec{r}, t)}{\partial t} = D_{\text{Pb}} \Delta {}^{210}\text{Pb} + \nabla_r \cdot (\vec{V} \cdot {}^{210}\text{Pb}) + \lambda_{222} \cdot {}^{222}\text{Rn}(\vec{r}, t) \quad (3-7-49)$$

where D_{Rn} and D_{Pb} are the coefficients of diffusion of Rn and Pb in water. It is to be noted that in this case, too, the normalized stationary values of the concentrations will comply with the equality:

$$\text{Pb}(t \rightarrow \infty) + \text{Rn}(t \rightarrow \infty) = 1 \quad (3-7-50)$$

In numerical calculations the closeness of the sum of isotopes to unity provides a check on how close the calculated value approaches the stationary one. It is also useful for testing the accuracy of different calculation algorithms.

Boundary conditions

Geometry. We chose a channel-cone geometry with a channel diameter of 0.1 cm and an angle of the cone's opening of 45° . Our calculations covered distances up to 5 cm from the top of the cone. We chose this simplified geometry with cylindrical symmetry as an approximation for the intersection between a thin water-bearing fracture and the lithophysal cavity. The latter (natural) geometry is three-dimensional, which makes modeling computationally difficult. We found that the numerical solutions for the channel-cone geometry are qualitatively similar to those for the channel-sphere geometry.

Distribution of isotopes. On the cavity wall, the normalized concentration of the Rn-derived lead $\text{Pb}_{\text{Rn}} = 0$ (see discussion above) and the concentration of Rn equaled 1. At time $t = 0$, the concentrations of

Rn and Pb across the channel far from the cavity

$\left(L > \frac{V \cdot R_0^2}{D} \right)$ were considered equal to 0 (which

follows from Postulate 2 of the model). Because L was large, both concentrations reach steady-state values before the water approached the channel-cone junction. The shapes of the concentration profiles across the channel were discussed above (see Figures 3-7-13 and 3-7-14).

Flow velocities. Variants with uniform and parabolic flow velocity fields were examined. Inside the cone we assumed that for a given cross-section the velocities were equal, and their

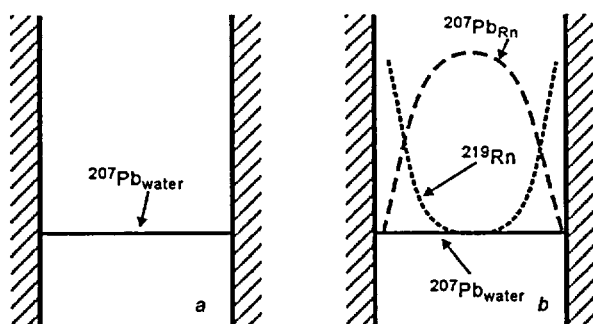


Figure 3-7-14. Schematic presentation of the concentration profiles for "common" ${}^{207}\text{Pb}_{\text{water}}$ (a), as well as concentrations of ${}^{219}\text{Rn}$ and "additional" ${}^{207}\text{Pb}_{\text{Rn}}$ formed through the decay of ${}^{235}\text{U}$ in the rock, diffusion, and decay of ${}^{219}\text{Rn}$ (b). Fracture width is 0.1 cm. ${}^{220}\text{Rn}$ and ${}^{208}\text{Pb}_{\text{Rn}}$ give distributions fairly similar to those of ${}^{219}\text{Rn}$ and ${}^{207}\text{Pb}_{\text{Rn}}$.

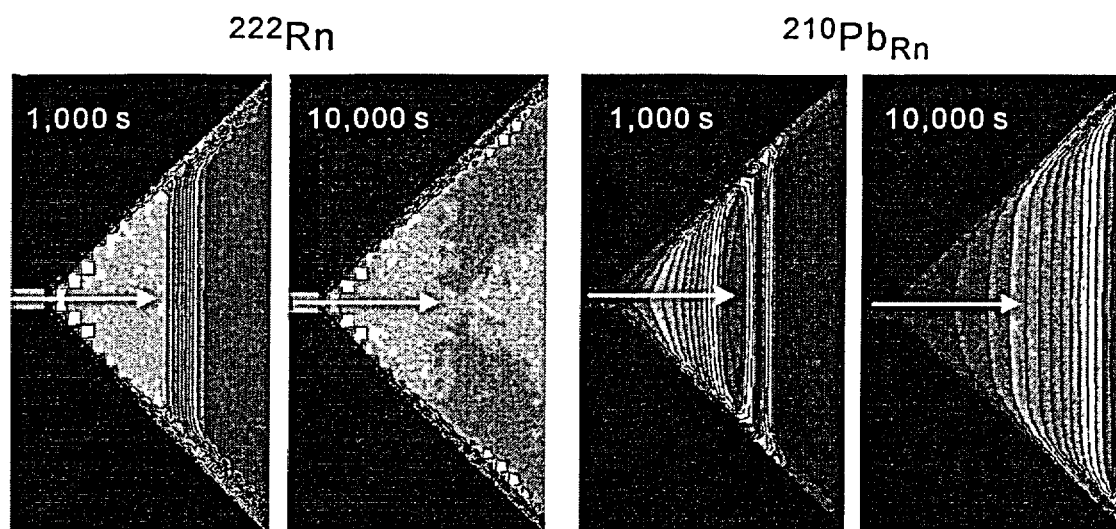


Figure 3-7-15. Example numeric calculation showing qualitative distribution of isotopes ^{222}Rn and $^{210}\text{Pb}_{\text{Rn}}$ in water. Model geometry – a funnel: a channel with diameter of 1 mm (shown off scale for clarity) enters a cone (length shown on the plates is approximately 5 cm). The water flow direction is shown by white arrow. Water in the cavity changes completely in about 5 days. Abundances of isotopes are color-coded with cool colors corresponding to low abundances and warm colors – to high abundances.

Due to its relatively long half-life (3.8 days), ^{222}Rn advances as a front and fills the entire cavity. The input of additional ^{222}Rn continues from cavity walls. The greatest normalized concentration of $^{210}\text{Pb}_{\text{Rn}} = 1.4 \cdot 10^{-3}$ (shown by red color) is achieved after 1000 s; after 10,000 s (~3 hours) the maximum concentration of $6 \cdot 10^{-3}$ is achieved.

values were inversely proportional to the cross-sectional area. This assumption is realistic for a water exchange rate in the cavity of 3 to 30 day^{-1} (i.e., the water in the cavity is completely changed every 3 to 30 days).

Results

The results of the numerical calculations are shown in Figures 3-7-15 through 3-7-17. For ^{222}Rn and ^{210}Pb the results are shown in Figure 3-7-15. As was discussed above, the concentration of the relatively long-lived ^{222}Rn across the channel equaled 1. Therefore, in the Figure the Rn advances as a front, gradually filling the whole volume of the cavity. Near the cavity walls, there is an additional supply of Rn from the rock; the superposition of these two "fronts" still yielded values not exceeding unity, mostly due to the movement of water. The water redistributes Rn from near the cavity walls, which leads to a slight thickening of the Rn layer in comparison with the results obtained for a cavity filled with stagnant water.

The distribution of $^{210}\text{Pb}_{\text{Rn}}$ shows a much more complex pattern. In a thin channel, most atoms formed from the decay of ^{222}Rn "die" due to adsorption on the walls. After entering the opening of the cone, however, the residence time for every Pb_{Rn} atom sharply increases, which leads to the accumulation of $^{210}\text{Pb}_{\text{Rn}}$ at the Rn front. In model calculations for 1,000 s, the maximum normalized concentrations (red

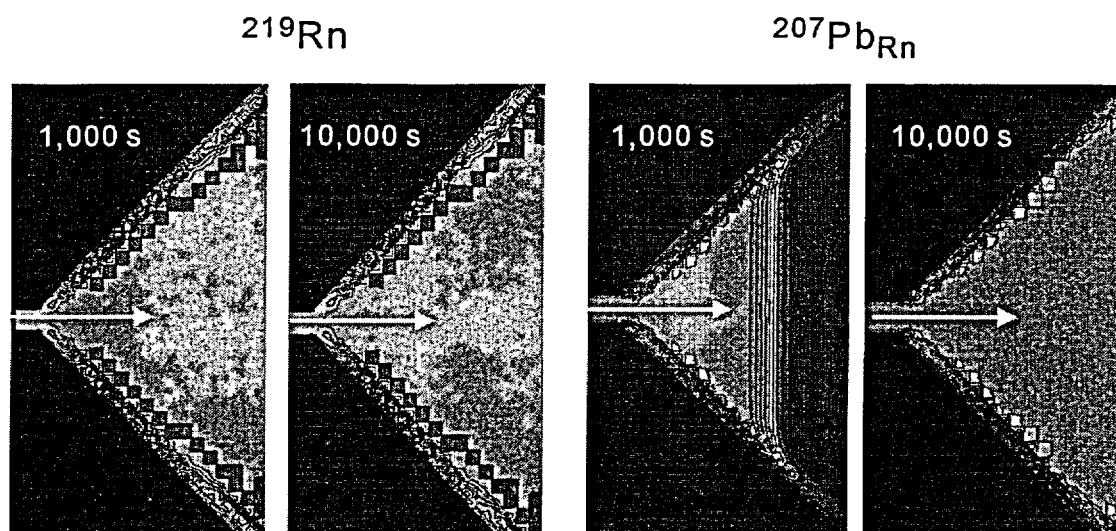


Figure 3-7-16. Example numeric calculation showing qualitative distribution of isotopes ^{219}Rn and $^{207}\text{Pb}_{\text{Rn}}$ in water. Model geometry – a funnel: a channel with diameter of 1 mm (shown off scale for clarity) enters a cone (length shown on the plates is approximately 5 cm). The water flow direction is shown by white arrow. Water in the cavity changes completely in about 5 days. Abundances of isotopes are color-coded with cool colors corresponding to low abundances and warm colors – to high abundances.

Because of its short half-life (4 s) the ^{219}Rn does not advance as a front like ^{222}Rn ; instead its abundances are increased near the cavity walls. By contrast, $^{207}\text{Pb}_{\text{Rn}}$ does form a front, producing with time uniform distribution inside cavity (normalized $^{207}\text{Pb}_{\text{Rn}} = 1$). Near cavity walls, however, there is a zone of low concentrations due to the boundary condition $^{207}\text{Pb}^*_{\text{wall}} = 0$ (see discussion for a model for cavity filled with stagnant water). Note that the zone of low concentrations is shown out of scale, because its thickness is only ~ 1 mm.

color) on the figure correspond to $1.4 \cdot 10^{-3}$, whereas for 10,000 s (~ 3 hours) the maximum value is $6 \cdot 10^{-3}$. The time comparable to the half-life of ^{222}Rn (i.e., 3-4 days) is required for the maximum value to reach $n \cdot 10^{-1}$. For a spherical geometry (cavity with $R = 10$ cm) the maximum would coincide with the approximate center of the cavity (at the selected flow velocities). After that time, the concentrations of ^{210}Pb cease to grow and the concentrations of Rn substantially diminish. The model thus predicts a strongly non-uniform distribution of ^{210}Pb inside the cavity in the direction of flow.

The results for ^{219}Rn and ^{207}Pb are shown in Figure 3-7-16. Apparently, the distributions of isotopes sharply differ from those of the previous pair. Because the ^{219}Rn half-life is only 4 s, the isotope is "stuck" to the walls and does not penetrate into the bulk of the water. By contrast, $^{207}\text{Pb}_{\text{Rn}}$ fills the entire cavity and moves along with the water. The steady state of the system is characterized by a largely uniform filling of the cavity volume with the $^{207}\text{Pb}_{\text{Rn}}$.

It is important to note that the time required to reach the steady state in a cavity with moving water differs significantly from the analogous time for a cavity with stagnant water. For the first case this time equals several days, whereas for the second, it would be several years.

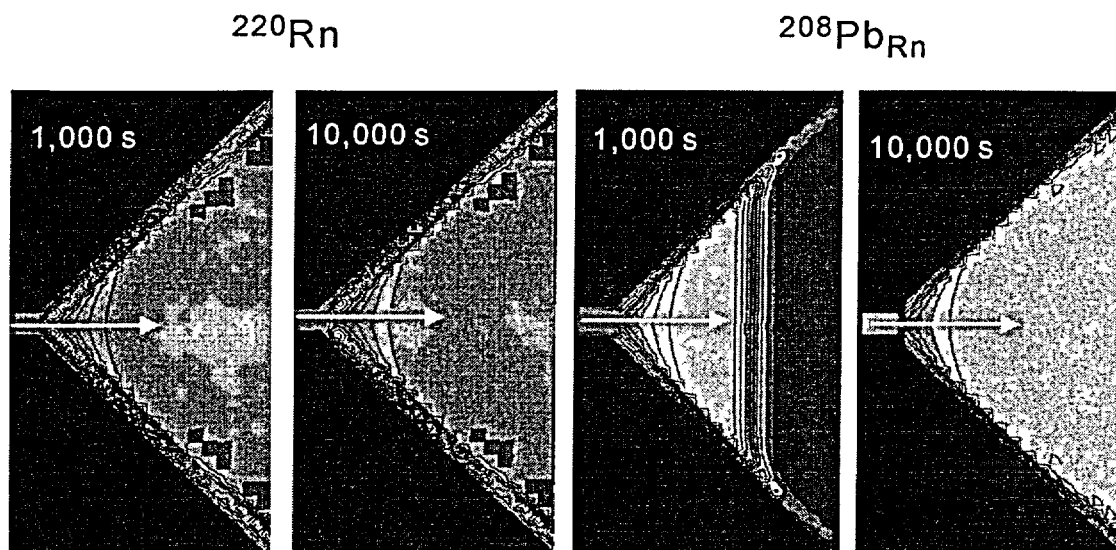


Figure 3-7-17. Example numeric calculation showing qualitative distribution of isotopes ^{220}Rn and $^{208}\text{Pb}_{\text{Rn}}$ in water. Model geometry – a funnel: a channel with diameter of 1 mm (shown off scale for clarity) enters a cone (length shown on the plates is approximately 5 cm). The water flow direction is shown by white arrow. Water in the cavity changes completely in about 5 days. Abundances of isotopes are color-coded with cool colors corresponding to low abundances and warm colors – to high abundances.

Having intermediate between ^{222}Rn and ^{219}Rn half-life (56 s), ^{220}Rn forms small zone of elevated concentrations near the channel's entry into the cavity (green color). The $^{208}\text{Pb}_{\text{Rn}}$ moves as a front at early stages but, because of the short half-life of parent ^{220}Rn with time fills the cavity virtually uniformly (normalized $^{208}\text{Pb}_{\text{Rn}} = 1$).

Figure 3-7-17 reflects the fact that the half-life of ^{220}Rn (56 s) is almost an order of magnitude greater than that of ^{219}Rn . The water movement leads to a slight advancement of ^{220}Rn into the cavity from the channel's entry (1-2 cm), after which the steady state is reached and the picture does not change. By contrast, $^{208}\text{Pb}_{\text{Rn}}$ uniformly fills the cavity at advanced stages of the process.

As has been shown, the enhanced model that takes into account the movement of water through the cavity leads to a substantially different pattern of distribution of Pb isotopes in the cavity's volume. The model predicts largely uniform distributions of the "additional" Rn-derived $^{207}\text{Pb}_{\text{Rn}}$ and $^{208}\text{Pb}_{\text{Rn}}$ across the cavity. At the same time, it predicts substantial differences in the $^{210}\text{Pb}_{\text{Rn}}$ contents, which may reach 3 to 4 orders of magnitude.

3.7.4. Accumulation of Pb_{Rn} on micelles

3.7.4.1. Assessment of the role of colloids in accumulation of Pb_{Rn}

The mineral-forming fluid may contain colloidal particles composed of silica. Such particles could take part in the deposition of opals (see Chapter 3-4 for details). Pb_{Rn} residing in the fluid may be adsorbed on the surface of the colloidal particles. The characteristic time for this process to take place may be defined as:

$$t_{coll} = \frac{1}{(4\pi \cdot D_{Pb_water} \cdot r_{coll} \cdot N_{coll})} \quad (3-7-51)$$

where r_{coll} is the radii of the colloidal particles and N_{coll} is the concentration of colloidal particles in water. By varying r_{coll} between 0.001 and 1.0 μm and N_{coll} between 10 and 10^5 particles cm^{-3} , one may calculate the minimum time required for isotopes of lead to be adsorbed on the surface of colloidal particles. The time for adsorption may be as small as 1000 s (e.g., for $r_{coll} = 1 \mu\text{m}$ and $N_{coll} = 10^5$ particle $\cdot\text{cm}^{-3}$). In this case, the effective radius of the volume within which isotopes of Pb_{Rn} may migrate via Brownian motion (R_{eff}), will equal ~ 0.1 cm. The R_{eff} does not depend on the diffusion coefficients of Pb atoms and is controlled solely by the parameter $Q = r_{coll} \cdot N_{coll}$.

$$R_{eff} = \left(\frac{1}{4\pi Q} \right)^{0.5} \quad (3-7-52)$$

A comparison with the radius of a cavity (R_{cavity}) yields:

$$Q_0 = \left(\frac{0.1}{R_{cavity}^2} \right) \quad (3-7-53)$$

In a cavity where the condition $Q \gg Q_0$ (condition 1) is fulfilled, virtually all Pb_{Rn} will be adsorbed on colloidal particles. The migration of this lead will be governed by migration (possible gravity sedimentation) of these particles. If $Q \ll Q_0$ (condition 2), all Pb_{Rn} isotopes formed in the volume of the cavity move via diffusion and become adsorbed on the cavity surface (including surfaces of crystals growing inside the cavity).

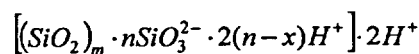
3.7.4.2. Nucleation and growth of micelles

The hydrolysis of silicates involves formation of sols of polysilicon acids, in particular H_2SiO_3 , $\text{H}_2\text{Si}_2\text{O}_5$ and more complex acids. Ions of SiO_3^{2-} form in the solution. The subsequently formed colloidal solutions of silicon acid may be very stable. It is known, however, that in certain conditions (e.g., freshly formed gel), micelles re-dissolve upon contact with the solid phase (e.g., a cavity wall) (Kreshkov, 1976).

With time the primary molecular complexes, which contain molecules of silicon oxide and water in different combinations, merge and increase in size. At a certain stage of evolution micelles appear. A micelle is comprised of two parts: the core and the ionic shell; the latter may be subdivided into adsorption and diffusion layers (Kuznetsov and Ust-Katchintsev, 1976; Figure 3-7-18). The growth of micelles may proceed by a condensation mechanism (i.e., the consecutive attachment of molecular complexes to a particle), as well as by coagulation (the fusion of two large particles that may consist of hundreds and thousands of molecules).

The core of a silicon acid micelle is negatively charged due to surface electrolytic dissociation of the molecules of the dispersed phase. Molecules of SiO_2 located in the near-surface positions react with water forming H_2SiO_2 , which then dissociates: $\text{H}_2\text{SiO}_2 \leftrightarrow 2\text{H}^+ + \text{SiO}_3^{2-}$.

All SiO_3^{2-} ions (n ions) formed in this manner are strongly bonded to the core. The total number of the oppositely charged ions equals $2n$. Some of the ions reside in the diffusion layer ($2x$), and the remainder – in the adsorption layer. The structural formulae of a micelle of silicon acid is written as:



(3-7-54)

The highest weight concentration of colloids is reached when the concentration of the sol particles is between 10^{15} - 10^{16} cm^{-3} .

Typically, colloidal chemistry considers the equilibrium state of already-formed micelles in solution, as well as their precipitation. The kinetic aspects, such as the growth of micelles from monomolecular complexes to particles containing hundreds of thousands of silicon oxide molecules

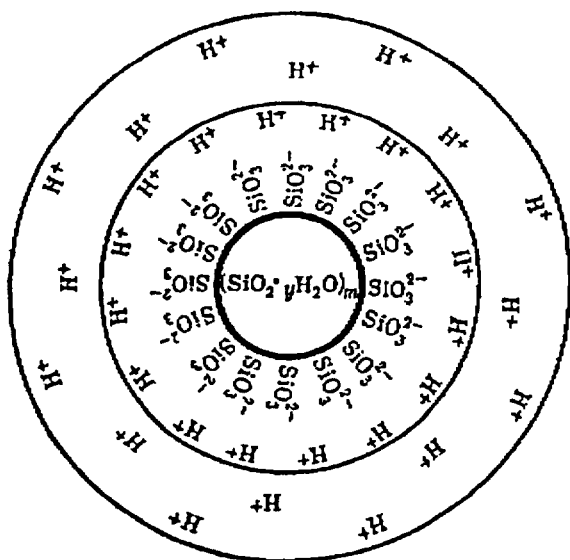


Figure 3-7-18. Micelle of SiO_2 (from Kuznetsov and Ust-Katchintsev, 1976).

Table 3-7-1

Sedimentation time as a function of particle's size
(by Kuznetsov and Ust-Kachkintsev, 1976)

Radius of particle, cm	10^{-3}	10^{-4}	10^{-5}	10^{-6}	10^{-7}
Sedimentation time (for 1 cm)	30 s	52 min	86 hours	360 days	100 years

have not been studied well. The subject poses serious problems related to the high growth rate characteristics of the initial stages of micelle growth, as well as to technical problems with the study of very small particles suspended in a liquid phase. (By contrast, the methods for the study of clusters and particles in the gaseous phase are fairly well developed; see e.g., Pashenko and Sabelfeld, 1992; Pashenko et al., 1996). Below we will employ coagulation-kinetic models, widely used in aerosol science, to describe, semi-quantitatively, the process of formation of micelles in the model geometry.

The modern theory of electrolytic dissociation, developed by B.V. Deryagin and L.D. Landau (Livshitz and Landau, 1979) defines the threshold of coagulation as:

$$\lambda = C \cdot \frac{\xi^3 (kT)^5}{A^2 e^6 z^6} \quad (3-7-55)$$

where C is the coefficient, k is the Boltzmann's constant, e is the charge of the electron, T is the temperature (K), ξ is the inductivity, A is the constant of the van-der-Vaals attraction, z is the charge of the dominant ion. The equation shows a good fit with the experimental data obtained for different sols.

A noteworthy feature of Eq. 3-7-55 is the fifth degree of the temperature term. It means that for some parameters of the system, say $T = 300$ K and $\lambda = \text{const}$, it will be sufficient to increase the temperature by only 10 degrees to increase λ by 20%. This would trigger a very fast coagulation transformation, which would change the spectrum of size distribution of the micelles.

3.7.4.3. Growth of micelles: condensation and coagulation mechanisms

3.7.4.3.1. Qualitative analysis of the processes

A micelle of silica 10 nm in diameter contains approximately 10^5 molecules. We qualitatively address the question: what are the mechanisms and what are the characteristic times of formation for such aggregates? In order to form a micelle, molecules must approach and connect to each other. If the growth of a micelle occurs through the connection of individual molecules, the mechanism is termed "monomolecular growth". The maximum velocities of the growth are achieved if the approaching

molecule connects to the micelle upon the first contact. In this case, the growth velocity of the micelle will be controlled by the diffusion flux of molecules in the direction of the growing particles.

The following mechanism may then be realized. Upon reaching a certain size and approaching equilibrium with an ionic composition of the surrounding solution, the growth of micelles ceases. Such micelles remain in solution in a relatively stable state. If micelles have substantial sizes, they may slowly settle down. However, if either the ionic composition of the fluid changes or the temperature changes, the coagulation threshold may be reached and surpassed (see Eq. 3-7-55). It is highly probable that a stage of fast micelle growth by the coagulation mechanism will follow, and the rate of sedimentation of particles will sharply decrease.

Characteristic times for the sedimentation of particles of different sizes are given in Table 3-7-1. It is apparent that the increase of the particle size by one order of magnitude, from 0.01 to 0.1 μm , leads to an increase in the sedimentation velocity by 100 times. In the context of our model involving the movement of water through cavities in tuffs, the time for sedimentation has the following significance. If the water changes in a cavity every 10 days, colloidal particles of 0.01 μm may be considered as permanently suspended in the solution (i.e., no sedimentation). Meanwhile, practically all particles 0.1 μm in size will undergo sedimentation onto the cavity floor.

Khimicheva et al. (1991) studied the sorption properties of different varieties of silica in the sequence opal – quartz. They demonstrated that globular and aggregate-globular textures are characteristic of the early stages of silica mineral precipitation. Experiments on water adsorption have shown that opal and "mature" chalcedony possess the greatest specific surface (up to $150 \text{ m}^2 \cdot \text{g}^{-1}$), whereas for quartz this parameter is the smallest ($10 \text{ m}^2 \cdot \text{g}^{-1}$). Opal CT has intermediate values of about $40 \text{ m}^2 \cdot \text{g}^{-1}$. It may be estimated that the specific surface of $150 \text{ m}^2 \cdot \text{g}^{-1}$ requires particles with $R \cong 0.1 \mu\text{m}$.

3.7.4.3.2. Possible change in the ionic composition of water due to coagulation of micelles

Another important potential consequence of the enlargement of micelles is rarely discussed in the literature. As we mentioned above, experiments have shown that if the fresh gel of silicon acids is deposited on solid a surface and fresh water is added, the gel may dissolve (i.e., return to a state of ionic solution).

According to the chemical formula of the silica micelle (Eq. 3-7-54), we denote the number of ions of SiO_3^{2-} coming to the unit area of the micelle's core in the moment of time t as $n_{sur}(t)$; the radius of the core as $R(t)$; the concentration of molecules of different types of silicon acids in solution as $N_{mol}(t)$; and the number of micelles per unit volume as $N_{mich}(t)$. We assume for simplicity that the size distribution of particles at all times is mono-disperse (more realistic distributions will be discussed below). A system of

equations describing the total content of SiO_3^{2-} on the surface of all micelles ($N_{\text{tot-surf}}$) residing in a unit volume of the solution during coagulation process may then be written:

$$\frac{dN_{\text{tot-surf}}}{dt} = n_{\text{surf}} \cdot \frac{d}{dt} [4\pi R(t)^2 \cdot N(t)] \quad (3-7-56)$$

and

$$R(t) = R_0 \cdot \left(1 + \frac{1}{2} N_0 \cdot K \cdot t\right)^{\frac{1}{3}} \quad (3-7-57)$$

Finally, taking the derivative in Eq. 3-7-56 and assuming that the mass of the coagulating particles remains constant, after some algebraic transformations we obtain:

$$\frac{dN_{\text{tot-surf}}}{dt} = -4\pi R_0^2 n_{\text{surf}} N_0 \cdot \frac{\frac{1}{6} N_0 K t}{\left(1 + \frac{1}{2} N_0 K t\right)^{\frac{4}{3}}} \quad (3-7-58)$$

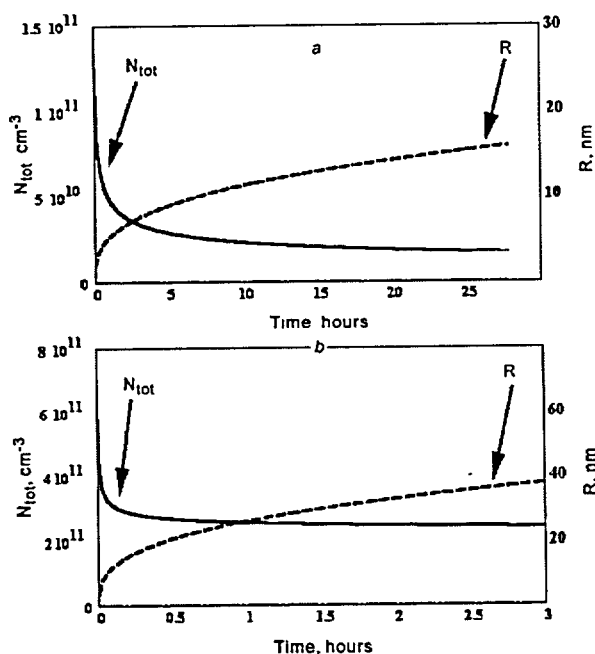


Figure 3-7-19. Kinetics of the decrease of the total number of SiO_3^{2-} ions on the surface of micelles (solid line) in the course of their growth through coagulation (dashed line). *a* – initial concentration of particles $N_0 = 10^{10} \text{ cm}^{-3}$, concentration of $\text{SiO}_2 = 10^{-5} \text{ mole} \cdot \text{l}^{-1}$; *b* – $N_0 = 10^{12} \text{ cm}^{-3}$, $\text{SiO}_2 = 10^{-3} \text{ mole} \cdot \text{l}^{-1}$.

where K is the constant of coagulation of the monodisperse particles in water and the subscript 0 denotes the initial moment of time. The Eq. 3-7-57 is the corollary of the solution of Smoloukhovski's equation for monodisperse particles (Smoloukhovski, 1936).

Because at any given set of parameters the surface density of SiO_3^{2-} is controlled by the properties of the surface of the micelle, we assume that it remains constant in the course of coagulation. Based on this assumption, the decrease of the total number of SiO_3^{2-} on the micelle's surface can be calculated. Figure 3-7-19 shows the kinetics of the decrease of the total number of SiO_3^{2-} ions on the surface of micelles following the enlargement of the latter. We carried out calculations for initial concentrations of SiO_3^{2-} of 10^{-3} and $10^{-5} \text{ mole} \cdot \text{l}^{-1}$. It is apparent

from the Figure that the decrease in the initial concentration lowers the rate of the process by an order of magnitude.

3.7.4.4. Accumulation of lead on micelles of silica in cavities and fractures

In this section we will assess the relationship between the content of SiO₂ and the Pb isotopes in micelles.

3.7.4.4.1. Flux of isotopes on a sphere

The intensity of the flux of molecules on a sphere, if attachment to the sphere upon the first contact is assumed (the so-called "black sphere" model), is defined as (e.g., Smirnov, 1969):

$$I = \frac{4\pi \cdot D \cdot r \cdot n_{\infty}}{1 + \lambda_0 \frac{l}{r}} \quad (3-7-59)$$

where D is the coefficient of diffusion for molecules, r is the radius of the sphere (micelle), n_{∞} is the concentration of molecules at an the infinite distance from the sphere (if many micelles are present at the distance equal to the average distance between spheres, and if the distance is at least 10 times greater than the size of spheres; in this case the precision of Eq. 3-7-59 is about 1%), l is the effective free length of the molecular path in water, and λ_0 is the coefficient. Devison (1951) has demonstrated that at $r/l \ll 1$

$$\lambda_0 = \frac{4}{3} - \frac{5}{9} \frac{r}{l} + \dots \quad (3-7-60)$$

and at $r/l \gg 1$

$$\lambda_0 = 0.7104 + 0.5047 \frac{l}{r} + \dots \quad (3-7-61)$$

where the ellipsis indicates terms that are an order of magnitude smaller than the ones shown.

If the probability of the accommodation of a molecule upon contact with the sphere is smaller than unity ($\alpha < 1$), the equation for the flux may be written, analogous to Eq. 3-7-59:

$$I_{\alpha} = \frac{4\pi \cdot D \cdot r \cdot n_{\infty}}{1 + \lambda_0(\alpha) \frac{l}{r}} \quad (3-7-62)$$

where

$$\lambda_0(\alpha) = \lambda_0 + \frac{4(1-\alpha)}{3\alpha} \quad (3-7-63)$$

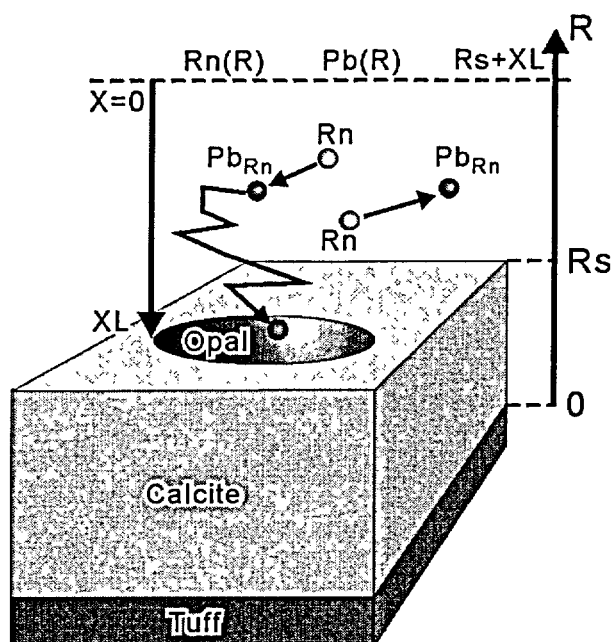


Figure 3-7-20. Conceptual representation of the accumulation of Pb_{Rn} on opal via diffusion. See text for explanation of symbols.

3.7.5. Uptake of lead in opal

In the preceding text we discussed the processes of the generation of Pb_{Rn} isotopes and their accumulation in the fluid filling the open cavities in the rock. The atomic form of these isotopes may be present in the solution as chemical compounds and complexes. They also may become adsorbed on micelles, in which case the character of their migration and their ultimate fate may change dramatically.

We now address the question: how does this "excess" Pb get into opals growing from the fluid. Consistent with the different forms of occurrences discussed above, there can be two paths for Pb_{Rn} to be incorporated in depositing minerals: (1) diffusion and (2) coagulation and

sedimentation of micelles. These paths are not mutually exclusive. Minerals, forming from ionic solutions acquire Pb_{Rn} through net diffusion, whereas minerals forming from colloidal solutions may be subject to both, diffusion and coagulation/sedimentation fluxes. Importantly, the coagulation/sedimentation of colloidal particles may change the boundary conditions of the diffusion flux, making it more intense. Below we evaluate the two mechanisms for the supply of Pb_{Rn} onto the surface of growing minerals.

3.7.5.1. Uptake of lead during the diffusion-controlled growth of minerals

In previous sections we examined distributions of Pb in a cavity with stagnant and moving water. Now, we assess the quantities of additional Pb_{Rn} that may accumulate in the system over time. We first must establish the baseline for our analysis of the Pb contents measured in opals from the vadose zone of Yucca Mountain. Then, the question we will address is: what is the time required to accumulate the amount of Pb found in a typical Yucca Mountain sample?

The model for the uptake of Pb via diffusion is graphically presented in Figure 3-7-20. In the process of growth of the calcite crystals, segregations of opal form on its surface. Above the surface of the deposited opal both Rn and Pb are present in the water. Their concentrations are functions of the distance from the tuff surface (R_s).

The model may be treated as either one-dimensional (when the characteristic size of opal is sufficiently large) or two-dimensional (when the area occupied by the opal is not large and the size needs to be taken into consideration). The one-dimensional problem may be defined as:

$$\frac{dPb}{dt} + D \frac{d^2 Pb}{dX^2} + \lambda_{Rn}(X) = 0 \quad (3-7-64)$$

where Pb and Rn are concentrations of Pb_{Rn} and Rn above the surface of the depositing opal. Setting the boundary conditions (geometry and time) for this problem is rather complex. A reasonable function of the uptake of Pb may be defined, for example, by using appropriate accommodation or distribution coefficients. The spatial distribution of Pb_{Rn} and Rn at $t = 0$ may be defined by the solution for the problem of the cavity with moving water (discussed in the previous section).

For $t > 0$, Eq. 3-7-64 was solved and the number of Pb atoms adsorbed at the surface of growing opal was calculated. Asymptotic boundary concentrations of Pb_{Rn} above the opal surface were also taken from the solution of the problem for a cavity with moving water. Then, the zone of the diffusion uptake of Pb_{Rn} above the opal surface (denoted as XL in Figure 3-7-20) was determined. The thickness of this zone depends on certain parameters of the cavity (the radius of the cavity, R , and the concentration of Rn), as well as the height of the crystal (R_s) at a given time.

For example for a cavity with $R = 10$ cm and a crystal located at $R_s = 1$ cm, the time to reach the steady state in terms of the accumulation of lead inside cavity requires 10 days. After that time, the flux of lead from the center of the cavity onto the surface of the depositing opal will stabilize at $\cong 0.04$ atoms·s⁻¹·cm⁻². The concentration of Rn at this point will be $\cong 2.5 \cdot 10^4$ atom·cm⁻³, and the concentration of the "excess" (Rn-derived) ²¹⁰Pb(²⁰⁶Pb) will be $1 \cdot 10^4$ atom·cm⁻³.

Solutions of Eq. 3-7-64 may be presented in analytical form with reasonable accuracy (for a relatively large cavity):

$${}^{210}\text{Pb}(X) = {}^{210}\text{Pb}(R_s + XL) \left[1 - \frac{0.5}{{}^{210}\text{Pb}(R_s + XL)} \cdot \frac{\lambda_{222} \cdot {}^{222}\text{Rn}(R_s + XL)}{D} \cdot (X)^2 \right] \quad (3-7-65)$$

Taking into account the boundary condition, which specifies that atoms of Pb_{Rn} are adsorbed on the opal surface, we obtain:

$$XL = \sqrt{\frac{2 \cdot {}^{210}\text{Pb}(R_s + XL) \cdot D}{\lambda_{222} \cdot {}^{222}\text{Rn}(R_s + XL)}} \quad (3-7-66)$$

The flux of atoms of Pb_{Rn} on the surface of opal is found from gradients of the concentration, taking into account the increasing area of opal segregation:

$$I_{opal} = S_{opal} \cdot D \cdot \left. \frac{d^{210}Pb}{dR} \right|_{R=R_s} = S_{opal} \cdot \sqrt{2 \cdot {}^{222}Rn(R) \cdot {}^{210}Pb(R) \cdot \lambda_{222}} \cdot D \quad (3-7-67)$$

Eq. 3-7-67 yields the flux of the Rn-derived Pb_{Rn} on an area of 1 cm². The average content of $^{206}Pb^*$ in the Yucca Mountain samples analyzed by Neymark et al. (2002) is 10¹¹ to 10¹² atoms. Taking the average area of opal samples as 0.1 cm² (i.e. 0.3×0.3 cm), the time necessary for accumulation of these amounts of lead may be established as 300 Ka to 3 Ma. The minimum values of $^{206}Pb^*$ reported for the Yucca Mountain opals are between 10⁹ and 10¹⁰ atoms. The time of accumulation of these amounts of ^{206}Pb through net diffusion is 3 to 30 Ka.

For the three samples of calcite reported in USGS (1997) the values of excess ^{206}Pb are equal to 6.43·10⁸, 5.95·10⁷, and 2.95·10⁸ atoms. From the known weights of the samples (3.25, 0.62, and 0.82 mg), assuming a cubic geometry, the equivalent surface area may be estimated as 0.014, 0.0046, 0.0055 cm², respectively. Assuming the maximum ^{206}Pb flux of 0.1 atom·s⁻¹·cm⁻², the time required to accumulate the requisite amounts of ^{206}Pb may be calculated as 14, 4, and 17 Ka. The respective growth rates would be 84, 170, and 43 mm per million years. We should emphasize that these are maximum estimates.

The assessment calculations presented above suggest that the accumulation of Pb_{Rn} through net diffusion on the surface of growing minerals is a relatively slow process. Significant times are required for the measured values of the $^{206}Pb^*$ to be achieved. The length of these times means that the decay of U contained in the sample will also produce substantial amounts of Pb. This source of radiogenic Pb must be accounted for.

3.7.5.2. Coagulation/sedimentation supply of Pb on the surface of growing minerals

In our discussion above we demonstrated that the accumulation of "excess" Rn-derived Pb isotopes on micelles of silica is a real process, which can be assessed quantitatively. The ensuing phase transitions in the system transform the micelles, suspended in solution, into the solid mineral phase – opal. This transformation may be broadly subdivided into two stages: (1) coagulation of micelles and (2) sedimentation of particles formed through coagulation. Below we briefly describe these processes.

3.7.5.2.1. Processes involved

Coagulation

In the framework of the proposed model, the accumulation of Pb_{Rn} isotopes occurs on micelles of silica with a characteristic $r = 1$ to 10 nm. According to recent research on the physics of the formation of

Table 3-7-2

Sizes of the silicon dioxide micelles from which, according to the model's predictions, opals containing Pb in amounts similar to those measured in the Yucca Mountain opals may form.

Isotope		Content of isotope, atom cm ⁻³	Minimum radius of micelle, nm	Maximum radius of micelle, nm	Lowermost abundances of Pb isotope in opal, ppb	Greatest abundances of Pb isotope in opal, ppb
²⁰⁶ Pb _{Rn}	min	1	1	5	7	500
	max	100	5	45	7	500
²⁰⁷ Pb _{Rn}		0.05	1	6	0.2	10
²⁰⁸ Pb _{Rn}		15	4	120	0.1	150
²⁰⁴ Pb		0.1	1	50	0.005	10

Notes: Results of calculations are also shown in Figures 3-7-21 through 3-7-25. For the calculations the water residence time in the cavity was taken as 10 days. Abundances of Pb isotopes in opals are experimental, from Neymark et al. (2002).

opals (e.g., Kalinin et al. 1998), upon reaching and surpassing a certain critical size for the micelles, the process of aggregation of the micelles and formation of dense structures begins. For suspensions of silica, $r_{crit} \cong 2.5$ nm (Vosel and Kalinin, 1999). This indicates that the micelles considered in our model are capable of coagulating. By means of the analytical model developed by Smolukhovski (see Appendix 3-7-3), it may be shown that in the process of coagulation the average concentration of Pb isotopes in silica remains unchanged.

Calculations shown in Table 3-7-2 indicate, that for the contents of U and Th in the tuffs of the Yucca Mountain vadose zone, the concentrations of Pb_{Rn} atoms in water will be low ($n \cdot 10^{-1}$ - $n \cdot 10^2$ cm⁻³). Meanwhile, the estimated concentrations of micelles in water filling the cavities may be as great as ($n \cdot 10^8$ - $n \cdot 10^{10}$ cm⁻³). It is apparent, then, that even if all of the atoms of Pb, which form in a cavity through the decay of Rn during the characteristic time of water exchange (1-10 days), precipitate on micelles, only one out of every $n \cdot 10^3$ - $n \cdot 10^5$ micelles would carry an atom of Pb.* Due to the discrete distribution of the Pb atoms on micelles, stochastic algorithms (e.g., Markus, 1968; Lushnikov, 1978) are preferable to the analytical equations of Smolukhovski. We employed the MPV algorithm (see Appendix 3-7-3 for a description of the algorithm).

Sedimentation

For micelles with $r = 5$ -10 nm (initial sizes before coagulation), the time required for their sedimentation from the 1 cm height would range from 300 to 1000 days. For particles with $r = 100$ nm

* It is to be noted that the average ratio Pb/SiO₂(micelle) may be as great as $n \cdot 10^1$ to $n \cdot 10^2$ ppb.

("ripe" particles appearing several hours after the onset of coagulation), the requisite time would be only 3 days. As is discussed in Appendix 3-7-3, by that time, the spectrum of size distribution for the particles attains a self-sustaining character. This makes it possible to carry out numerical calculations for the sedimentation of particles on the surface of the cavity (and on the surface of growing crystals), taking into account the particle sizes.

The brief discussion above demonstrates that the enrichment in Pb_{Rn} isotopes, acquired by micelles may readily be passed on to the silica minerals formed through the coagulation and sedimentation of these micelles.

3.7.5.2.2. Coagulation/sedimentation: Comparison of the theoretical predictions with the actual Pb isotope abundances in opals

In order to check the plausibility of the proposed mechanisms for the accumulation of additional Rn-derived Pb isotopes (Pb_{Rn}) via adsorption on micelles, we compare below predictions of the model with the Pb isotope abundances measured in the Yucca Mountain opal samples (data from Neymark et al. 2002). The change of radius of the micelle in the condensation regime of growth may be written as:

$$\frac{dr}{dt} = \frac{1}{R} v_{SiO_2} \frac{D_{SiO_2} \cdot n_{SiO_2}}{1 + \lambda_0(\alpha) \frac{l}{r}} \quad (3-7-68)$$

and the flux of an isotope on the micelle is defined by Eq. 3-7-62. We solved the system of equations 3-7-62 and 3-7-68 to establish the basis for our comparison with measured values. The results are shown in Figures 3-7-21 through 3-7-24 and in Table 3-7-2. The calculations were carried out on the basis of the asymptotic solutions of the equations of Smolukhovski obtained by the MPV algorithm (Appendix 3-7-3, Eqs. 3-7-A-25 and 3-7-A-28). Figure 3-7-21 shows the calculations for two initial concentrations of $^{206}Pb_{Rn}$ in the cavity water (1 and 100 atom·cm⁻³). The model predicts strongly non-uniform concentrations of the Rn-derived ^{206}Pb in the cavity (see Figure 3-7-15); so the values we used bracket the expected $^{206}Pb_{Rn}$ contents. For other isotopes (Figures 3-7-22 through 3-7-23) we used concentrations, which were predicted on the basis of Eqs. 3-7-23 and 3-7-24, and numeric calculations (see section 3.7.4.4.2. "Calculations for the model geometry: channel-cone"). In all calculations we assumed ten days as the time for the exchange of water in the cavity.

The results are summarized in Figure 3-7-25 and Table 3-7-2. The data reveal two important features. **First**, the calculated sizes of micelles are in reasonable agreement for all Pb isotopes. **Second**, the calculated sizes of micelles are close to or greater than the critical size. Upon surpassing the critical size, coagulation of the silica micelles begins ($r_{crit} \cong 2.5$ nm; Vosel and Kalinin, 1999). This supports the plausibility of the proposed model.

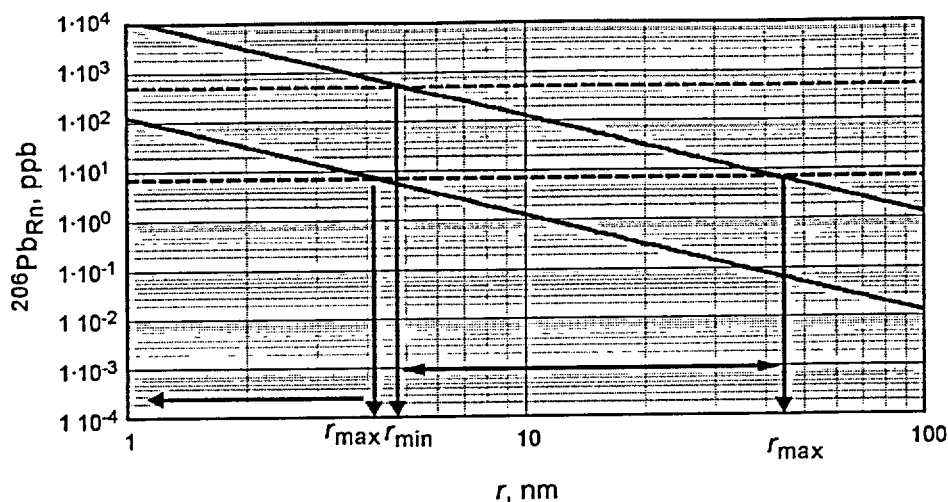


Figure 3-7-21. Calculated concentrations of $^{206}\text{Pb}_{\text{Rn}}$ in cavity, qualitative distribution of which was shown in Figure 3-7-15. Two curves (*solid lines*) were calculated for the highest ($100 \text{ atom}\cdot\text{cm}^{-3}$) and the lowermost ($1 \text{ atom}\cdot\text{cm}^{-3}$) concentrations of $^{206}\text{Pb}_{\text{Rn}}$ in cavity, obtained through numeric calculations for the model geometry. Horizontal *dashed lines* approximate the boundaries of the ^{206}Pb abundances in opals from Yucca Mountain (Neymark et al., 2000 and 2002). Intersections of these lines with the curves define radii of micelles (r) from which, according to the model, opals with given abundances of ^{206}Pb may form. The model time of water exchange in the cavity was 10 days.

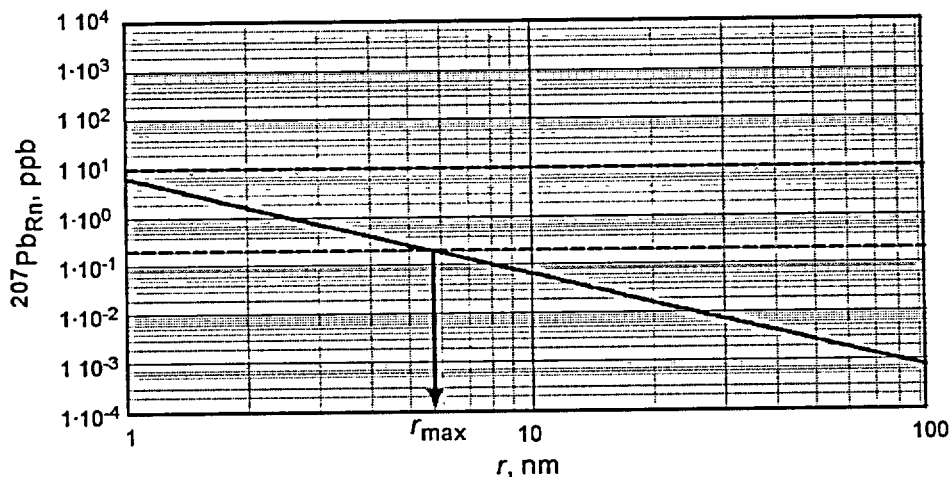


Figure 3-7-22. Calculated concentrations of $^{207}\text{Pb}_{\text{Rn}}$ in cavity, qualitative distribution of which was shown in Figure 3-7-16. Unlike ^{206}Pb , distribution of this isotope is uniform throughout the cavity (except for very thin layer near the cavity wall). The curve (*solid line*) was calculated for concentration of $^{207}\text{Pb}_{\text{Rn}}$ in the cavity ($0.05 \text{ atom}\cdot\text{cm}^{-3}$), obtained through numeric calculations for the model geometry. Horizontal *dashed lines* approximate boundaries of the ^{206}Pb abundances in opals from Yucca Mountain (Neymark et al., 2000 and 2002). Intersections of these lines and the curve define radii of micelles (r) from which, according to the model, opals with given abundances of ^{207}Pb may form. The model time of water exchange in the cavity was 10 days.

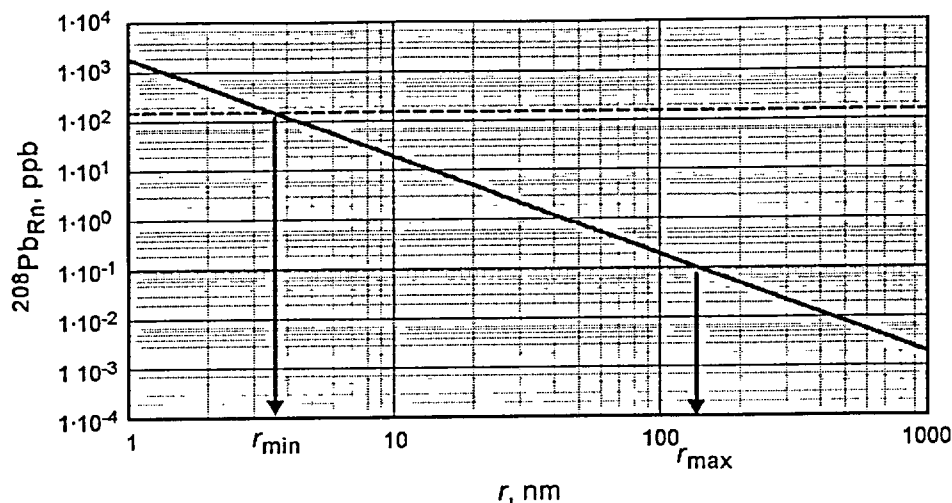


Figure 3-7-23. Calculated concentrations of $^{208}\text{Pb}_{\text{Rn}}$ in cavity, qualitative distribution of which was shown in Figure 3-7-17. Distribution of this isotope is uniform throughout the cavity (except for very thin layer near the cavity wall). The curve (*solid line*) was calculated for concentration of $^{208}\text{Pb}_{\text{Rn}}$ in the cavity ($15 \text{ atom}\cdot\text{cm}^{-3}$), obtained through numeric calculations for the model geometry. Horizontal *dashed lines* approximate boundaries of the ^{206}Pb abundances in opals from Yucca Mountain (Neymark et al., 2000 and 2002). Intersections of these lines and the curve define radii of micelles (r) from which, according to the model, opals with given abundances of ^{208}Pb may form. The model time of water exchange in the cavity was 10 days.

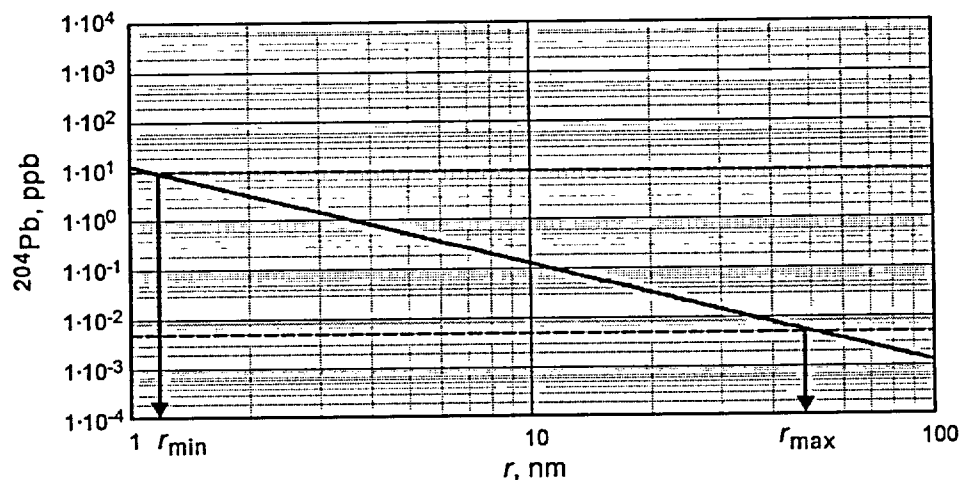


Figure 3-7-24. Calculated concentrations of ^{204}Pb in the cavity. The curve (*solid line*) was calculated for concentration of ^{204}Pb in the cavity ($0.1 \text{ atom}\cdot\text{cm}^{-3}$), obtained through numeric calculations for the model geometry. Horizontal *dashed lines* approximate boundaries of the ^{204}Pb abundances in opals from Yucca Mountain (Neymark et al., 2000 and 2002). Intersections of these lines and the curve define radii of micelles (r) from which, according to the model, opals with given abundances of ^{204}Pb may form. The model time of water exchange in the cavity was 10 days.

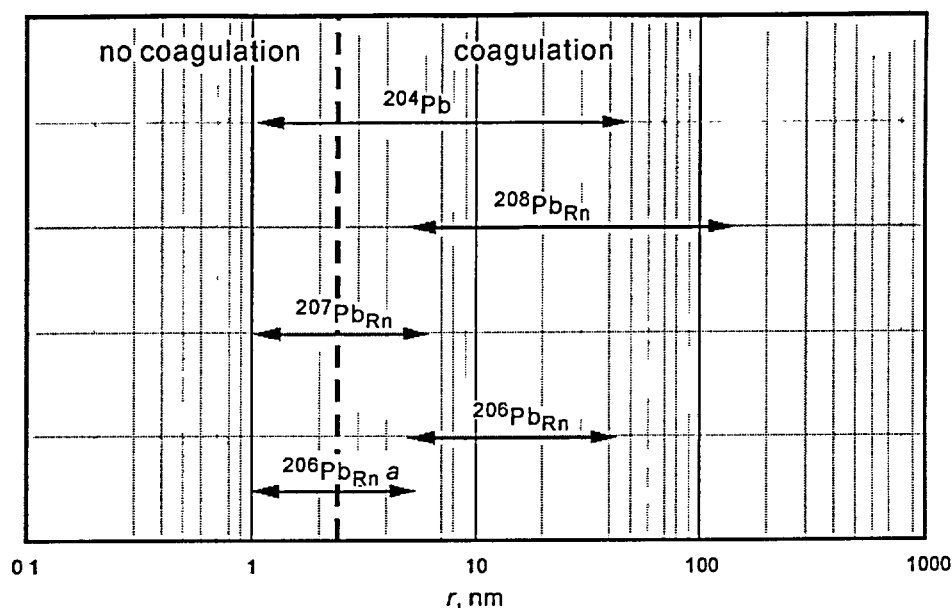


Figure 3-7-25. Calculated sizes of micelles of silicon oxide from which, according to the prediction of the model, opals with contents of Pb-isotopes measured in the Yucca Mountain (Neymark et al., 2002) may be deposited (based on Figures 3-7-21 through 3-7-24). Vertical dashed line indicates the critical size of micelles, $r = 2.5$ nm, above which micelles begin to coagulate (Vosel and Kalinin, 1999). $^{206}\text{Pb}_{\text{Rn } a}$ – micelle sizes for the minimum concentrations in the cavity (see Figure 3-7-21).

3.7.6. Pb_{Rn} and the "conventional" U-Pb age dates

In previous sections we focused our attention on the processes of generation, migration and uptake of the radon-derived radiogenic lead isotopes, Pb_{Rn} by growing opal. The opal, however, may also contain substantial amounts of uranium; therefore, the *in situ* production of radiogenic Pb isotopes will also take place. Below we evaluate the relationships between both of the "sources" of lead in opals in the context of radiometric age dating.

3.7.6.1. Evolution of lead isotope composition during the opal "lifetime"

The "life" of a mineral formed by the colloidal mechanism may be subdivided into two major stages.

Stage 1. The process of the accumulation of Pb and U on micelles suspended in water begins at the moment ($t_0 - dt$) and continues during the time dt until the micelle becomes a part of the opal segregation. It is assumed that after that time the mineral becomes "closed" with respect to U and Pb. We use the

simplified version of Eq. 3-7-62 to describe the flux of atoms (molecules, complexes) of Pb and U isotopes on the surface of a micelle:

$$I = 4\pi D \cdot r \cdot n_{\infty} \quad (3-7-69)$$

where D is the coefficient of diffusion of atoms (molecules, complexes) of the given isotope and n_{∞} is the concentration of the isotope far from the micelle. The equation is only several percent less precise than Eq. 3-7-62. Consider the example of the $^{238}\text{U} \rightarrow ^{210}\text{Pb}$ (^{206}Pb) decay chain. The total number of atoms of U adsorbed on the micelle over the time dt is defined by the integral:

$$^{238}\text{U}_{tot} = \int_{t_0-dt}^{t_0} 4\pi D_U \cdot r(t) \cdot ^{238}\text{U}_{\infty_water}(t) dt \quad (3-7-70)$$

The analogous equation may be written for Pb:

$$^{210}\text{Pb}_{tot} = \int_{t_0-dt}^{t_0} 4\pi D_{Pb} \cdot r(t) \cdot ^{210}\text{Pb}_{\infty_water}(t) dt \quad (3-7-71)$$

Consider the following relationship:

$$^{210}\text{Pb}_{\infty_water} = ^{206}\text{Pb}_{\infty_common_water} + ^{210}\text{Pb}_{\infty_222\text{Rn}_water} \quad (3-7-72)$$

The lower indices in the right part of the equation describe the "sources" of lead.

Stage 2. From the moment opal ceases to grow (t_0) to the present (t) the accumulation of ^{206}Pb occurs in the opal only from the *in situ* decay of ^{238}U . The process of accumulation of this ^{206}Pb in time may be described by a system of differential equations for all members of the ^{238}U decay chain. One source of uncertainty in such calculations is the disequilibrium condition commonly found in natural waters between ^{238}U and its daughter ^{234}U .

Groundwaters residing in different rock formations display different degrees of disequilibrium, expressed as the $^{234}\text{U}/^{238}\text{U}$ activity ratio, γ . Values of $\gamma > 1$ indicate an excess of ^{234}U relative to the equilibrium ratio. Atmospheric precipitation in arid zones typically are in equilibrium ($\gamma = 1$), whereas precipitation near the seashore are enriched in ^{234}U ($\gamma = 1.1$ to 1.5) due to the involvement of sea aerosols. Groundwaters from shallow parts of the phreatic zone typically have $\gamma = 1.5$ to 2.0 , whereas phreatic waters from deep zones with suppressed circulation have lower characteristic values of $\gamma = 1.0$ - 1.3 (Zverev, et al. 1980; Gascoyne, 1992). The highest values of γ (3.1 to 5.5) are characteristic of waters from the granitic rocks and acidic effusive rocks; even greater values (7.2 - 8.9) were reported from the fractured fault zones in such rocks (Zverev et al., 1980). According to Cherdintsev (1969), groundwaters

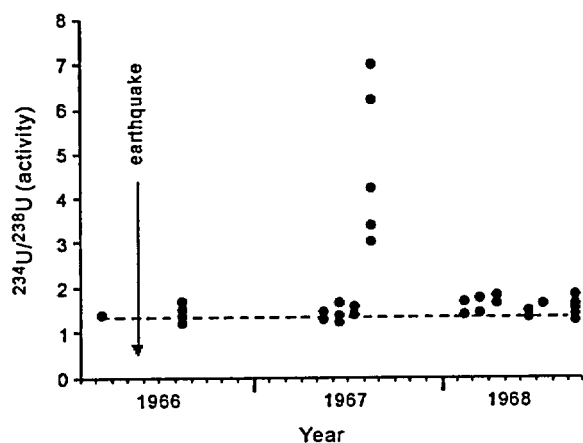


Figure 3-7-26. Variations of the $^{234}\text{U}/^{238}\text{U}$ activity ratio in groundwaters from the Tashkent artesian basin (Uzbekistan) in 1996-1998. Arrow indicates the time of occurrence of the catastrophic Tashkent earthquake (April 22, 1966). Water analyses from 10 boreholes. Plotted by the data reported in Zverev et al. (1980). The data suggest that substantial amounts of the ^{234}U -enriched waters have been introduced into the basin during the earthquake. The 15 months lag is related to the low flow velocities of the basinal fluids.

seismically active regions of the Caucasus (Georgia).

Figure 3-7-27 shows calculated ^{206}Pb accumulation curves for different initial $^{234}\text{U}/^{238}\text{U}$ activity ratios (the values are normalized to $^{238}\text{U} = 1$). If we define the normalized (at $^{238}\text{U} = 1$) concentration of ^{206}Pb as $F_{206\text{Pb}}(t, \gamma_0)$, where γ_0 is the initial $^{234}\text{U}/^{238}\text{U}$ activity ratio, the absolute amount of radiogenic ^{206}Pb accumulated due to decay of ^{238}U and ^{234}U will be:

$$^{206}\text{Pb}_U = F_{206\text{Pb}}(t, \gamma_0) \cdot ^{238}\text{U} \quad (3-7-73)$$

Using Eqs. 3-7-71 and 3-7-72 and assuming that the concentrations of Pb isotopes in water change slowly, the total amount of the ^{206}Pb concentrated on the micelles (and subsequently passed onto opal; see section 3-7-5-2) at time t may be expressed as:

$$^{206}\text{Pb}_{\text{tot}} = F_{206\text{Pb}}(t, \gamma_0) \cdot ^{238}\text{U} + 4\pi D_{\text{Pb}} r \left(^{206}\text{Pb}_{\text{common_water}} + ^{210}\text{Pb}_{222\text{Rn_water}} \right) dt \quad (3-7-74)$$

Consider now the accumulation of the non-radiogenic ^{204}Pb . By analogy with Eq. 3-7-71:

$$^{204}\text{Pb}_{\text{tot}} = \int_{t_0-dt}^{t_0} 4\pi D_{\text{Pb}} \cdot r(t) \cdot ^{204}\text{Pb}_{\infty_water}(t) dt \quad (3-7-75)$$

from the acidic intrusive rocks may have $\gamma = 10$ to 12. At Yucca Mountain, surface runoff has $\gamma = 1.5$ to 3.7, perched waters $\gamma = 2.4$ to 8.4, and groundwater from the volcanic aquifer beneath Yucca Mountain $\gamma = 4.5$ to 8.1 (Fabryka-Martin et al., 2000). In tectonically active areas the parameter γ may be time-dependent and may change with the changing degree of tectonic activity. Figure 3-7-26 shows a time series of the γ measurements in artesian groundwaters before and after a major earthquake. It is apparent from the figure that tectonic activity may cause transient but strong variations in the relative abundances of ^{234}U and ^{238}U isotopes. Zverev et al. (1975) reported similar seismic-related increases of γ (up to 14) for the thermomineral waters from the

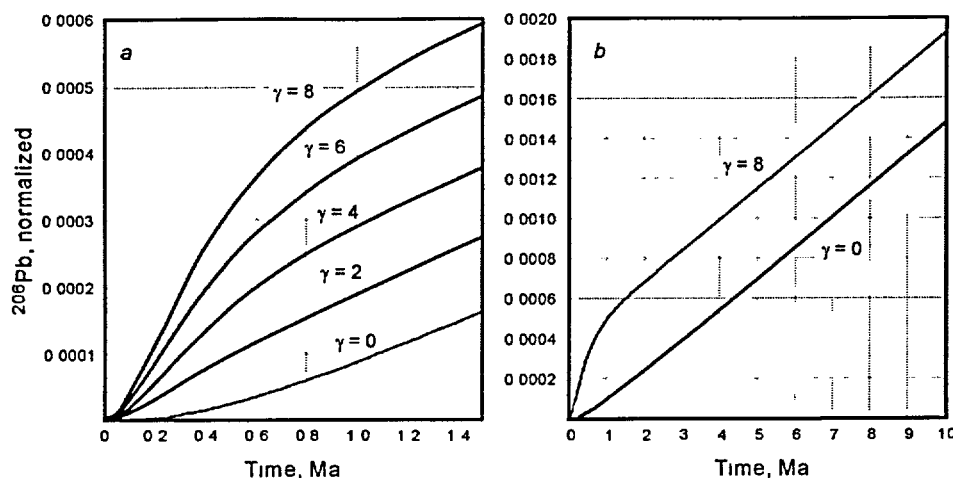


Figure 3-7-27. Growth of ^{206}Pb from decay of ^{234}U and ^{238}U at different initial $^{234}\text{U}/^{238}\text{U}$ activity ratios (γ). Initial $^{238}\text{U} = 1$. *a* – accumulation during the first 1.5 Ma; *b* – accumulation during 10 Ma.

3.7.6.2 The "common lead" and Pb_{Rn} corrections in computing the U-Pb radiometric ages

In order to find the content of the radiogenic lead produced by the *in situ* decay of ^{238}U and ^{234}U , the allogenic lead contributed by depositing fluids must be subtracted from the total $^{206}\text{Pb}_{\text{tot}}$ present in the sample (the so-called "common lead correction"):

$$^{206}\text{Pb}_{\text{common}} = \int_{t_0-dt}^{t_0} 4\pi D_{\text{Pb}} \cdot r(t) \cdot A^{206} \cdot ^{204}\text{Pb}_{\infty_water}(t) dt \quad (3-7-76)$$

where A^{206} is the proportionality coefficient between ^{204}Pb and ^{206}Pb measured in the "baseline" geologic material (at Yucca Mountain the coefficient, $A^{206} = 18.83 \pm 0.82$, was calculated from the analyses of "7 samples of Yucca Mountain filtered water and 22 samples of subsurface calcite with low U/Pb ratios"; Neymark et al., 2002). Subtracting Eq. 3-7-76 from Eq. 3-7-74 we obtain:

$$^{206}\text{Pb}^* = F_{^{206}\text{Pb}}(t, \gamma_0) \cdot ^{238}\text{U} + 4\pi D_{\text{Pb}} \cdot r \cdot ^{210}\text{Pb}_{222\text{Rn_water}} \cdot dt \quad (3-7-77)$$

In "conventional" U-Pb dating, the $^{206}\text{Pb}^*$ is used to calculate the age date for the sample. If our model is correct, however, this $^{206}\text{Pb}^*$ consists of the two components: the *in situ* produced ^{206}Pb (first term in the Eq. 3-7-77) and $^{206}\text{Pb}_{\text{Rn}}$ (second term). In order to obtain true ages, therefore, the latter component must be subtracted before calculating the radiometric age. The application of the Pb_{Rn} correction is schematically shown in Figure 3-7-28.

It is apparent from Figure 3-7-28 that even small (in terms of the absolute quantities) amounts of the Pb_{Rn} , which are added to the system may dramatically offset the apparent U-Pb ages calculated using

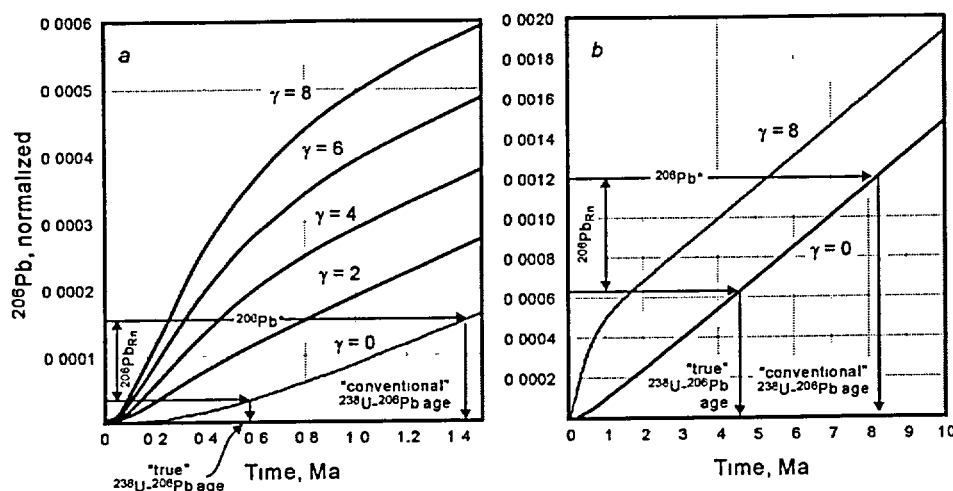


Figure 3-7-28. Application of the Pb_{Rn} correction for calculation radiometric age of a mineral (schematic presentation). *a* – first 1.5 Ma; *b* – 10 Ma. Example for ^{206}Pb is shown; ^{207}Pb and ^{208}Pb must be corrected as well. For explanation of curves see Figure 3-7-27. Note that the values of the $^{206}\text{Pb}_{\text{Rn}}$ on both graphs are taken arbitrarily.

"conventional" equations for radiometric dating. It is also apparent that if any Pb_{Rn} is present in the mineral, the true age of the latter will always be younger than the "conventional" age date calculated by using uncorrected values of radiogenic $^{206}\text{Pb}^*$ for Pb_{Rn} .

3.7.6.4. Variability and evolution trends of the Pb_{Rn}

As was discussed in section 3.7.5.2.2 above (see Figures 2-7-21 through 3-7-24), the values of Pb_{Rn} are a strong function of the sizes of micelles involved in the precipitation of opal. The sizes of micelles suspended in real solutions, however, are not uniform; in practice they are characterized by a size distribution or "spectrum". As discussed in Appendix 3-7-3, the spectrum of sizes for coagulating particles should have a characteristic "self-sustained" shape. The characteristics of the size distributions of micelles (e.g., the mode and dispersion of the distribution) are controlled by the parameters of the mineral-forming medium. Among the later, the chemistry of fluids (controlling the charges of chemical species) and the temperature are the most important parameters (see Eq. 3-7-55). Therefore, it is to be expected that in the a chemically and thermally evolving environment the size distributions of micelles will also evolve. As a consequence, a substantial variability of Pb_{Rn} in opals formed at slightly different conditions (i.e., from micelles with slightly different size distributions) on one hand, and the overall tendency of the unidirectional change of the Pb_{Rn} (due to the unidirectional character of evolution of the chemistry and the temperatures of the fluids; see Chapters 3-4 through 3-6 for discussion) on another hand, are expected at Yucca Mountain.

Neymark et al. (2002) reported the "conventional" ^{235}U - ^{207}Pb age dates calculated for different parts of the mineral crusts from the ESF. The data are summarized in Figure 3-7-29. It is likely that the high variability of the data, as well as the apparent overall trend of the "decrease" of the radiometric ages across the crusts, reflect the variability of the Pb_{Rn} and its overall increase in the process of mineral growth.

To summarize this part of our analysis, we need to assess the values of Pb_{Rn} expected for the Yucca Mountain mineral forming system. Were they large enough to substantially offset the "conventional" U-Pb age dates? Our calculations show that the concentrations for Pb_{Rn} that may be accumulated on micelles in the environment similar to that at Yucca Mountain are comparable, within orders of magnitude, with the total abundances of the radiogenic Pb isotopes measured in the Yucca Mountain samples. In other words, most of radiogenic lead isotopes that are present in the Yucca Mountain opals may be accounted for by the input of Pb from the decay of radon, and, by comparison, the share of the *in situ* radiogenic lead may be negligible.

Under such circumstances, the calculation of "U-Pb ages" for the Yucca Mountain samples by means of the "conventional" radiometric dating equation is totally inappropriate. The calculated "radiometric ages" do not provide a measure of the true ages of the samples.

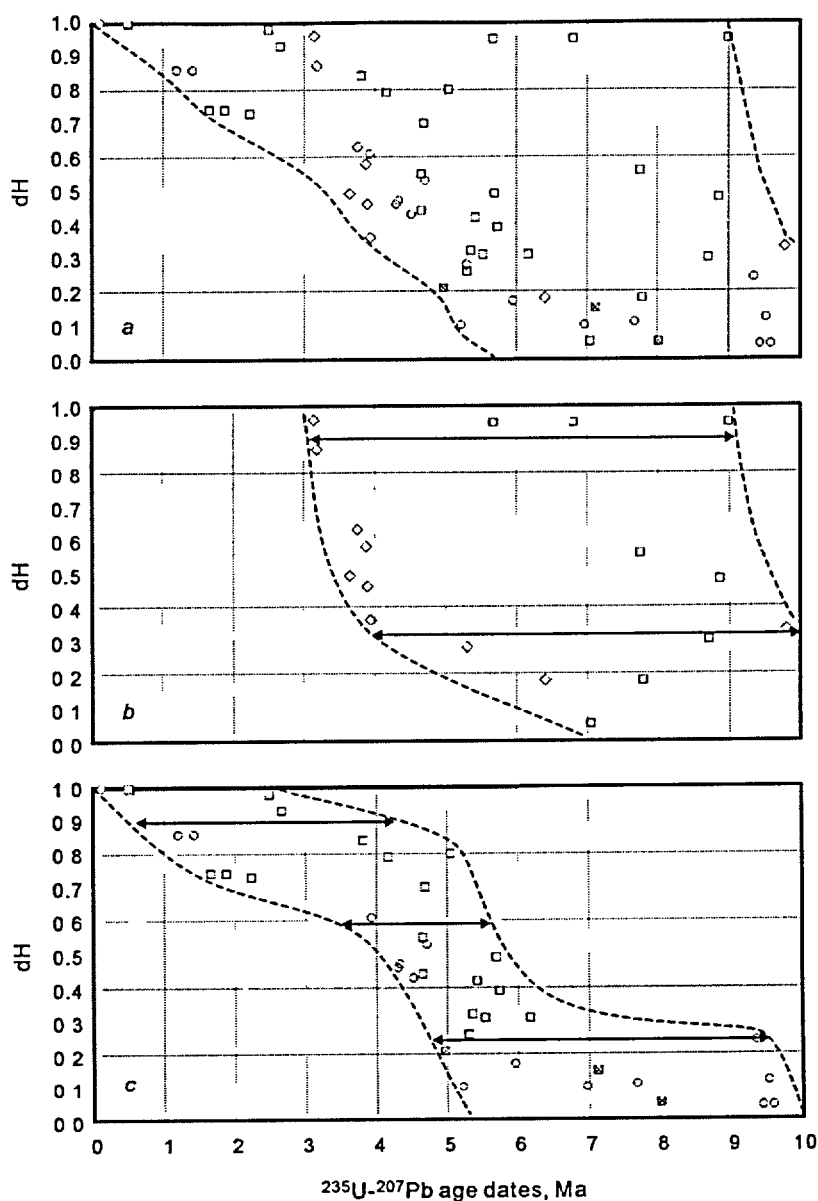


Figure 3-7-29. "Conventional" ^{235}U - ^{207}Pb age dates as a function of the normalized height of the dated subsample location above the base of the mineral crust. *a* – all data; *b* – data on 2 mineral crusts located close to the horst-bounding (near North Portal of the ESF; host rock is welded Tiva Canyon tuff, TCw); *c* – data on 5 mineral crusts located near the central part of the repository block (near the North bend of the ESF; host rock is welded Topopah Spring tuff, TSw). *Dashed lines* indicate boundaries of the data field; *arrows* – variability of the data. One outlier of 15.3 ± 3.2 Ma at $dH = 0.7$ is not plotted. $dH = 0$ corresponds to the base and $dH = 1$ corresponds to the outer surface of the crust. Plotted by the data reported in Neymark et al. (2002).

3.7.7. Summary and conclusions

3.7.7.1. The model

In this chapter we present a theoretical model, which describes the role of radon and colloids in the accumulation of additional radiogenic lead in opals from Yucca Mountain. This additional lead is in excess of the *in situ* decay of U and Th in the opals and as a consequence may cause significant distortion of the age dates computed using the "conventional" U-Pb radiometric dating equations. In constructing the model we took into account the following processes and features.

3.7.7.1.1. Assumptions

1. Lead contained in opals grown in open cavities in the rhyolite tuffs of Yucca Mountain may represent a mix of the three "sources": (a) allogenic Pb trapped by a growing mineral from the mineral forming fluid; (b) Pb formed through *in situ* decay of the of U and Th contained in the opal; and (c) lead accumulated in water filling the open cavity due to the decay of U and Th residing in the surrounding rock and the subsequent migration of intermediate Rn isotopes into the cavity (this lead is denoted as Pb_{Rn}).

2. The deposition of opals took place in a "flowing water" environment (i.e., significant volumes of water moved through the cavity during the time of mineral growth). This stems from the fact that in order to deposit the amounts of minerals present in cavities, the mineralized water must have changed many times.

3. Opal grows from colloidal solutions, the major component of which are micelles of silica. The latter, after enlargement caused by coagulation and the ensuing sedimentation, precipitate on the cavity floor and/or on pre-existing minerals.

3.7.7.1.2. Limitations of the model

Substantial uncertainty in the model calculations is caused by the poor knowledge of the boundary conditions. The most important in this regard is the absence of factual data for the emanation and contents of radon in the underground atmosphere and groundwaters at Yucca Mountain. To our surprise, we could not find any information in this regard in the U.S. DOE bibliographic database available to us. Consequently, we had to use "generic" data for Rn emanation in the rocks with chemical compositions similar to that of the Yucca Mountain rhyolitic tuffs. Obviously, the numeric results of the model may be refined when, and if, the site-specific data became available.

In addition, the comparison of the predicted results with the factual data on the U and Pb isotope contents in the Yucca Mountain opals is difficult. This is because the data are lacking for the sizes and shapes of mineralized cavities, the exact position of samples inside the cavities and similar spatial

parameters. These parameters, however, may be crucial in both confirming the validity of the model and increasing the reliability of the calculations.

In the current version of the model we do not discuss interactions between particles and chemical species caused by their charges (in other words, we consider SiO_2 micelles and Pb atoms/complexes as electro-neutral).

3.7.7.2. The most important results

As long as there exists an emanation of Rn from the rock mass, the Pb_{Rn} isotopes originating from the decay of radon will accumulate in open cavities in the rock. The distributions of different isotopes of Pb_{Rn} in a cavity depend on the size of the cavity, so that accumulations of each Pb_{Rn} isotope is different in a narrow fracture (0.1 mm or less) as compared to large open cavities (e.g., lithophysa). For a simplified model of a cavity filled with stagnant water, we calculated the kinetics for the accumulation of the Pb_{Rn} isotopes. As it is shown in Figures 3-7-7 through 3-7-9, the profiles for the concentrations of Pb_{Rn} in a cavity have maxima, whose positions depend on the half-life of the specific parent Rn isotope.

The movement of water leads to a more complex distribution of Pb_{Rn} isotopes in a cavity (see Figures 3-7-15 through 3-7-17). In the thin layer of water adjacent to the cavity walls (~1 cm), however, the distributions obtained for the model for a cavity filled with stagnant water persist.

Growing opal may trap Pb_{Rn} through two major mechanisms: (a) the direct diffusion flux of Pb_{Rn} on the surface of the opal; and (b) the diffusion entrapment of Pb_{Rn} on micelles followed by coagulation and sedimentation of the latter. Numeric calculations show that the mechanism involving colloids is orders of magnitude more efficient than the direct diffusion mechanism.

The model of accumulation of Pb_{Rn} on micelles during their growth from minimal sizes to the critical size of 5-10 nm, as well as during coagulation was constructed. The concentration of Pb_{Rn} isotopes in micelles (and in opals formed from these micelles) is controlled, primarily, by the average size of particles. For micelles with sizes of 5 to 50 nm, the calculated concentrations of Pb_{Rn} yielded values similar to the total Pb values measured in the Yucca Mountain opals.

The time scales of the formation of opal by the coagulation mechanism may be assessed as follows. In order to deposit 1 g of opal in a cavity with $R = 10$ cm from a fluid containing 10^{-4} - 10^{-5} mole·l⁻¹ of dissolved SiO_2 , some $n \cdot 10^3$ l of water is required if all silica dissolved in the water is precipitated. Assume a fracture, through which the water enters cavity, has a cross-section of 1 mm², and the water flow velocity in the fracture is 1 cm·s⁻¹ (these parameters were taken for numeric modeling, the results of which are shown in Figures 3-7-15 through 3-7-17), the passage of $n \cdot 10^3$ l of water in such a cavity would take between 1 and 10 years. The assumption of 100 % precipitation of silica is rather unrealistic; a more-

realistic efficiency of silica precipitation of 0.01% would yield an estimate of $n \cdot 10^6$ l of water and, respectively, $n \cdot 10^3$ years.

Opals formed through the coagulation and sedimentation of colloids may thus be formed (and accumulate substantial amounts of Pb_{Rn}) within thousands of years. By contrast, the net diffusion mechanism of Pb_{Rn} entrapment requires orders of magnitude greater times. For example, for a hypothetical mineral that contains about 200 ppm of U and grows continuously in an open cavity for 1 Ma, the amount of Pb_{Rn} supplied by diffusion will roughly be equal to the amount of Pb produced by *in situ* decay of U (in this calculation we assumed that the bedrock rock contains 5 ppm of U).

Minerals formed in open cavities in the rhyolitic tuffs ($U_{tuff} = 4-5$ ppm, $Th_{tuff} = 14-16$ ppm) from colloidal solutions via enlargement, coagulation and sedimentation of micelles are expected to trap substantial amounts of Pb_{Rn} . If the "conventional" equations of the U-Pb dating are applied to such minerals, the resulting age dates will be overestimates of the actual ages. Situations are possible whereby minerals formed, say 1,000 years ago, would produce "conventional" (erroneous) age dates of several Ma.

Based on the discussion presented in this Chapter we conclude that the "conventional" U-Pb technique is not suitable for dating geological materials that are: (a) geologically young (Miocene and younger); (b) formed in open cavities; and (c) formed with the involvement of colloids (Pashenko and Dublyansky, 2002). Silica minerals from the Yucca Mountain vadose zone must be placed in the category of minerals that are not datable by the conventional U-Pb method.

Appendix 3-7-1: Distributions of elements and isotopes in samples from the ESF

The database

For our analysis we used tabulated data from three publications, specifically, USGS (1998), and Neymark et al. (2000 and 2002). The database may be broadly subdivided into three parts by the types of data. These are: data from the outside (i.e., the latest) crystal surfaces (which was the focus of the Neymark et al., 2000 publication), data collected across mineral crusts in lithophysal cavities, and data collected across mineral crusts in fractures. It might be expected, from general considerations, that the physicochemical processes controlling growth in the last two settings might be different. The inventory of samples along with a brief description of the data available is presented in Tables 3-7-A-1 and 3-7-A-2.

Table 3-7-A-1

Inventory of samples for which U-Th-Pb isotope data are available
(data published by Neymark et al., 2002)

N	ESF station	Sample ID	Type of sample	Number of analyses	Note
1	01+11.55	HD1838	Fracture	11	
2	12+15 58	HD2093	Fracture	1	
3	12+21.83	HD2021	Fracture	8	
4	15+33 25	HD2029	Fracture	2	
5	28+28	HD2357	Cavity	15	Alcove 5 (28 5 m)
6	28+80 0a	HD2019A1	Cavity	6	
7	28+80.0b	HD2019A	Cavity	4(8)	4 results are reported for leached samples, these results are not discussed here.
8	28+81.0	HD2019	Cavity	5	
9	28+81 6	HD2054	Cavity	1	
10	29+11.2	HD2055	Cavity	3	
11	30+17.78	HD2059	Cavity	3	
12	30+50 70	HD2074U	Cavity	14	
13	66+00	HD2238	Fracture	1	
14	71+65 8	HD2247	Fracture	1	
15	75+06 8	HD2257	Fracture	9	
16	75+74.7	HD2260	Fracture	1	
				Total	
				85	

Table 3-7-A-2

Inventory of samples for which U-Th-Pb isotope data are available (data published by Neymark et al., 2000)

N	ESF station	Sample ID	Type of sample	Number of analyses
1	22+72.0	HD2008		1
2	26+78 1	HD2098		3
3	29+11.2	HD2055	Cavity	4
4	29+22 9	HD2056		2
5	30+17.8	HD2059	Cavity	3
6	31+16.1	HD2063		1
7	33+16.2	HD2065		3
8	33+95 8	HD2066		3
9	38+17.2	HD2079		5
10	40+26 9	HD2100		2
11	57+71.7	HD2168		1
12	63+20 2	HD2179		4
13	63+38 1	HD2181A		1
14	76+81 0	HD2281		1
15	78+06.4	HD2281		1
16	79+90 0	HD2283		1
				Total
				35

The samples listed in Table 3-7-A-1 were deemed the most informative because either photographs or line drawings of the studied samples were presented in the original publication. This made it possible to analyze the data considering the position of the analytical spots within individual crusts. In Appendix 1 we present a visual representation of composition data for the elements (U, Th, Pb) and the non-radiogenic isotope ^{204}Pb in opals in different crusts from the ESF. We use a dimensionless parameter dH which denotes the relative position of the data points within the analyzed crusts. The parameter changes from 0 (base of the crust) to 1 (top of the crust).

Distribution of total U, Pb, Th and ^{204}Pb across the crusts

The series of figures below shows distributions of U, Pb, Th and ^{204}Pb across mineral crusts sampled at different locations in the ESF. We removed one outlier (UPb5) in sample HD2074. The concentration of U listed for this sample was 789 ppm, which is significantly greater than the rest of the data. Additionally, since the weight of this sample was one of the smallest among the analyzed samples (0.035 mg), we suspect that the high U content for this sample may be an artifact.

The isotope, ^{204}Pb , is the only stable isotope of lead. The isotope is used to assess the content of "common lead" which needs to be deducted before the radiometric U-Pb ages can be calculated.

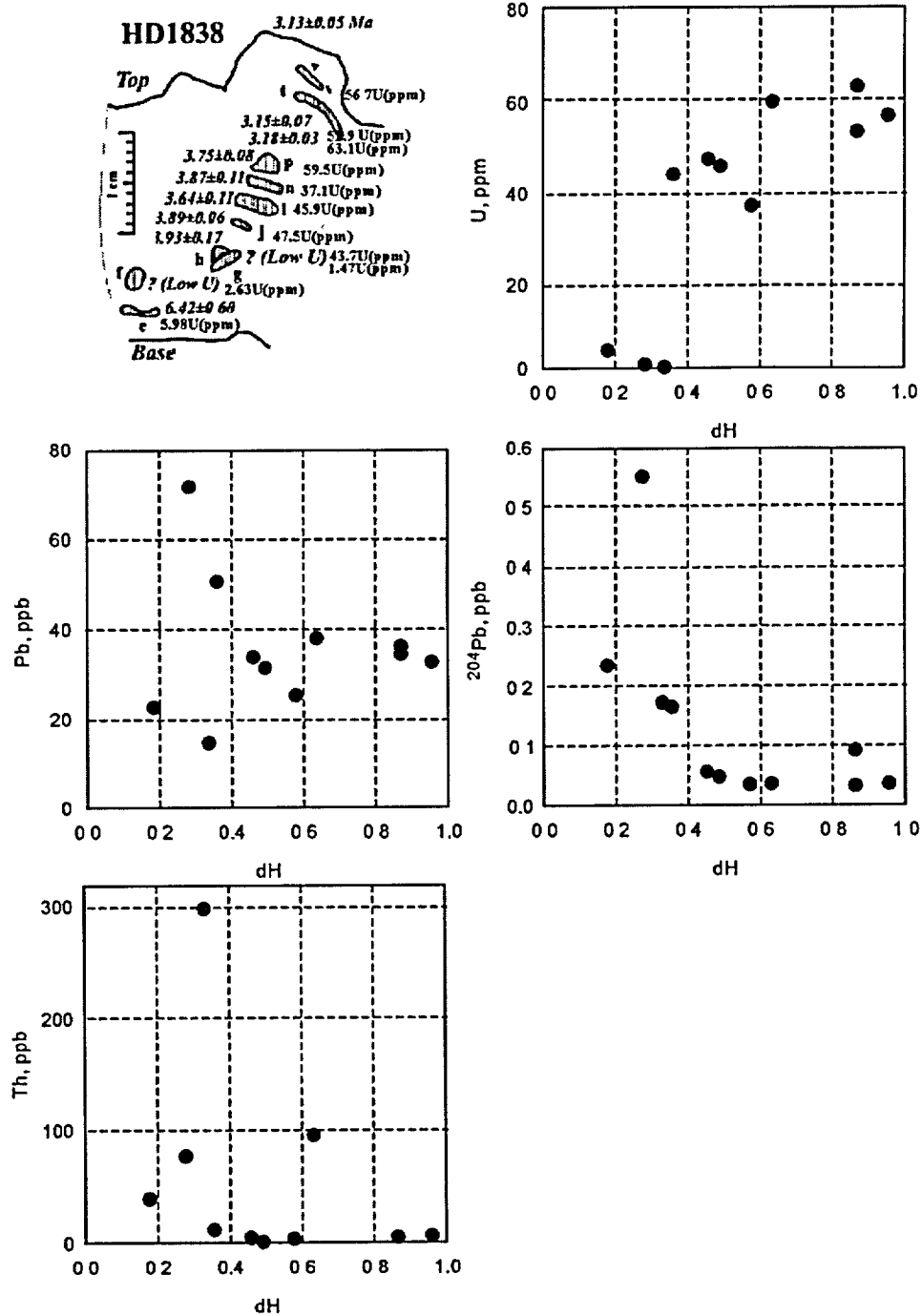


Figure 3-7-A-1. Contents of U, Pb, ^{204}Pb and Th across mineral crust from the ESF station 01+11.55. Data from Neymark et al. (2002). *dH* is the normalized thickness of the crust.

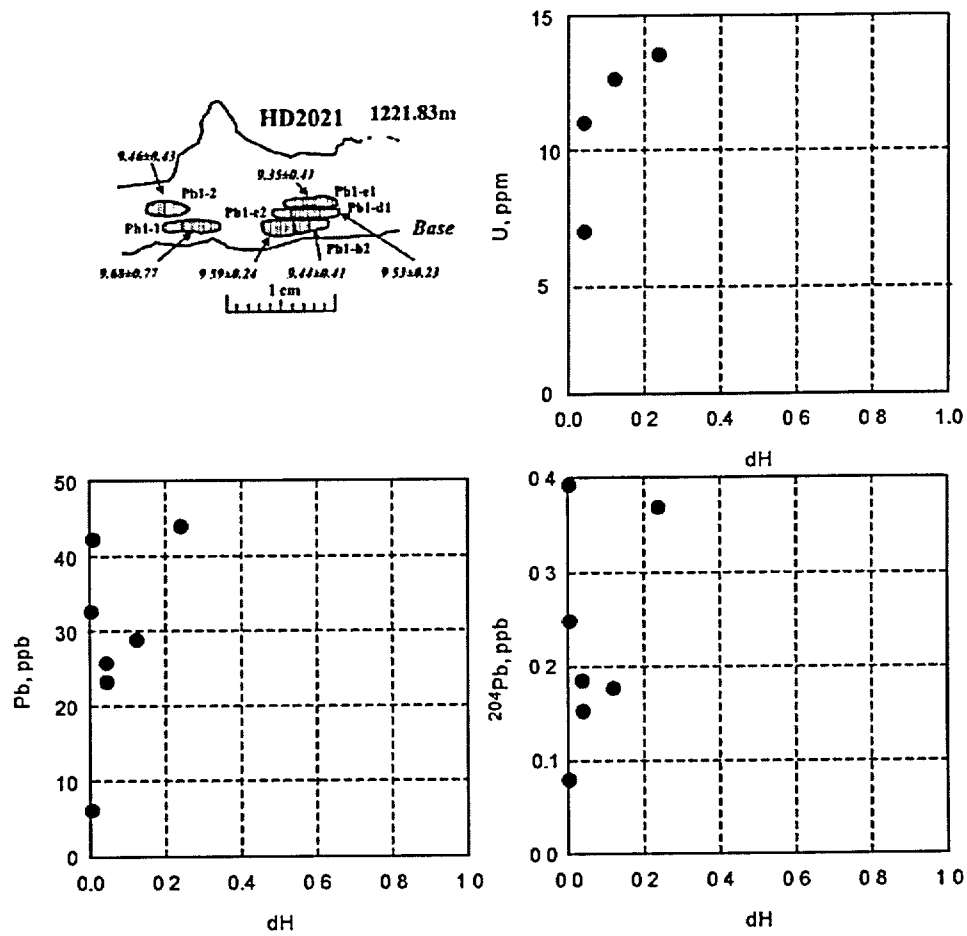


Figure 3-7-A-2. Contents of U, Pb, and ²⁰⁴Pb across mineral crust from the ESF station 12+21.83. Data from Neymark et al. (2002). *dH* is the normalized thickness of the crust.

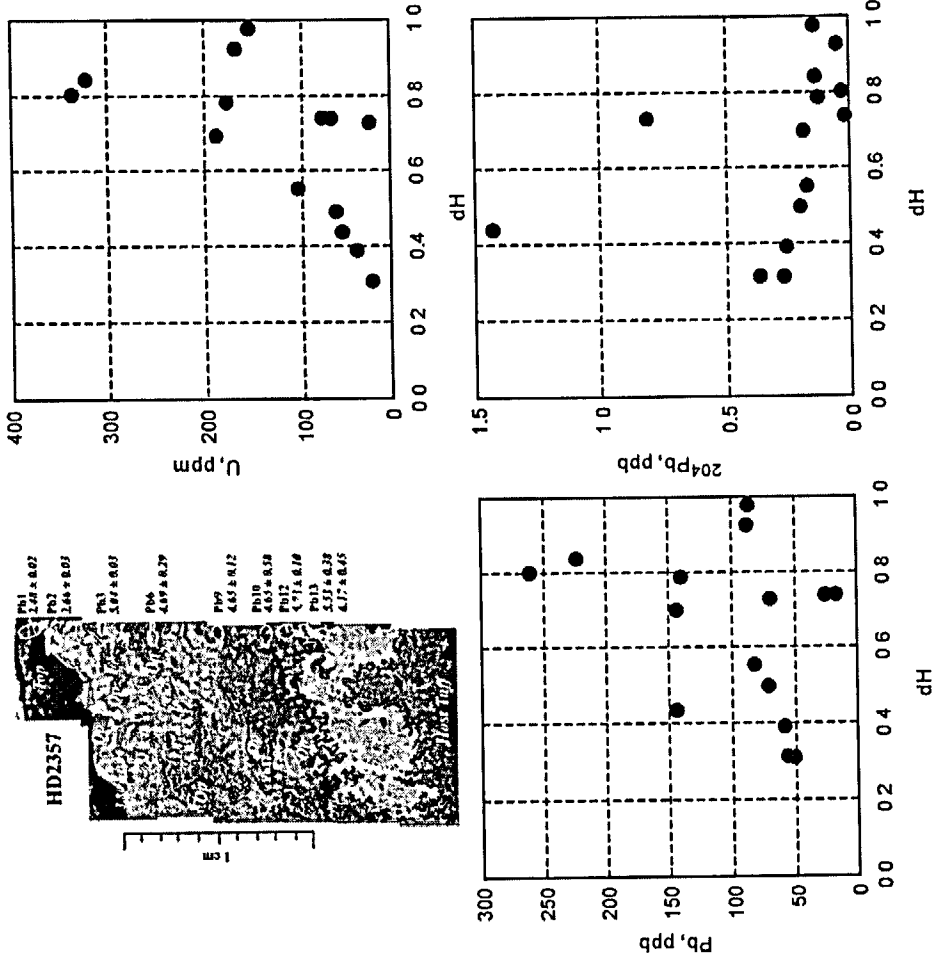


Figure 3-7-A-3. Contents of U, Pb, and ²⁰⁴Pb across mineral crust from the ESF station 28+28. Data from Neymark et al. (2002). *dH* is the normalized thickness of the crust.

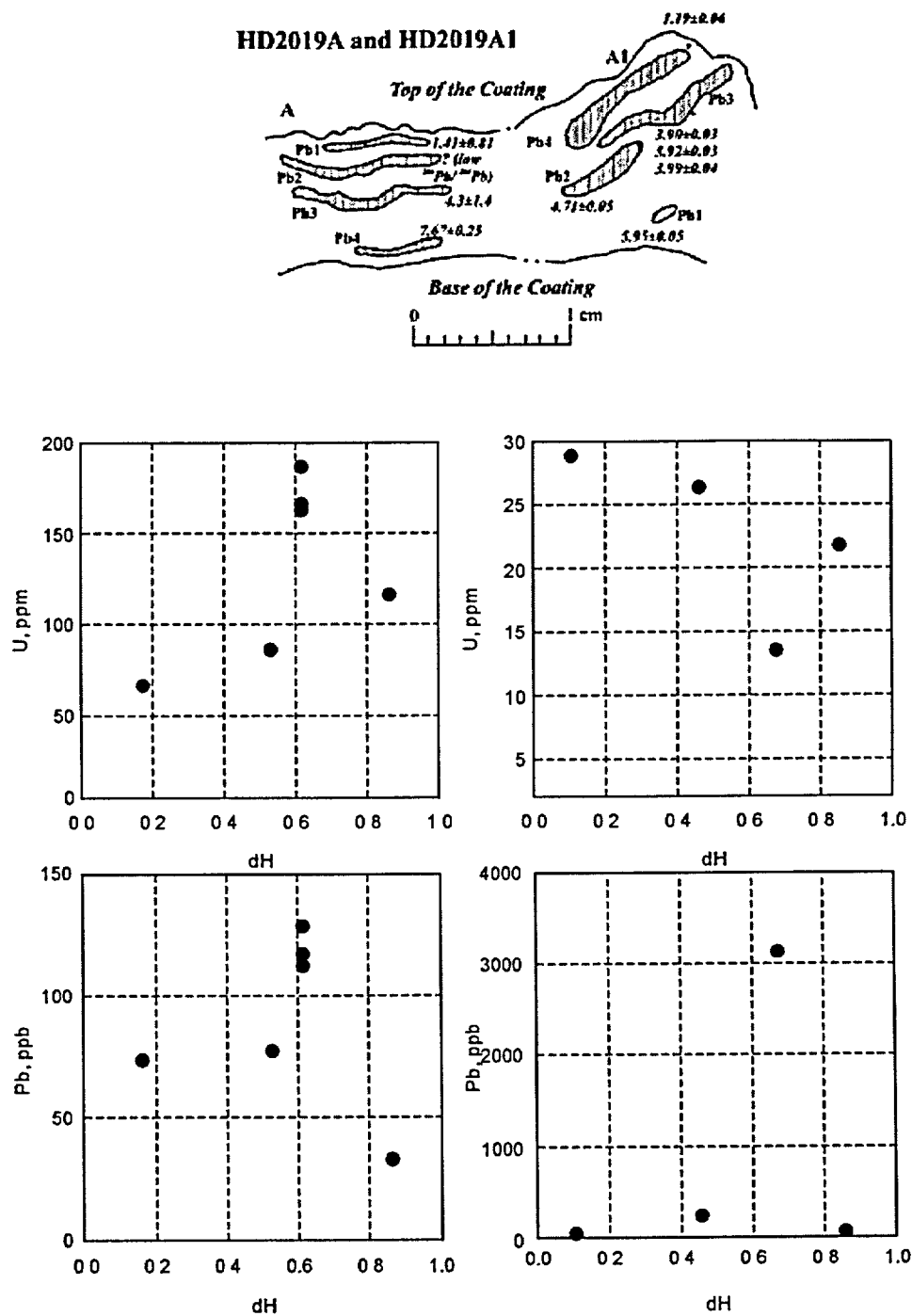


Figure 3-7-A-4. Contents of U and Pb across mineral crust from the ESF station 28+80 in two split samples (A – left and A1 – right). Data from Neymark et al. (2002). *dH* is the normalized thickness of the crust.

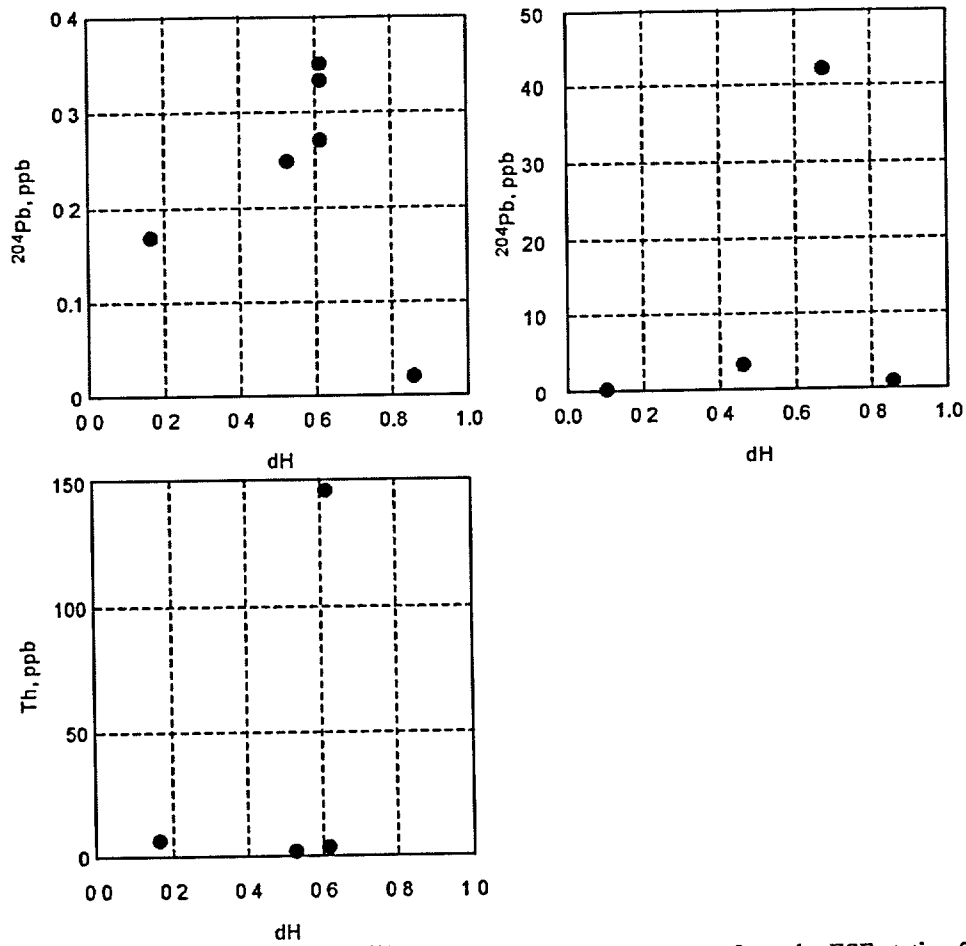


Figure 3-7-A-4 (continued). Contents of ^{204}Pb and Th across mineral crust from the ESF station 28+80 in two split samples (A – left and A1 – right). Data from Neymark et al. (2002). *dH* is the normalized thickness of the crust.

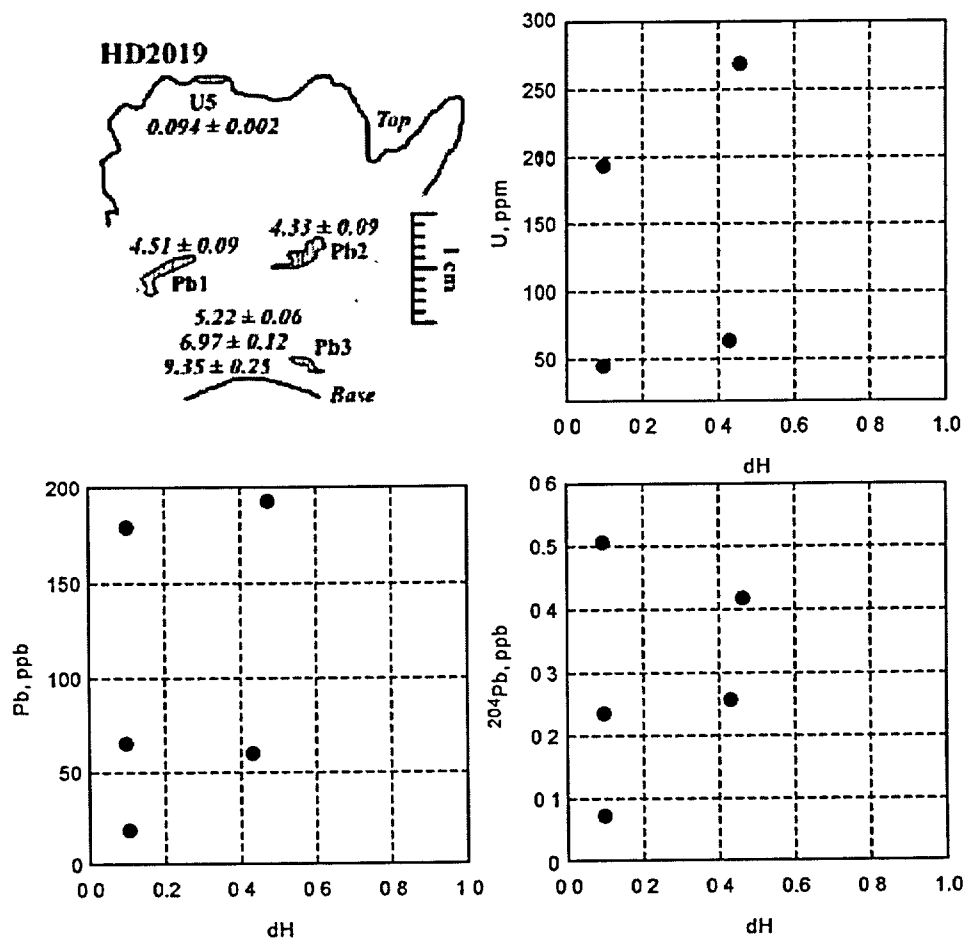


Figure 3-7-A-5. Contents of U, Pb, and ^{204}Pb across mineral crust from the ESF station 28+81. Data from Neymark et al. (2002). dH is the normalized thickness of the crust.

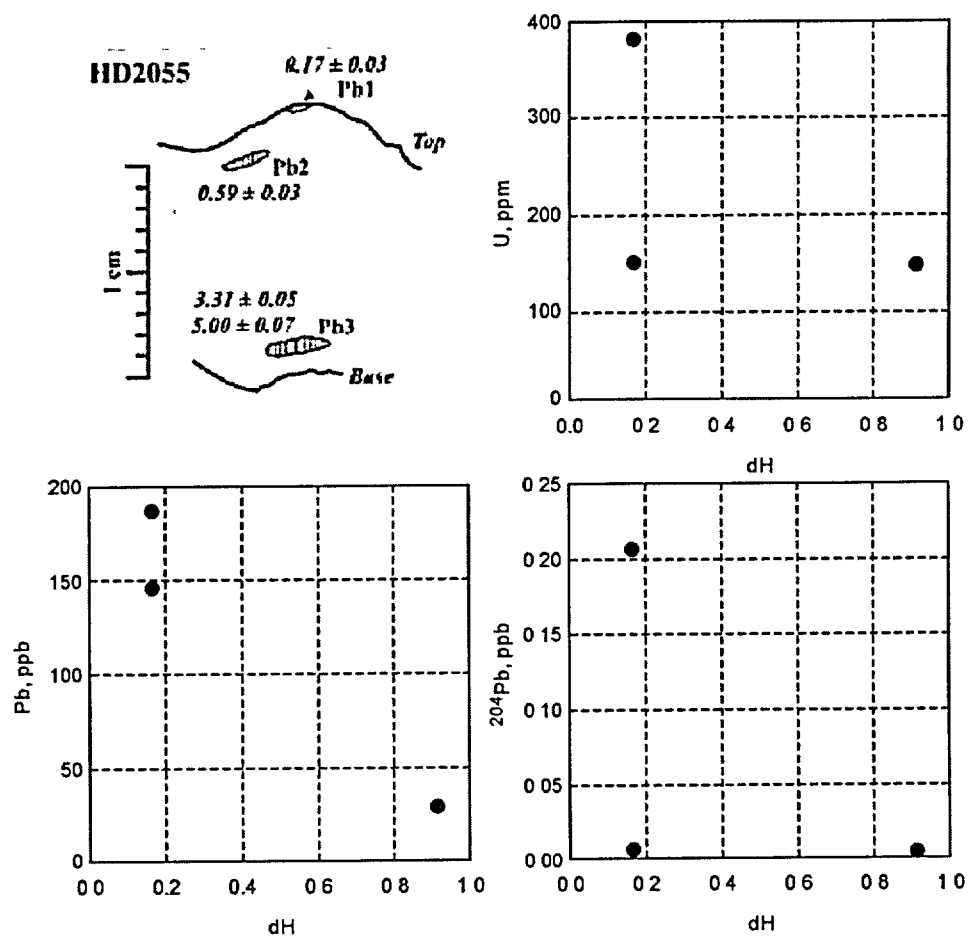


Figure 3-7-A-6. Contents of U, Pb, and ^{204}Pb across mineral crust from the ESF station 29+11.2. Data from Neymark et al. (2002). dH is the normalized thickness of the crust.

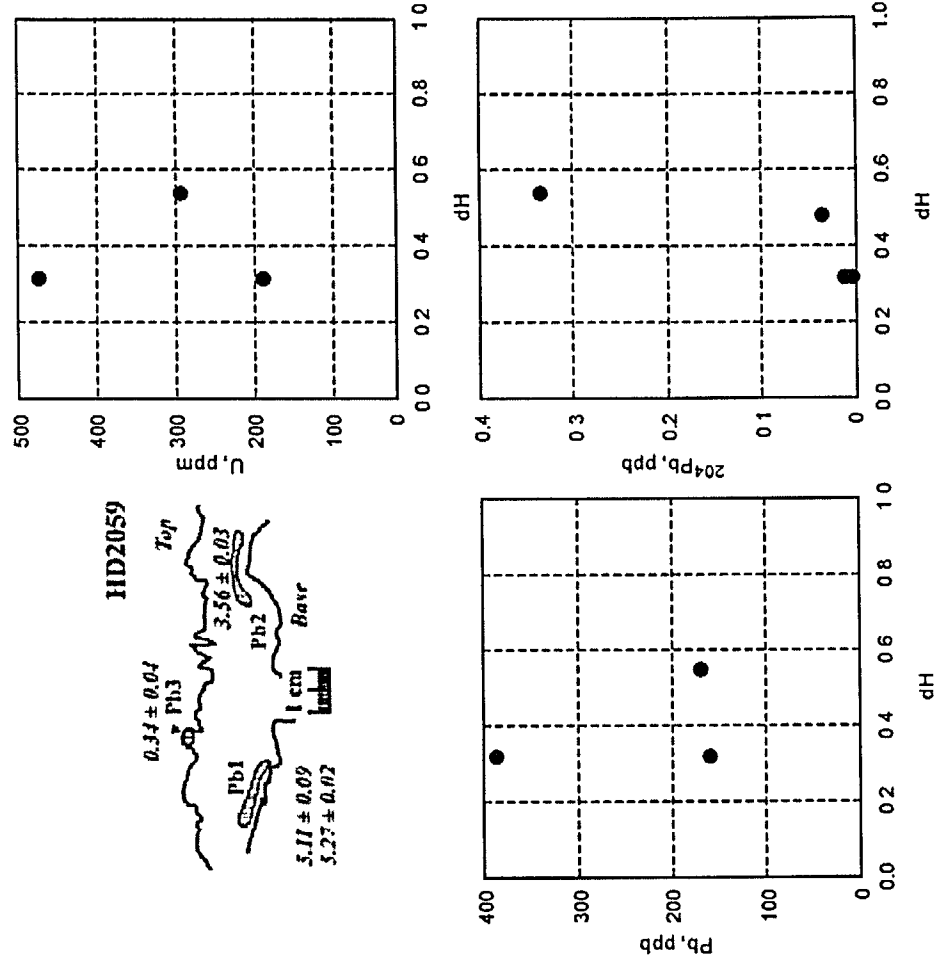


Figure 3-7-A-7. Contents of U, Pb, and ^{204}Pb across mineral crust from the ESF station 30+17.78. Data from Neymark et al. (2002). dH is the normalized thickness of the crust.

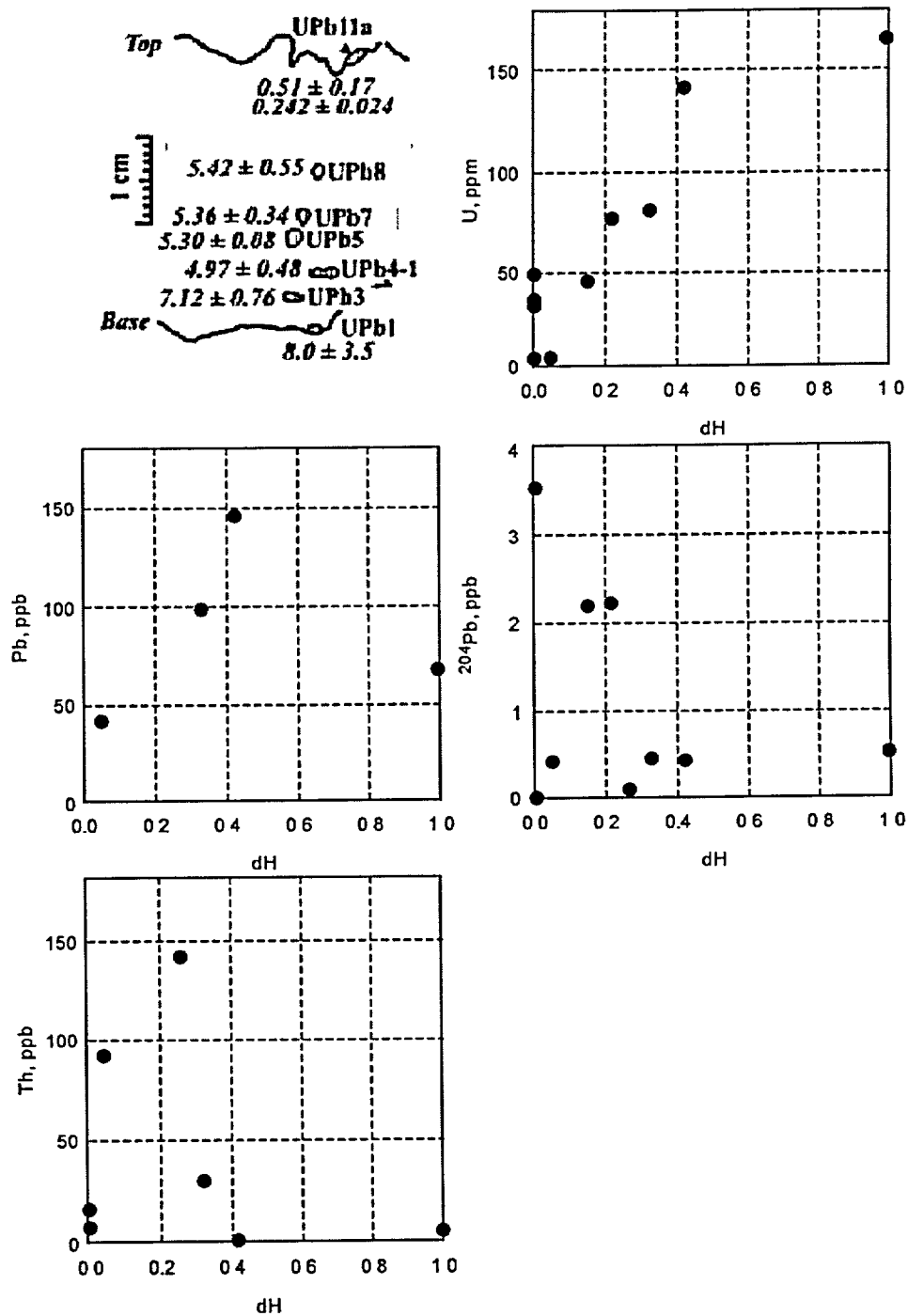


Figure 3-7-A-8. Contents of U, Pb, ²⁰⁴Pb, and Th across mineral crust from the ESF station 30+50.7. Data from Neymark et al. (2002). *dH* is the normalized thickness of the crust.

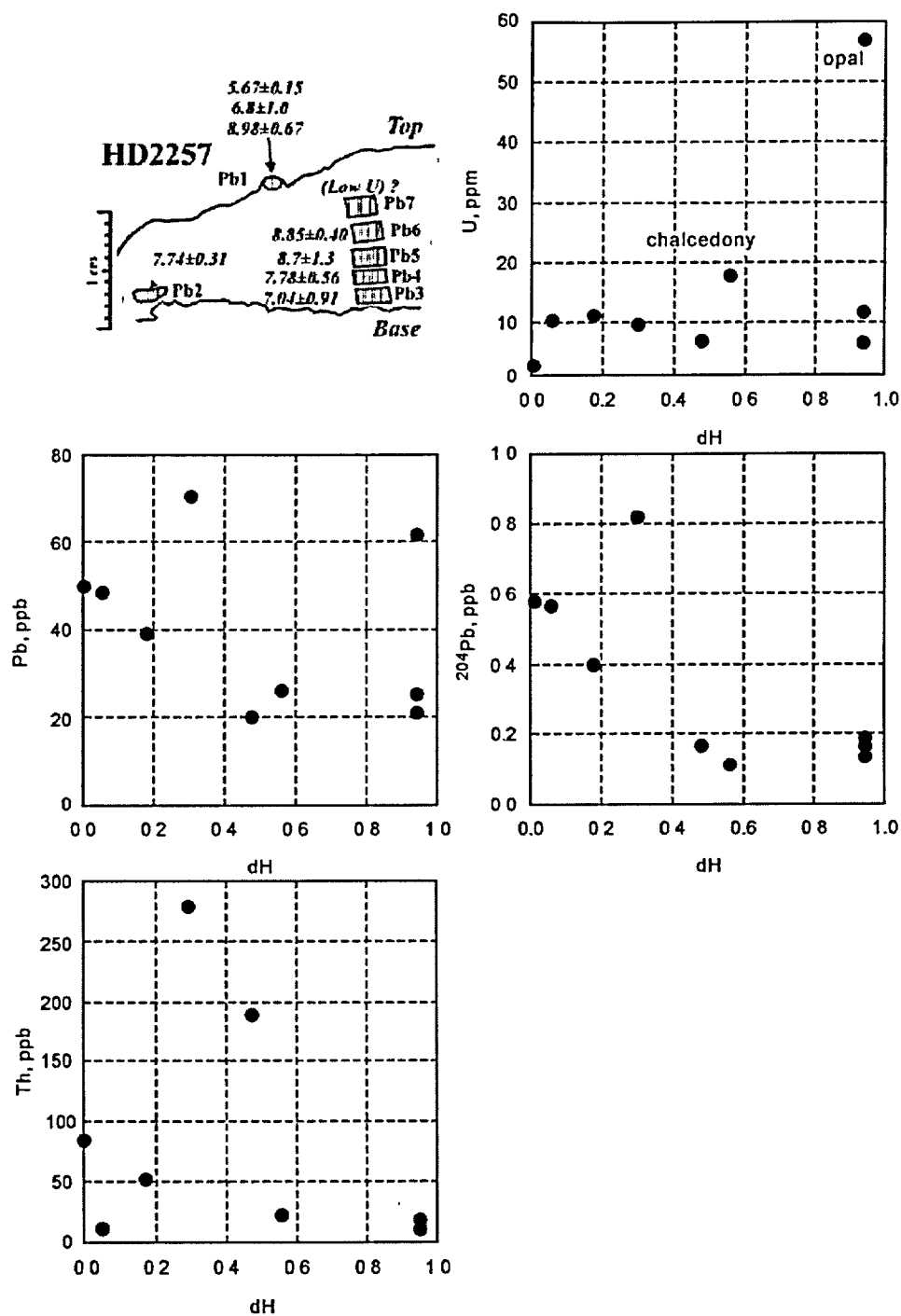


Figure 3-7-A-9. Contents of U, Pb, ^{204}Pb , and Th across mineral crust from the ESF station 75+06.8. Data from Neymark et al. (2002). dH is the normalized thickness of the crust.

Distribution of elements and isotopes in the ESF

The open cavities from which minerals were sampled differ spatially. Near the North and South portals of the ESF minerals are present typically in cavities that are best described as relatively narrow fractures, whereas in the area between, approximately 2500 and 3500 m, minerals primarily reside in relatively large lithophysal cavities. It was shown in Figure 3-7-1 that different morphologies of the mineral-hosting cavities are associated with very different distributions of U and Pb abundances. In addition, the geochemical studies presented in the previous chapters of this report indicate that parameters for the mineral-forming fluids vary spatially within the ESF block of the vadose zone. For instance, the distribution of maximum paleotemperatures (i.e., the highest temperatures to which the rock was exposed during the growth of minerals) is non-uniform along the ESF and has a pronounced minimum in the vicinity of the North bend of the ESF and in the northern part of the north-south drift (see Figure 3-6-7 in Chapter 3-6).

The general model developed in this chapter predicts that the processes responsible for the accumulation of isotopes in depositing silica minerals must be sensitive to both the geometry of the open space surrounding the growing mineral and the parameters of the mineral-forming fluid. Below we evaluate distributions of the elements U, Th, and Pb and isotopes of lead (^{204}Pb , ^{206}Pb , ^{207}Pb , and ^{208}Pb) in silica minerals as a function of the distance along the ESF.

Abundances of U along the ESF

Figure 3-7-A-10 shows the data on distribution of the U abundances along the ESF. The database includes data from the outer surfaces of crystals (squares; from Neymark et al. 2000) and data from across the mineral crusts (circles, Neymark et al. 2002). Since the measured values span three orders of magnitude, the data are presented in both normal (*a*) and logarithmic (*b*) scales.

Figure 3-7-A-10 shows that two areas in which the distributions of the maximum U-abundances are substantially different. Area 1 lies between 2600 and 3500 m; Area 2 – lies between 0 and 2600 m and between 3500 and 7800 m. Graph *c* presents an approximation for the distribution of the maximum U-abundances by the two Gauss exponents of the form:

$$U_{\max} = A_i \exp\left(-\frac{(L - B_i)^2}{C_i^2}\right) \quad (3-7-A-1)$$

where L is the distance along the ESF (measured from the North Portal, m), and A_i , B_i , and C_i are coefficients. For the two Gauss distributions shown in Figure 3-7-2, the coefficients are: Gauss 1 – $A_1 = 600$, $B_1 = 3050$, and $C_1 = 400$; Gauss 2 – $A_2 = 120$, $B_2 = 3050$, and $C_2 = 5000$.

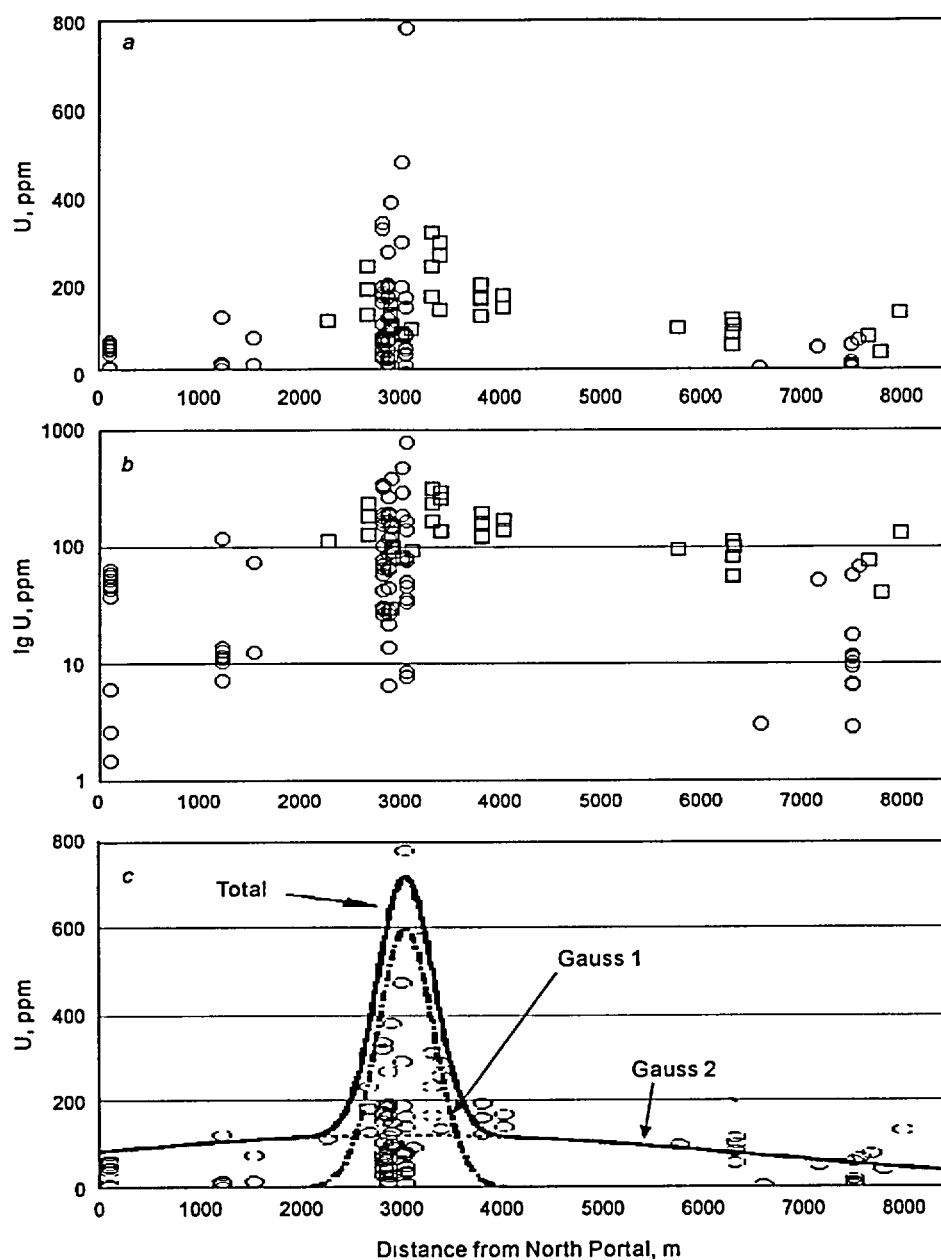


Figure 3-7-A-10. Distribution of U-abundances along the ESF shown in normal (a) and logarithmic (b) scales, as well as approximation of the maximum U-abundance values by two Gauss distributions (c). Data from opals from the outer surfaces of crusts (*squares*; Neymark et al., 2000) and from chalcedony and opal sampled across the crusts (*circles*; Neymark et al., 2002).

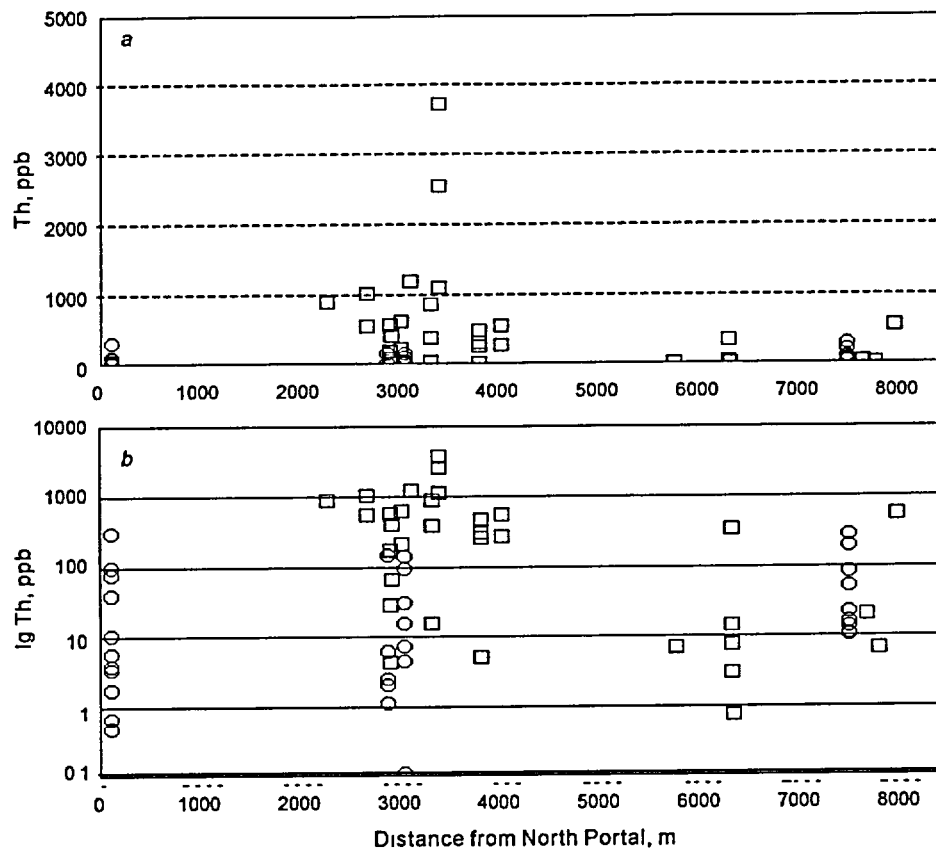


Figure 3-7-A-11. Distribution of Th-abundances along the ESF shown in normal (*a*) and logarithmic (*b*) scales. Data from opals from the outer surfaces of crusts (*squares*; Neymark et al., 2000) and from chalcedony and opal sampled across the crusts (*circles*; Neymark et al., 2002).

Abundances of Th along the ESF

Figure 3-7-A-11 shows the distribution of Th-abundances along the ESF. It is apparent that the two datasets, taken from outer surfaces of crusts (*squares*) and from across the crusts (*circles*) seem to show a systematic difference. The data from across the crusts demonstrate that near the North Portal the Th abundances vary within 3 orders of magnitude; around stations 28+00 to 30+00 they vary somewhat more than 2 orders of magnitude, and near the South Portal (past ESF station 70+00) they vary less than 1.5 orders of magnitude.

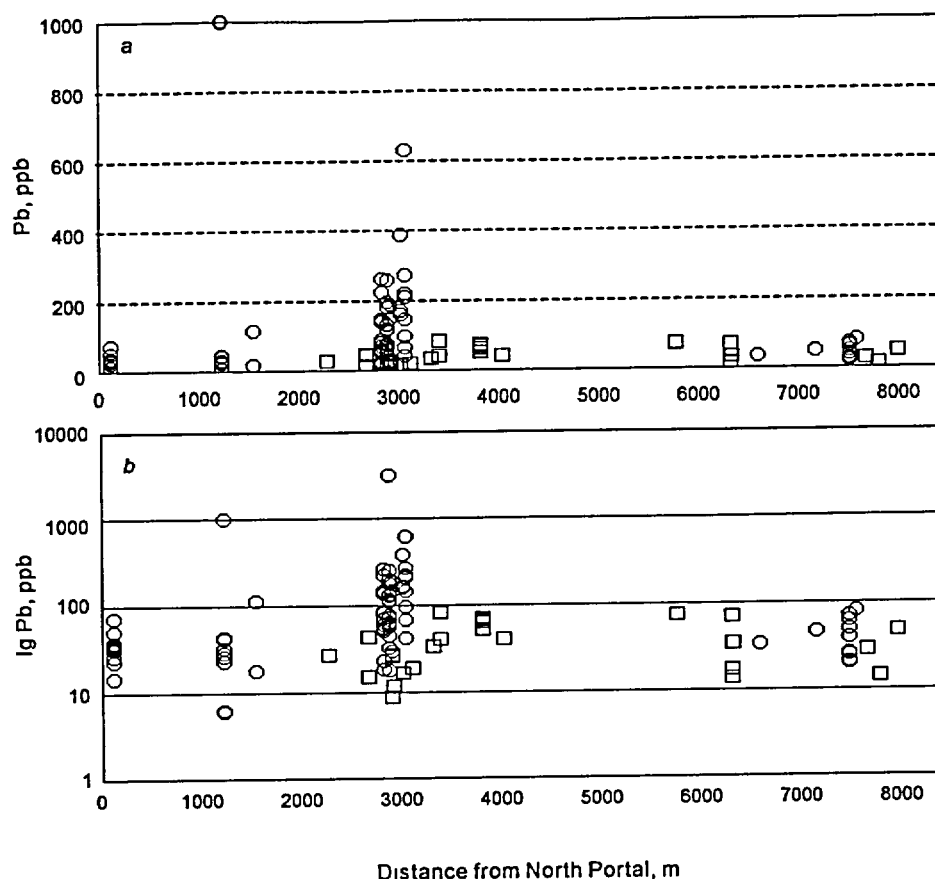


Figure 3-7-A-12. Distribution of Pb-abundances along the ESF shown in normal (a) and logarithmic (b) scales. Data from opals from the outer surfaces of crusts (*squares*; Neymark et al., 2000) and from chalcedony and opal sampled across the crusts (*circles*; Neymark et al., 2002).

Abundances of Pb along the ESF

The distribution of abundances of Pb in silica minerals along the ESF is shown in Figure 3-7-A-12. Like the distribution of U and Th abundances, Pb exhibits a maximum variability in the central part of the ESF (two orders of magnitude as compared to less than one order of magnitude in the other parts). The largest values of Pb abundances are also restricted to the central part of the ESF. The data from the outside surfaces of crusts typically yield the smallest values of the Pb-abundances.

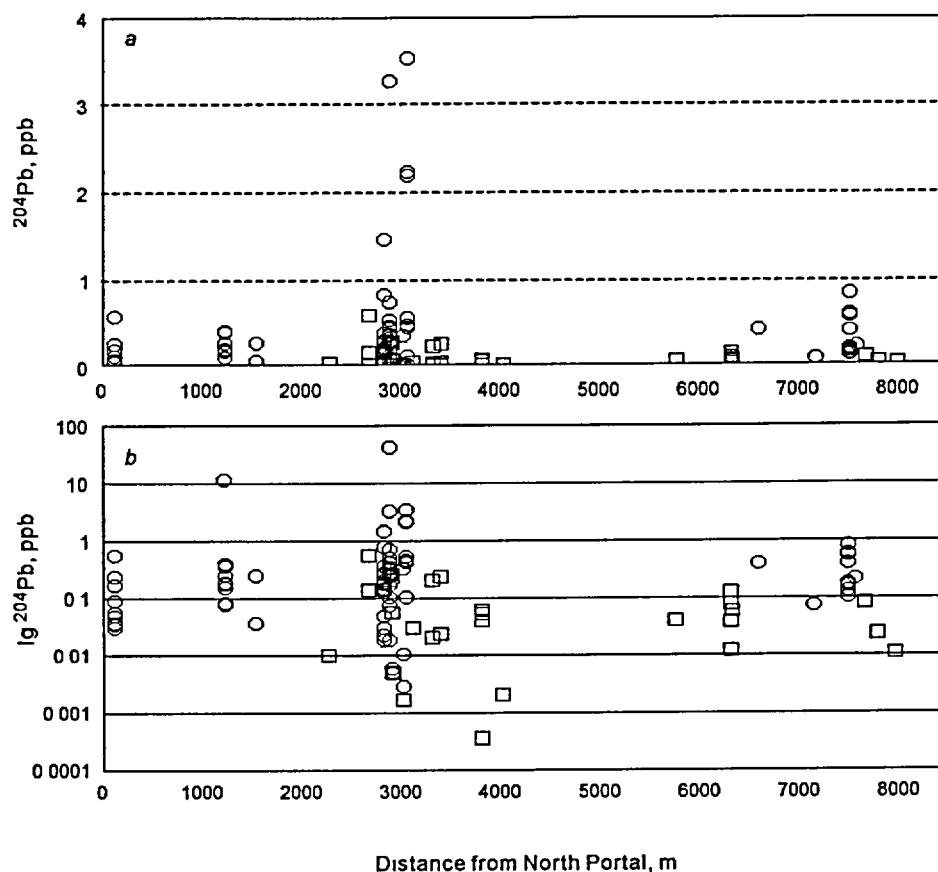


Figure 3-7-A-13. Distribution of ^{204}Pb -abundances along the ESF shown in normal (a) and logarithmic (b) scales. Data from opals from the outer surfaces of crusts (squares; Neymark et al., 2000) and from chalcedony and opal sampled across the crusts (circles; Neymark et al., 2002).

Abundances of ^{204}Pb along the ESF

The distribution of the abundances of the non-radiogenic isotope ^{204}Pb in silica minerals along the ESF is shown in Figure 3-7-A-13. Again, it shows the greatest variability in the central part of the ESF (three orders of magnitude as opposed to one order of magnitude in other parts). It is noteworthy that unlike other elements, the variability of data is produced not only by the greatest values, but also by values that are orders of magnitude smaller than the smallest values measured in other parts of the ESF. Samples from the outside surfaces of crusts typically show the smallest values of ^{204}Pb -abundances.

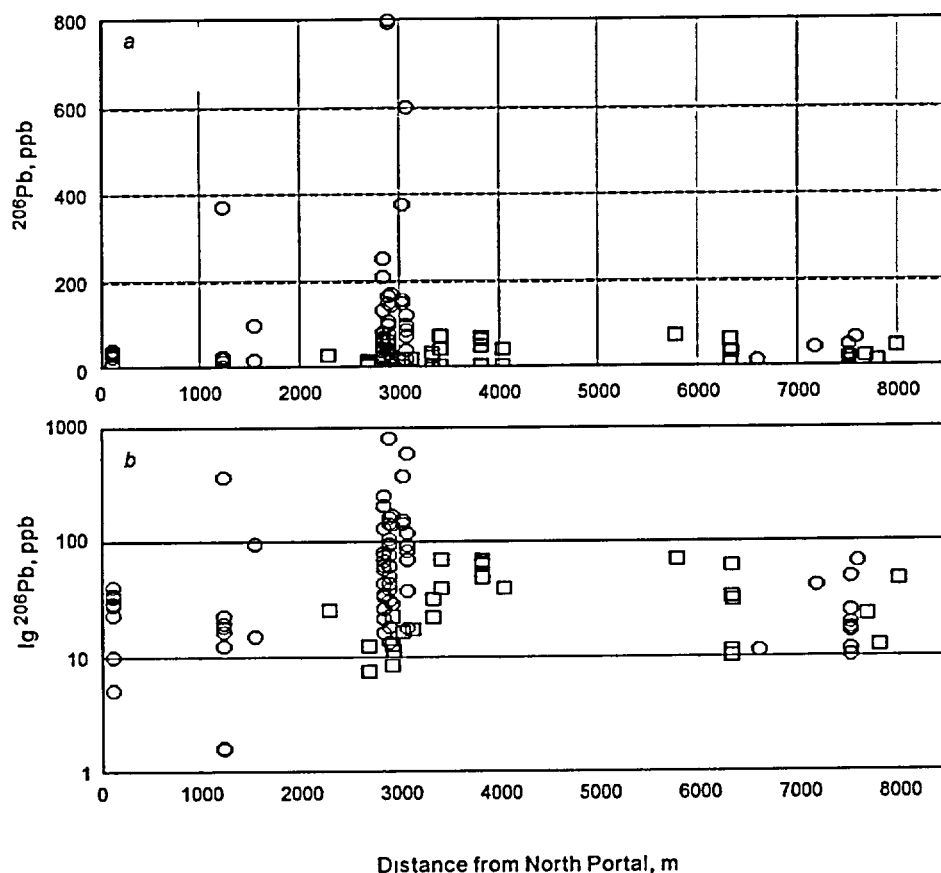


Figure 3-7-A-14. Distribution of ^{206}Pb -abundances along the ESF shown in normal (a) and logarithmic (b) scales. Data from opals from the outer surfaces of crusts (squares; Neymark et al., 2000) and from chalcedony and opal sampled across the crusts (circles; Neymark et al., 2002).

Abundances of ^{206}Pb along the ESF

The distribution of the abundances of the radiogenic isotope ^{206}Pb in silica minerals along the ESF is shown in Figure 3-7-A-14. The greatest variability (2 orders of magnitude) and the greatest absolute values of the ^{206}Pb abundances are both restricted to the central part of the ESF. The data from the outside surfaces of the crusts typically show the smallest values of the ^{206}Pb -abundances. The smallest values of ^{206}Pb are more or less uniform, which is in sharp contrast with the ^{204}Pb abundance pattern (compare with Figure 3-7-A-13).

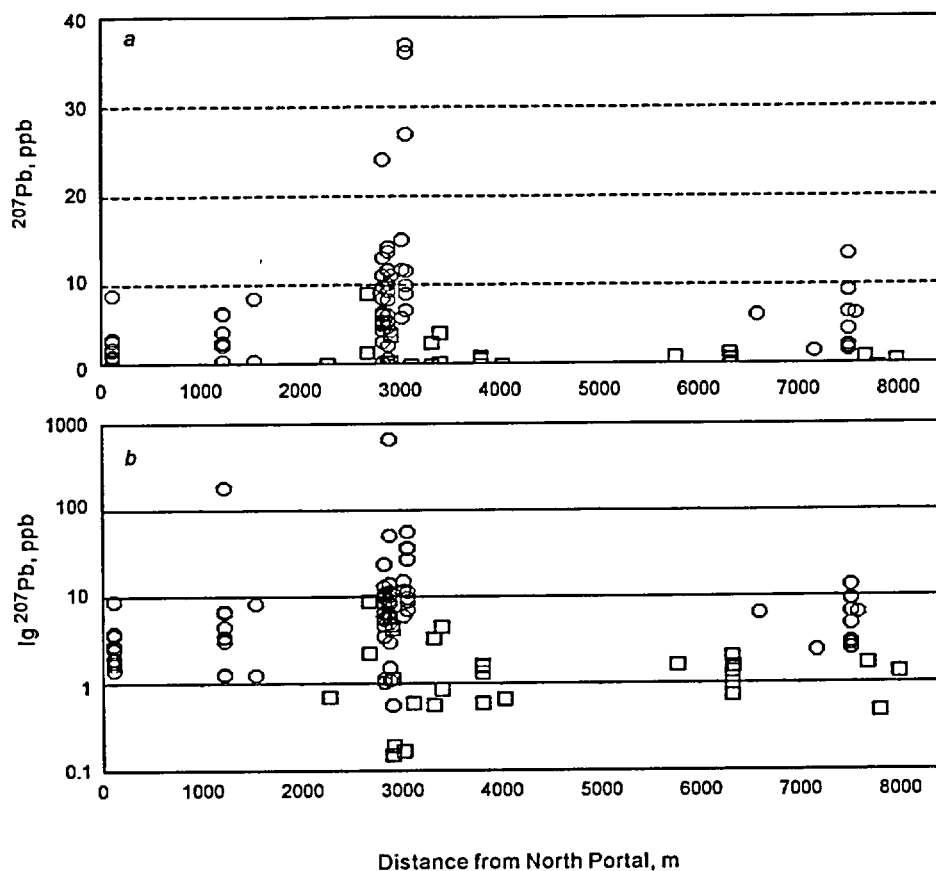


Figure 3-7-A-15. Distribution of ^{207}Pb -abundances along the ESF shown in normal (a) and logarithmic (b) scales. Data from opals from the outer surfaces of crusts (*squares*; Neymark et al., 2000) and from chalcedony and opal sampled across the crusts (*circles*; Neymark et al., 2002).

Abundances of ^{207}Pb along the ESF

The distribution of the abundances of the radiogenic isotope ^{207}Pb in silica minerals along the ESF is shown in Figure 3-7-A-15. The greatest variability is in the central part of the ESF (4 orders of magnitude as opposed to ~ 1 order of magnitude at the portals). The outside surfaces of crusts typically carry the smallest values of the ^{207}Pb -abundances. The distribution of the smallest values of the ^{207}Pb has a pronounced minimum in samples from the central part of the ESF, which makes the pattern similar to that of ^{204}Pb and dissimilar to the pattern of ^{206}Pb .

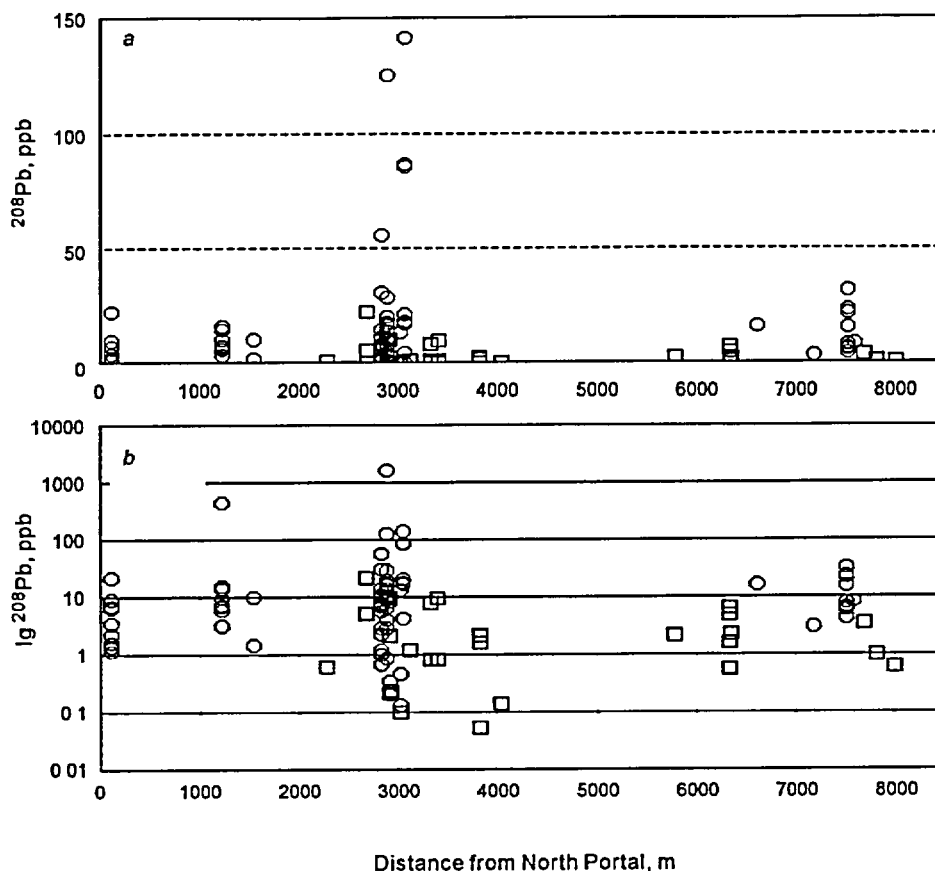


Figure 3-7-A-16. Distribution of ^{208}Pb abundances along the ESF shown in normal (a) and logarithmic (b) scales. Data from opals from the outer surfaces of crusts (squares; Neymark et al., 2000) and from chalcedony and opal sampled across the crusts (circles; Neymark et al., 2002).

Abundances of ^{208}Pb along the ESF

The distribution of the abundances of the thorogenic isotope ^{208}Pb in silica minerals along the ESF is shown in Figure 3-7-A-16. The greatest variability is in the central part of the ESF (4 orders of magnitude as opposed to ~ 1 order of magnitude in other parts of the ESF). The outside surfaces of crusts typically show the smallest values of the ^{208}Pb abundances. Similar to ^{204}Pb and ^{207}Pb , the distribution of the smallest values of ^{208}Pb has a pronounced minimum in samples from the central part of the ESF.

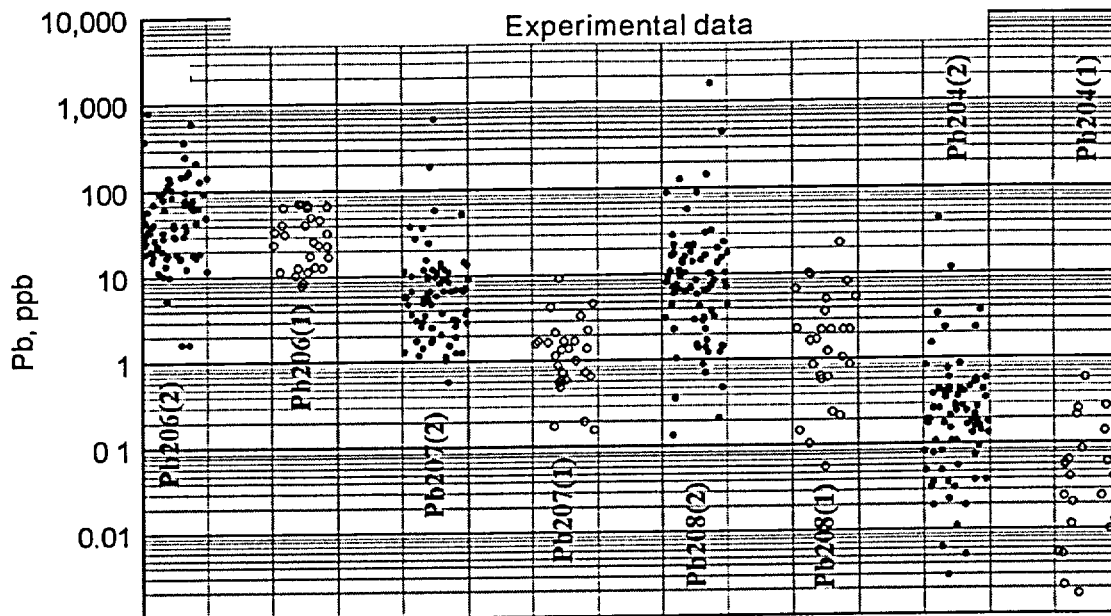


Figure 3-7-A-17. Abundances of lead isotopes in silica minerals from the ESF: a comparison between the data from the whole crusts (1) and their outer surfaces (2). Data from Neymark et al. (2000 and 2002).

Summary on the lead isotope database

The contents of different lead isotopes are about one order of magnitude smaller in samples collected from the outer surfaces of mineral crusts in comparison with samples from across the crusts (see Figure 3-7-A-17).

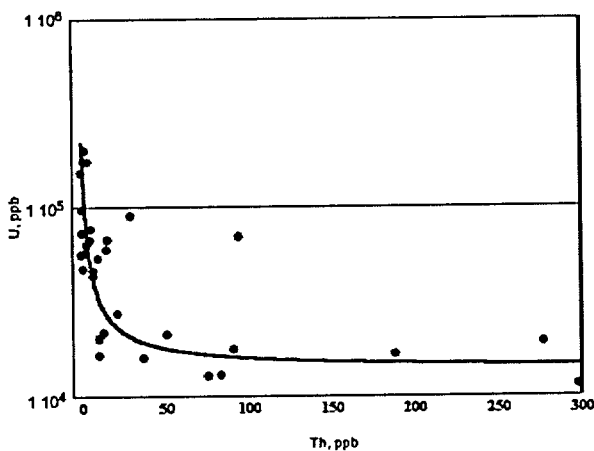


Figure 3-7-A-18. U vs. Th cross-plot and theoretical approximation for silica minerals from the ESF. Data from Neymark et al. (2002).

The U/Th ratios in silica minerals along the ESF and in individual crusts

Uranium and thorium have very different properties in terms of their mobility in aqueous solutions. Thus, the U/Th ratio may provide information with regard to the geochemistry of the mineral-forming fluids. In this section we analyze the U/Th ratios on the scale of the ESF, as well as on the scale of individual crusts.

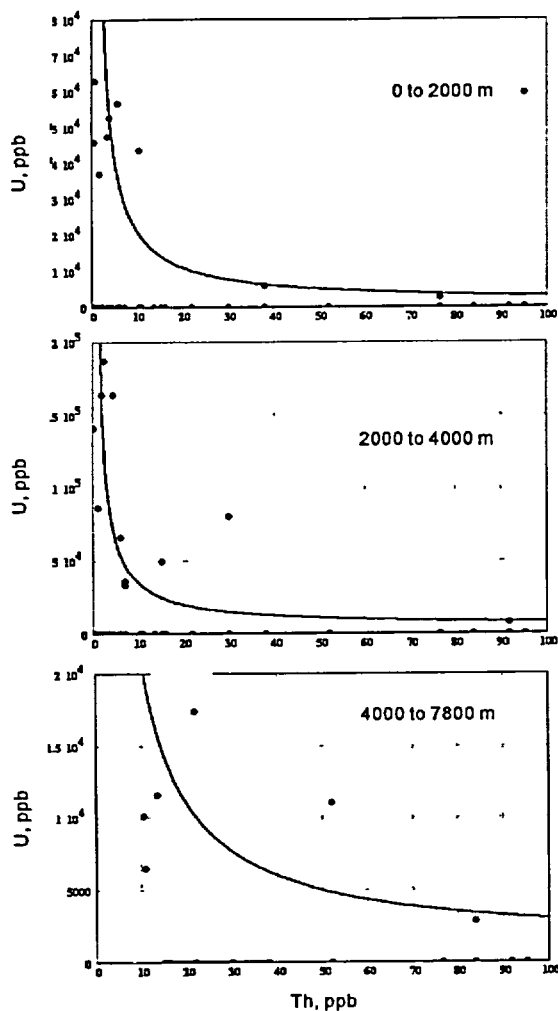


Figure 3-7-A-19. U vs. Th cross-plots and theoretical approximations for silica minerals from three zones in the ESF. Data from Neymark et al. (2002).

for the first 1000 m of the ESF. Numbers on the figure indicate the relative locations of the data points in mineral crusts, dH (0 corresponds to the base and 1 to the top of the crust). The figure shows that as mineral growth proceeds, the contents of Th increase slowly, while the contents of U gradually diminish. Upon reaching $dH = 0.4$, the trend reverses: the abundances of Th sharply decrease and those of U – increase. After reaching $dH = 0.7$, the contents of U remain fairly constant. It is apparent, that the lower (early) half of the crust grew at sharply changing U/Th ratios and Th abundances (more than 1 order of magnitude), whereas the second half recorded relatively small variations in the U/Th ratios.

The data from the outer surfaces of the mineral crusts (Neymark et al., 2000) split in two massifs. The "large" values of the U/Th ratios decrease in an almost-linear manner between the 2000-3000 m-zone

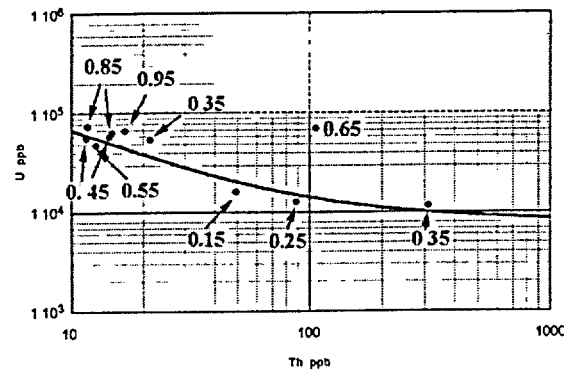


Figure 3-7-A-20. U vs. Th cross-plot and theoretical approximation for silica minerals from the first 1000 m of the ESF. Numbers near points indicate the relative position of samples within the crusts with 0 corresponding to the base and 1 – to the top of the crust. Data from Neymark et al. (2002).

Figure 3-7-A-18 shows the U vs. Th cross-plot for all samples collected across individual crusts (Neymark et al., 2002). The dataset was subdivided into three zones that were defined by the dissimilar abundances and patterns of distribution of U, Th, Pb, as well as Pb isotopes (0 to 2000 m; 2000 to 4000 m, and 4000 to 7800 m). In Figure 3-7-A-19, the data are shown separately for the three zones. Both figures show an apparent overall inverse correlation between U and Th.

Figure 3-7-A-20 shows the U vs. Th cross-plot

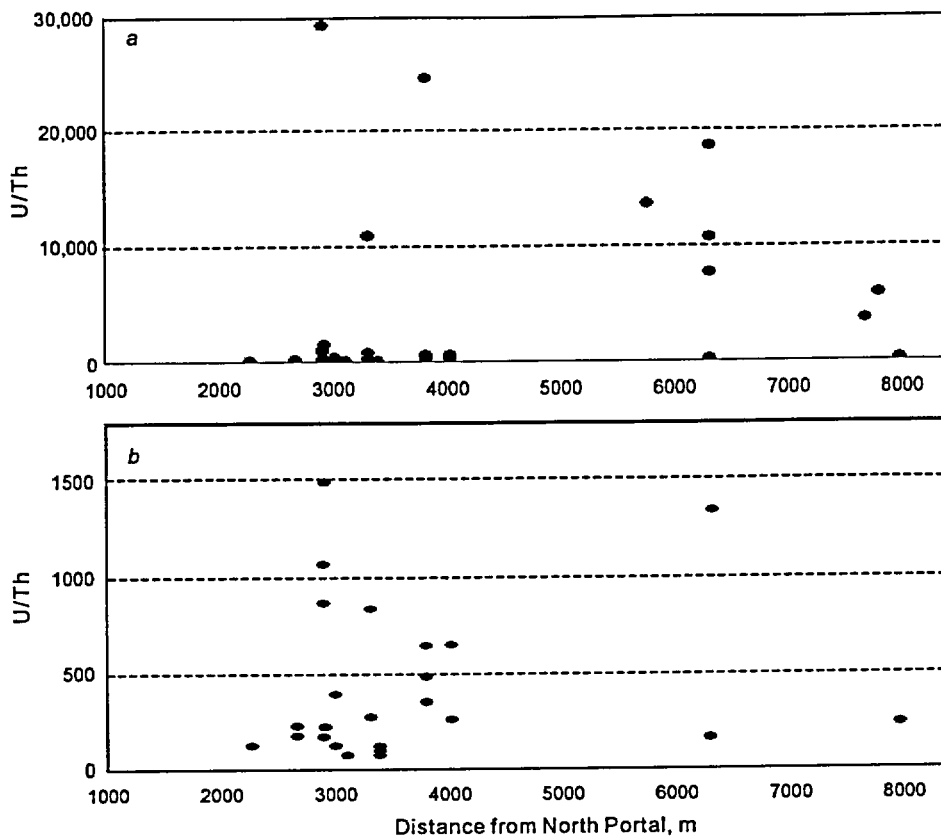


Figure 3-7-A-21. Distribution of "large" (a) and "small" (b) U/Th ratios along the ESF. Data from Neymark et al. (2000 and 2002).

and the end of the ESF (South Portal, Figure 3-7-A-21-a); U/Th ratios, an order of magnitude smaller, are concentrated between 2000 and 4000 m in the ESF (Figure 3-7-A-21-b).

It is to be noted that the trends described above are consistent with the data from across the crusts (Neymark et al., 2002). The apparent pattern of the negatively correlated behavior (see Figure 3-7-A-18) is caused primarily by the lowermost layers of crusts, which contain higher concentrations of Th and lower concentrations of U. In samples from the outer parts of the crusts analyzed by Neymark et al., 2000, the negative correlation is absent.

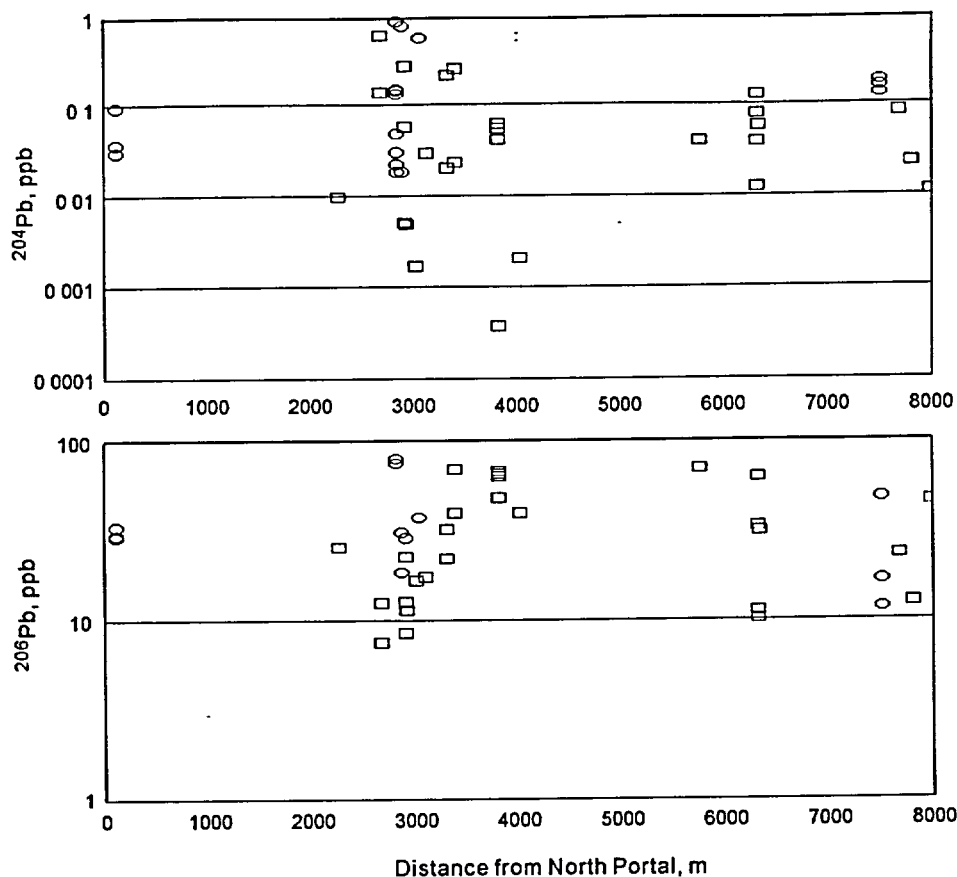


Figure 3-7-A-22. Comparison of abundances of ²⁰⁴Pb and ²⁰⁶Pb in samples from outer surfaces of crusts (*squares*; data from Neymark et al., 2000) and from outer parts of crusts (*circles*; $dH > 0.8-0.85$; data from Neymark et al., 2002).

Concentrations of Pb isotopes in the upper parts of crusts

There is an apparent systematic difference between the data from across the crusts and the data from the outer surfaces of crusts (see Figure 3-7-A-17). In this section we compare the isotope abundances from two datasets representing the outer surfaces (data from Neymark et al. 2000) and the outer parts of crusts ($dH > 0.5$ to 0.85, data from Neymark et al. 2002). Figures 3-7-A-22 and 3-7-A-23 demonstrate that data from the two publications show a fair degree of consistency. Variations of ²⁰⁶Pb-abundances are within one order of magnitude. The greatest variations were found for ²⁰⁴Pb and ²⁰⁸Pb (greater than 3 orders of magnitude) and ²⁰⁷Pb (about 2 orders of magnitude). In all cases, the maximum variability of the Pb-isotope contents is characteristic of the central part of the ESF.

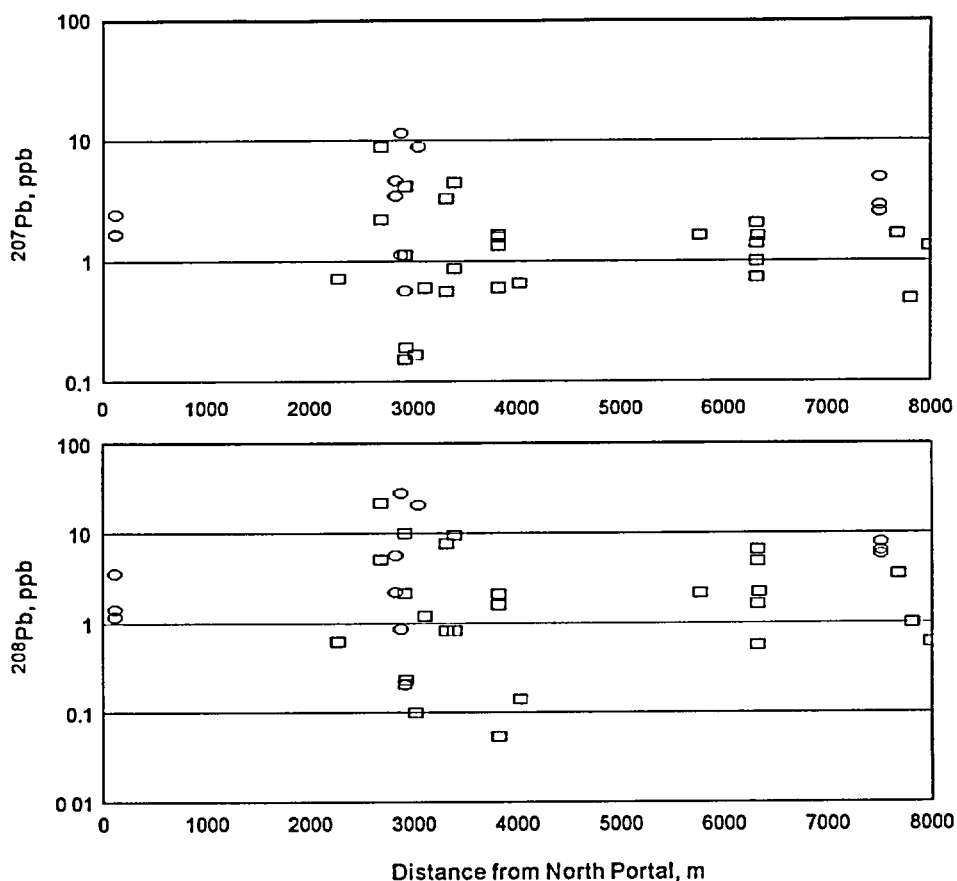


Figure 3-7-A-23. Comparison of abundances of ^{207}Pb and ^{208}Pb in samples from outer surfaces of crusts (*squares*, data from Neymark et al., 2000) and from outer parts of crusts (*circles*, $dH > 0.85$; data from Neymark et al., 2002).

Concentrations of U in the upper parts of crusts

Figure 3-7-A-24-a compares data for the outer surfaces of crusts (Neymark et al., 2000) and data for the upper halves of crusts ($dH > 0.5$) reported in Neymark et al. (2002). Like the Pb isotopes, the consistency of the data is fair. A line representing the sum of the two Gauss distributions approximates the upper boundary of the distribution:

$$U = 120 \cdot \exp\left[-\left(\frac{L-4000}{4800}\right)^2\right] + 300 \cdot \exp\left[-\left(\frac{L-3100}{500}\right)^2\right] \quad (3-7-A-2)$$

where L is the distance along the ESF.

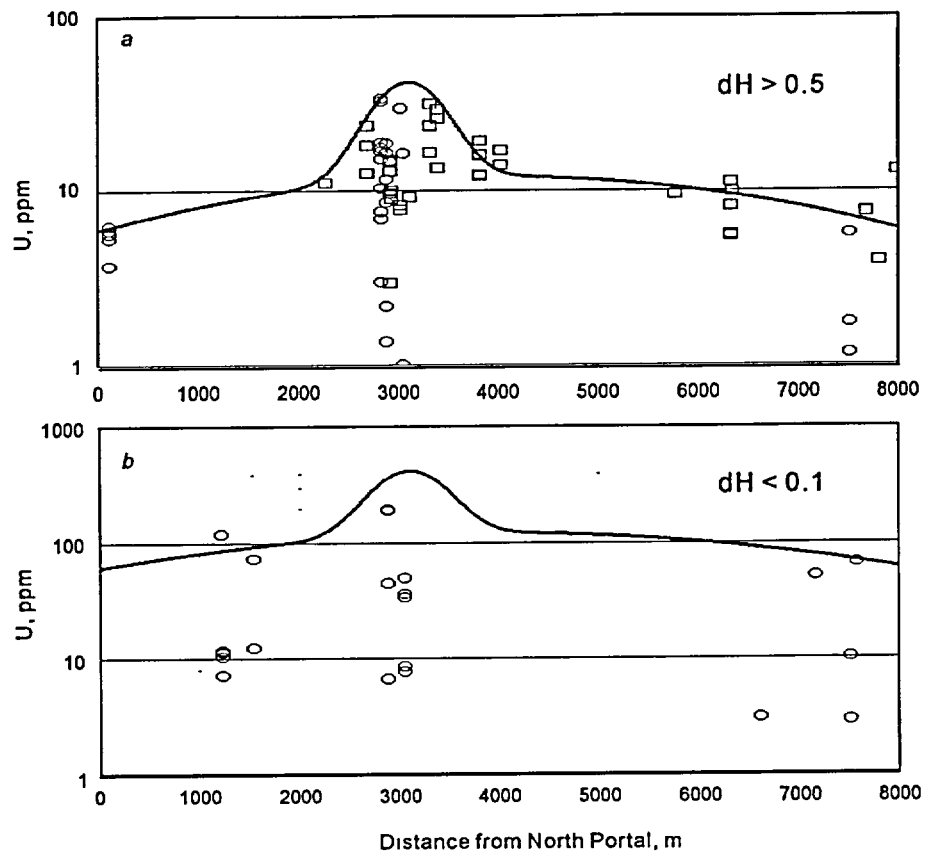


Figure 3-7-A-24. Abundances of U in upper (a) and lower (b) parts of crusts. *Squares* - data from Neymark et al. (2000), *circles* - data from Neymark et al. (2002).

Figure 3-7-A-24-b shows the distribution of U abundances and an approximation of the data for the bases of mineral crusts ($dH < 0.1$).

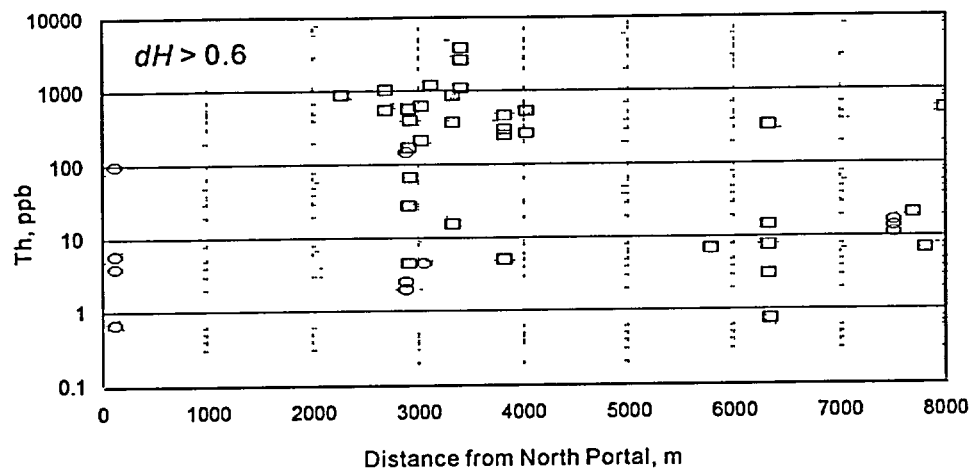


Figure 3-7-A-25. Abundances of Th in upper parts of crusts ($dH > 0.6$). Squares - data from Neymark et al. (2000), circles - data from Neymark et al. (2002).

Concentrations of Th in the upper parts of crusts

Using similar methodology we compared the results for the Th abundances. It is apparent from Figure 3-7-A-25 that concentrations of Th reported for the outer surfaces of crusts by Neymark et al. (2000) are systematically and substantially (almost an order of magnitude) greater than the values reported for the upper part of crusts ($dH > 0.6$) in Neymark et al. (2002).

Appendix 3-7-2: Statistical analysis of the elemental abundances and isotope ratios

Distribution of U- and Pb-abundances along the ESF

Outliers. There is one outlier in the Pb dataset, sample HD2019AP with Pb = 3136 ppb, which is almost one order of magnitude greater than the rest of the database. The same sample also has the lowest U-abundance for its zone. Another large value is Pb = 1004 ppb in sample HD2093Pb1 (ESF station 12+15.58, the sample weight 0.086 mg). Figure 3-7-A-26 compares the distribution of Pb and U, as a function of the distance along the ESF.

Figure 3-7-A-26 shows that the contents of U and Pb in opals from the 2200-4200 m-zone of the ESF are conspicuously high. The distribution of U in this zone may be approximated as:

$$U = 600 \cdot \exp\left[-\frac{(L - 3050)^2}{400^2}\right] \quad (3-7-A-3)$$

and the distribution of Pb as:

$$Pb = 600 \cdot \exp\left[-\frac{(L - 3000)^2}{120^2}\right] \quad (3-7-A-4)$$

Thus, the zone of the high U-contents is three times as wide as the corresponding zone for Pb. The latter is located between 2800 and 3200 m, which gives a width for the zone of 400 m. At the same time, locations of the centers of the zones practically coincide.

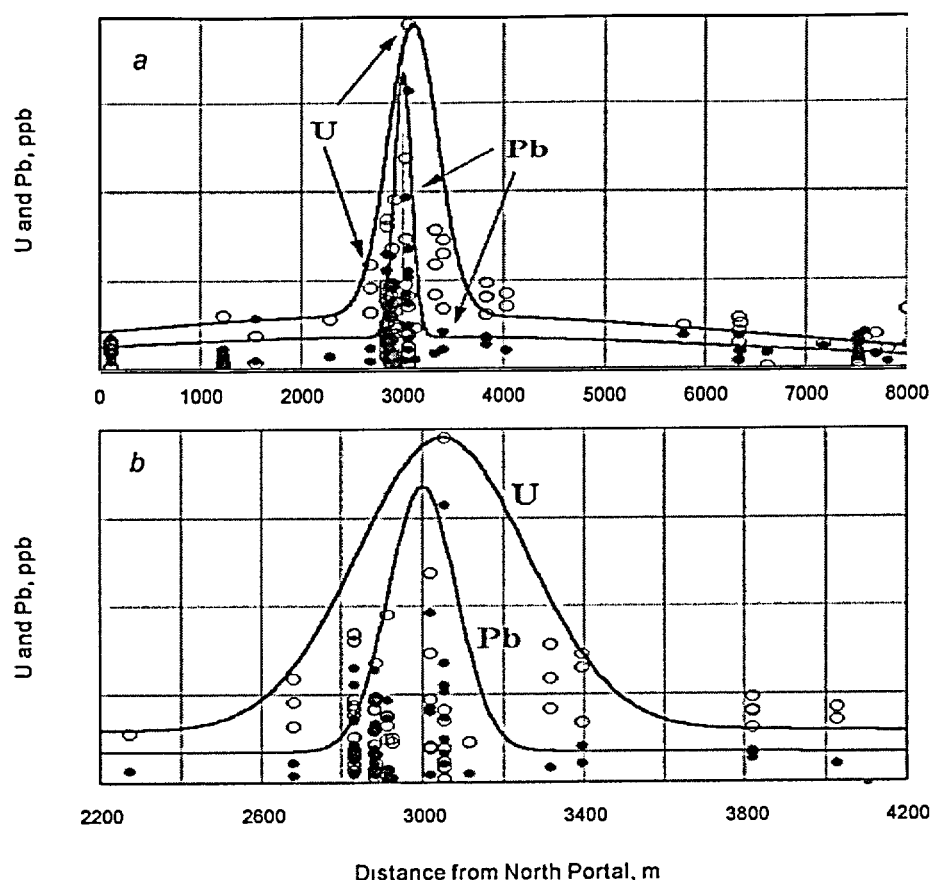


Figure 3-7-A-26. Distribution of U and Pb in silica samples from ESF. *Black* – U, *red* – Pb. Figure *b* represents a zoom-in on the 2200-4200 m zone in the ESF, showing elevated abundances of the elements. Data from Neymark et al. (2002).

Pb in chalcedony and opal

There is a systematic difference in Pb-abundances between the two types of silica minerals, chalcedony and opal (Figure 3-7-A-27). The contents of Pb are substantially higher in many opals, as compared to the chalcedonies. The difference in the distribution of Pb is very similar to that found for U (see discussion and Figure 3-7-A-28 below).

Most of the Pb values in opals plot between 7 and 300 ppb, whereas for chalcedony the range is 6 to 70 ppb. The distribution of Pb in opals is bi-modal (Figure 3-7-A-27-b) with values clustering at: $10 < Pb_{\text{opal I}} < 100$ ppb and $100 < Pb_{\text{opal II}} < 220$ ppb. The distribution of maximum Pb contents may be approximated by a sum of the two Gauss exponents:

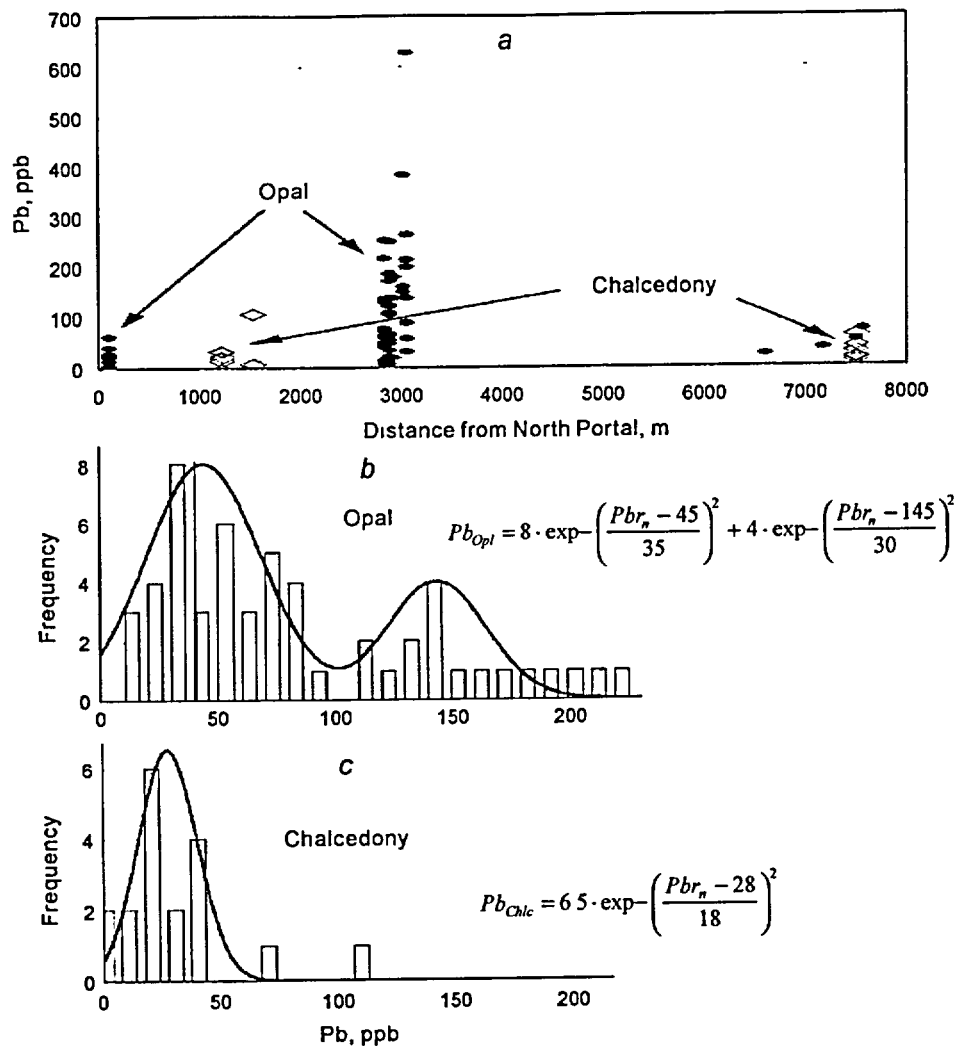


Figure 3-7-A-27. Pb in different varieties of silica from ESF. *a* – distribution of Pb-abundances along the ESF; *b* and *c* – frequency distributions of Pb-abundances in opal and chalcedony from ESF along with approximation curves (Gauss exponents). Data from Neymark et al. (2002).

$$Pb_{Opal} = 8 \cdot \exp\left(-\left(\frac{Pbr_n - 45}{35}\right)^2\right) + 4 \cdot \exp\left(-\left(\frac{Pbr_n - 145}{30}\right)^2\right) \quad (3-7-A-5)$$

The distribution of the maximum Pb contents in chalcedony may be approximated as:

$$Pb_{Chlc} = 6.5 \cdot \exp\left(-\left(\frac{Pbr_n - 28}{18}\right)^2\right) \quad (3-7-A-6)$$

The main mode of the distribution is at 28 ppb, and the width for the distribution is 18 ppb. The parameters of Pb distributions in opal and chalcedony are compiled in Table 3-7-A-3.

Table 3-7-A-3

Parameters of Gauss exponents approximating distribution of Pb in opal and chalcedony from the ESF

Area	Mean mode (ppb)	Dispersion (ppb)	Relative dispersion
Pb _{Opal I}	45	35	0.77
Pb _{Opal II}	145	30	0.21
Pb _{Chlc}	28	18	0.64

The value Pb \cong 100 ppb separates the two main modes in opals. Below we evaluate whether there is any regularity in the appearance of the two modes of Pb distribution in opals by tracing the appearance of the 100 ppb-boundary as a function of the relative depth inside crusts (dH). The results are summarized in Table 3-7-A-4.

Table 3-7-A-4

Contents of Pb in opals from the ESF at different relative depth (dH) within mineral crusts

Station ESF	dH									
	0.1	0.2	0.3	0.4	0.5	0.6	0.7	0.8	0.9	1.0
01+11		23	71	14 50	34 31	25	38		35 35	32
12+21	23 25	29	43							
28+28				59 54 51	143 81	70	145	139 23 18	259 223	86 85
28+80.0 a		73				76	129 117 113		32	
28+80.0 b		45			296		313		58	
28+81.0	64 17 179				59 193					
29+11.2		146 187								29
30+17.78				387 159		169				
30+50.70	41	207	220 628	98	146					67
75+07	49	20	70			26				61

Table 3-7-A-5

Relative thickness of the crust (H^*) at which the second mode in Pb frequency distribution in opals appears in different parts of the ESF

Station ESF	01+11	12+21	28+28	28+80 a	28+80 b	28+81	29+11	30+17	30+50	75+07
dH*	-	-	0.5	0.70	0.5	0.1	0.2	0.3	0.2	-

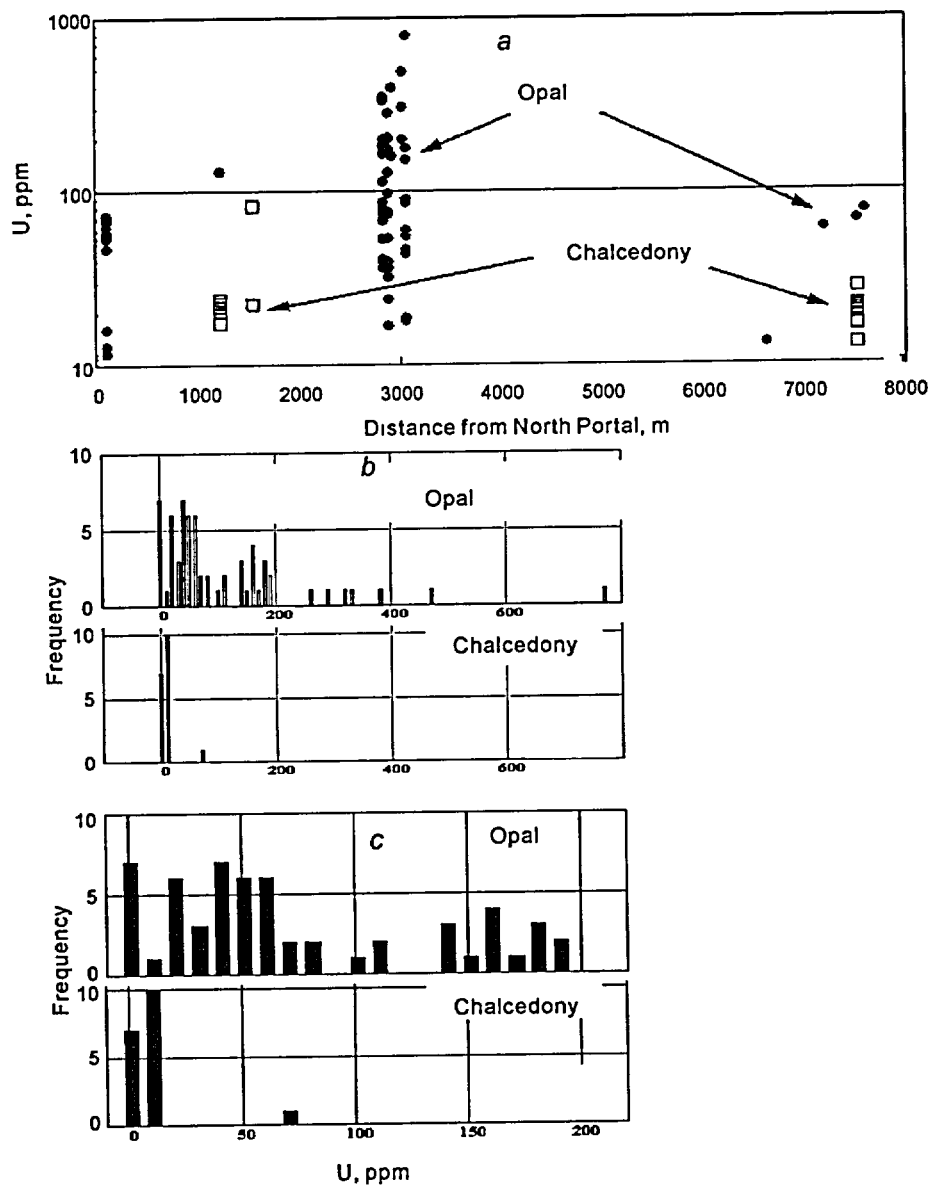


Figure 3-7-A-28. Contents of U in different varieties of silica from the ESF. *a* – distribution of U-abundances along the ESF; *b* and *c* – histograms showing frequency distributions of U-abundances in opal and chalcedony from ESF. *c* – "zoom in" on the 0-200 ppm area. Data from Neymark et al. (2002).

It is apparent from the table that the 100 ppb-boundary may be located at different depths inside crystals and that it forms a clearly defined zone. In samples from the 2000-4000 m-zone of the ESF, the abundances of Pb are substantially (several times) greater in the middle parts of the mineral crusts. Thus, the second frequency maximum (see Figure 3-7-A-27-b) may be traced downward to the middle parts of the crusts. Denoting the relative thickness of the mineral crust at which the second-mode values appear as dH^* , it is possible to depict the distribution of this feature along the ESF (see Table 3-7-A-5).

Concentrations of U in different silica minerals

Of 85 measurements reported in the paper by Neymark et al. (2002), 61 are from opal, 18 are from chalcedony, and 2 are from quartz. Figure 3-7-A-28 shows the distribution of total U in opals and chalcedonies along the ESF. There is a striking difference between the U-abundances from these varieties of silica. Some 90% of values for chalcedonies lie between 6 and 14 ppm (with one outlier at $U = 72.4$ ppm; sample weight of 34.64 mg). Of all measured U-concentrations in opals 97% fall below 600 ppm. An analysis of the distribution frequencies shows that there are four modes of U concentrations:

$$0 < U_{\text{Opal I}} < 15 \text{ ppm (13\%)}$$

$$20 < U_{\text{Opal II}} < 100 \text{ ppm (55\%)}$$

$$140 < U_{\text{Opal III}} < 200 \text{ ppm (22\%)}$$

$$300 < U_{\text{Opal IV}} < 500 \text{ ppm (6\%)}$$

The distribution can be approximated by a sum of the four Gauss exponents:

$$dN = 6.8 \cdot \exp\left(-\left(\frac{U-5}{3.5}\right)^2\right) + 7 \cdot \exp\left(-\left(\frac{U-45}{24}\right)^2\right) + 4 \cdot \exp\left(-\left(\frac{U-160}{40}\right)^2\right) + 1 \cdot \exp\left(-\left(\frac{U-350}{150}\right)^2\right) \quad (3-7-A-7)$$

For chalcedony, the major mode is at 11 ppm (the distribution width is 3.5 ppm). The distribution can be approximated as:

$$dN = 7 \cdot \exp\left(-\left(\frac{U-40}{30}\right)^2\right) + 4 \cdot \exp\left(-\left(\frac{U-160}{40}\right)^2\right) \quad (3-7-A-8)$$

An approximation for opal and chalcedony are graphically shown in Figure 3-7-A-29 and their parameters are presented in Table 3-7-A-6. Importantly, no mode for opal distribution coincides with the mode for U distribution in chalcedony. The multi-modal character for the distribution of U-abundances in opals suggests that more than one geochemical process was involved in the deposition of opals at Yucca Mountain.

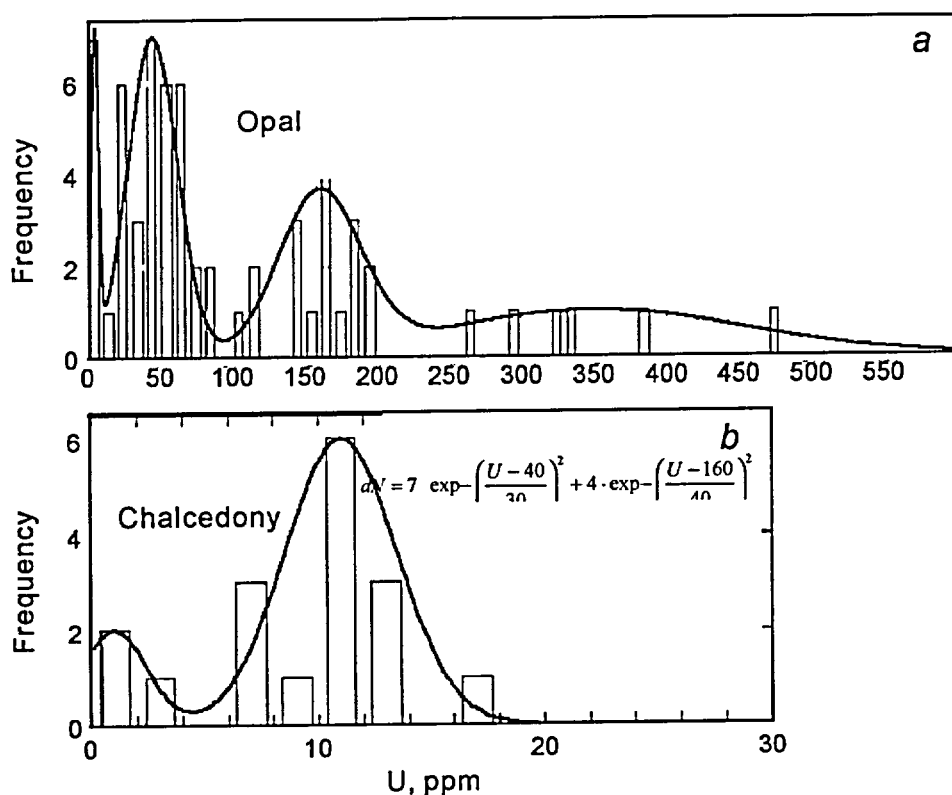


Figure 3-7-A-29. Contents of U in different varieties of silica from the ESF. *a* – distribution and approximation of U-abundances in opal; *b* – distribution and approximation of U-abundances in chalcedony. Data from Neymark et al. (2002).

From an examination of the frequency functions of the U-distribution in different zones of the ESF (Figure 3-7-A-30), it is apparent that in the zone with abundant lithophysal cavities (Zone 1; $2600 < L < 3500$ m), the function of the distribution becomes complex, and large modal values of U-concentrations appear.

Based on the relationships between the determined modes of U-contents and the spatial distribution of samples in the ESF, we earlier defined two zones characterized by different distributions of elements and isotopes in silica minerals (see Figure 3-7-A-10). The distribution of uranium in the Zone 1 was approximated by the equation:

$$U_{Zone1} = 600 \cdot \exp\left(-\frac{(L - 3050)^2}{400^2}\right) \quad (3-7-A-9)$$

and in Zone 2 by the equation

Table 3-7-A-6

Parameters of the Gauss exponents approximating the distribution of U in opal and chalcedony from the ESF

Mode	% of data	Mean mode (ppm)	Dispersion (ppm)	Relative dispersion
U _{Opal I}	13	5	3.5	0.7
U _{Opal II}	55	45	24	0.53
U _{Opal III}	22	160	40	0.25
U _{Opal IV}	6	350	150	0.43
U _{Chlc I}	18	1	2	2.0
U _{Chlc II}	82	11	3.5	0.32

$$U_{Zone2} = 120 \cdot \exp\left(-\frac{(L - 3050)^2}{5000^2}\right) \quad (3-7-A-10)$$

where U is uranium content [ppm], and L is the distance along ESF [m]. Both distributions have maximums at the same location (3050 m), but their dispersions differ by more than one order of magnitude.

The critical height of the sample (dH^*), at which values $U = 100-120$ ppm appear, mark the boundary between the two main modes of the distribution. The data are presented in Table 3-7-A-7. It is apparent that the "second mode" values appear in samples at different relative heights (Table 3-7-A-8), and form a distinct zone.

Table 3-7-A-7

Distribution of U in silica minerals of the ESF as a function of relative height in the sample (dH)

ESF station	dH									
	0 1	0 2	0 3	0 4	0 5	0 6	0 7	0 8	0 9	1
01+11		6	3	2 44	46 48		60		5 53	57
12+21	7 12	13	14							
28+28				26 29 43	57 65	104	189	30 70 76 176	322 337	154 167
28+80 0 a		66				86	164 166 187		117	
28+80 0 b		29			26		13		22	
28+81.0		6 44 194			64 270					
29+11.2		150 382								147
30+17.78				188	475			293		
30+50 70	8	45	76	80	141					164

Table 3-7-A-8

Critical relative height (dH^*) at which the "second mode" of U distribution appears in mineral crusts in the ESF

ESF station	01+11	12+21	28+28	28+80	28+81	29+11.	30+17	30+50	75+07
dH^*	-	-	0 65	0 70	0 2	0 2	0 4	0 5	-

Note: $dH = 0$ corresponds to the base, and $dH = 1$ – to the top of the crust.

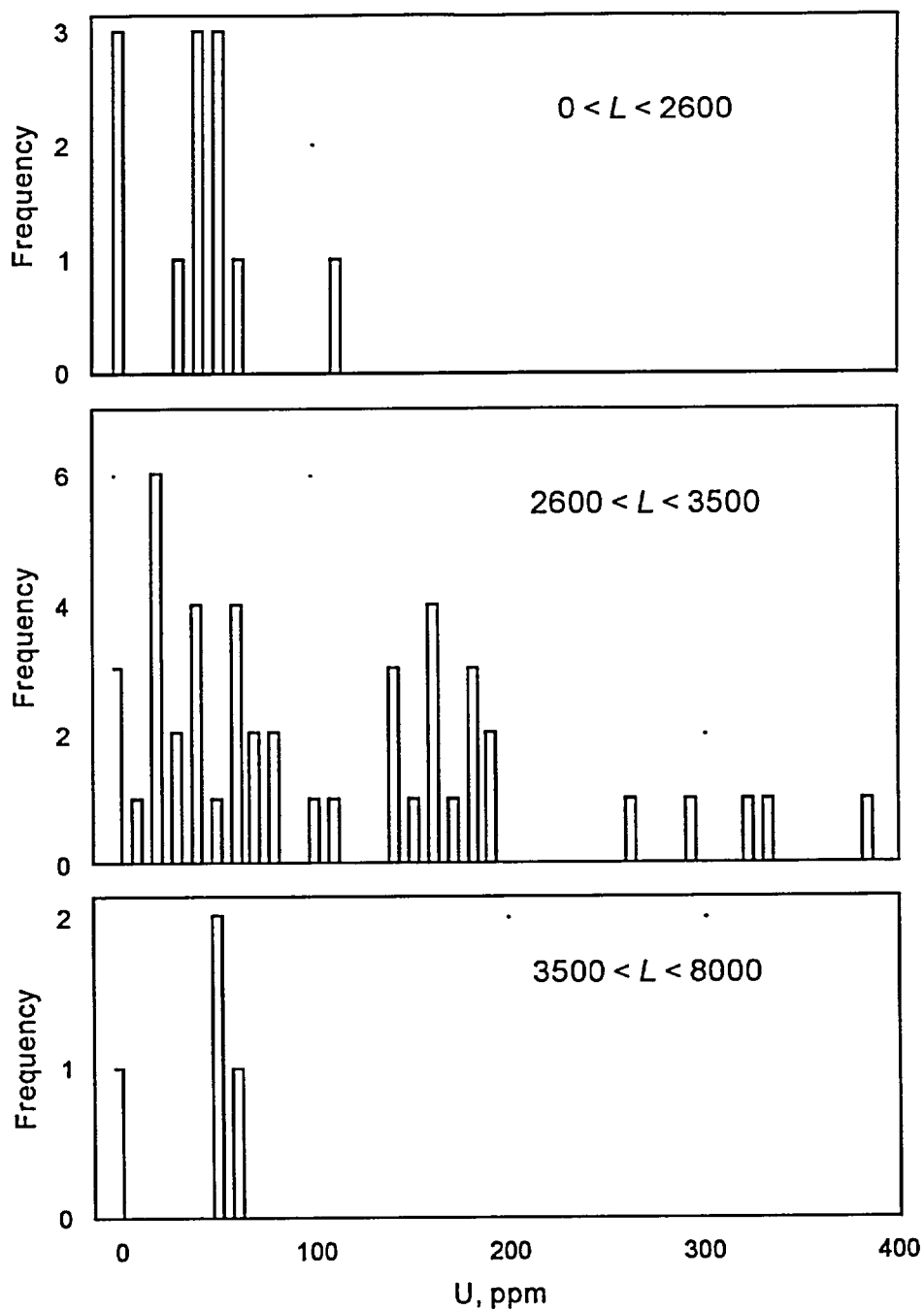


Figure 3-7-A-30. Distribution of U-contents in opal from the three zones in the ESF. Data from Neymark et al. (2002).

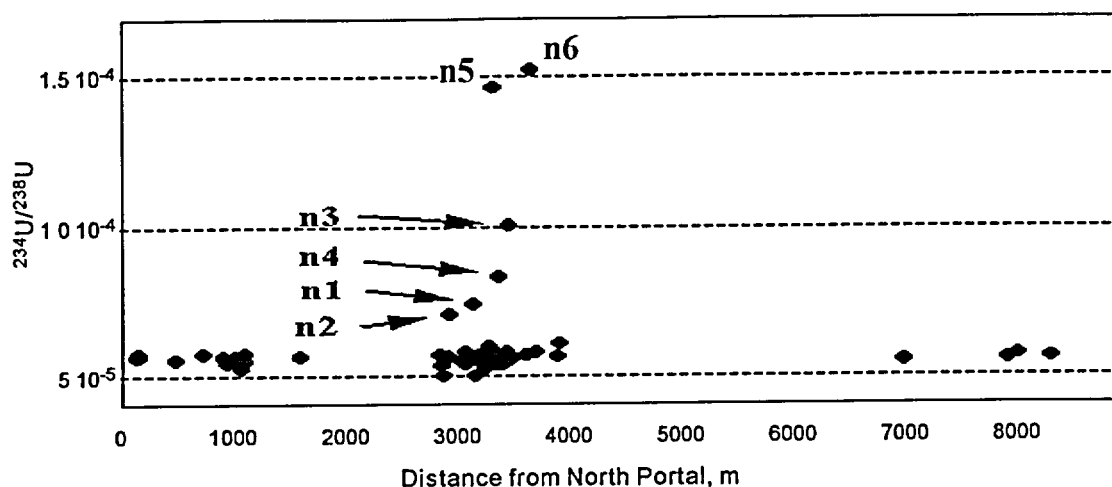


Figure 3-7-A-31. Distribution of $^{234}\text{U}/^{238}\text{U}$ concentration ratios in minerals of silica along the ESF. Outliers: n1 – lowermost opal in sample HD2019A1pb4; n2 – lowermost opal in sample HD2019Apb1; n3 – upper part of the crust; n4 – lower part of the crust; n5 – sample that cannot be used for quantitative analysis (Neymark et al., 2002); and n6 – sample from the outer surface of the crust. Data from Neymark et al. (2002).

$^{234}\text{U}/^{238}\text{U}$ (concentration) ratios

For 65 of 71 analyzed samples the $^{234}\text{U}/^{238}\text{U}$ concentration ratios fall between $5 \cdot 10^{-5}$ and $6 \cdot 10^{-5}$, whereas for 6 outliers these ratios range between $7 \cdot 10^{-5}$ and $16 \cdot 10^{-5}$ (Figure 3-7-A-31). Only 5 outliers are suitable for a statistical analysis, and out of those, three were collected from the bases of crusts and two – from the outer surfaces of crusts. All outliers are from lithophysal cavities in the central part of the ESF (Zone 2).

For the 65 "normal" samples, deviations from the equilibrium values of the $^{234}\text{U}/^{238}\text{U}$ range between $< 5 \%$ for ^{234}U contents of < 0.01 ppm, and $< 2 \%$ for ^{234}U contents of > 0.01 .

Radiogenic Pb-isotopes vs. ^{204}Pb

Figure 3-7-A-32-a shows the $^{206}\text{Pb}/^{204}\text{Pb}$ ratios. It is apparent that at large ^{204}Pb values ($> 1\text{-}5$ ppb) the distribution may be enveloped from below by a straight line $^{206}\text{Pb} = 18.8 \text{ }^{204}\text{Pb}$. According to the rationale of the physicochemical model of Neymark et al. (2000 and 2002), the multiplier 18.8 corresponds to the ratio of $^{206}\text{Pb}/^{204}\text{Pb}$ in the mineral-forming solution ("common lead" correction). Analogous values for the two other isotopes are: $^{207}\text{Pb}/^{204}\text{Pb} = 15.5$ and $^{208}\text{Pb}/^{204}\text{Pb} = 39.0$. Note the nearly perfect correlation between ^{208}Pb and ^{204}Pb (Figure 3-7-A-32-c)

By using the values of the common lead correction indicated above, it is possible to calculate the $^{206}\text{Pb}_{\text{water}}$ and $^{207}\text{Pb}_{\text{water}}$ abundances, which will represent the contents of the isotopes transported by the mineral-forming fluid. If these values are deducted from the total ^{206}Pb and ^{207}Pb contents, the correlations

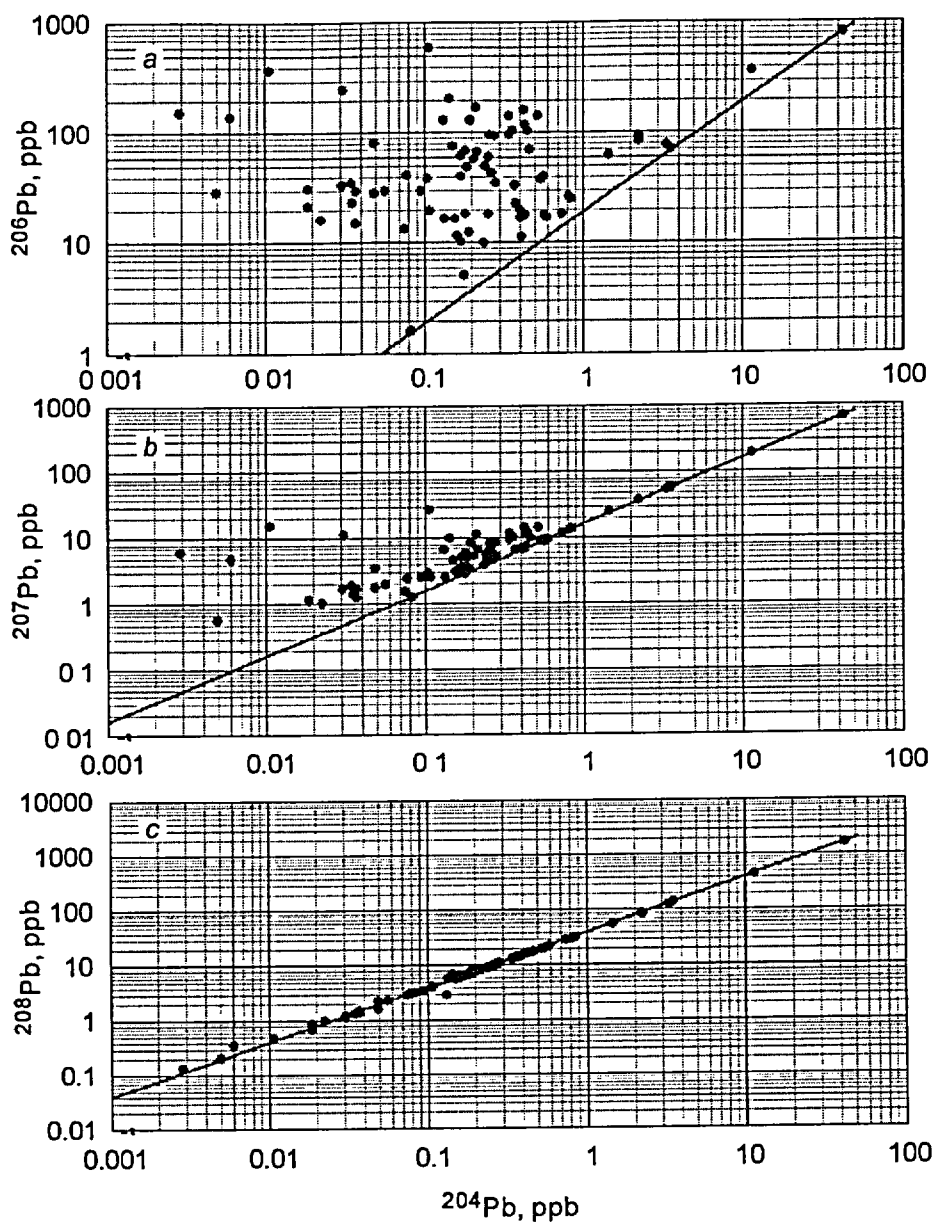


Figure 3-7-A-32. ^{206}Pb vs. ^{204}Pb , ^{207}Pb vs. ^{204}Pb , and ^{208}Pb vs. ^{204}Pb ratios plotted based on the data from (Neymark et al., 2002). Blue lines represent the lower boundaries of the experimental data distributions and correspond to the values of respective radiogenic Pb isotope vs. ^{204}Pb in the mineral-forming solutions. Data points left of the line indicate the excess of the radiogenic Pb-isotope.

of the resulting $^{206}\text{Pb}^*$ and $^{207}\text{Pb}^*$ values with the non-radiogenic ^{204}Pb disappears (Figure 3-7-A-33). Instead, however, a very good correlation appears between the two uranium isotopes, $^{206}\text{Pb}^*$ and $^{207}\text{Pb}^*$ (Figure 3-7-A-34-b). This correlation may be approximated by a straight-line equation:

$$^{206}\text{Pb}^* = 24.5(\pm 3.5)^{207}\text{Pb}^* \quad (3-7-A-11)$$

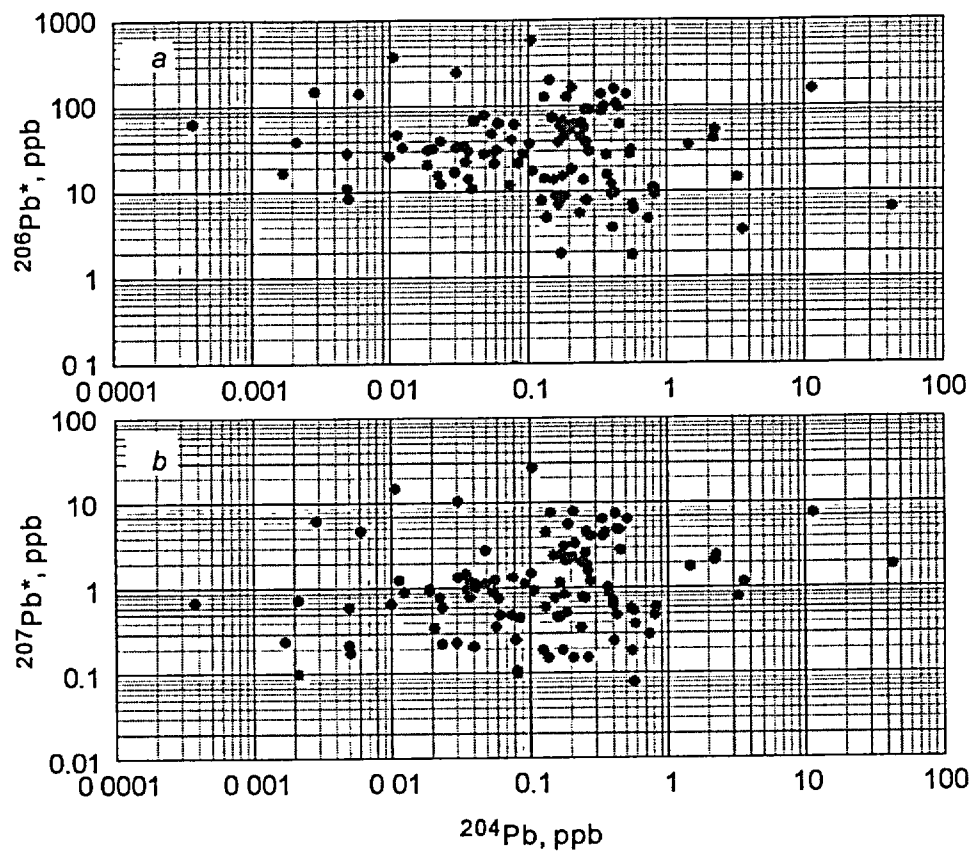


Figure 3-7-A-33. Absence of correlation between $^{206}\text{Pb}^*$ and ^{204}Pb , and $^{207}\text{Pb}^*$ and ^{204}Pb . *Blue dots* – Neymark et al. (2000); *red dots* – Neymark et al. (2002).

The correlation is good for the data from across the crusts; the data from the outer parts of the crusts, however, show a much poorer correlation, although still better than for the non-corrected data.

The correlation shown in Figure 3-7-A-34-b is important. The best correlation between ^{206}Pb and ^{207}Pb is expected in the case where measured quantities of the isotopes are produced by *in situ* decay of their parents, ^{238}U and ^{235}U . This would be the case in the framework of the USGS model. Hence, any alternative models, to be viable, must also provide a satisfactory explanation for this empirical correlation.

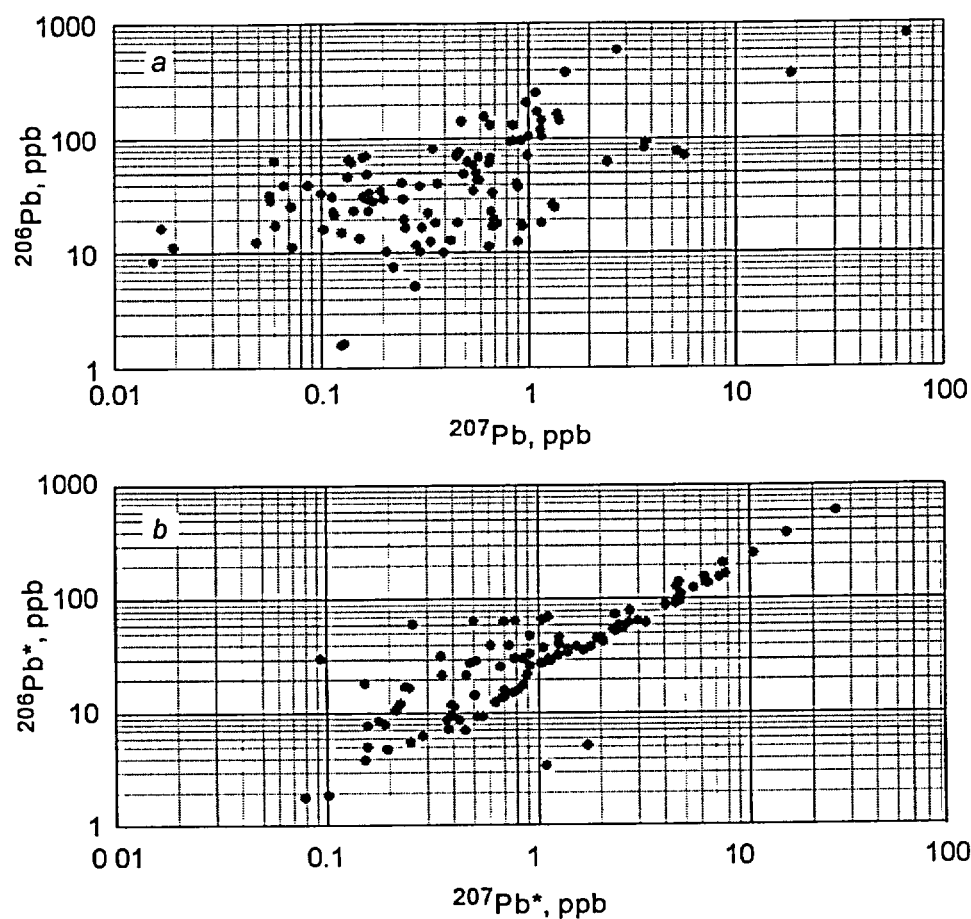


Figure 3-7-A-34. Correlations between ^{206}Pb and ^{207}Pb , and between $^{206}\text{Pb}^*$ and $^{207}\text{Pb}^*$ (values after the removal of $^{206}\text{Pb}_{\text{water}}$ and $^{207}\text{Pb}_{\text{water}}$ related to the mineral-forming fluid). *Green dots* – Neymark et al. (2000); *red dots* – Neymark et al. (2002).

Elements and isotopes in quartz and calcite

In addition to the large number of analyses of opal, the data available to us contain three analyses of calcite, three analyses of chalcedony and two analyses of quartz. The data are present in Table 3-7-A-9. It is apparent that concentrations of U in calcites are very low, hundreds and thousands of times smaller than those in opals. Table 3-7-A-10 compares the lead isotope ratios measured in calcite with the ratios employed for the "common lead" correction. The calcite does not seem to accumulate any appreciable amounts of ^{207}Pb and ^{208}Pb in excess of those that may be attributed to the mineral-forming fluid. Meanwhile, there is a very strong, hundred- to thousand-fold, enrichment of calcite samples with ^{206}Pb .

Table 3-7-A-9

Results of analyses for three calcite and three chalcedony samples (by USGS, 1997)

Mineral	Sample ID	Weight, mg	U, ppm	Pb, ppb	Pb common, pg	$^{206}\text{Pb}/^{207}\text{Pb}$	$^{206}\text{Pb}/^{208}\text{Pb}$	$^{206}\text{Pb}/^{204}\text{Pb}$	$^{206}\text{Pb}/^{238}\text{U}$	$^{207}\text{Pb}/^{235}\text{U}$	$^{234}\text{U}/^{238}\text{U}$ (activity)
Calcite-1	2059-Pb3	3.25	0.027	0.033	5.9	109.21	43.22	1751.00	n/a	n/a	n/m
Calcite-1	2098-Pb1	0.62	0.013	0.016	5.0	9.95	3.69	155.56	n/a	n/a	n/m
Calcite-1	2065-Pb1	0.82	0.06	0.019	2.46	71.93	30.45	1171.20	n/a	n/a	n/m
Chalc-1	2029-Pb1	1.62	12.26	0.018	5.9	12.00	10.39	408.73	0.001359	0.008835	1.00
Chalc-1	2021-Pb1	42.28	10.21	0.042	12.16	2.92	1.28	50.17	0.001397	0.009534	1.00
Chalc-2	2021-Pb1	43.53	11.48	0.033	793.8	4.00	1.87	73.18	0.001365	0.009318	1.00

Table 3-7-A-10

Comparison of the lead isotope ratios in calcite and quartz samples with the values, employed for the "common lead" correction

Isotope ratio	Calcite			Quartz		Common lead correction
	2059-Pb3	2098-Pb1	2065-Pb1	2021Pb1-b1	2021Pb1-c1	
$^{206}\text{Pb}/^{204}\text{Pb}$	1751.00	155.56	1171.20	19.92	19.77	18.83±0.82
$^{207}\text{Pb}/^{204}\text{Pb}$	16.00	15.60	16.28	15.73	15.61	15.62±0.09
$^{208}\text{Pb}/^{204}\text{Pb}$	40.51	42.15	38.46	39.29	39.02	38.78±0.53

Abundances of different lead isotopes in calcite are shown in Table 3-7-A-11.

A comparison of the values shown in 3-7-A-11 with the data for opals shows that abundances of such Pb isotopes as ^{204}Pb , ^{206}Pb and ^{208}Pb in calcite are comparable with the smallest values measured in opal. The content of ^{207}Pb in calcite is at the absolute minimum of values measured in the Yucca Mountain samples.

Table 3-7-A-11

Abundances of the lead isotopes in calcite and quartz samples (ppb)

Mineral	Sample	²⁰⁴ Pb	²⁰⁶ Pb	²⁰⁷ Pb	²⁰⁸ Pb
Calcite	2059-Pb3	0.018	31.95	0.293	0.739
	2098-Pb1	0.075	11.61	1.167	3.147
	2065-Pb1	0.015	18.13	0.252	0.596
Quartz	2021Pb1-b1	0.080	1.60	1.20	3.200
	2021Pb1-c1	0.150	16.50	3.00	6.000

Samples of quartz were analyzed from the fracture at ESF station 12+21.83. The quartz had very low U contents: 0.045 ppm for sample HD2021Pb1-b1 and 0.067 ppm for sample HD2021Pb1-c1. The Pb isotope ratios in the quartz samples correspond to those used for the "common lead" correction (see Table 3-7-A-10). The abundances of different lead isotopes in the quartz samples are shown in Table 3-7-A-11. The contents of ²⁰⁶Pb in quartz are the smallest among all samples studied from the ESF.

Mineralogic studies suggest that the calcite grew by the diffusion mechanism (see Chapter 3-4). Thus, the Pb isotope abundances measured in calcite may be considered characteristic of diffusion controlled growth. The very high ²⁰⁶Pb/²⁰⁴Pb ratios (in excess of 1,000) measured in two calcite samples require some mechanism of concentration for the excess ²⁰⁶Pb, which existed during the calcite deposition. Such high concentrations of ²⁰⁶Pb cannot be accounted for by the *in situ* decay of ²³⁸U in calcite.

The low abundances of Pb isotopes in chalcedonies and quartz may indicate diffusion-controlled growth of these phases, whereas greater Pb-abundances characteristic of the opals may correspond to the mixed or the predominantly coalescent (colloidal) growth. The concentrations, indicative of the change in the growth mechanism may be estimated as: ²⁰⁴Pb – 0.01 to 0.1 ppb, ²⁰⁶Pb – 10-30 ppb, ²⁰⁷Pb – 0.1-1.0 ppb, and ²⁰⁸Pb – 0.1-3.0 ppb.

Appendix 3-7-3: The theory of formation of micelles through condensation and coagulation

In this appendix we present the basic theory of the processes of formation of micelles through condensation and coagulation, which is best developed from principles of aerosol physics. Knowledge of these processes is necessary for the analyses of colloid-assisted processes in cavities. The formation, growth and precipitation of micelles of silica in solution is accompanied by a number of simultaneously occurring processes, such as:

- heterogeneous adsorption of monomers (i.e., molecules, containing one atom of Si) on the surface of the existing particles (i.e., condensation growth of the particles);

- formation of a new condensed phase if supersaturation and initial concentration of silica monomers are sufficiently high;

and

- diffusion (Brownian) coagulation.

The processes listed above are included in the equations of Smolukhovski (Smolukhovski, 1912). The major difficulties encountered in solving these equations arise from the difficulty of setting meaningful physical and chemical boundary conditions (this problem is analyzed in detail by Sabelfeld et al. 1996). In many cases, solutions appear that yield the so-called "self-sustaining" spectra for the distributions of particle sizes (Sutugin et al., 1971, 1978). This makes it possible to use empirical formulae instead of complex and computer time-intensive numerical calculations.

Algorithms for solving Smolukhovski's equations for fast coagulation

The analysis of publications dealing with the formation of the highly disperse aerosols at high supersaturations (Petrov, 1982) has demonstrated that many authors tend to use the theory of classic nucleation for very early stages of the process. Frenkel (1975) and Voloschuk and Sedunov (1975) demonstrated that the critical nucleus, defined by the classic equation of Thomson (Strickland-Constable, 1971) in the theory of Becker-Frenkel-Zeldovich is composed of between several molecules and several tens of molecules:

$$r^* = \frac{2 \cdot \sigma \cdot v}{kT \cdot \ln(p/p_\infty)} \quad (3-7-A-12)$$

where r^* is the radius of critical nucleus, σ is the surface tension, v is the volume of a molecule, k is the Boltzman's constant, T is the temperature (K), p is the pressure of the vapor of molecules, and p_∞ is the pressure of saturated vapor at a given T . Taking the characteristic parameters for solid matter, e.g., $\sigma \cong 100 \text{ erg}\cdot\text{cm}^{-2}$, $v \cong 0.3 \text{ nm}^3$, and $\ln(p/p_\infty) \cong 5$, at $T = 500 \text{ K}$, we obtain $r^* = 0.2 \text{ nm}$ or 2\AA .

Obviously, at such small sizes for the critical nucleus the applicability of the classic theory of nucleation is problematic. In such conditions, the process of formation of the condensed phase is conventionally described by a system of the modified coagulation equations of Smolukhovski (Smolukhovski, 1936; Voloschuk and Sedunov, 1975, Daniel and Gillespie, 1981).

$$\frac{dn_i}{dt} = \frac{1}{2} \sum_{j=1}^{\infty} a_{ij} K_{ij} n_i n_j - n_i \sum_{j=1}^{\infty} a_{ji} K_{ji} n_j + \beta_{i+1} n_{i+1} - \beta_i n_i \quad (3-7-A-13)$$

where n_i is the concentration of clusters*, composed of i molecules, K_{ij} are the constants of collision, a_{ij} are the coefficients of the efficiency of collisions, and β_j are the coefficients of the desorption of molecules from clusters.

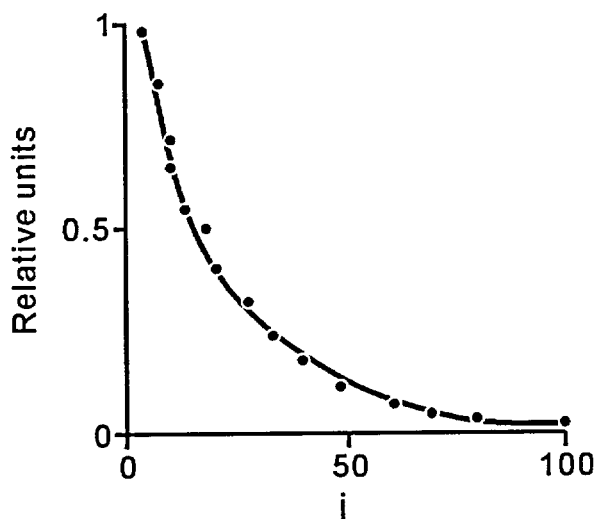


Figure 3-7-A-35. Analytical solution of the coagulation equation of Smolukhovski (Eq. 3-7-A-14) at $K_{ij} = \text{const}$ (line) compared with the numerical calculation by the MPV algorithm (dots) at dimensionless time $\Theta = 32$ (see text for explanation).

The role of coagulation during nucleation at high supersaturations has been addressed in detail both by analyzing numeric solutions of equations of the type of Eq. 3-7-A-13, as well as through the comparison of calculated and experimental values by Strikland-Constable (1971), Frenkel (1975), and Daniel and Gillespie (1981). Experiments with large particles (number of molecules $j > 100$), require that a great number of constants be used in calculations (on the order of 10^4 a_{ij} 's and β_j 's). Therefore, until recently only qualitative analysis of the experimental data was possible.

Concentrations of micelles $\geq 10^{10} \text{ cm}^{-3}$ are typical of natural hydrological systems (Kuznetsov and Ust-Kachkintsev, 1976). At such concentrations, the characteristic times of coagulation processes in a cavity may be quite short (e.g., less than 1 s) in

* The term cluster defines a small micelle that has already lost the physicochemical properties characteristic of molecules, but has not yet acquired properties characteristic of large particles (Petrov, 1982). Typically, the size of the clusters is in the range of 1 to 10 nm.

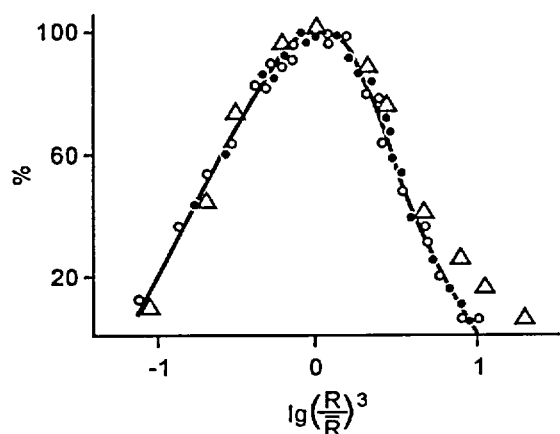


Figure 3-7-A-36. Self-sustaining spectrum of the particle size distribution. *Triangles* – calculations by the Rozinski-Snow algorithm (Rozinski and Snow, 1961; Sutugin et al., 1971), *circles* – calculations by the MPV algorithm (*open* – at the number of mergers $KO = 19$; *filled* – at $KO = 28$). R is the radii of micelles, \bar{R} is the mean radius.

$KO = 19$ corresponds to the number of monomers in a micelle $j \sim 5 \cdot 10^5$ or radius of the micelle $R \sim 8$ nm; $KO = 28$ corresponds to $j \sim 3 \cdot 10^8$ and $R \sim 65$ nm.

comparison to the characteristic times of other processes (e.g., water exchange time of 1 to 10 days). Because of these short times, the term describing desorption may be neglected (i.e., $\beta_j = 0$) at early stages of coagulation. Eq. 3-7-A-13 thus transforms into the classic equation of Smolukhovski:

$$\frac{dn_i}{dt} = \frac{1}{2} \sum_{l=i+j} a_{ij} K_{ij} n_l n_j - n_i \sum_{l=1}^{\infty} a_{il} K_{il} n_l \quad (3-7-A-14)$$

The methods of solving this equation are described in the literature (Rosinski and Snow, 1961; Sutugin et al., 1971, 1978; Pashenko et al. 1980). Pashenko and Sabelfeld (1992) developed some new approaches to the solution of the coagulation equations, which combined Eq. 3-7-A-14 and the traditional Monte-Carlo method. The resulting

method was named "Method of merging physical volumes (MPV)". Theoretical contributions by Markus (1968) and Lushnikov (1978) have demonstrated that the statistical-probabilistic approach to coagulation problems leads to equations unambiguously linked to the equations of the coagulation theory of Smolukhovski (Daniel and Gillespie, 1981; Kodenev, 1984). Figure 3-7-A-35 compares the distributions of micelles by the number of molecules in a particle (j), obtained through the analytical solution of Smolukhovski's equation and distributions calculated numerically using the MPV algorithm. It is shown that the later algorithm gives a precision of better than 1%.

One of the advantages of the MPV algorithm is that it allows solutions even in those cases where coagulation constants are set in the non-analytical form or where the constants are time-dependent.

Using the MPV algorithm for calculating the "self-sustaining" spectra of particle size distribution

An example for a typical self-sustaining spectrum is shown in Figure 3-7-A-36. The question of how the constants of collision, $K_{i,j}$, affect the shape of the stationary particle size distribution was extensively discussed in the literature (Voloschuk and Sedunov, 1975; Chatterjee et al., 1975; Sutugin et al., 1978). Because two parameters that are typically measured in experiments are the mean radius $R(t)$

and the coefficient of variation (α), Pashenko et al. (1980) carried out model calculations in order to determine the influence of K_y on these parameters. Experimental measurement of $R(t)$ is the most difficult and in many cases cannot be done correctly, because the concentration of monomers at the initial moment of time is not known (Kondratiev et al., 1982; Clouds..., 1989). Meanwhile, changes in the coefficient of variation at large times $\alpha(t \rightarrow \infty)$ may show whether or not the system has reached a state characterized by the self-sustained particle size distribution spectrum.

Theoretical analysis predicts that at $t \rightarrow \infty$ the coefficient of variation α for different constants of coagulation K_y acquire near-stationary values. Direct modeling using the MPV algorithm has demonstrated good agreement with theory (Figure 3-7-A-37).

Approximation formulae for different stages of the coagulation process

When the monomolecular growth is completed, the process of coagulation of micelles with different sizes begins. The process may lead to the appearance of particles built up of tens of thousands of monomers. For a numerical description of the process, semi-empirical formulae obtained by the MPV method are useful. We introduce for this purpose:

$$\alpha = 1/2 \cdot K_0 N_0 t \quad (3-7-A-15)$$

where K_0 is the constant of coagulation, N_0 is the number of micelles in a unit volume at the outset of coagulation, and t is the time. It is convenient to carry out the calculations using dimensionless time Θ :

$$\Theta = K_0 N_0 t \quad (3-7-A-16)$$

Solutions of the Smolukhovski's equation at $K_y = K_0 = \text{const}$ will then assume the following forms.

- concentration of particles built up of j atoms (molecules, monomers):

$$n_j(t) = N_0 \frac{\alpha^{j-1}}{(1+\alpha)^{j+1}} \quad (3-7-A-17)$$

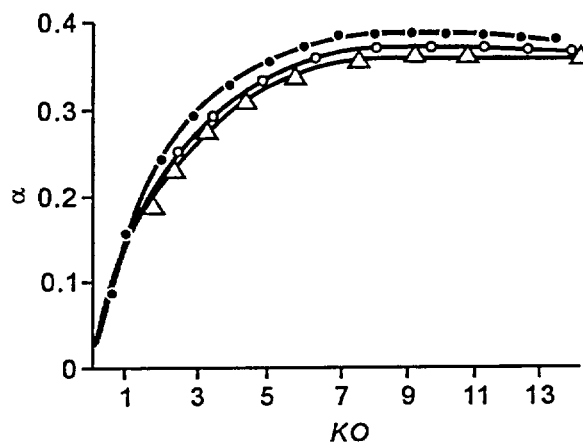


Figure 3-7-A-37. Dependence of the variation coefficient α on the number of mergers KO in the MPV algorithm for varying constants of coagulation in the Smolukhovski's equation. *Filled circles* – model constant $K_y = (i^l + j^l) \cdot (i+j)$, *unfilled circles* – molecular and diffusion constants; and *triangles* – $K = 1$.

- total concentration of particles, containing j^* and more atoms:

$$N^* = N_0 \cdot \frac{\alpha^{j^*-1}}{(1+\alpha)^{j^*}} = \sum_{j=j^*}^{\infty} n_j(t) \quad (3-7-A-18)$$

- mass of all particles (expressed as the mass of monomers) for particles with $j > j^*$:

$$M^* = \sum_{j=j^*}^{\infty} j \cdot n_j(t) = N_0 \cdot \frac{(\alpha + j^*) \cdot \alpha^{j^*-1}}{(1+\alpha)^{j^*}} = N^* \cdot (j^* + \alpha) \quad (3-7-A-19)$$

- concentration $n_j(t)$ reaching a maximum at:

$$\alpha = \frac{1}{2} \cdot K_0 N_0 t = \frac{(j^* - 1)}{2} \quad (3-7-A-20)$$

- maximum concentration:

$$n_j(\text{max}) = 4N_0 \frac{(j-1)^{j-1}}{(j+1)^{j+1}} \quad (3-7-A-21)$$

or, at $j > 5$, with sufficient accuracy

$$n_j(\text{max}) \cong 0.5 \cdot j^{-2} \quad (3-7-A-22)$$

The concentration of clusters composed of j monomers increases rapidly during the initial period of time until it reaches a maximum, defined by Eq. 3-7-A-21; the concentration growth then gradually slows down.

The time after which clusters containing more than j atoms appear is defined as:

$$t_{\text{exp}} = 2\Theta \left(\frac{n_{\text{min}}}{N_0} \right)^{\frac{1}{j-1}} \quad (3-7-A-23)$$

The constants of coagulation between micelles composed of i and j monomers in the Brownian diffusion regime equal:

$$K_{ij} = K_0 (i^{1/3} + j^{1/3}) \left(\frac{1}{i^{1/3}} + \frac{1}{j^{1/3}} \right) \quad (3-7-A-24)$$

In this case, the solution of Smolukhovski's equation assumes the form:

$$n(j,t) = \frac{1}{j} \cdot \frac{N}{\ln \sigma(t) \cdot 3\sqrt{2\pi}} \cdot \exp\left(-\frac{\ln^2\left(\frac{j}{j_g(t)}\right)}{18 \ln^2(\sigma(t))}\right) \quad (3-7-A-25)$$

where j is the number of molecules in a cluster, j_g is the first momentum of the time t in the function of distribution $n(j,t)$, σ is the second momentum, and N is the number of clusters in the unit volume at the outset of the coagulation. Eq. 3-7-A-25 is commonly used for the approximation of the self-sustaining spectrum and its transformation with time.

The change for the total concentration of clusters (particles) in time may be defined as:

$$\frac{N(t)}{N_0} = \frac{1}{1 + [1 + \exp(\ln^2 \sigma_0)]KN_0t} \quad (3-7-A-26)$$

where σ_0 is the second moment of the distribution function in the initial moment of time ($n(j,0)$). The solution for the second moment is:

$$\ln^2 \sigma = \frac{1}{9} \ln \left[2 + \frac{\exp(9 \ln^2 \sigma_0) - 2}{1 + [1 + \exp(\ln^2 \sigma)]KN_0t} \right] \quad (3-7-A-27)$$

If the *a priori* form of the solution for the Smolukhovski's equation with the coagulation constants (Eq. 3-7-A-24) in analytical form (Eq. 3-7-A-25) is not known, the exact solution requires the use of analytical methods. Using the MPV algorithm, Pashenko and Sabelfeld (1992) obtained approximating equations for the second moment $n(j,t)$:

$$\begin{aligned} \sigma &= (\sigma_0 - \Delta)(KN_0t + 1)^{-0.37} + \Delta \\ \sigma &= (\sigma_0 - \Delta)(KN_0t + 1)^{-1.38} + \Delta \end{aligned} \quad (3-7-A-28)$$

where Δ is the second moment of the function $n(j,t)$ at large times ($\Theta > 10^4$), when the spectrum of distribution of particles by sizes approaches the self-sustaining form (see Figure 3-7-A-36).

It should be noted that all formulae presented above are used only at $KN_0t \geq 1$, which stems from the physical meaning of the problem: at least one act of collision (coagulation) of particles must occur for all particles in the spectrum. Figure 3-7-A-38 compares the results of the calculations using both types of formulae (3-7-A-27 and 3-7-A-28).

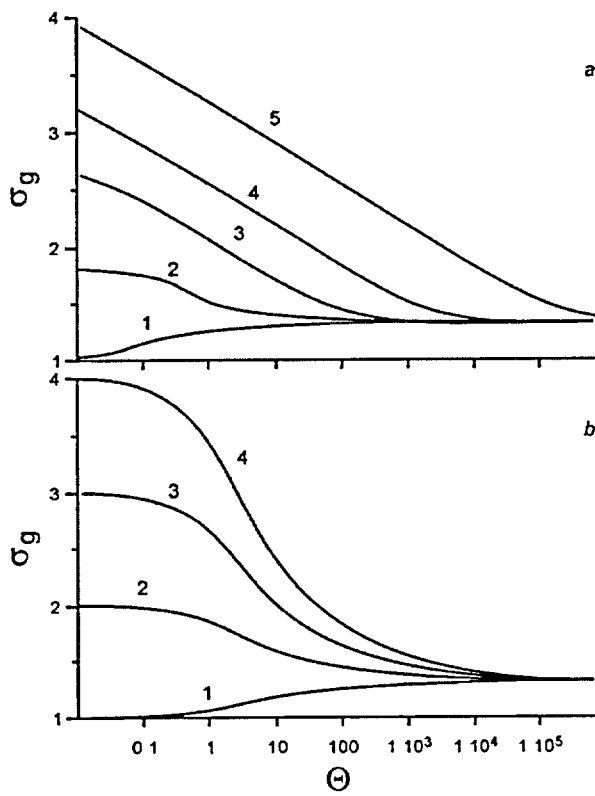


Figure 3-7-A-38. The change of the second moment of the size distribution function for micelles as a function of the dimensionless time of coagulation Θ . *a* – using analytical Eq. 3-7-A-27) at initial σ_0 : 1 – 1; 2 – 1.8, 3 – 2.6, 4 – 3.2, and 5 – 4; *b* – using Eq. 3-7-A-28 at initial σ_0 : 1 – 1, 2 – 2, 3 – 3, and 4 – 4.

Chapter 3-8. Thermal History of Yucca Mountain

By Y.V. Dublyansky and J.S. Szymanski

Table of contents

Chapter 3-8. Thermal History of Yucca Mountain	464
3.8.1. Thermal modeling	465
3.8.1.1. USGS thermal model	465
3.8.1.2. Thermal modeling of igneous-related geothermal systems: constraints and uncertainties	466
3.8.1.3. Magmatic preheating of the Earth's crust in the vicinity of Yucca Mountain	466
3.8.1.4. Hydrothermal activity around the Timber Mountain Caldera	468
3.8.1.5. Geometry of the model	470
3.8.1.6. Summary: constraints of the thermal modeling	472
3.8.2. Thermal history of Yucca Mountain based on geologic evidence	473
3.8.2.1. Deposition and cooling of the tuffs	473
3.8.2.3. Timber Mountain Caldera hydrothermal event	474
3.8.4. Summary	481

Chapter 3-8. Thermal History of Yucca Mountain

By Y.V. Dublyansky and J.S. Szymanski

The data presented in the preceding chapters demonstrate that waters with elevated temperatures (up to 60-85 °C) circulated and deposited minerals in the upper part of the vadose zone of Yucca Mountain in the geologic past. We believe the following question needs to be answered: what was the source of energy that heated these waters to unambiguously "hydrothermal" temperatures? Our answer is discussed in this chapter.

The Yucca Mountain Project researchers have made a number of suggestions in an attempt to reconcile the elevated temperatures with their contention that secondary minerals found in the ESF are a product of rainwater percolating through the mountain. They attempt to connect the elevated temperatures with Miocene silicic volcanism. They speculate: (a) that the deposition of secondary calcite and silica minerals found in the ESF "*...likely began during cooling of the tuffs...*" (Whelan et al., 2000); (b) that the Yucca Mountain vadose zone has experienced a gradual cooling of the rocks over millions of years, in response to the cooling of a magma chamber located beneath the Timber Mountain caldera north of Yucca Mountain (Marshal and Whelan, 2000), or (c) that the rocks in the vadose zone were heated conductively by thermal waters that circulated at a depth of >1000 m, under Yucca Mountain, during the Timber Mountain Caldera hydrothermal episode some 10.5 Ma ago (Whelan et al., 2001). Thus far, these and similar claims remain largely unsupported by any substantive evidence; moreover, some of the published data flatly contradict these speculations. The latest example of the rather cavalier treatment of the problem can be found in the U.S. Department of Energy's Yucca Mountain Science and Engineering Report (U.S. DOE, 2001). The report dismisses the significance of the fluid inclusion data by bluntly stating "*... there was a well-documented thermal period that affected the volcanic rock for a long time after its formation.*" (p. 4-402).

In this chapter our intent is to provide the background for interpreting the paleotemperature results obtained from secondary minerals at Yucca Mountain. We first evaluate the feasibility of numerical thermal modeling by assessing the constraints of the methodology. Then we summarize what is known and what can be inferred with reasonable certainty about the thermal history of Yucca Mountain (and specifically about the proposed repository zone) on the basis of the geologic record. We put special emphasis on two aspects of the history: (1) what temperatures and heat flows could have existed at the

proposed repository horizon during the known thermal events, and (2) when did these events happen and how long did they last.

3.8.1. Thermal modeling

Igneous-related geothermal systems (i.e., geothermal systems, for which bodies of magma residing in the upper 10 km of the Earth's crust serve as a source of heat) constitute a significant part of the geothermal resource base of the United States (White and Williams, 1975). The need to assess the heat contents of igneous-related geothermal systems has prompted the development of a methodology for thermal modeling. The methodology makes use of such parameters as the probable volumes of high-level magma chambers and the ages of the youngest volcanism from these chambers (Smith and Shaw, 1975; Wohletz and Heiken, 1992). The initial heat content, heat losses over the time elapsed since the last eruption, and the heat remaining in the system are assessed through thermal calculations. Researchers studying Yucca Mountain have used such calculations.

3.8.1.1. USGS thermal model

A model that was recently advanced by the Yucca Mountain Project researchers in an attempt to reconcile the fluid inclusion record with the geochronological data obtained from secondary minerals, envisages *"...a gradual cooling of the rocks over millions of years, in agreement with thermal modeling of magma beneath the 12-Ma Timber Mountain caldera just north of Yucca Mountain. This model predicts that temperatures significantly exceeding current geotherm values occurred prior to 6 Ma."* (Marshall and Whelan, 2000). The model thus envisages that the rock mass in the vadose zone of Yucca Mountain was heated conductively and remained hot for up to 6.3 million years (between 12.7 and 6 Ma). Purportedly, rainwater percolating through this mass of hot rock became heated (up to 60-85 °C) and deposited secondary minerals.

By the time of preparation of this report, the thermal model proposed by the Yucca Mountain Project researchers (Marshall and Whelan, 2000, U.S. DOE, 2001) had not been published in a form allowing for its critical evaluation. Judging from oral presentations at different venues, a one-dimensional modeling of conduction was employed. In early variants of the model, a sphere about 10 km in diameter approximated the shape of the magma body. In later versions of the model the body acquired the shape of an ~7 km-thick disc with a diameter of 30 km ($V = 5000 \text{ km}^3$) residing at a depth of 5 km some 5-7 km to the north of the ESF (U.S. NWTRB, 2001). The magma body was assumed to be long-lived and capable of maintaining a temperature of 900 °C for 3 million years, a period from 13 to 10 Ma. The cooling was assumed to occur through conductance only, so that the model did not take into account the convective heat removal by thermal waters – a process that has certainly occurred around the Timber Mountain

caldera as the mineralogical record and geochronological data show (e.g., Bish and Aronson, 1993; Weiss et al., 1994).

In subsequent sections we discuss the methodology of thermal modeling, and the constraints of the method. The purpose of the discussion is to further an understanding of the reliability of the results that are achievable through thermal modeling, particularly as it applies to the characterization of the thermal history of Yucca Mountain.

3.8.1.2. Thermal modeling of igneous-related geothermal systems: constraints and uncertainties

As is generally the case with numerical modeling, the selection of boundary conditions and input parameters for the calculations are the most important steps in carrying out quantitative thermal modeling. In the case of the thermal modeling of igneous-related systems, some of the input parameters may be determined with reasonable accuracy. For example, the K-Ar radiometric dating allows for a reasonably precise determination of the age of the last eruption. Other parameters are not so easily quantified and, as a consequence, serve as sources of uncertainty. For example, the volume of the magma chamber for a time when it is known to contain magma is a parameter that is needed for thermal calculations. The reliable quantification of this parameter is difficult.

In most cases thermal modeling relies on two major assumptions. The first assumption is that the effects of magmatic preheating and the gains of magma by the chamber after the time of the last eruption are ignored. The second assumption is that the heat transfer in the rocks surrounding the magma chamber is by solid-state conduction only. This means that heat losses caused by other heat-transfer mechanisms, particularly by hydrothermal convection, are neglected. As Smith and Shaw (1975) argued, both of these assumptions are unavoidable, because "*there are no uniform quantitative criteria for adjustments*". They also opined that "*The net effects of the two assumptions relative to the present igneous-related resource tend to compensate one another, but the proportional amounts are not known with any confidence.*" (p. 58).

Below we evaluate these two assumptions in the context of the geologic history of the Yucca Mountain area.

3.8.1.3. Magmatic preheating of the Earth's crust in the vicinity of Yucca Mountain

The geochronologic studies of the volcanism in the vicinity of the Timber Mountain caldera complex, summarized by Weiss et al. (1994), indicate that the high-level silicic magma chamber (or cluster of chambers) was both discharging and replenishing magma for an extended period of time (Figure 3-8-1). The Silent Canyon caldera complex (adjacent to the Timber Mountain caldera complex from the north) erupted the Belted Range tuff 14.9 Ma ago. Then followed the Lithic Ridge tuff (14.0 Ma), for

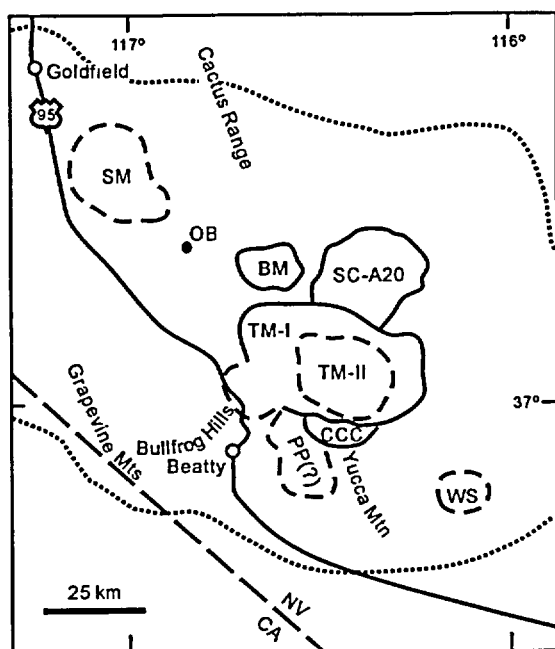


Figure 3-8-1. Calderas and major volcanic centers of the Southwestern Nevada volcanic field (modified from Weiss et al., 1994). BM – Black Mountain; CCC – Claim Canyon Cauldron; OB – Obsidian Butte; PP(?) – proposed Prospector Pass caldera (Carr et al., 1986), SC-A20 – Silent Canyon – Area 20 center; SM – Stonewall Mountain; TM-I and TM-II – Timber Mountain Calderas; WS – Wahmonie-Salyer center. Dotted line – approximate present limit of ash-flow sheets of the southwestern Nevada volcanic field.

which the volcanic center is unknown. The Silent Canyon complex reactivated 13.7 Ma ago, erupting more of the Belted Range tuff. The Crater Flat tuff erupted 13.2 Ma ago (location of volcanic center is uncertain, but it is thought to be in the vicinity of the Timber Mountain Caldera complex). The Calico Hills formation (12.9 Ma) is associated with the flow-dome complexes southeast of the Claim Canyon cauldron and Area 20 caldera. Paintbrush tuff erupted from the Claim Canyon cauldron and an area of the Timber Mountain caldera complex between 12.8 and 12.7 Ma. Then followed voluminous eruptions of Timber Mountain tuff (at 11.6 Ma from Timber Mountain Caldera- I and at 11.45 Ma from the Timber Mountain Caldera-II). Eruptions from the western part of the Timber Mountain caldera complex produced tuffs of Cutoff Road, Fleur de Lis Ranch, and Buttonhook Wash (11.4 Ma) and tuffs and lavas of Bullfrog Hills (10.5-10 Ma).

Upon the termination of the Timber Mountain Magmatic stage 10-10.5 Ma ago, magmatic centers began to migrate to the northwest (Black Mountain Caldera complex – 9.2-9.4 Ma; Obsidian Butte center – 8.8 Ma; and Stonewall Mountain caldera complex – 7.6-7.5 Ma).

Thus, the high-level magma chamber residing beneath the area just north of Yucca Mountain was continually replenishing heat and matter and discharging them through eruptions for almost 5 million years (between at least 14.9 and 10 Ma). The preheating of the Earth's crust before the formation of Yucca Mountain (12.7-12.8 Ma) lasted for about 2 million years, and certain magma gains occurred for almost 3 million years thereafter. Unfortunately little is known with any degree of certainty regarding the volumes of magma involved, the compositions, depth, shapes of magma chambers, rates of magma convection, differentiation (the data that are necessary to make the thermal modeling a rigorous method for

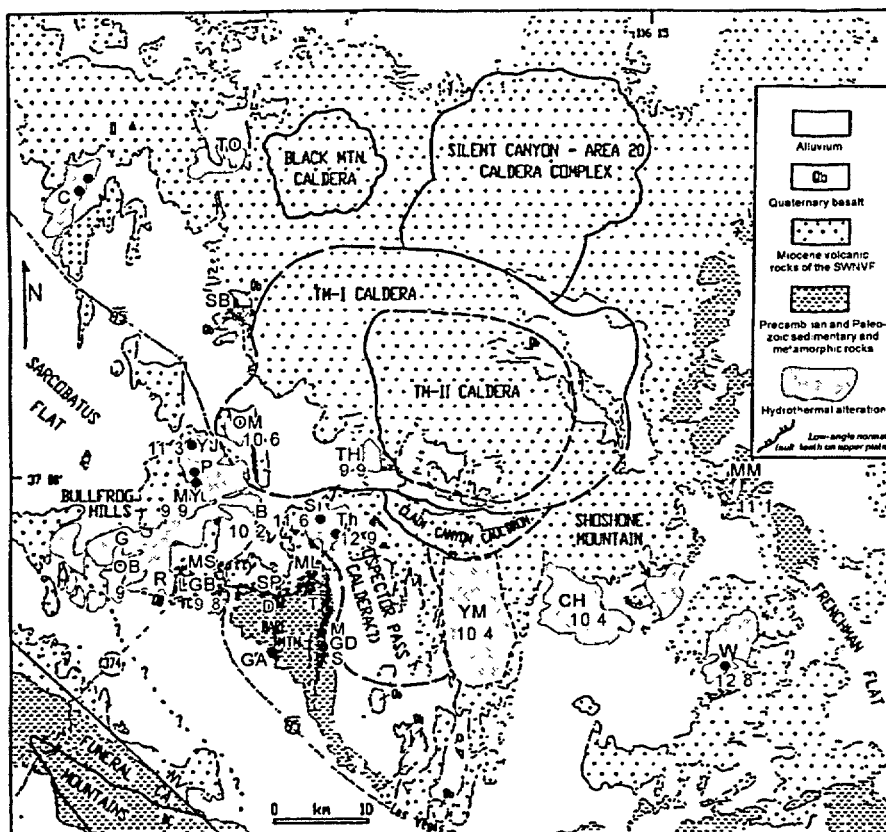


Figure 3-8-2. Locations of areas of the hydrothermally altered rocks, selected mineral deposits and prospects in the vicinity of the Timber Mountain caldera complex. Red numbers indicate K/Ar ages of the alteration minerals (alunite, adularia, or illite-smectite; Bish and Aronson, 1993; Weiss et al., 1994). B – Bailey's hot spring, C – Clarkdale district; CH – Calico Hills, D – Daisy mine, G – Gold Bar mine, GA – Gold Ace mine, GD – Goldspar/Diamond Queen mine, LGB – Lac Gold Bullfrog mine, M – Mary mine, ML – Mother Lode mine, MM – Mine Mountain, MS – Montgomerly Shoshone mine, MY – Mayflower mine, OB – Original Bullfrog mine, OM – Oasis Mountain, P – Pioneer mine, R – Denver-Tramps and Gibraltar mines near Rhyolite, S – Sterling mine, SB – Sleeping Butte, Si – Silicon mine, SP – Secret Pass prospect, T – Telluride mine, Th – Thompson mine, TH – Transwaal Hills, TO – Tolicha-Quartz Mountain district, W – Wahmonie, YJ – Yellowjacket mine, YM – Yucca Mountain deep-seated alteration (note that the exact area of the alteration is not known).

TM-I caldera associated with the eruption of the 11.6 Ma Rainier Mesa Member of the Timber Mountain Tuff; TM-II caldera associated with the eruption of the 11.45 Ma Ammonia Tanks Member of the Timber Mountain Tuff.

quantitative estimation of thermal regimes rather than one for making crude assessments). This lack of information is the major source of uncertainty in any attempt to employ quantitative thermal modeling for evaluating the thermal history of Yucca Mountain.

3.8.1.4. Hydrothermal activity around the Timber Mountain Caldera

In addition to the transfer of heat into the upper part of the Earth's crust by the ejection of magma from deeper levels and its subsequent loss to the atmosphere via eruptions and solid state conduction

through the country rocks, igneous heat was also removed from the magma chamber by the action of hydrothermal convection systems. The fact that such systems played an important role in the vicinity of the Timber Mountain caldera complex becomes obvious from an examination of the extent of hydrothermal alteration and mineralization in the area. Figure 3-8-2 shows outcrops of altered rocks as well as radiometric (K-Ar) ages of the alterations. With the exception of the Yucca Mountain area where hydrothermal alteration was discovered in boreholes at a depth of more than 1000 m, the rest of the hydrothermal alterations are expressed as surface exposures. It may be expected that areas exist where, like Yucca Mountain, hydrothermally altered rocks are not exposed at the topographic surface but are present at depth. As White and Williams (1975, p. 2) stated "*The hot dry rocks ... may not always be as hot and as dry at shallow and intermediate depths as generally envisioned because hydrothermal convection in natural fractures may be more common than is indicated from surface evidence*". The extent of such alteration, however, is unknown.

In any case, the extent of the known hydrothermal alteration and mineralization in the area is impressive. Weiss et al. (1994, p. 11) provided the following overview: "*Hydrothermal alteration and epithermal mineralization of Neogene age affected volcanic rocks of the SWNVF [Southwestern Nevada Volcanic Field] and underlying, basement rocks of pre-Mesozoic age ... Precious-metal and fluorite mines with significant present or past production include the Montgomery-Shoshone, Lac Gold Bullfrog, Sterling, Mother Lode, Gold Bear and Daisy mines ... The Wahmonie, Mine Mountain, northern Bullfrog Hills, Clarkdale and Tolicha districts have little recorded production, although rich ores are locally present. In addition, dozens of shallow prospect workings are scattered in areas of hydrothermal alteration near Sleeping Butte, Oasis Mountain, north of Bare Mountain, and in the Transvaal Hills, the Calico Hills and northwestern Yucca Mountain.*"

Figure 3-8-3 shows radiometric ages of the hydrothermal alteration minerals at different locations. The data indicate that hydrothermal alteration was penecontemporaneous with and followed, sometimes for 1-1.5 Ma, after every significant volcanic event in the area. Although separated in space, magma chamber-based hydrothermal systems persisted in the area between 14 and 9 Ma (and probably later to 7.8 Ma). The Figure further shows that the Timber Mountain caldera hydrothermal event reconstructed from studying alteration minerals in deep boreholes at Yucca Mountain (indicated as YM in the Figure) was not the only event that followed the Timber Mountain caldera eruption. Concurrently, hydrothermal solutions were circulating at Bullfrog Hills, Transvaal Hills, East and West Calico Hills, Oasis Mountain and Mine Mountain (see Figure 3-8-2).

Water has a very high heat capacity; therefore, although the removal of heat associated with hydrothermal activity is hard to quantify, there is little doubt that it was significant. Thus, the assumption

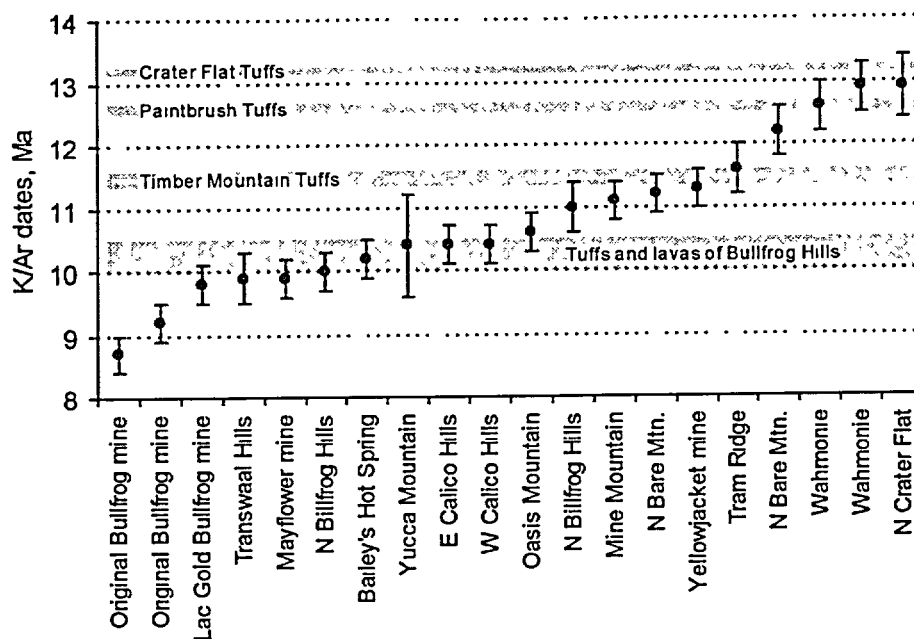


Figure 3-8-3. K/Ar age dates of hydrothermal alteration minerals (alunite, adularia, or illite-smectite) in the vicinity of the Timber Mountain caldera complex. Ages of eruptions are shown for comparison. Location of eruption centers (cf. Figure 3-8-1): *Crater Flat tuff* – uncertain; likely the area of Timber Mountain, Silent Canyon, NW Yucca Mountain, and/or proposed Prospector Pass caldera complex; *Paintbrush tuff* – Timber Mountain caldera complex and Claim Canyon cauldron; *Timber Mountain tuff* – Timber Mountain caldera I (11.6 Ma Rainier Mesa Member) and II (11.45 Ma Ammonia Tanks Member); *Tuffs and lavas of Bullfrog Hills* – periphery and west of the Timber Mountain caldera II.

Age for Yucca Mountain is shown as mean of the 12 reported K/Ar ages measured on illite/smectite from deep boreholes (>1100 m; Bish and Aronson, 1993). The rest of the data are individual analyses of alunite and adularia (Weiss et al., 1994). Error bars show 1 σ -intervals.

regarding the absence of the convective heat removal or redistribution would be clearly inappropriate in any quantitative thermal modeling of the Yucca Mountain area. Meanwhile, reliable quantification of the heat removal by this mechanism would be very difficult, if not impossible.

3.8.1.5. Geometry of the model

In addition to the uncertainties related to the poorly constrained input parameters discussed above, there is another problem associated with the quantitative thermal modeling of the Timber Mountain caldera magma chamber and thermal regimes of the Yucca Mountain vadose zone. The problem is caused by the geometry of the model, which is shown in Figure 3-8-4.

In order to model quantitatively the time distribution of the temperatures in the rocks overlying the magma chamber shown in the Figure, an important boundary condition such as the temperature at the interface of the Earth's surface with the atmosphere must be specified. It is apparent that, for a given geometry of the problem, the most intensive flux of heat would be directed upward from the center of the magma chamber (most heat stored in the central part of the chamber would have to be removed in this

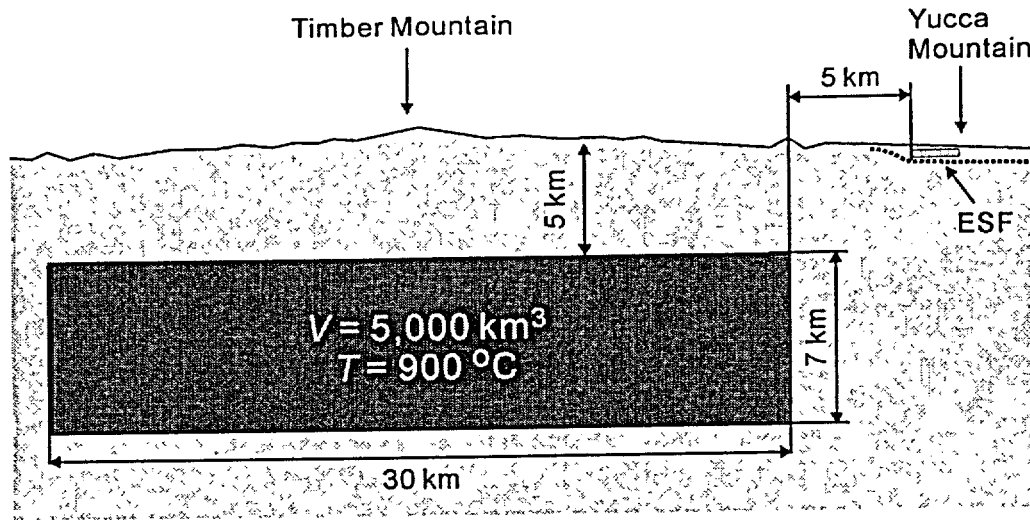


Figure 3-8-4. Schematic presentation of the USGS thermal model, as described in U.S. NWTRB (2001). The shape of the Timber Mountain magma chamber is a 7 km-thick disc with diameter of 30 km ($V = 5,000 \text{ km}^3$) residing at a depth of 5 km to 7 km to the north of the ESF. The chamber was assumed to maintain $T = 900 \text{ }^\circ\text{C}$ for 3 million years (from 13 to 10 Ma). The cooling was assumed to occur through conductance only, so that the model did not take into account convective heat removal by thermal waters. Dotted line shows the approximate location of the present-day water table beneath Yucca Mountain. No vertical exaggeration. Outline of the relief is approximate.

direction) through the Earth's surface and into the atmosphere. For the axial part of the chamber the stationary heat flow may be defined as:

$$Q = \frac{(T_{chamber} - T_{surf}) \cdot \lambda}{h} \quad (3-8-1)$$

where T is the temperature in the magma chamber and at the topographic surface (denoted by subscripts), λ is the thermal conductivity of rocks (for example, for the Yucca Mountain tuffs $\lambda = 1.74 \text{ W}\cdot\text{m}^{-1}\cdot\text{K}^{-1}$), and h is the depth. It is apparent that setting the appropriate value of T_{surf} , or a function, $T_{surf}(t)$, is crucial for the overall reliability of the model.

If the temperature of the magma chamber "source" is maintained at $900 \text{ }^\circ\text{C}$ for 3 million years, as the USGS modelers suggests (U.S. NWTRB, 2001), and the heat transfer in the rocks is through net conduction, the temperatures of the rocks at the topographic surface would increase substantially. In order to define the temperature at the ground surface, a very complex and physically indeterminate problem of heat transfer from a heated surface into the atmosphere must be solved. Heat removal from the rocks primarily occurs through either infrared emission of the heated body, or convection of the air mass. In reality, these two mechanisms would be coupled because of the "greenhouse" effect of the water vapor and clouds above the heated surface. The formation of clouds would be controlled by the uplift of the heated air mass, which would result in the creation of a localized column of heated air. Within such a

column, water vapor may be lifted to a height of 10-15 km, and probably more. Strong airflows directed from the periphery of the heated region (30 km in diameter, according to the model) toward its center would develop; the airflows would be expected to reach windstorm velocities. Uplifted warm vapor would condense in the upper parts of the column and precipitate outside the heated area (Kachurin, 1973).

If the heat is supplied continuously for 3 million years, as the USGS model stipulates, these extreme atmospheric processes are expected to last for comparable amounts of time. Such a long-lasting thermal structure may be expected to change climatic pattern over hundreds and, possibly, thousands of kilometers in the prevailing direction of movements of the air masses. It would also have a strong influence on the relief of the land surface, due to the development of a very dynamic precipitation system.

The historic meteorological record corroborates the plausibility of the hypothetical scenario outlined above. For example, conflagrations caused by massive bombing raids of the Allied Forces on German and Japanese cities during World War II caused the development of short-lived air circulation systems in the form of giant tornadoes (Kachurin, 1973).

The effects described above may be assessed numerically. Equation 3-8-2 is used in atmospheric physics (Kachurin, 1973) for determination of the height of the uplift of hot air above the heated area (as, for example, in connection with a forest fire):

$$\Delta H = \frac{1.5 \cdot w \cdot R}{u} \cdot \left(2.5 + \frac{3.3 \cdot g \cdot R \cdot \Delta T}{T_{atm} \cdot u^2} \right) \quad (3-8-2)$$

where w is the initial velocity of the air, ΔT is the overheating of the air; R is the characteristic linear dimension of the heated area (e.g., of the surface covered by wildfire or, in our problem, of the magma chamber footprint), u is the wind velocity, g is the gravity acceleration, T_{atm} is the temperature of the atmosphere. It is apparent that at large values of R , the height of the uplift is proportional to R squared, and may be as great as 10 km and more.

In summary, the behavior of the atmosphere above such a large and long-lasting thermal anomaly as the one postulated in the USGS thermal model (see U.S.NWTRB, 2001), at present, defies numerical modeling. This means that reliable boundary conditions for the whole problem of cooling of the magma chamber of a given size and shape (see Figure 3-8-4) cannot be established.

3.8.1.6. Summary: constraints of the thermal modeling

The purpose of thermal modeling, in the context of the Yucca Mountain studies, is to establish the extent and timing of the heating of the vadose zone in the vicinity of the proposed repository by a cooling magma chamber that resided under the Timber Mountain Caldera. The numeric results would have to be

obtained for the specific area (denoted ESF in the Figure 3-8-4) and, ideally, would portray the function $T(t)$, i.e., the change of the temperature with time within the ESF zone.

On the basis of our discussion of the constraints of the thermal modeling method we have to conclude that the chances of getting reliable numeric estimates with respect to this specific problem are slim. The gaps in our knowledge regarding important input parameters and boundary conditions, such as gains and losses of igneous heat in the vicinity of Yucca Mountain, are very significant and potential uncertainties associated with these gaps are great. In addition, the geometry of the model is unfavorable for obtaining reliable solutions. Under such circumstances, any results of future numeric thermal modeling must be interpreted with extreme caution. The ultimate verification of the results of thermal modeling must come from establishing consistent trends with the known thermal history of the area, which have been independently determined on the basis of the geologic record. In the following sections we provide an overview of this history.

3.8.2. Thermal history of Yucca Mountain based on geologic evidence

Two thermal events are considered well established with respect to the Yucca Mountain geological history. The first event was the deposition of the ash-flow tuffs, which built up layers of the mountain. Following deposition approximately 12.7 Ma ago, the tuff "pile" was hot, and cooling to ambient temperatures took time. The second was the so-called Timber Mountain Caldera hydrothermal event that occurred ~10-11 Ma ago (e.g., Bish and Aronson, 1993). It is thought that a hydrothermal convection system was set off by a granitic magma body, which resided under the Timber Mountain caldera, some 8-10 km to the north of Yucca Mountain. The Timber Mountain event is held responsible for pervasive zeolitic, montmorillonitic and carbonate alteration of the rhyolitic tuffs and the deposition of abundant calcite and silica below depth of $>\sim 1.2$ km under the surface of Yucca Mountain. Below we examine the time and the heat constraints on these two events.

3.8.2.1. Deposition and cooling of the tuffs

It is a matter of common geologic knowledge that cooling of layers of effusive rocks deposited on the Earth's surface takes a relatively short time. Natural analogs are known throughout the world where geologically young (Quaternary) and even historic effusive volcanic rocks have reached ambient temperatures in short periods of time. According to Schuraytz et al. (1989), thick pyroclastic deposits like the Topopah Spring and Tiva Canyon tuffs were erupted and emplaced at temperatures from $> 650^{\circ}\text{C}$ to 985°C , and, according to Rhiele (1973) they cooled to ambient temperatures within about 100 to 1,000

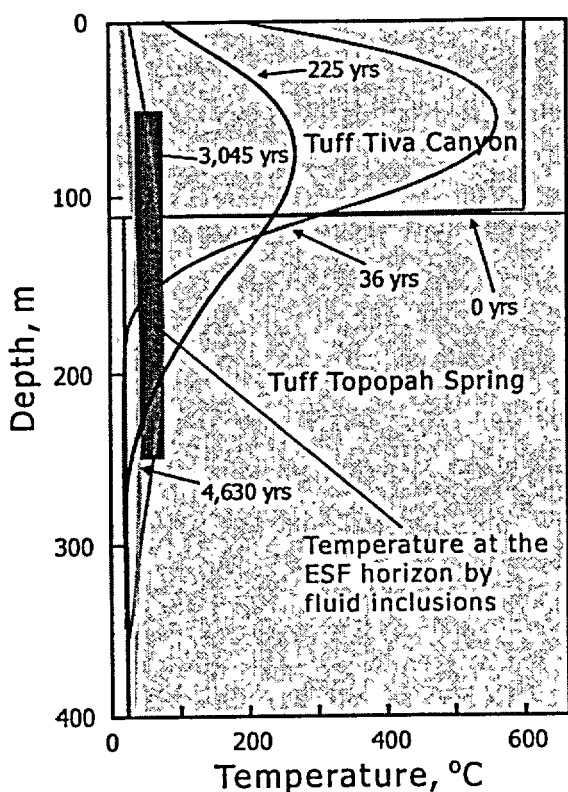


Figure 3-8-5. Kinetics of the conductive cooling of tuffs (results of the mathematical modeling).

Assumption: 110 m of the ash flow material with initial temperature $T(t_0) = 600^\circ\text{C}$ were deposited instantaneously.

of curves in Figure 3-8-5 shows that even under such unrealistically “insulated” conditions, the cooling of tuffs occurs fairly rapidly. In the model, temperatures of 35–85°C (corresponding to the interval of the fluid inclusion homogenization temperatures measured in the ESF minerals) existed within the depth interval of the proposed repository for approximately 1.5 thousand years some 4 thousand years after deposition of tuffs. We want to re-emphasize that cooling of real tuffs most probably occurred even faster. We conclude, thus, that the time estimates of Rhielo (1993) are more realistic than those of Whelan et al. (2001). These estimates indicate that minerals deposited in the ESF, whose ages are less than ~12.5 Ma, cannot be related to the cooling of the Yucca Mountain bedrock tuffs.

3.8.2.3. Timber Mountain Caldera hydrothermal event

The Timber Mountain Caldera hydrothermal event was caused by the cooling of a granitic magma chamber, which was the “parent” to the youngest pyroclastic units in the Yucca Mountain area, the Rainier Mesa and Ammonia Tank tuffs (~11.6–11.45 Ma). Being emplaced inside fractured and water-saturated rock, the magma set off a large-scale convective hydrothermal system, which induced pervasive

years. By contrast, Whelan et al. (2001) believe that the cooling time was several orders of magnitude longer, “on the order of tens-to-hundreds of thousand years”.

In order to put numeric constraints on the process of cooling, we performed mathematical modeling for the cooling of a tuff pile with characteristics similar to those of the Yucca Mountain’s Tiva Canyon tuff. Conservatively, we assumed that the 110 m-thick layer of hot ash (Topopah Spring tuff and Tiva Canyon tuffs combined) was deposited instantaneously (the geologic record indicates that in reality, the surface of the Topopah Spring tuff was cooled to relatively low temperatures before the deposition of the Tiva Canyon tuff).

The temperature of the freshly deposited tuffs was taken as $T_0 = 600^\circ\text{C}$. No credit was taken for air convection above the hot rocks or for their interaction with atmospheric precipitation. A series

montmorillonite clay (illite-smectite) and Na-zeolitic alteration of the rhyolitic tuffs, as well as the localized deposition of veins and irregular cavity fillings of fluorite, barite, quartz and calcite in the phreatic zone deep under Yucca Mountain. Adularia and albite replaced feldspar phenocrysts in some intervals (Warren et al., 1984). Silicic lavas in drill hole USW G2 were silicified; they contain abundant veins of drusy quartz and, locally, calcite and fluorite, and have undergone pervasive quartz-calcite-albite (\pm chlorite and pyrite) propilitic alteration (Caporuscio et al., 1982). The minimum lateral extent of this alteration is estimated as 20 km² (Spengler et al., 1981; Caporuscio et al., 1982; Bish, 1987).

Bish and Aronson (1993) studied the distribution and K/Ar ages of illite/smectite clay minerals from three boreholes in the vicinity of the proposed repository zone (USW G-1, G-2, and G-3/GU-3). They provided the following description of the inferred system:

The distribution of alteration minerals and the K/Ar ages of I/S [illite/smectite] in USW G-1 and G-2 (~10.4 my) are consistent with Timber Mountain moat volcanism as the major source of hydrothermal alteration, rather than caldera-forming main ash-sheet eruptions. The rocks at depth at Yucca Mountain were apparently altered in a hydrothermal outflow plume. The nature of schematic paleogeothermal gradients suggests that a rain-curtain effect existed in USW G-2 to about ~1067 m, below which there is an abrupt rise in temperature and then the thermal gradients appear essentially isothermal. The widespread distribution of volcanic centers in the area allows for the possibility that some of the alteration may have preceded the Timber Mountain volcanism, perhaps during Paintbrush volcanism, culminating with Timber Mountain volcanism, particularly the later stages, at 10-11 my. It is noteworthy, however, that the mineralogical data suggest that no hydrothermal alteration has occurred since the waning of Timber Mountain volcanism about 10 my ago. (p. 159).

Bish and Aronson noted a pronounced asymmetry of the system: "*...it is apparent that a significant thermal event has occurred in the northern end of Yucca Mountain but has not significantly affected the southern end*" (p. 153). A schematic presentation of the Timber Mountain event is given in Figure 3-8-6.

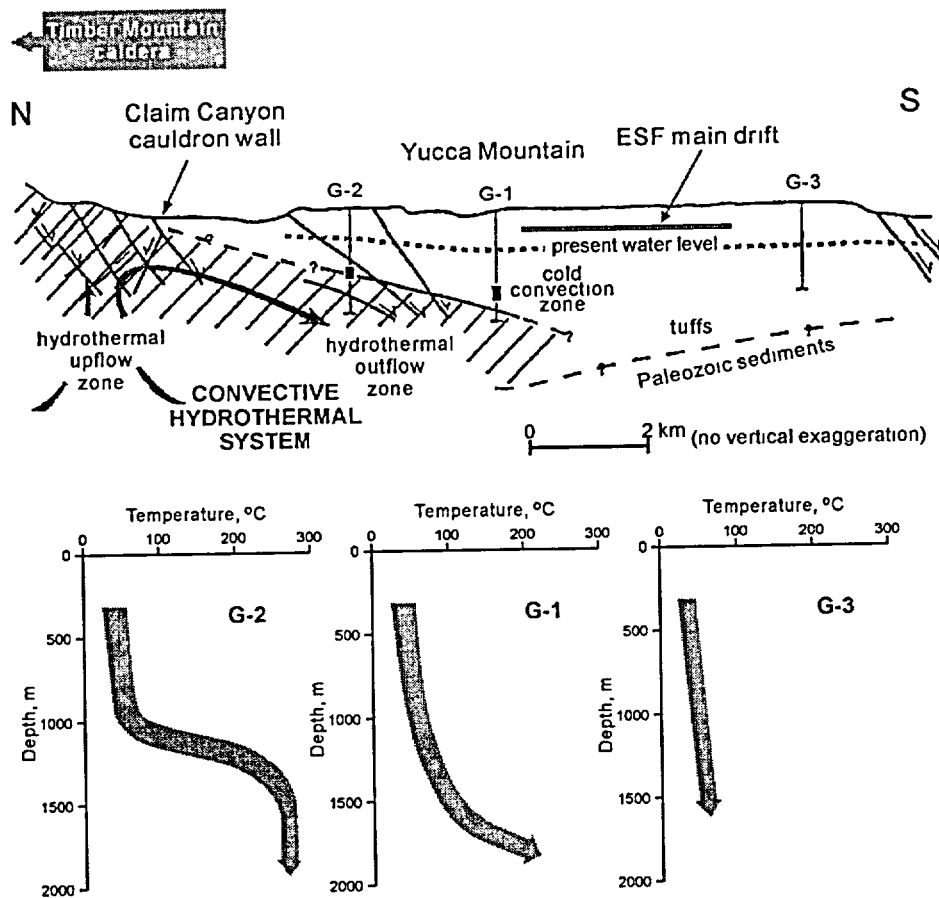


Figure 3-8-6. Reconstruction of the Timber Mountain hydrothermal circulation system near Yucca Mountain 10-11 Ma ago and schematic temperature profiles for boreholes USW G-1, G-2 and G-3 estimated from illite/smectite mineralogy and fluid inclusion data. Black rectangles on the upper plate indicate approximate depth at which the temperature of 100 °C was reached in boreholes G-2 and G-1. (Modified from Bish and Aronson, 1993).

The timing of the event is fairly well constrained on the basis of the K-Ar dating of clay minerals and zeolites. The data of Aronson and Bish (1987), WoldeGabriel (1991), and Bush and Aronson (1993) constrain the age of this alteration to 10.0-10.6 Ma (Figure 3-8-7) after which the source of heat was exhausted and the hydrothermal activity ceased. Weiss et al. (1994) concluded that the radiometric ages they obtained are "... consistent with alteration coeval with post-collapse volcanism and magmatic activity of the Timber Mountain II caldera to the north. These ages are 1.7 to 2.7 million years younger than the youngest altered unit and therefore cannot reflect diagenetic or deuteric water-rock interaction during cooling of the host units as suggested by Castor et al. (1992). Taken together, the age data, mineralogy and textural features are best interpreted as the result of a large, south-flowing hydrothermal system driven by heat from magmatic activity in the nearby Timber Mountain caldera system " (p. 23).

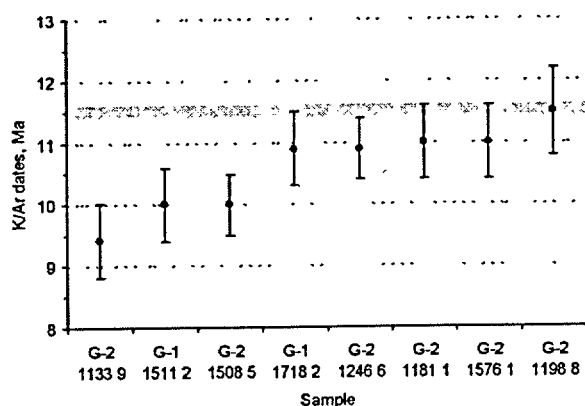


Figure 3-8-7. K/Ar dates for illite/smectite samples from Yucca Mountain (plotted by data of Bish and Aronson, 1993). For samples G-1 1511.2, G-2 1133.9, and G-2 1198.8, average values of two or three duplicate measurements are shown. *Gray line* indicates the time of eruption of the Rainier Mesa and the Ammonia Tank tuffs from the Timber Mountain caldera complex (11.6 and 11.45 Ma, respectively).

The paleo-geothermal reconstruction by Bish and Aronson (1993) presented in Figure 3-8-6 is revealing because it clearly shows the overall southward direction of the outflow from the vicinity of the Timber Mountain caldera. One shortcoming of this reconstruction is that the three boreholes used for the analysis are aligned to form the north-south transect and do not provide, therefore, information on the two-dimensional configuration of the temperature field. Below we present an attempt at constructing a paleo-temperature map of the Yucca Mountain area during the Timber Mountain Caldera thermal alteration event. Reconstruction of paleo-temperatures is based on two independent

mineralogical geothermometers, as graphically explained in Figure 3-8-8.

Figure 3-8-9 shows a reconstructed distribution of temperatures during the Timber Mountain Caldera hydrothermal event at a depth of 1 km beneath the modern topographic surface of Yucca Mountain. It is apparent from the figure that both geothermometers yield fairly consistent results and show the structure of the thermal field with a prominent high to the north and to the east of Yucca Mountain. For the purpose of this analysis, it is important to note that, within the proposed repository footprint, the temperatures at a 1 km-depth ranged between 85 and 135°C. This translates into heat flows (which is, the product of thermal gradient and thermal conductivity of the rock) ranging from 2.9 to 5.0 HFU and maximum temperatures at the ESF level (at a reference depth of ~250 m) of less than 45°C.

In addition we point out that the reliability of the thermal paleo reconstructions related to the Timber Mountain Caldera hydrothermal episode would have been greatly improved if, in addition to the mineralogic geothermometry, the fluid inclusion homogenization temperatures had been obtained. As of now, only seven measurements obtained from the deep-seated calcites have been published, with the homogenization temperatures ranging from 74 to 260 °C (U.S. DOE, 1993-b). The absence of systematic fluid inclusion data from the minerals related to the Timber Mountain Caldera hydrothermal episode represents a significant and unfortunate gap in the Yucca Mountain Project database, which adds to the ambiguity of the paleothermometric reconstructions.

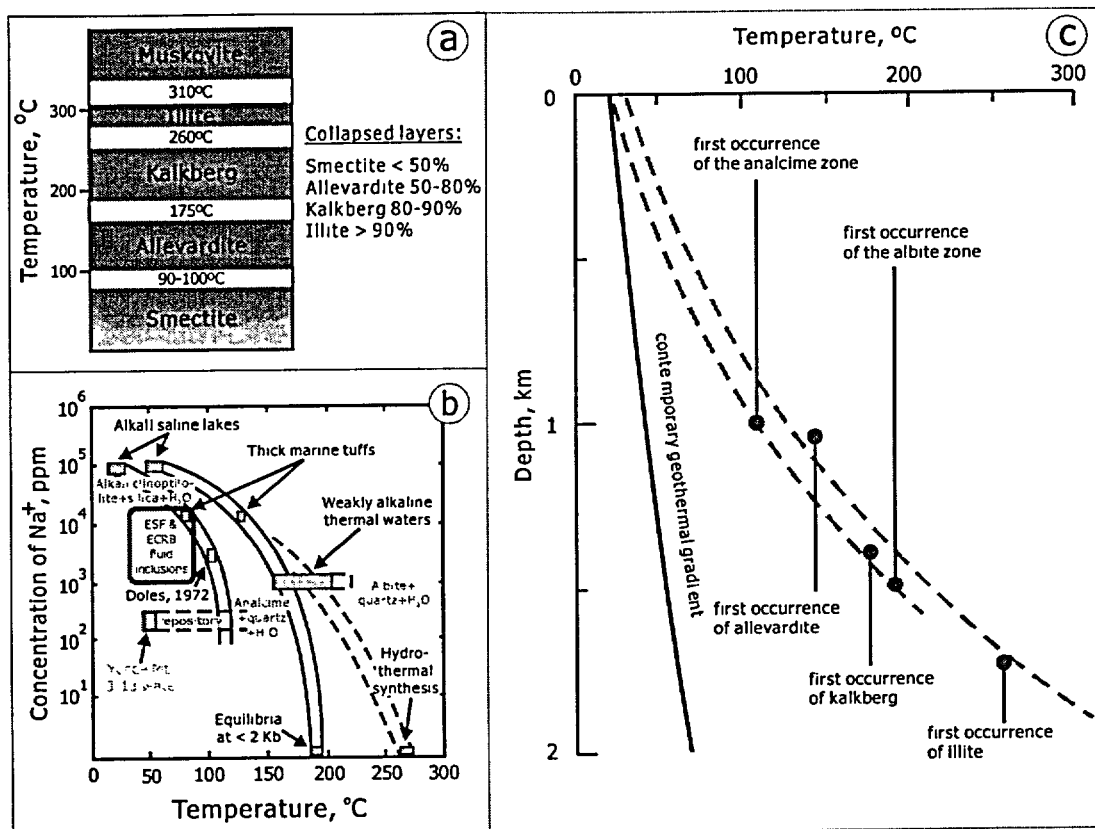


Figure 3-8-8. Explanation of the mineralogical thermometry based on zeolitic and illite-smectite alteration series.

a – Temperatures of transition in the illite-smectite series (modified from Bish, 1989). Smectite transforms into allevardite at ~90-100°C, the latter grades into kalkberg clay at ~175°C, which in turn transforms into illite at ~260°C. *b* – Evolution of zeolitic facies as a function of temperature and the Na⁺ concentration (modified from Smith and Caporuscio, 1981). Top of the analcime zone may be interpreted as having been formed at ~110°C; top of the albite zone – at ~130°C. Red rectangle shows parameters of waters that deposited secondary calcite in the ESF (fluid inclusion data from Dublyansky et al. 2001); *c* – Examples (schematic) of paleogeothermal gradients deduced from evolution of zeolitic (red) and illite-smectite (blue) alteration series in boreholes. Original data are from boreholes USW G-1 (zeolites) and USW G-2 (illite-smectite). Contemporary geothermal gradient is from borehole USW G-1.

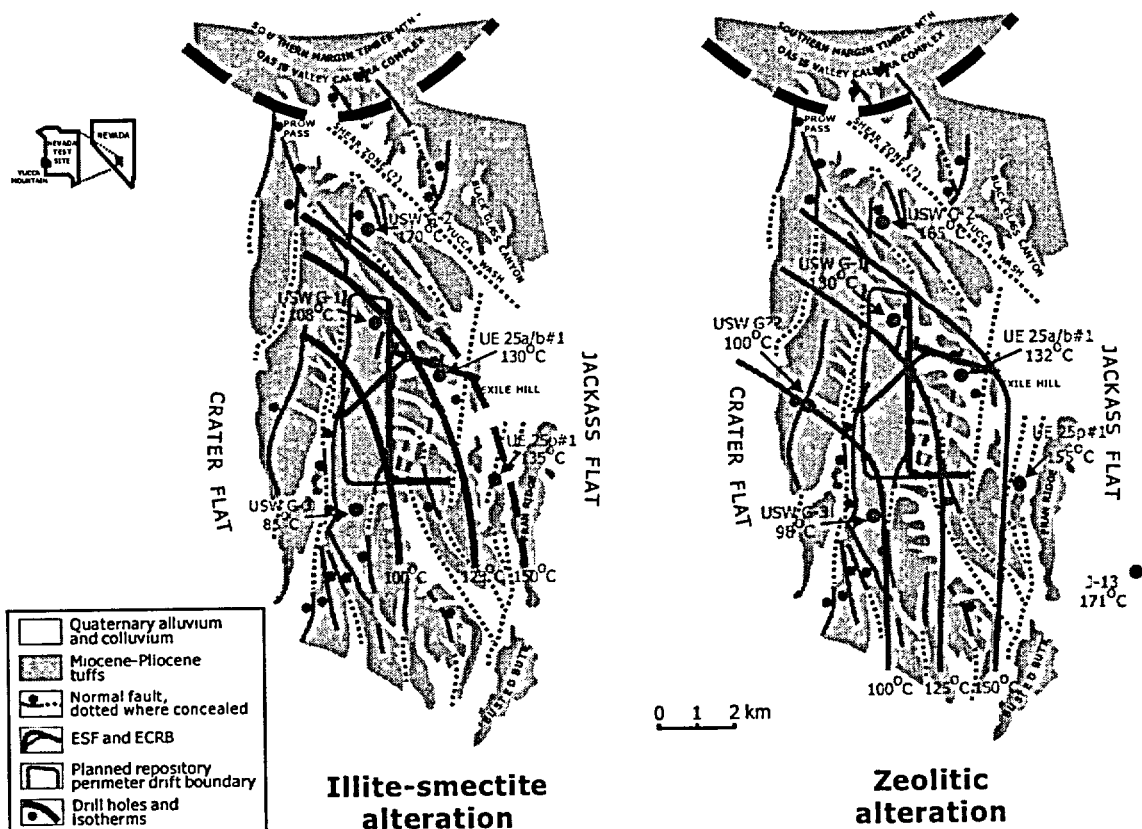


Figure 3-8-9. Reconstruction of the temperature at a depth of 1 km from modern land surface during alteration of the Yucca Mountain tuffs 10-11 million years ago.

Reconstruction is based on two independent mineralogical geothermometers: illite-smectite and zeolitic. K-Ar ages of 10-11 million years were reported for illite-smectite and zeolites from the boreholes used for this reconstruction by Aronson and Bish (1987) and WoldeGabriel (1991). Methodology of the thermometry is explained in Figure 3-8-8.

An attempt to quantify the temperatures that occurred at the ESF level during the Timber Mountain caldera event was made by Whelan et al. (2001). The authors modeled the temperatures along the ESF assuming a temperature at the water table of 100 °C and linear thermal gradients from the water table to the land surface. The results of the model calculations are shown in Figure 3-8-10.

In their analysis, Whelan with co-authors adopted a set of assumptions that, in our opinion, rendered their assessment totally unrealistic and unreliable. For example, they arbitrarily assigned the temperature at the water table a value of 100 °C (purportedly, in order to provide "an upper bound for the period of shallow hydrothermal activity"). There is, however, no geological data supporting such a high temperature at the water table during the Timber Mountain thermal event. To the contrary, the mineralogical data

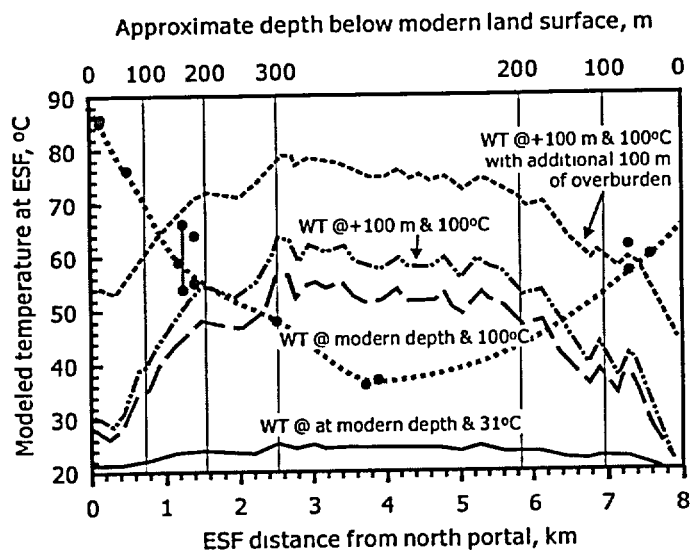


Figure 3-8-10. Modeled ESF temperatures (black lines; from Whelan et al. (2001) compared with the fluid inclusion homogenization temperatures measured in secondary minerals from the ESF (red dashed line and colored symbols).

Modeling assumptions: Thermal gradients are linear from water table (WT). Temperature at WT are fixed at either 31 °C (present conditions) or 100°C. Temperature at the land surface is 20°C. Calculations are also done for conditions of an elevated water table (+100 m) and for 100 m of overburden added uniformly to modern land surface. **Fluid inclusion data:** Dublyansky et al., 2001 (red symbols) and Whelan et al., 2001 (blue symbols)

discussed above indicate that the temperatures at the water table were well below 100 °C (see, for example, Figures 3-8-6 and 3-8-9).

If the temperature at the water table was indeed 100 °C, and if the water table were 100 m higher than it is today, and if the thickness of the overburden were 100 m greater than it is today (all of these assumptions were made by Whelan et al., 2001), nevertheless the computed temperatures at the ESF would not match the actual homogenization temperatures determined for fluid inclusions in the secondary minerals. This becomes obvious from a comparison of the results of the modeling of Whelan and co-authors with the fluid inclusion data reported by these authors in the same paper (Whelan et al., 2001) and by

Dublyansky et al. (2001). It is apparent from Figure 3-8-10 that measured fluid inclusion temperatures show an almost perfect inverse correlation with the modeled (calculated) paleo-temperatures. The calculated temperatures increase, as they should, with depth as the ESF tunnel approaches the heat source, which in this model is the water at the water table. In striking contrast, the measured fluid inclusion temperatures are the highest at the shallow parts of the ESF near the portals and lower in the deepest parts. Two conclusions may readily be drawn from the data presented in Figure 3-8-10. The first conclusion is that the involvement of hot waters of the Timber Mountain Caldera hydrothermal system (or, likewise, of any other heat source located underneath the Yucca Mountain tuffs) in the conductive heating of the vadose zone is clearly contradicted by the factual data. The second conclusion is that the concept of the conductive heating, *per se*, does not seem to offer a plausible explanation of the temperature distribution indicated by the fluid inclusions. Higher temperatures closer to the topographic surface and cooler temperatures at depth would require that the heat source be located at the topographic surface, which of course is not possible. The structure of the paleo-thermal field was discussed in section 3.6.4.5 of Chapter 3-6. Based on this discussion we concluded that the fluid inclusion thermometric data dictate that the heat

source must have been linear, located to the east of the ESF zone, and relatively short-lived. These features unequivocally point to a convective supply of heat transported by water moving through the high-permeability fault zone (Paintbrush fault) rather than to the conductive heating of the whole tectonic block of Yucca Mountain.

Summarizing our discussion of the Timber Mountain Caldera hydrothermal event we reiterate the major points. The event occurred between about 10 and 11 Ma ago and represented, under Yucca Mountain, a major out flowing plume. Mineralogical data indicate that values of heat flow in the planned repository area did not likely exceed 2.9 to 5.0 HFU and temperatures at the ESF level (reference depth of ~250 m) were less than approximately 45°C. Therefore, any minerals with an established temperature of formation in excess of 45°C and/or ages younger than ~10 Ma cannot be related to the Timber Mountain Caldera hydrothermal event.

3.8.3. Summary

It is apparent from the discussion above that secondary minerals sampled in the ESF cannot be related to either of the two thermal events that are known to have occurred at Yucca Mountain (both events are genetically related to silicic volcanism). The minerals in question are located some 700-900 m above rock horizons that are known to have been affected by the Timber Mountain outflow plume (some of the minerals were found within 30-50 m from the present-day topographic surface). We have demonstrated above that a hypothesis about the conductive heating of the bedrock tuff by thermal water, during the Timber Mountain caldera episode, could not have produced the requisite temperatures. (In this chapter we deliberately concentrate on only the temperatures and do not discuss other problems with the rainwater model. These other problems are discussed elsewhere in Part Three).

Part 3

References

Suitability of the Yucca Mountain Site to Accommodate a permanent
Repository for High-Level Radioactive Waste
and Spent Nuclear Fuel: an Independent Assessment

By

J.S. Szymanski,
Y.V. Dublyansky,
T.R. Harper,
S.Z. Smirnov,
S.E. Pashenko,
and
G.P. Palianova

References

A

- Aliev (1966) Aliev R. 1966 Ontogenetic studies of calcite crystals from Dashkesan iron-ore deposit. In: D.P. Grigoriev, ed., *Origin of mineral individuals and aggregates*. Moscow, Nauka. pp. 181-200.
- Allmendinger et al. (1987) Allmendinger, R. W., Hauge, T. A., Hauser, E.C., Potter, S. L., Klemperer, K. D., Nelson, K. D., Kneupfer, P, and Oliver, J. 1987 Overview of the COCORP 40 °N Transect, Western United States: The Fabric of an Orogenic Belt. *Geological Society of America Bulletin*, 98.
- Amundson et al. (1988) Amundson, R. G., Chadwick, O. A., Sowers, J. M., and Doner, H. E. 1988 Relationship between Climate and Vegetation and the Stable Carbon Isotope Chemistry of Soils in the Eastern Mojave Desert, Nevada. *Quaternary Research*, 29, pp. 245-254.
- Archambeau and Price (1991) Archambeau C.B. and Price, N.J. 1991 An assessment of J.S.Szymanski's Conceptual Hydro-Tectonic Model and Its Relevance to Hydrologic and Geologic Processes at the Proposed Yucca Mountain Nuclear Waste Repository. *Minority Report of the Special DOE Review Panel*. pp. 98-112.
- Atkinson (1977) Atkinson, T.C. 1977 Carbon dioxide in the atmosphere of the unsaturated zone: an important control of ground water hardness in limestones. *J Hydrol.*, 35, pp. 111-123.
- Atkinson et al. (1983) Atkinson, T.C., Smart, P.L., and Wigley, T.M.L. 1983 Climate and natural radon levels in Castleguard Cave, Columbia Icefields, Alberta, Canada *Arctic and Alpine Research*, 15, 4, pp. 487-502.

B

- Bak (1996) Bak, P. 1996 How nature works. New York: Copernicus. 212 p.
- Bak and Tang (1989) Bak, P. and Tang, C. 1989 Earthquakes as a Self-Organized Critical Phenomenon. *Journal of Geophysical Research*, 94., B11, pp. 15635-15637.
- Barnes et al. (1996) Barnes, C.M., James, J.M. and Whittlestone, S. 1996 Radon and its decay products in caves. *Helveticite*, 34(2). pp. 33-37.

- Barsukov and Borisov (1989) Barsukov, V.L. and Borisov, M.V. 1989 Inversion of solution acidity during the self-rebuilding of hydrothermal flow structure. *In: V.A. Zharikov, Ed Physico-chemical analysis of mineral-forming processes.* Moscow, Nauka, pp. 168-175. (*In Russian*)
- Bender (1981) Bender, M.M. 1971 Variations in the $^{13}\text{C}/^{12}\text{C}$ ratios of plants in relation to the pathway of photosynthetic carbon dioxide fixation. *Phytochemistry* 10, pp. 1239-1244.
- Benning et al., 2000 Benning L.G., Wilkin R.T., and Barnes H.L. 2000 Solubility and Stability of Zeolites in Aqueous Solutions: II. Calcic Clinoptilolite and Mordenite, *American Mineralogist*. 85. pp. 495-508.
- Benson and McKinley (1985) Benson, L. V. and McKinley, P. W. 1985 Chemical composition of ground water in the Yucca Mountain area, Nevada, 1971-84. *USGS, Open-file report, 85-484.*
- Bergna (1994) Bergna, E. 1994 The colloid chemistry of silica - an overview. *In: The colloid chemistry of silica. Ed: E. Bergna.* Washington, D.C., American Chemical Society, pp. 4-47.
- Bish (1989) Bish, D.L. 1989 Evaluation of past and future alterations in tuff at Yucca Mountain, Nevada based on clay mineralogy of drill cores USW G1, G2, and G3. *Los Alamos Natl Lab Report LA-10667-MS.* 41 p.
- Bish and Aronson (1993) Bish, D.L. and Aronson, J.L. 1993 Paleogeothermal and Paleohydrologic Conditions in Silicic Tuff from Yucca Mountain, Nevada. *Clays and Clay Minerals*. 41, 2, pp. 148-161.
- Bish and Chipera (1989) Bish, D.L. and Chipera, S.J. 1989 Revised Mineralogical summary on Yucca Mountain, Nevada. *Los Alamos Natl Lab Report 11497-MS.*
- Bish and Vaniman (1984) Bish, D.L. and Vaniman, D.T. 1985 Mineralogic Summary of Yucca Mountain, Nevada. *Los Alamos Natl Lab Rept. LA-10543-MS* 55 p.
- Blakely (1988) Blakely, R. J. 1988 Curie Temperature Isotherm Analysis and Tectonic Implications of Aeromagnetic Data from Nevada. *Journal of Geophysical Research*, 93.
- Blankenegel and Weir (1973) Blankenegel, R. K. and Weir, J.E. 1973 Geohydrology of the Eastern Part of Pahute Mesa, Nevada Test Site, Nye County, Nevada. *USGS Professional Paper 712-B*, Washington, DC.
- Blyth et al. (1998) Blyth, A.R., Frape, S.K., Blomqvist, R., and Nissinen, P. 1998 Combining fluid inclusion studies with isotopic investigations of fracture calcite to assess the past thermal and fluid history of the Olkiluoto research site, Finland. *GSA Abstracts with*

- Program*. Toronto, Canada. A-88.
- Bodvarsson et al. (1997) Bodvarsson, G. S., Bandurraga, T. M., and Wu, Y.S. 1997 The Site-Scale Unsaturated Zone Model of Yucca Mountain, Nevada, for the Viability Assessment. *LBNL-40376 #UC-814*, Berkeley, California: Lawrence Berkeley National Laboratory, MOL. 19971014.0232.
- Boles (1972) Boles, J. R. 1972. Composition, optical properties, cell dimensions and thermal stability of some heulandite group zeolites. *Am Miner.* 57, pp. 1463-1493.
- Bottrell (1991) Bottrell, S. 1991 Radon production and release from cave sediments. *Cave Science (UK)*. 18, 2, pp. 79-82.
- Bottyinga (1969) Bottyinga, Y. 1969 Calculated fractionation factors for carbon and hydrogen isotope exchange in the system calcite-carbon dioxide-graphite-methane-hydrogen-water vapor. *Geochim et Cosmochim Acta*, 33, pp. 49-64.
- Boughton (1986) Boughton, C. 1986 Integrated Geochemical and Hydraulic Analysis of the Nevada Test Site Groundwater Systems. *M. S Thesis, University of Nevada-Reno, Reno, Nevada*.
- Bredehoeft (1997) Bredehoeft, J.D. 1997 Fault permeability near Yucca Mountain. *Water Resources Research*. 33, 11. pp. 2459-2463.
- Brock ... (2000) Brock Biology of Microorganisms. Ninth Edition. Eds.: M.Mdigan, J.Martineo, and J. Parker. Prentice Hall. Upper Saddle River, NJ, 2000.
- Broxton et al. (1987) Broxton, D.E., Bish, D.L., and Warren, R.G. 1987 Distribution and chemistry of diagenetic minerals at Yucca Mountain, Nye County, Nevada. *Clay and Clay Minerals*, 35, 2, pp. 89-110.
- Bryxina and Sheplev (1997) Bryxina N. A. and Sheplev V. S. 1997 Oscillatory zoning in calcite growing from an aqueous solution. *Mathematical Modeling*, 9, pp. 32-38. *(In Russian)*
- Bryxina et al. (2000) Bryxina N.A., Dublyansky Y.V., Halden N.M., Campbell D.L. and Tysdale V.D. 2000 Statistic characteristics of rhythmic zonation of cave calcite - Hungarian popcorn. *Doklady RAS*, 372, pp. 514-517. *(In Russian)*
- Bukata et al. (1998) Bukata, A.R., Kotzer, T., and Cornett, R.J. 1998 Fracture-infilling calcite as a proxy for the paleohydrogeology of a fractured granitic gneiss, an integration of stable isotopes, fluid inclusions and U-series dating. *GSA Abstracts with Program*. Toronto, Canada. A-225.
- Burke (2001) Burke E. 2001 Raman microspectrometry of fluid inclusions. *Lithos*, 55, pp. 139-158.

C

-
- Cahn (1967) Cahn, J.W. (1967) On the morphological stability of growing crystals. *In: Crystal Growth*, H. S. Peiser (Ed.). Pergamon Press, Oxford.
- Caporuscio et al. (1982) Caporuscio, F., Vaniman, D.T., Bish, D.L., Broxton, D.E., Arney, D. Heiken, G., Byers, F.M., and Gooley, R. 1982 Petrographic studies of drill cores USW-G2 and UE25b-1H, Yucca Mountain, Nevada. *Los Alamos Natl. Lab Report LA-9255-MS* 114 p.
- Carbon... (1978) Carbon and its compounds in endogene processes of mineral formation (Based on the results of fluid inclusion studies in minerals). (G.N. Dolenko, G.M. Gigashvili, V.A. Kaliuzhnyi, and A.S. Schiritsa Eds). Kiev, Naukova Dumka PH. 171 p. (*In Russian*)
- Carlos (1987) Carlos, B. A. 1987 Minerals in Fractures of the Saturated Zone from Drill Core USW G-4, Yucca Mountain, Nye County, Nevada. *Los Alamos National Laboratory Report LA-10927* Los Alamos, New Mexico.
- Carlos et al. (1993) Carlos, B.A., Chipera, S.J., Bish, D.L., and Craven, S.J. 1993 Fracture-Lining Manganese Oxide Minerals in Silicic Tuff, Yucca Mountain, Nevada, USA. *Chemical Geology*. 107, 1-2, pp. 47-69.
- Carlos et al. (1995-a) Carlos B.A., Chipera S.J., and Bish D.L. 1995-a Distribution and Chemistry of Fracture-Lining Materials at Yucca Mountain, Nevada. *Los Alamos Natl Lab Report LA-12977-MS*, 92 p.
- Carlos et al. (1995-b) Carlos, B., Chipera, S.J., and Snow, M.G. 1995-b Multiple episodes of zeolite deposition in fractured silicic tuff. *A A Balkema Publishers 8th International Symposium on Water-Rock Interaction*. Vladivostok, Russia, August 13-28, 1995.
- Carr and Parish (1984) Carr, W.J. and Parish, L.D. 1984 Geology of Drill Hole USW VH-2, and Structure of Crater Flat, Southwestern Nevada. *USGS Open File Report 85-475*, Denver, CO.
- Carr et al. (1986) Carr, M. D., Waddell, S. J., Vick, G. S., Stock, J. M., Monsen, S. A., Harris, A. G., Cork, B. W., and Byers, F.M. 1986 A Test Hole into Pre-Tertiary Rocks Near Yucca Mountain, Southern Nevada. *USGS Open File Report 86-175*, Menlo Park, CA.
- Castor et al. (1989) Castor, S. B., Feldman, S. C., and Tingley, J V. 1989 Mineral Evaluation of the Yucca Mountain Addition, Nye County, Nevada. Nevada Bureau of Mines and Geology - Desert Research Institute, Reno, Nevada.
- Castor et al. (1999) Castor, S.B., Garside, L.J., Tingley, J.V., LaPointe, D.D., Desilets, M.O., Hsu, L.C., Goldstrand, P.M., Lugaski, T.P., and Ross, H.P. 1999 Assessment of metallic and

- mined energy resources in the Yucca Mountain Controlled Area, Nye County, Nevada. *Nevada Bureau of Mines and Geology Open-file Report 99-12*. 204 p.
- Cathlineau et al (1999) Cathlineau, M., Freiberger, R., Boiron, M.-C., Ayt Ougougdal, M., Cuney, M., Coulibaly, Y., Banks, D., Aranyossy, J.F., Virlogeux, D. and Leuth, Y. 1999 Reconstruction of paleofluid percolation in the Vienne granites: Evidence of fluid circulation restricted to major geodynamic events (abs.); in Luders, V.; Schmidt-Mumm, A.; and Thomas, R (eds.) *Abstracts of ECROFI XV Conference*. Potsdam, June 21-24, 1999, pp. 63-65.
- Cerling (1984) Cerling, T.E. 1984 The stable isotopic composition of soil carbonate and its relationship to climate. *Earth and Planetary Science Letters* 71, pp. 229-240.
- Chafetz and Lawrence (1994) Chafetz, H. and Lawrence, R. 1994 Stable Isotopic Variability within Modern Travertines *Geographie physique et Quaternaire*. 48, 3, pp. 257-273.
- Chatterjee et al. (1975) Chatterjee, A., Kerker, M., and Cooke, D.D. 1975 Brownian coagulation of Aerosols in the Transition Regime. *J Coll and Inter. Science*. 53, 1, pp. 71-78.
- Chebotarev (1955) Chebotarev, I.I. 1955 Metamorphism of Natural Waters in the Crust of Weathering. *Geochimica et Cosmochimica Acta*, 8.
- Chepizhko and Dublyansky (1995) Chepizhko, A. and Dublyansky, Y. 1995 Accessory minerals from bedrock tuffs, mosaic breccias and calcite/opal veins at Yucca Mountain (Feasibility Study). *Report submitted to the Nuclear waste project office State of Nevada*, 139 p.
- Chepizhko et al. (1998) Chepizhko, A. Dublyansky, Y., and Lapin, B., 1998 Ontogenetic studies of accessory minerals at Yucca Mountain, Nevada, and the ascending vs. descending water controversy. *GSA Abstracts with Program*, Toronto, Canada.
- Cherdintsev (1969) Cherdintsev, V.V. 1969 Uranium-234. Moscow, Atomizdat. (*In Russian*)
- Chernov et al. (1980) Chernov, A.A., Givargizov, E.I., Bagdasarov, Kh. S., Kuznetsov, V.A., Demyanets, L.N., and Lobachev, A.N. 1980 Modern crystallography. Moscow, Nauka 407 p.
- Chesnokov (1966) Chesnokov, B. V. 1966 Morphological method for determination of relative age of minerals. *In: The genesis of mineral individuals and aggregates (ontogeny of minerals)*, Ed. D.P. Grigoryev, Moscow, Nauka, pp. 9-24.
- Chipera and Bish (1997) Chipera, S. J. and Bish, D. L. 1997 Thermodynamic Modeling of Zeolite Stability. 11th International Clay Conference, Ottawa, Ontario, Canada., June 15-21, 1997.
- Choquette (1968) Choquette, P.W. 1968 Marine Diagenesis of shallow marine lime-mud sediments: Insights from O¹⁸ and C¹³ data. *Science*, 161, pp. 1130-1132.

- Chrustschoff (1887) Chrustschoff, K. 1887 Über gelungene Versuche zur Darstellung des Quarzes auf nassem und des Tridymit auf trockenem Wege. *N Jb Min* 1.
- Chukhrov (1955) Chukhrov, F.V. 1955 Colloids in the Earth crust. Moscow, Academy of Sciences of the USSR Press. 672 p.
- Clouds ... (1989) Clouds and cloudy atmosphere. Reference book. 1989 I.P. Mazin, A.Kh. Khrigian, Eds. Gidrometeoizdat, Leningrad. (*In Russian*)
- Cohon (1998) Cohon, J.L. 1998 Letter of the Chairman of the U.S. NWTRB J.L. Cohon to Acting Director of the U.S. DOE Office of Civilian Radioactive Waste Management Lake Barrett. July 24, 1998, p. 2.
- Coplen et al. (1994) Coplen, T. B., Winograd, I. J., Landwehr, J. M., and Riggs, A. C. 1994 500,000-Year Stable Carbon Isotopic Record from Devils Hole, Nevada. *Science*, 263. pp. 361-365.
- Craig (1953) Craig, H. 1953 The Geochemistry of the stable carbon isotopes. *Geochim et Cosmochim Acta*, 3. pp. 53-92.
- Cunningham and LaRock (1991) Cunningham, K.I. and LaRock, E.J. 1991 Recognition of microclimate zones through radon mapping, Lechuguilla Cave, Carlsbad Caverns National Park, New Mexico. *Health Physics*, 61, 4, pp. 493-500.

D

- Daniel and Gillespie (1981) Daniel, T. and Gillespie, A. 1981 A stochastic analysis of the homogeneous nucleation of vapor condensation. *J Chem Phys*. 74, 1, pp. 661-678.
- Davies and Archambeau (1997) Davies, J. B.; Archambeau, C. B. 1997 Geohydrological models and earthquake effects at Yucca Mountain, Nevada. *Environmental Geology*, 32(1). pp. 23-25.
- Davis and De Wiest (1966) Davis, S.N. and De Wiest, J.M. 1966 Hydrogeology. John Wiley and Sons, Inc. New York-London-Sydney.
- Deines (1980) Deines, P. 1980 The isotopic composition of reduced organic carbon. *In*: P. Fritz and J.Ch. Fontes (Eds.) Handbook of Environmental Isotope Geochemistry, 1. The Terrestrial Environment, A. Elsevier, Amsterdam, pp. 329-406.
- Denniston et al. (1997) Denniston, R.F., Shearer, C.K., Layne, G.D., and Vaniman, D.T. 1997 SIMS analyses of minor and trace element distribution in fracture calcite from Yucca Mountain, Nevada, USA. *Geochim et Cosmochim Acta*. 61, 9, pp. 1803-1818.
- Devison (1951) Devison, B. 1951 Influence of a black sphere and of black cylinder upon the neutron density in an infinity non capturing medium. *Proc Phys Soc A* 64, pp. 981-992

- density in an infinity non-capturing medium. *Proc. Phys. Soc. A.* 64, pp. 881-902.
- Dolidze et al. (1975) Dolidze, N.I., Zverev, V.Y., Spiridonov, A.I. et al. 1975 Notes of the Academy of Sciences of Georgia. 78, 2, p 385.
- Donaldson (1979) Donaldson, C.H. 1979 An experimental investigation of the delay in nucleation of Olivine in mafic magmas. *Contrib. Mineral. Petrol.*, 69, 21-32.
- Donovan et al. (1974) Donovan, T.J., Friedman, I., Gleason, J.D. 1974 Recognition of petroleum-bearing traps by unusual isotopic compositions of carbonate-cemented surface rocks. *Geology*, 2, pp. 351-354.
- Dublyansky (1994-a) Dublyansky Y. V. 1994-a Paleotemperature Environment at Yucca Mountain, Nevada (Status Report). Annual Report-Nevada, Submitted to the Nuclear Waste Project Office of the State of Nevada.
- Dublyansky (1994-b) Dublyansky, Y.V. 1994-b Dialogs by Yuri V. Dublyansky regarding "Fluid Inclusion Studies of Calcite Veins From Yucca Mountain, Nevada, Tuffs: Environment of Formation". *TRAC Special Report No. 15* submitted to the Nuclear Waste Project Office State of Nevada, July, 1994, 61 pp.
- Dublyansky (1998-a) Dublyansky, Y. 1998-a Fluid inclusion studies of samples from the Exploratory Studies Facility, Yucca Mountain, Nevada. *Institute for Energy and Environmental Research*, Dec. 1998, 49 p. + Appendices.
- Dublyansky (1998-b) Dublyansky, Y. 1998-b Traces of epigenetic hydrothermal activity in the Yucca Mountain volcanic tuffs: Fluid inclusion and gas chemistry evidence. *Abst. 7th PACROFI Meeting*, Las Vegas, Nevada, 1-4 June, 1998 (no pages)
- Dublyansky (1999) Dublyansky, Y. 1999 Fluid Inclusions in Calcite from the ESF, Yucca Mountain, Nevada: Evidence of Saturated Environments and Elevated Temperatures. *Supplement to EOS*, April 27, 1999. p. S4.
- Dublyansky (2001-a) Dublyansky, Y.V. 2001 Environment of deposition suggested by all-gas inclusions and stable isotopes in secondary minerals from Yucca Mountain, Nevada, USA. in: F. Noronha and A. Guedes, Eds. XVI ECROFI Faculdade de Ciencias do Porto, Departamento de Geologia, Memoria no. 7, pp. 131-134.
- Dublyansky (2001-b) Dublyansky Y.V. 2001 Paleohydrology at Yucca Mountain by coupled stable isotopic and fluid inclusion studies of secondary minerals. Report Submitted to the Agency for Nuclear Projects, State of Nevada, May 2001. Part II. 80 p + Appendices.
- Dublyansky (2001-c) Dublyansky Y.V. 2001 Stable Isotope and Chemistry Data on the Carbonate-Opal Surface Deposits in the Solitario Canyon, Yucca Mountain, Nevada. Report

- Surface Deposits in the Solitario Canyon, Yucca Mountain, Nevada Report Submitted to the Agency for Nuclear Projects, State of Nevada, June 2001. 36 p + Appendices.
- Dublyansky (2002) Dublyansky Y.V. 2002 Extreme crystal-scale variability of $\delta^{13}\text{C}$ in hydrothermal calcite from Yucca Mountain, Nevada. *2002 International Goldschmidt Conference on Geochemistry*. Zurich, 14-25 August 2002.
- Dublyansky and Lapin (1996) Dublyansky, Y. V. and Lapin, B.N. 1996 Bedrock Tuffs, Mosaic Breccias, and Young Volcanic Rocks at Yucca Mountain: Field Observations, Petrography, and Chemistry. *In: TRAC-NA Final Report, Research Conducted During FY' 92 through FY' 95, Submitted to the Nuclear Waste Project Office of the State of Nevada.*
- Dublyansky and Mazurova (2000) Dublyansky, Y. and Mazurova, S. 2000 Stable isotopes and fluid inclusions in calcite-opal-fluorite crusts from Yucca Mountain, Nevada, USA. *GSA Abstracts with Program*. 32, 7. p. A-259
- Dublyansky and Reutsky (1995) Dublyansky, Y. and Reutsky, V. 1995 Preliminary Data on Fluid Inclusions in Epigenetic Minerals from Tunnel Excavated under Yucca Mountain. *TRAC Report to the Nuclear Waste Project Office, State of Nevada*. 78 pp.
- Dublyansky and Reutsky (1998) Dublyansky, Y. and Reutsky, V. 1998 Epigenetic Quartz-Opal-Calcite Crusts in the Yucca Mountain Subsurface: Fluid Inclusion and Stable Isotopic Evidence of Hydrothermal Origin. *GSA Abstracts with Program*, Toronto, Canada.
- Dublyansky and Smirnov (1999) Dublyansky, Y. and Smirnov, S. 1999 Ontogenetic Observations on the Scepter-like Calcite and Hyalite Opal from the ESF, Yucca Mountain, Nevada: Evidence of Depositional Environment. *Supplement to EOS*, April 27, 1999. p. S8.
- Dublyansky et al. (1996-a) Dublyansky, Y., Reutsky, V., and Shugurova, N. 1996-a Fluid Inclusions in Calcite from the Yucca Mountain Exploratory Tunnel. *In: Brown, P. E.; Hageman, S. G., (eds.), Proceedings of the VI PACROFI Conference*. Madison, Wisconsin, USA. pp. 38-39.
- Dublyansky et al. (1996-b) Dublyansky, Y., Shugurova, N., and Reutsky, V. 1996-b Preliminary Data on Gases Trapped in Fluid Inclusions in Calcite from the Yucca Mountain Exploratory Tunnel. *GSA Abstracts with Program*, Denver, Colorado, USA. 28, 7. p. A-522.
- Dublyansky et al. (1998) Dublyansky, Y., Szymanski, J., Chepizhko, A., Lapin, B., and Reutsky, V. 1998 Geological History of Yucca Mountain (Nevada) and the Problem of a High-Level Nuclear Waste Repository. *In: M.J. Stenhouse and V.I. Kirko (Eds.) Defence Nuclear Waste Disposal in Russia*. NATO ASI Series. Kluwer Academic Publishers,

- The Netherlands. pp. 279-292.
- Dublyansky et al. (1999) Dublyansky, Y., Szymanski, J., Chepizhko, A., Lapin, B., and Reutsky, V. 1999 Paleohydrology of Yucca Mountain (Nevada, USA): A key to the assessment of the suitability of the proposed radioactive waste disposal site. *Geoecology*. 1, pp. 77-87. (In Russian)
- Dublyansky et al. (2001) Dublyansky, Y., Ford, D., and Reutski, V. 2001 Traces of epigenetic hydrothermal activity at Yucca Mountain, Nevada: preliminary data on the fluid inclusion and stable isotope evidence. *Chemical Geology*. 173, pp. 125-149.
- Dudley et al. (1971) Dudley, W.W., Wollitz, L.E., Baldwin, D.A., and Claassen, H.C. 1971 Geologic and Hydrologic Effects of the Handley Event, Pahute Mesa, Nevada Test Site (Effects on Wells and Aquifers). *USGS Open File Report, 95-474*, Denver, CO.

E

- Ebinger (1992) Ebinger, M.H. 1992 Water-rock interactions and the pH stability of groundwaters from Yucca Mountain, Nevada, USA. *Water-Rock Interaction*. Kharaka & Maest (eds). Balkema, Rotterdam. pp. 783-786.
- Ebler (1911) Ebler, E. 1911 Über die Adsorption radioactiver Stoffe durch kolloide Kieselsäure. *Kolloids*, 9.
- Eckert and Drake (1959) Eckert, E. and Drake, R. 1959 Introduction to the transfer of heat and mass.
- Ellis and Mahon (1977) Ellis, A.J. and Mahon, W.A.J. 1977 Chemistry and Geothermal Systems. Academic Press, New York, San Francisco, London.
- Else et al. (1999) Else, T.A.L., Pantle, C., Amy, P.S., Dublyansky, Y., Southam, G., and Mielke, R. 1999 Moderately Thermophilic, Calcium-Precipitating Bacteria Found in Calcite Deposits at Yucca Mountain. *American Society of Microbiology 99th General Meeting*. Chicago, IL, May 31, 1999. p. 448.
- Ermolaev et al. (1965) Ermolaev, N.P., Zhidkova, A.P., Zarinski, V.A. 1965 Transport of uranium in aqueous solutions in the form of complex silicate ions. *Geochemistry International*, 2, pp. 629-640.

F

- Fabryka-Martin et al. (2000) Fabryka-Martin, J. Meijer, A., Marshall, B., Neymark, L., Paces, J., Whelan, J., and Yang, A. 2000 Analysis of Geochemical Data from the Unsaturated Zone. *ANL-*

- NBS-HS-000017, Rev. 00.* 156 p.
- Faiia et al. (2000). Faiia, A.M., Aronson, J.L., Feng, X., and WoldeGabriel, G. 2000 K/Ar in Clinoptilolite: K variability and rock permeability. *GSA Abstracts with Program*, **32**, 7.
- Faure (1986) Faure, G. 1986 Principles of Isotope Geology. Second Edition. John Wiley & Sons. New York. 589 p
- Fauver (1987) Fauver, D.N. 1987 Survey of Radon and Radon Daughter Concentrations in Selected Rainier Mesa Tunnels. *DOE/NV 10327-31*.
- Feng et al, 1999 Feng, X., Faiia, A., WoldeGabriel, G., Aronson, J.L., Poage, M.A., Chamberlain, C.P. 1999 Oxygen isotope studies of illite/smectite and clinoptilolite from Yucca mountain: implication for paleohydrologic conditions. *Earth and Planetary Science Letters*, **171**, 95-106.
- Fhrohlich (1994) Fhrohlich, C. 1994 Earthquakes with Non-Double Couple Mechanisms. *Science*, **264**.
- Fleischer (1988) Fleischer, R.L. 1988 Alpha-recoil damage: Relation to isotopic disequilibrium and leaching of radionuclides. *Geochim. et cosmochim Acta*. **52**, 6, pp. 1458-1466.
- Fontes (1980) Fontes, J.Ch. 1980 Environmental isotopes in groundwater hydrology. In: P. Fritz and J.Ch. Fontes, Eds. *Handbook of Environmental Isotope Geochemistry, 1. The Terrestrial Environment, A* Elsevier, Amsterdam, pp. 75-140.
- Forester et al. (1998) Forester, R.M., Bradbury, J.P., Carter, C., Elvidge-Tuma, A.B., Hemphill, M.L., Lundstrom, S C., Mahan, S.A., Marshall, B.D., Neymark, L.A., Paces, J.B., Sharpe, S.E., Whelan, J.F., and Wigand, P.E. 1998 The Climatic and Hydrologic History of Southern Nevada During the Quaternary. *USGS Open File Report, 98-635*, Denver, CO.
- Frenkel (1975) Frenkel, J.I. 1975 Kinetic theory of liquids. Nauka, Leningrad. (*In Russian*)
- Fridrich et al. (1994) Fridrich, C.J., Dudley, W.W., and Stuckless, J.S. 1994 Hydrogeologic analysis of the saturated-zone ground-water system *J Hydrol.* **154**, pp. 133-168.
- Friedman (1970) Friedman, I. 1970 Some Investigations of the Deposition of Travertine from Hot Springs. – I. The isotopic chemistry of a travertine-depositing spring. *Geochim. et Cosmochim Acta*. **34**. pp. 1303-1315.
- Friedman and O'Neil (1977) Friedman, I. and O'Neil, J.R. 1977 Compilation of stable isotope fractionation factors of geochemical interest. In: M. Fleischer, ed., Data of Geochemistry, sixth ed., Chapter KK, U.S. Geol. Survey Prof. Paper 440-KK, 12 pp. and 49 figures.

- Fritz (1965) Fritz, P. 1965 Composizione isotopica dell'ossigeno e del carbonio nei travertini della Toscana. *Boll Geofis. Teor. Applic* 7, 25.
- Frolov (1976) Frolov, N.M. 1976 Hydrogeothermia. Nedra, Moscow. 280 p. (*In Russian*)
- Fuex (1977) Fuex, A.N. 1977 The use of stable isotopes in hydrocarbon exploration. *J. Geochem Exploration* 7, 2, pp. 155-188.

G

- Garrels and Christ (1965) Garrels, R. M. and Christ, C. L. 1965 Solutions, Minerals, and Equilibria. Harper and Row, New York, N.Y.
- Garside (1994) Garside, L.J. 1994 Nevada Low-Temperature Geothermal Resource Assessment: 1994. *Final Report Nevada Bureau of Mines and Geology OF 94-2*. 118 p.
- Gascoyne (1992) Gascoyne, M. 1992 Geochemistry of actinides and their daughters. *In: Ivanovich, M., and Harmon, R.S. (Eds) Uranium-series disequilibrium: Applications to Earth, Marine and Environmental Sciences, Second ed., Clarendon Press, Oxford, UK.* p. 34-61.
- Gilbert (1875) Gilbert, G.K. 1875 Report on the geology of portions of Nevada, Utah, California, and Arizona. *US Geol Surveys W 100th Mer.*, 3, pp. 17-178.
- Glikin and Petrov (1966) Glikin A.E. and Petrov T.G. 1966 Experimental investigation of growth forms of fluorite in hydrothermal conditions. *Mineralogical digest of Lvov University*. 20, 3, pp. 443 - 446. (*In Russian*)
- Glossary of Geology (1972) Glossary of Geology 1972 M. Gary, R. McAfee (J), and C.L. Wolf (Eds.) American Geological Institute, Washington, D.C.
- Godovikov et al. (1987) Godovikov, A. A., Rippinen, O. I. and Motorin, S. G. 1987. *Agates*. Moscow, Nedra, 368 p.
- Goldstein (2001) Goldstein, R.H. 2001 Fluid inclusions in sedimentary and diagenetic systems. *Lithos* 55, pp. 159-193.
- Goldstein and Reynolds (1994) Goldstein, R. and Reynolds, J. 1994 Systematics of fluid inclusions in diagenetic minerals. *SEPM Short Course*, 31. 199. p.
- Gonfiantini et al. (1968) Gonfiantini, R., Panici, C., and Tongiorgi, E. 1968 Isotopic Disequilibrium in Travertine Deposition. *Earth and Planetary Science Letters* 5. pp. 55-58.
- Gorrell (1958) Gorrell, H.A. 1958 Classification of Formation Waters Based on Sodium Chloride Content. *Bull. Amer. Assoc. Petrol Geologists*, 42.

- Gottardi and Galli (1985) Gottardi, G. and Galli, E. 1985. Natural zeolites. Berlin, Heidelberg, New-York, Tokyo, Springer-Verlag, 409 p.
- Graetsch (1994) Graetsch H. 1994 Structural characteristics of opaline and microcrystalline silica minerals. In: P.J. Heaney, C.T. Prewitt, G.V. Gibbs, Eds. *Silica Physical behavior, geochemistry and material applications*. Reviews in Mineralogy, **29**, pp. 209-232.
- Graton (1933) Graton, L.C. 1933 The depth zones in ore deposition. *Econ Geol.* **28**, pp. 513-555.
- Graves (1998) Graves, R.P., 1998 Water levels in the Yucca Mountain area, Nevada, 1996. *U.S. Geol. Survey Open-File Report 98-169*.
- Green (1959) Green, J. 1959 Geochemical table of elements for 1959. *Geol. Soc. Amer. Bull.* **70**. pp. 1127-1184.
- Grigoriev (1961) Grigoriev D.P. 1961 Ontogenesis of minerals Lvov, Lvov University Press. 315 p. (*In Russian*).
- Grigoriev and Zhabin (1975) Grigoriev, D.P., and Zhabin, A.G. 1975 *Ontogenesis of minerals*. Moscow, Nauka. 337 p. (*In Russian*).
- Grow et al. (1994) Grow, J., Barker, C., and Harris, H. 1994 Oil and gas exploration near Yucca Mountain, Southern Nevada. *High-Level Radioactive Waste Management*. Proc. Int. Con., Amer. Nucl. Soc., La Grande Park, Illinois. pp. 1298-1315.
- Gunn, et al. (1990) Gunn, J., Fletcher, S., and Prime, D. 1990 Research on radon in British limestone caves and mines, 1970-1990. *Cave Science (UK)*, **18**, 2, pp. 63-65.
- Guthrie et al. (1995) Guthrie, G.D. (Jr), Raymond, R. (Jr), and Chipera, S. 1995 Eolian-deposited minerals around drill hole USW SD-9, Yucca Mountain, Nevada. *Proc. Int. Con., Amer. Nucl. Soc. "High-Level Radioactive Waste Management"*. La Grande Park, Illinois. pp 135-136.

H

- Halden (1996) Halden N. M. 1996 Determination of Lyapunov exponents to characterize the oscillatory distribution of trace elements in minerals. *Can Mineral.* **34**, pp. 1127-1135.
- Halden and Hawthorne (1993) Halden N. M. and Hawthorne F. C. 1993 The fractal geometry of oscillatory zoning in crystals: Application to zircon. *Am Mineral* **78**, pp. 1113-1116
- Hanks et al. (1999) Hanks, T.S., Winograd, I.J., Anderson, E.R., Reilly, T.E., and Weeks, E.P. 1999 Yucca Mountain as a Radioactive-Waste Repository. A Report to the Director, U.S.

- Geological Survey. *Circular 1184*. 19 p
- Hanson et al. (1987) Hanson, G. N., Baker, V.R., Bethke, P.M., Hudleston, P.J., and Roquemore, G.R. 1987 Report of the Peer Review Panel on the Proposed Program of Studies of the Calcite and Opaline-Silica Deposits in the Yucca Mountain Area, Nevada. U.S. Department of Energy, Las Vegas, Nevada.
- Harmon (1993) Harmon, R. S. 1993 Isotopic and Fluid Inclusion Study of Yucca Mountain Samples. TRAC-NA Quarterly Report No.6. Submitted to the Nuclear Waste Project Office of the State of Nevada.
- Haskell and McKeever (1994) Haskell, E. H. and McKeever, S.W.S. 1994 Determination of Historical Thermal Gradients and Dates of Calcite Formation Using Thermoluminescence, Optically Stimulated Luminescence and Electron Spin Resonance Analysis of Minerals Removed from Excavated and Cored Samples at Yucca Mountain: *Interim Progress Report*, Submitted to the Nuclear Waste Project Office of the State of Nevada.
- Haukwa et al. (1998) Haukwa, C., Wu, Y.S., Hinds, J.J., Zhang, W., Ritcey, A.C., Pan, L.H., Simmons, A.M., and Bodvarsson, G.S. 1998 Results of Sensitivity Studies of Thermo-Hydrologic Behavior Conducted on Hydrologic Parameter Sets. *Yucca Mountain Project Level 4 Milestone Report SP3CK5M4*. Lawrence Berkeley National Laboratory, Berkeley, CA.
- Hay (1978) Hay, R. L. 1978 Geologic occurrences of zeolites. In Natural zeolites. Ed: L. B. Sand and F. A. Mumpton. Oxford, Pergamon Press, 135-144.
- Hay et al. (1986) Hay, R.L., Pexon, R.E., Teague, T.T., and Kyser, T.K. 1986 Spring-Related Carbonate Rocks, Mg Clays, and Associated Minerals in Pliocene Deposits of the Amargosa Desert, Nevada and California. *Geological Society of American Bulletin*, 97. pp. 1488-1503.
- Hearn et al. (1990) Hearn, T., Beghoul, N., and Barazangi, M. 1990 First Tomographic Study of Western U. S. - Completed Transactions. *EOS*, American Geophysical Union, 71, 36.
- Heiken et al. (1996) Heiken, G., Woldegabriel, G., Morley, R., Plannerer, H., and Rowley, J. 1996 Disposition of Excess Weapon Plutonium in Deep Boreholes. Site Selection Handbook. *LA-13168-MS*. 48 p.
- Helz and Holland (1969) Helz, G.R. and Holland, H.D. 1969 The solubility and geologic occurrence of strontianite. *Geochim et Cosmochim Acta*, 29, pp. 1303-1315.
- Henish (1970) Henish H.K. 1970 Crystal growth in gels The Pennsylvania State University Press, University Park and London // 1973 Russian translation, Moscow, Mir, 112 p

- University Park and London // 1973 Russian translation, Moscow, Mir, 112 p.
- Hickman et al. (1994) Hickman, S., Sibson, S., and R. Brune 1994 Proceedings of Workshop LXIII, the Mechanical Involvement of Fluids in Faulting. *USGS Open-File Report 94-228*, Menlo Park, CA.
- Hill and Dublyansky (1999) Hill, C.A. and Dublyansky, Y.V. 1999 Response to Stuckless and others (1998) on "Overview of calcite/opal deposits at or near the proposed high-level nuclear waste site, Yucca Mountain, Nevada, USA: Pedogenic, hypogene, or both?" *Environmental Geology* 38, 1, pp. 77-81.
- Hill and Forti (1997-a) Hill C. and Forti P. 1997 (Eds.) *Cave minerals of the World*. National Speleological Society.
- Hill and Forti (1997-b) Hill, C.A. and Forti, P. 1997 Monocrystalline and macrocrystalline speleothems. In C. Hill and P. Forti, Eds. *Cave minerals of the world*. Second edition. National speleological society. p 463.
- Hill and Livingston (1993) Hill C.A. and Livingston D.E. 1993 Chemical analyses of rocks, minerals and detritus, Yucca Mountains—Preliminary report *TRAC Special Report No 11* Submitted to the State of Nevada Nuclear Waste Project Office.
- Hill et al. (1995) Hill, C.A., Dublyansky, Y.V., Harmon, R., Schluter, C. 1995 Overview of calcite/opal deposits at or near the proposed high-level nuclear waste site, Yucca Mountain, Nevada: pedogenic, hypogene, or both? *Environmental Geology*, 26, 1, pp. 69-88.
- Hoefs (1980) Hoefs, J. 1980 Stable Isotope Geochemistry. Second, Completely Revised and Updated Edition. Springer-Verlag. Berlin Heidelberg New York.
- Hoefs (1987) Hoefs, J. 1987 Stable Isotope Geochemistry. Springer-Verlag, Berlin, Heidelberg, New York, London, Paris, Tokyo.
- Holloway et al. (1989) Holloway, R.W, Carilli, J.T., Faller, S.H., Chung-King Liu, and Kuroda, P.R. 1989 Thorium-230 Dating of Thermal Waters in the Vicinity of the Nevada Test Site. *Journal of Radioanalytical and Nuclear Chemistry*, 131, 2.
- Holmes (1928) Holmes, A. 1928 The nomenclature of petrology. N.Y., D. Van Nostrand Co., Inc. 284 p.
- Holten et al. (2000) Holten, T., Jamtveit, B., and Meakin, P. 2000 Noise and oscillatory zoning of minerals. *Geochim et Cosmochim. Acta* 64, 11, pp. 1893–1904.
- Hower and Altaner (1983) Hower, J. and Altaner, S. P. 1983 The petrologic significance of illite/smectite. In *Program, Abstracts*, 20th Annual Meeting of Clay Minerals Society, Buffalo, NY,

I

-
- Ikornikova (1975) Ikornikova N. 1975 Hydrothermal crystal synthesis in chloride systems. Moscow, Nauka 224 p. (*In Russian*)
- Iler (1955) Iler, R.K. 1955 The colloid chemistry of silica and silicates. Ithaca, New York, Cornell University Press. 323 p.

J

-
- Johannesson et al. (2000) Johannesson, K. H., Xiaoping, Z., Ciaxia, G., Stetzenbach, K. J. and Hodge, V. F. 2000. Origin of rare earth element signatures in groundwaters of circumneutral pH from southern Nevada and eastern California, USA. *Chemical Geology* 164, 239-257.

K

-
- Kachurin (1973) Kachurin, L.G. 1973 Physical bases of the influence on atmospheric processes. Moscow, Gidrometeoizdat.
- Kalb (1929) Kalb G. 1929 Bemerkungen zu den minerogenetischen Kristalltrachtstypen des Kalkspates *Zbl Mineral., Abt. A*, 4. ss. 137-138.
- Kalinin et al. (1998) Kalinin D.V., Vosel, S.V., and Sedobintseva, V.V. 1998 New interpretation of the structure of the precious opal and energetic analysis of the interaction of the spherical particles of silica during its formation. *Russian Geology and Geophysics*, 39, 7, pp. 1013-1016.
- Keilis-Borok (1990) Keilis-Borok, V.I. 1990 The Lithosphere of the Earth as a Non-Linear System with Implications for Earthquake Prediction. *Review of Geophysics*, 28.
- Keith and Padden (1963) Keith, H.D. and Padden, F.J. 1963 A phenomenological theory of spherulitic crystallization. *Journal of applied physics*. 34, 8, pp. 2409-2421.
- Keller (1960) Keller, G.V. 1960 Physical Properties of the Oak Spring Formation, Nevada. *USGS Professional Paper 400-B*, Denver, CO.
- Keller (1962) Keller, G.V. 1962 Electrical Resistivity of Rocks in the Area 12 Tunnels, Nevada Test Site, Nye County, Nevada. *Geophysics*, 27, 2.
- Kendall and Broughton Kendall, A.C. and Broughton, P.L. 1978 Origin of fabric in speleothems composed

- (1978) of columnar calcite crystals. *Jour. Sed. Petrol.* 48, 2, 519-538.
- Khimcheva et al. (1991) Khimcheva, N.V., Plusnina, I.I., and Isirikian, F.F. 1991 Sorptive properties of minerals from the sequece opal-quartz. *Newsletters of the Moscow University, Series 4, Geology.* 1. pp. 33-44. (*In Russian*)
- Khmelnitsky (1988) Khmelnitsky, R.A. 1988 Physical and colloidal chemistry. Moscow, Vishaya Shkola. 400 p. (*In Russian*)
- King et al. (2000) King, C.-Y., Azuma, S., Asaai, Y., He, P., Kitigawa, Y., Igarashi, G., Wakita, H. 2000 In search of earthquake precursors in the water-level data of 16 closely clustered wells at Tono, Japan. *Geophysical Journal International*, 143, p. 469-477.
- Kinsman (1969) Kinsman, J.J. 1969 Interpretation of Sr concentrations in carbonate minerals and rocks. *Journal of Sedimentary Petrology*, 39, pp. 486-508.
- Kipp (1987) Kipp, K.L. Jr. 1987 Effect of Topography on Gas Flow in Unsaturated Fractured Rock: Numerical Simulation. In D.D. Evans and T.J. Nicholson, (Eds.) Flow and Transport Through Unsaturated Fractured Rock. American Geophysical Union. pp. 171-176.
- Kirkpatric (1975) Kirkpatric, R.J. 1975 Crystal growth from the melt: A overview. *Amer. Mineral.* 60, 798 – 814.
- Klimchuk and Nasedkin (1992) Klimchuk, A.B. and Nasedkin, V.M. 1992 Radon in caves of the FSU. *Svet*, 4, (6) pp. 21-35. (*In Russian*)
- Kodenev (1984) Kodenev, G.G. 1984 Formation of fluctuating nuclei in supersaturated vapor. Institute of Geology and Geophysics, Preprint 3, Novosibirsk, A. of Sci. USSR. 11 p. (*In Russian*)
- Kondratiev et al. (1982) Kondratiev, K.Y., Moskalenko, N.I., Pozdniakov, D.V. 1982 Atmospheric aerosol. *Gidrometeoizdat, Leningrad.* (*In Russian*)
- Krasnova and Petrov (1997) Krasnova, N. I. and Petrov, T. G. 1997. Genesis of mineral individuals and aggregates. St. Petersburg, Nevsky kuryer, 228 p. (*In Russian*)
- Kreshkov (1976) Kreshkov, A.P. 1976 Fundamentals of the analytical chemistry. Chemistry. Moscow. 401 p. (*In Russian*)
- Kuznetsov and Ust-Kachkintsev (1976) Kuznetsov, V.V. and Ust-Kachkintsev, V.F. 1976 Physical and colloidal chemistry. *Visshaya Shkola. Moscow.* (*In Russian*)

L

-
- Lachenbruch and Sass (1978) Lachenbruch, A.H., and Sass, J.H. 1978 Models of an Extending Lithosphere and Heat Flow in the Basin and Range Province. *In: Cenozoic Tectonics and Regional Geophysics of the Western Cordillera, Geological Society of America Memoir, 152.*
- Langmuir (1978) Langmuir, D. 1978 Uranium solution-mineral equilibria at low temperature with applications to sedimentary ore deposits. *Geochim. et Cosmochim. Acta.* 43, pp. 547-569.
- Langmuir and Herman (1980) Langmuir, D. and Herman, J.S. 1980 The mobility of thorium in natural waters at low temperatures. *Geochim et Cosmochim Acta.* 44, pp. 1753-1766.
- Lebedev (1975) Lebedev, L.M. 1975 Modern ore-forming hydrotherms. Moscow, Nedra. 261 p. (*In Russian*)
- Lebedev (1979) Lebedev, L.M. 1979 Minerals of modern hydrotherms. Moscow, Nauka, 200 p. (*In Russian*)
- Lee and Morse (1999) Lee, Y-J, Morse, J. W. 1999 Calcite precipitation in synthetic veins: implications for the time and fluid volume necessary for vein filling. *Chemical Geology, 156*, pp. 151-170.
- Lehman and Brown (1995) Lehman, L.L. and Brown, T.P. 1995 Compartmentalized saturated flow at Yucca Mountain. *High-Level Radioactive Waste Management Proc. Int. Con., Amer. Nucl. Soc., La Grande Park, Illinois.* pp. 206-208.
- Levy (1984) Levy, S. S. 1984 Studies of altered vitrophyre for prediction of nuclear waste repository-induced thermal alteration at Yucca Mountain, Nevada. Materials Research Society Symposium Proceedings, v. 26959-966
- Levy (1992) Levy, S.S. 1992 Natural gels in the Yucca Mountain area, Nevada, USA. *Applied Clay Science, 7*, pp. 79-85.
- Levy and Naeser (1991) Levy, S. and Naeser, C. 1991 Bedrock Breccias Along Fault Zones Near Yucca Mountain, Nevada. Paper Submitted to United States Geological Survey Bulletin.
- Levy et al. (1995) Levy, S., Chipera, S., and Norman, D. 1995 Alteration History Studies in the Exploratory Studies Facility, Yucca Mountain, Nevada, USA. *Scientific Basis for Nuclear Waste Management XIX, Proceedings Materials Research Society Symposium V*, Boston, 27 November- 1 December 1995.
- Lifshitz and Landau (1979) Lifshitz, E.M. and Landau, L.P. 1979 Physical kinetics. Nauka. Moscow. (*In Russian*)

- Lindgren (1933) Lindgren, W. 1933 Mineral Deposits. 4th edn. McGraw-Hill, New York.
- Liu et al. (1995) Liu, N., Sorensen, C.D., Tung, C.-H., and Orchard, C.R. 1995 Continuous, environmental radon monitoring program at the Yucca Mountain Site Characterization Project. *High-Level Radioactive Waste Management*. Proc. Int. Con , Amer. Nucl. Soc., La Grande Park, Illinois. pp.
- Livingston (1993) Livingston, D. E. 1993 A review of the major element geochemistry of Yucca mountain, Nye county, Nevada. TRAC Technology and resource Assessment Corporation, Special Report No. 4, 46p. + Appendix
- Lorens (1981) Lorens, R.B. 1981 Sr, Cd, Mn and Co distribution coefficients in calcite as a function of calcite precipitation rate. *Geochim et Cosmochim Acta*, 45, pp. 553-561.
- Lovering (1954) Lovering, T.G. 1954 Radioactive Deposits of Nevada. A contribution to the geology of uranium. *Geological Survey Bulletin 1009-C*. U.S. Government Printing Office, Washington. 106 p.
- Lushnikov (1978) Lushnikov, A.A. 1978 Some new aspects of the theory of coagulation. *Newsletters of the A of Sci USSR*. Ser. FAO, 14, 10, pp. 1048-1055. (In Russian)

M

- Machette (1985) Machette, M.N. 1985 Calcic soils of the southwestern United States *GSA Special Paper* 203. 21 p
- Marcus (1968) Marcus, A.H. 1968 Stochastic coalescence. *Technometrics* 10, 1, pp. 133-148.
- Marshall and Futa (2001) Marshall, B.D. and Futa, K. 2001 Strontium Isotope Evolution of Pore Water and Calcite in the Topopah Spring Tuff, Yucca Mountain, Nevada. *Proc. Int Con , Amer. Nucl Soc.* "High-Level Radioactive Waste Management". La Grande Park, Illinois
- Marshall and Mahan (1994) Marshall, B.D. and Mahan, S.A. 1994 Strontium isotope geochemistry of soil and playa deposits near Yucca Mountain, Nevada. *Proc. Int Con , Amer. Nucl Soc.* "High-Level Radioactive Waste Management". La Grande Park, Illinois. pp. 2685-2691.
- Marshall and Whelan (2000) Marshall, B. and Whelan, J. 2000 Isotope geochemistry of calcite coatings and the thermal history of the unsaturated zone at Yucca Mountain, Nevada. *GSA Abstracts with Program*. 32, 7. p. A-259.

- Marshall et al. (1990) Marshall, B.D., Peterman, Z.E. Futa, K., Stuckless, J. S. Mahan, S A., Downey, J. S., and Gutentag, E. D. 1990. Origin of Carbonate Deposits in the Vicinity of Yucca Mountain, Nevada: Preliminary Results of Strontium-Isotope Analyses. . *Proc. Int. Con, Amer. Nucl Soc* "High-Level Radioactive Waste Management". La Grande Park, Illinois.
- Marshall et al. (1993) Marshall, B.D., Peterman, Z.E, and Stuckless, J.S., 1993 Strontium isotopic evidence for a higher water table at Yucca Mountain. *Proc. Int Con, Amer. Nucl Soc*. "High-Level Radioactive Waste Management". La Grande Park, Illinois. pp. 1948-1952.
- Marshall et al. (1995) Marshall, B. D., Kyser, K.T., and Peterman Z.E. 1995 Oxygen Isotopes and Trace Elements in the Tiva Canyon Tuff, Yucca Mountain and Vicinity, Nye County, Nevada. *U.S. Geological Survey Open-File Report 95-431*. 49 p.
- Marshall et al. (1998) Marshall, B D , Paces, J.B., Peterman, Z.E., Neymark, L.A., Whelan, J.F., and Futa, K. 1998 Isotopic evidence for the origin of low-temperature calcite and opal exposed in an underground laboratory at Yucca Mountain, Nevada. *GSA Abstracts with Program*. Toronto, Canada. p. A-363.
- McConnaughey (1989) McConnaughey, T. 1989 ^{13}C and ^{18}O isotopic disequilibrium in biological carbonates. 1. Patterns. *Geochim et Cosmochim Acta*, 53, pp. 163-171.
- McConnaughey et al. (1994) McConnaughey, T.A., Whelan, J.F., Wickland, K.P., and Moscati, R.J. 1994 Isotopic Studies of Yucca Mountain Soil Fluids and Carbonate Pedogenesis. *Proc Int Con, Amer. Nucl Soc* "High-Level Radioactive Waste Management". La Grande Park, Illinois. pp. 2584-2589.
- Michaelis et al. (1985) Michaelis, J., Usdowski, E., and Menschel, G. 1985 Partitioning of ^{13}C and ^{12}C on the degassing of CO_2 and the precipitation of calcite – Rayleigh-Type fractionation and a kinetic model. *Amer J of Sci*. 285, pp. 318-327.
- Michard and Albarede (1986) Michard, A. and Albarede, F. 1986 The REE Content of Some Hydrothermal Fluids. *Chemical Geology*, 55.
- Michard et al. (1987) Michard, A.C., Beaucaire, C., and Michard, D. 1987 Uranium and Rare Earth Elements in CO_2 -Rich Waters from Vals-Les-Bains (France). *Geochimica at Cosmochimica Acta*, 51.
- Mineev and Rozenkova (1962) Mineev, D. A. and Rozenkova, N. I. 1962 On the zonation of Vyshnevogorsky pyrochlore. *ZVMO*. 91, 1, pp. 89 - 93. (In Russian)
- Moore et al. (2001) Moore, J.N., Norman, D.I., and Kennedy, B.M. 2001 Fluid inclusion gas compositions from an active magmatic hydrothermal system: a case study of The

- compositions from an active magmatic–hydrothermal system: a case study of The Geysers geothermal field, USA. *Chemical Geology* 173 pp. 3–30.
- Morey and Niggli (1913) Morey, G.W. and Niggli, P. 1913 The hydrothermal formation of silicates, a review. *Jour. Am Chem Soc.* 35, pp. 1086-1130.
- Morse (1983) Morse, J.W. 1983 The kinetics of calcium carbonate dissolution and precipitation. In: Reeder, R.J. (Ed.), *Carbonates: Mineralogy and Chemistry*. Mineral. Soc. Am. pp. 227-264.
- Mozgova, 1963 Mozgova, N.N. 1963 Mineralized cavities in the Tetiukhe Skarns. *Zapiski Vsesoyuznogo Mineralogicheskogo Obschestva (Notes of the All-Union Mineral Soc)*, 6, 42, pp 645-663. (In Russian)
- Mucci and Morse (1983) Mucci, A. and Morse, J.W. 1983 The incorporation of Mg²⁺ and Sr²⁺ into calcite overgrowths: Influence of growth rate and solution composition. *Geochim Cosmochim Acta*, 47, pp. 217 - 233.
- Muir-Wood and King (1993) Muir-Wood, R. and King, G.C.P. 1993 Hydrological Signatures of Earthquake Strain. *Journal of Geophysical Research*, 98.
- Mukherjee (1986) Mukherjee A.L. 1986 Fluorite mineralisation in Garampani thermal spring area, Palamau district, Bihar. *J Geol Soc Indian*, 28, 6, pp. 442-448.
- Murphy (1979) Murphy, H.D. 1979 Convective Instabilities in Vertical Fractures and Faults. *Journal of Geophysical Research*, 84.

N

- NAS/NRC (1992) NAS/NRC 1992 Ground Water at Yucca Mountain: How High Can It Rise? *Final Report of the Panel on Coupled Hydrologic/Tectonic/ Hydrothermal Systems at Yucca Mountain*. National Research Council. National Academy Press. Washington D.C. 231 p
- NBMG/UNR 1999 NBMG/UNR 1999 Geochemical Anomalies at Yucca Mountain and Implications for Metallic Mineral Potential. Report by Nevada Bureau of Mines and Geology, University of Nevada Reno to TRW Environmental Safety Systems Inc. *TDR-NBS-GS-000001 REV. 00*. 34 pp. + Appendices.
- NC NWRPO (2000) NC NWRPO (Nye County Nuclear Waste Repository Project Office) 2000 Summary Annual Report, Grant DE-FG08-96NV 12027, May 1999 - April 2000.
- NEA/IAEA (2001) NEA/IAEA 2001 Joint NEA-IAEA International Peer Review of the Yucca Mountain Site Characterisation Project's Total System Performance Assessment

- Supporting the Site Recommendation Process, *Final Report* December 2001
- Nelson and Giles (1985) Nelson, C. E., and Giles, D. L. 1985 Hydrothermal Eruption Mechanisms and Hot Spring Gold Deposits *Economic Geology*, **80**.
- Newman et al. (1996) Newman, B.D., Norman, D.I., Gundimeda, N., and Levy, S.S. 1996 Understanding the genesis of nonmarine calcite deposits through quadrupole mass spectrometric analysis of fluid inclusion gases. *Chemical Geology*, **132**. pp. 205-213.
- Newman et al. (1997) Newman, B.D., Campbell, A.R., Norman, D.I., and Ringelberg, D.B. 1997 A model for microbially induced precipitation of vadose-zone calcites in fractures at Los Alamos, New Mexico, USA. *Geochim et Cosmochim Acta* **61**, 9, pp. 1783-1792.
- Neymark and Paces (2000) Neymark, L.A. and Paces, J.B. 2000 Consequences for Slow Growth for $^{230}\text{Th}/\text{U}$ Dating of Quaternary Opals, Yucca Mountain, Nevada, USA. *Chemical Geology*, **164**.
- Neymark et al. (1998-a) Neymark L. A., Paces J. B., and Amelin Y. V. 1998-a Neogene to Quaternary U–Th–Pb geochronology using opal, Yucca Mountain, Nevada, USA. *Mineral Mag.* **62A**, pp. 1077–1078.
- Neymark et al. (1998-b) Neymark, L.A., Amelin, Y.V., Paces, J.B., and Peterman, Z.E. 1998-b U-Pb age evidence for long-term stability of the unsaturated zone at Yucca Mountain. *Proc Int Con , Amer Nucl Soc. "High-Level Radioactive Waste Management"*. La Grande Park, Illinois. pp. 85-87.
- Neymark et al. (2000) Neymark A.L. Amelin, Y.V., and Paces, J.B. 2000 ^{206}Pb - ^{230}Th - ^{234}U - ^{238}U and ^{207}Pb - ^{235}U geochronology of Quaternary opal, Yucca Mountain, Nevada. *Geochemica et Cosmochemica Acta*, **64**, 17, pp. 2913-2928.
- Neymark et al. (2002) Neymark, L.A., Amelin, Y., Paces, J.B. and Peterman, Z.E. 2002 U-Pb ages of secondary silica at Yucca Mountain, Nevada: Implications for the paleohydrology of the unsaturated zone. *Applied Geochemistry (In press)*
- Nicolis and Prigogine (1977) Nicolis, G. and Prigogine, I. 1977 Self-organization in nonequilibrium systems From dissipative structures to order through fluctuations. John Wiley and Sons. 491 p.
- Nilsson and Sternberg (1999) Nilsson, O. and Sternberg, J. 1999 A mechanistic model for calcite crystal growth using surface speciation. *Geochim. et Cosmochim Acta*, **63**, pp. 217-225.
- Noble et al. (1991) Noble, D.C., Weiss, S.I., and McKee, E.H. 1991 Magmatic and hydrothermal activity, caldera geology, and regional extension in the western part of the southwestern Nevada volcanic field. In G.L. Raines, R.E. Lisle, R.W. Shafer, and W.W. Wilkinson, *Eds. Geology and Ore Deposits of the Great Basin*. Reno, Geol.

- Soc. of Nevada. pp. 913-934.
- Norman and Moore (1999) Norman, D.I. and Moore, J.N. 1999 Methane and excess N₂ and Ar in geothermal fluid inclusions *Proc. 24th Workshop Geotherm Reservoir Eng.*, Stanford Univ., pp. 196-202.
- Nur (1972) Nur, A. 1972 Dilatancy, Pore Fluids and Premonitory Variations of Vs/Vp Travel Times. *Seismological Society of America Bulletin*, 62.

O

- O'Neil and Silberman (1974) O'Neil, J.R. and Silberman, M.L. 1974 Stable Isotope Relations in Epithermal Au-Ag Deposits. *Econ Geol.* 69. pp. 902-909.
- Ohmoto (1972) Ohmoto, H. 1972 Systematics of sulfur and carbon isotopes in hydrothermal ore deposits. *Econ Geol.* 67, 551-578.
- Ohmoto (1986) Ohmoto, H. 1986 Stable Isotope Geochemistry of Ore Deposits. *In: Valley, J., Taylor, H. and O'Neil, J., Eds Stable Isotopes in High-Temperature Geological Processes.* Reviews in Mineralogy, 16. pp. 491-559.
- Ohmoto and Rye (1979) Ohmoto, H. and Rye, R.O. 1979 Isotopes of sulfur and carbon. *In: H.L. Barnes, ed., Geochemistry of Hydrothermal Ore Deposits, second ed., pp. 509-567.* John Wiley, New York, 798 p.
- Okamoto et al. (1963) Okamoto, G., Okura, T., and Goto, K. 1963 Silica properties in water. *In Geochemistry of lithogenesis.* Moscow, Inostrannaya Literatura. pp. 196-208 (*In Russian*)
- Onac (1997) Onac B.P. 1997 Crystallography of Speleothems. *In. Hill C., Forti P., Eds. Cave minerals of the World.* National Speleological Society. pp. 230-236.
- Osmond and Cowart (1982) Osmond, J.K. and Cowart, J.W. 1982 Ground Water. *In: Uranium Series Disequilibrium: Applications to Environmental Problems.* Clarendon Press, Oxford.

P

- Paces and Whelan (2001) Paces, J.B. and Whelan, J.F. 2001 Water-Table Fluctuations in the Amargosa Desert, Nevada. *Proc. Int Con , Amer Nucl Soc.* "High-Level Radioactive Waste Management". La Grande Park, Illinois.
- Paces et al. (1993) Paces, J.B., Taylor, E.M., and Bush, Ch., 1993 Late Quaternary History and Uranium Isotopic Compositions of Ground Water Discharge Deposits, Crater Flat,

- Nevada. *Proc Int Con, Amer. Nucl. Soc* "High-Level Radioactive Waste Management". La Grande Park, Illinois. pp. 1573-1580.
- Paces et al. (1996) Paces, J., Neymark, L.A., Marshall, B.D., Whelan, J.F., and Peterman, Z.E. 1996 Ages and origins of subsurface secondary minerals in the Exploratory Studies Facility (ESF). *USGS Milestone Report 3GQH450M* 55 p.
- Paces et al. (1998) Paces, J., Neymark, L.A., Marshall, B.D., Whelan, J.F., and Peterman, Z.E. 1998 Inferences for Yucca Mountain unsaturated zone hydrology from secondary minerals. *High-Level Radioactive Waste Management. Proc. Int. Con., Amer. Nucl. Soc., La Grande Park, Illinois.* pp 36-39.
- Paces et al. (2000) Paces, J. B., Whelan, J. F., Peterman, Z. E., Marshall, B. D., and Neymark, L. A. 2000 Formation of calcite and silica from percolation in a hydrologically unsaturated setting, Yucca Mountain, Nevada. *GSA Abstracts with Program*, 32, 7, p. A-259.
- Palyanova et al. (2002) Palyanova, G., Smirnov, S., and Dublyansky, Y. 2002 Thermodynamic modeling of the rhyolite-water interaction and the mineralogy of secondary assemblages at Yucca Mountain, Nevada. *Russian Geology and Geophysics* (in press)
- Panichi and Tongiorgi (1975) Panichi, C. and Tongiorgi, E. 1975 Carbon isotopic composition of CO₂ from springs, fumaroles, mofettes and travertines of central and southern Italy: a preliminary prospection method of geothermal area. *Proc 2nd Symp Development and Use of Geothermal Resources, San Francisco, Calif.* Pp. 815-825.
- Parker et al. (1983) Parker, L.W., Miller, J., Steinberger, Y., and Whitford, W.G. 1983 Soil respiration in a Chihuahuan desert rangeland. *Soil Biology and Biochemistry* 15, pp. 303-309.
- Pashenko and Dublyansky (2002-a) Pashenko, S.E. and Dublyansky, Y.V. 2002-a The role of radon and colloids in distorting the U-Pb age dates of geologically young minerals deposited in open cavities. 2002 International Goldschmidt Conference on Geochemistry. Zurich, 14-25 August 2002.
- Pashenko and Dublyansky (2002-b) Pashenko, S.E. and Dublyansky, Y.V. 2002-b Theoretical investigation of production, migration in fluid and incorporation in growing minerals of the Rn-derived Pb isotopes. Internal Report of the Institute of Mineralogy and Petrography, Russian Academy of Sciences, Siberian Branch, Novosibirsk, June 2002. 110 p.
- Pashenko and Sabelfeld (1992) Pashenko S.E. and Sabelfeld, K.K. 1992 Atmospheric and technogene aerosol: kinetic, microprobe and numerical methods of studies. *Acta of Institute of Chemical Kinetics and Combustion*, Russian Academy of Sciences, Novosibirsk. 310 p. (*In Russian*)

- Pashenko et al. (1980) Pashenko, S.E., Kutsenogy, K.P., Pashenko, A.E., Ankilov, A.I., and Baklanov, A.M. 1980 Experimental studies of the kinetics of the non-steady-state nucleation in gaseous phase. *Letters to Journal of Theoretical and Experimental Physics*, 6, 22, pp. 1380-1383. (*In Russian*)
- Pashenko et al. (1996) Pashenko, S., Vlasenko, A., Ankilov, A., Baklanov, A., Eremenko, S., Korolev, V., Shirokov, Y., Wyers, G P, Ten Brink, H.M, Khlystov, A., Waijers-Ypelaan, A. 1996 A study of emission sources at Novosibirsk. *J Aerosol Sci* 27, Suppl.1, pp. S129-130.
- Penrose (1991) Penrose, R. 1991 *The Emperor's new mind*. Penguin Group. 466 p.
- Peterman et al. (1992) Peterman, Z.E., Stuckless, J.S., Marshall, B.D., Mahan, S.A., and Futa, K. 1992 Strontium isotope geochemistry of calcite fracture fillings in deep core, Yucca Mountain, Nevada – A progress report. *Proc Int Con, Amer. Nucl Soc* “High-Level Radioactive Waste Management”. La Grande Park, Illinois. pp. 1582-1586.
- Peterman et al. (1993) Peterman, Z.E., Spengler, R.W., Singer, F.R., and Dickerson, R.P., 1993 Isotopic and trace element variability in altered and unaltered tuffs at Yucca Mountain, Nevada. *Proc. Int. Con, Amer. Nucl Soc* “High-Level Radioactive Waste Management”. La Grande Park, Illinois. pp. 1940-1947.
- Peterman et al. (1994) Peterman, Z. E., Widmann, B. L., Marshall, B. D., Aleinikoff, J. N., Futa, K. and Mahan, S. A. 1994 Isotopic tracers of gold deposition in Paleozoic limestones, Southern Nevada. *Proc Int Con, Amer Nucl Soc*. “High-Level Radioactive Waste Management”. La Grande Park, Illinois. pp. 1316-1323.
- Petrov (1982) Petrov, Y.I. 1982 *Physics of small particles*. Nauka, Moscow. (*In Russian*)
- Pokrovsky (1989) Pokrovsky, V. A. 1989 Theoretical prediction of differential mobility of components in hydrothermal systems on the basis of phase diagrams. *In: Physico-chemical analysis of mineral forming processes*. Ed: V. A. Zharikiov. Moscow, Nauka, pp. 212-245.
- Pollack and Chapman (1977) Pollack, H.N. and Chapman, D.S. 1977 On the Regional Variation of Heat Flow, Geotherms, and Lithospheric Thickness. *Tectonophysics*, 38.
- Principles of Hydrogeology... (1982) Principles of Hydrogeology. Geological activity and history of water in the Earth's interiors. (E.V. Pinneker, Ed.) Novosibirsk, Nauka PH 1982. 239 p. (*In Russian*)

Q

- Quade (1994) Quade, J. 1994 Spring Deposits and Late Pleistocene Ground Water Levels in Southern Nevada. *Proc Int Con, Amer Nucl Soc* “High Level Radioactive Waste

- Southern Nevada. *Proc Int Con, Amer. Nucl Soc* "High-Level Radioactive Waste Management". La Grande Park, Illinois.
- Quade and Cerling (1990) Quade, J., Cerling, T.E. 1990 Stable isotopic evidence for a pedogenic origin of carbonates in trench 14 near Yucca Mountain, Nevada *Science*, 250, pp. 1549-1552.
- Quade et al. (1988) Quade, J, Cerling, T. E., and Bowman, J. R. 1988 Systematic Variations in $\delta^{13}\text{C}$ and $\delta^{18}\text{O}$ of Soil Carbonate Along Elevation Transects in the Southern Great Basin, USA. Update Report: The Paleohydrology and Paleoenvironments in the Vicinity of the Proposed Yucca Mountain Nuclear Waste Repository. W. G. Spaulding, ed. Submitted to the Nuclear Waste Project Office of the State of Nevada.
- Quade et al. (1989) Quade, J., Cerling, T.E., and Bowman, J.R. 1989 Systematic variations in the carbon and oxygen isotopic composition of pedogenic carbonate along elevation transects in the southern Great Basin. *Geol Soc. Amer Bull.* 101, p. 464-475.
- Quinke (1902) Quinke, J. 1902 Die oberflächenspannung an der Grenze wässriger Kolloidlösungen von verschiedener Contentration *Ann. Physik.*, 9, 13.

R

- Ranalli (1987) Ranalli, G. 1987 Rheology of the Earth. Allen and Urwin, Boston, Mass.
- Reheis et al. (1992) Reheis, M C., Sowers, J.M., Taylor, E.M., McFadden, L.D., and Harden, J.W. 1992 Morphology and Genesis of Carbonate Soils on the Kyle Canyon Fan, Nevada, USA. *Geoderma*, 52, pp. 302-342.
- Rhiele (1973) Rhiele, J.R. 1973 Calculated Compaction Profiles of rhyolitic ash-flow tuffs. *Geol Soc. Amer Bull* 84, pp. 2193-2216.
- Rimstidt et al. (1998) Rimstidt, J.D., Balog, A., and Webb, J. 1998 Distribution of trace elements between carbonates and aqueous fluids. *Geochim et Cosmochim Acta*, 62, pp. 1851-1863.
- Robie and Hemingway (1995) Robie R.A. and Hemingway B.S. 1995 Thermodynamic properties of minerals and related substances at 298.15 and 1 bar (10^5 Pascals) pressure and at higher temperatures. *Geol Surv. Bull.* 2131. 461 p.
- Robison (1984) Robison, J. H. 1984 Ground-Water Level Data and Preliminary Potentiometric-Surface Maps, Yucca Mountain and Vicinity, Nye County, Nevada. *United States Geological Survey, Water Resources Investigations Report, USGS-WRI-84-4197.*
- Roedder (1984) Roedder, E. 1984 Fluid Inclusions. Review in Mineralogy. v. 12. Min. Soc. Amer. 644 p.

- Roedder and Whelan (1998) Roedder, E. and Whelan, J.F. 1998 Ascending or descending water flow through Yucca Mountain tuffs? – Fluid Inclusion Evidence. *Abst 7th PACROFI Meeting*, Las Vegas, Nevada, 1-4 June, 1998, p. 56.
- Roedder et al. (1994) Roedder, E., Whelan, J.F., and Vaniman, D.T. 1994 Fluid Inclusion Studies of Calcite Veins from Yucca Mountain, Nevada, Tiffs: Environment of Formation. *Proc Int Con, Amer Nucl Soc* “High-Level Radioactive Waste Management”. La Grande Park, Illinois. pp. 1854-1860.
- Rollinson (1993) Rollinson, H. 1993 Using Geochemical Data: Evaluation, Presentation, Interpretation Pearson Education Limited. 352 p.
- Romberger (1986) Romberger, S.B. 1986 Ore Deposits #9, Disseminated Gold Deposits. *Geoscience Canada*, 13, pp. 23-31.
- Rosinski and Snow (1961) Rosinski, I. and Snow, J. 1961 Mathematical survey of the coagulation. *J Matarol.* 18, p. 739.
- Russell (1987) Russell, C.E. 1987 Hydrologic Investigations of Flow in Fractured Tuffs, Rainier Mesa, Nevada Test Site. *M S Thesis, University of Nevada-Reno*, Reno, Nevada.
- Rye and Ohmoto (1974) Rye, R. O. and Ohmoto, H. 1974 Sulfur and Carbon Isotopes and Ore Genesis: A Review. *Econ Geol.* 69, pp. 826-842.
- Ryzhenko and Krainov (2000) Ryzhenko, B.N. and Krainov, S.R. 2000 Influence of the weight relationships of the reacting rocks and water on the chemical composition of natural water solutions in systems, open for CO₂. *Geochemistry.* 8, pp. 725-737. (In Russian)
- Ryzhenko et al. (1996) Ryzhenko, B.N., Barsukov, V.L., and Kniazeva, S.N. 1996 Chemical characteristics (composition, pH, Eh) of the rock/water systems: I. Systems “granite/water” and “syenite/water”. *Geochemistry.* 5, pp. 436-454. (In Russian)
- Ryzhenko et al. (2000) Ryzhenko, B.N., Barsukov, V.L., and Kniazeva, S.N. 2000 Chemical characteristics (composition, pH, Eh) of the rock/water systems: III. Systems “pyroxenite/water” and “dunite /water”. *Geochemistry.* 6, pp. 618-642. (In Russian)

S

- Sabelfeld et al. (1996) Sabelfeld, K.K., Rogasinsky, S.V., Kolodko, A.A., Levykin, A.I. 1996 Stochastic algorithms for solving Smolukhovski coagulation equation and applications to aerosol growth simulation. *Monte Carlo Methods and Applications*, 2, 1, pp. 41-87.
- Salomons and Mook (1986) Salomons, W and Mook, W.G. 1986 Isotope geochemistry of carbonates in the weathering zone. In. P. Fritz and J.Ch Fontes, Eds. *Handbook of Environmental*

- Isotope Geochemistry 2. The terrestrial Environment*, B. Elsevier, Amsterdam. pp. 239-269.
- Sass (1998) Sass, J. 1998 Thermal tracking of water flow under Yucca Mountain. *Proc. Int Con , Amer Nucl. Soc.* "High-Level Radioactive Waste Management". La Grande Park, Illinois pp. 269-271.
- Sass (1999) Sass, J. 1999 Thermal Manifestation of Hydrologic Phenomena in the Great Basin of the Southwestern United States. *Supplement to EOS*, April 27, 1999
- Sass and Lachenbruch (1982) Sass, J.H. and Lachenbruch, H. 1982 Preliminary Interpretation of Thermal Data from the Nevada Test Site. *USGS Open File Report 82-973*, Denver, CO.
- Sass et al. (1971) Sass, J., Lachenbruch, A., Munroe, R., Greene, G., and Moses, T. (Jr) 1971 Heat flow in the Western United States. *Journ of Geophys Res.* 76, 26, pp. 6376-6413.
- Sass et al. (1980) Sass, J.H., Lachenbruch, H.A., and Mase, T. 1980 Analysis of Thermal Data from Drill Holes UE-25a3 and UE-25a1, Calico Hills and Yucca Mountain, Nevada Test Site. *USGS Open File Report 80-826*, Denver, CO.
- Sass et al. (1983) Sass, J. H , Lachenbruch, H.A., Grubb, H., and Mase T. 1983 Status of Thermal Observations at Yucca Mountain, Nevada. *USGS Letter Report to DOE*.
- Sass et al. (1987) Sass, J.H., Lachenbruch, A.H., Dudley, W.W., Priest, S.S., and Munroe, R.J. 1987 Temperature, Thermal Conductivity, and Heat Flow near Yucca Mountain, Nevada: Some Tectonic and Hydrologic Implications. *US Geological Survey Open-File Report 87-649*, Denver, CO. - 118 p.
- Sass et al. (1995) Sass, J.H., Dudley, W.W., and Lachenbruch, A.H. 1995 Regional thermal setting, chap. 8, in Major Results of Geophysical Investigations at Yucca Mountain and Vicinity, Southern Nevada, H.W. Oliver, D.A. Ponce and W.C. Hunter, Eds. *U S Geol Survey Open File Rep 95-74*, 23 pp.
- Schmitt (1993) Schmitt, R. A., 1993. Technical Report, Radiation Center Project No. 926. In Livingston D. E., Trace Element and REE Composition of Five Samples of the Yucca Mountain Calcite/Silica Deposits. *Special Report No 8*, Submitted to the Nuclear Waste Project Office, State of Nevada.
- Schuraytz et al. (1989) Schuraytz, B.J., Vogel, T.A., and Younker, L.W. 1989 Evidence for dynamic withdrawal from a layered magma body: The Topopah Spring Tuff, southwestern Nevada. *J Geophys Res.* 94-B5, pp. 5925-5942.

- Schwartz et al. (1976) Schwartz, H.P., Harmon, R.S., Thompson, R., and Ford, D.C. 1976 Stable isotope studies of fluid inclusions in speleothems and their paleoclimatic significance. *Geochim Cosmochim Acta*. 40, 657-665.
- Scott and Castellanos (1984) Scott, R. and Castellanos, M. 1984 Preliminary report on the geologic character of the drill hole USW GU-3/G-3. *USGS, Open-file report, 84-491*
- Senderov and Khitarov (1970) Senderov E.E. and Khitarov N.I. (1965) Zeolites, Their Synthesis and Conditions of Formation in Nature. Moscow, Nauka. 283 p. (*In Russian*)
- Shafranovsky (1968) Shafranovsky, I.I. 1968. Lectures on crystal morphology. Moscow, Vyshaya Shkola, 174. (*In Russian*)
- Shannon and Prewit (1969) Shannon, R.D. and Prewit, C.T. 1969 Effective ionic radii in oxides and fluorides. *Acta Crystallographica*. 25, pp. 925-1047.
- Sharp (1992) Sharp, Z.D. 1992 In situ laser microprobe techniques for stable isotope analysis. *Chemical Geology*. 101. pp. 3-19.
- Sharp and Cerling (1996) Sharp, Z.D. and Cerling, T.E. 1996 A laser GC-IRMS technique for in situ stable isotopic analyses of carbonates and phosphates. *Geochim. et Cosmochim Acta*. 60, 15, pp. 2909-2916.
- Shepherd et al. (2000) Shepherd, T.J., Naden, J., Chenery, S.R., Milodowski, A.E., Gillespie, M.R. 2000 Chemical analysis of palaeogroundwaters: a new frontier for fluid inclusion research. *Journal of Geochemical Exploration*. 69–70. pp. 415–418.
- Sheppard (1971) Sheppard, R. A. 1971 Zeolites in sedimentary deposits of the United States - a review. *Am Chem Soc Adv. Chem Ser Ed* 101, pp. 279-310.
- Sherbina and Naumov (1963) Sherbina, V.V. and Naumov, G.B. 1963 Basic features of uranium, governing its geochemistry. *In: A.P. Vinogradov, Ed Basic features of uranium geochemistry*. Academy of Sciences of the USSR Press, Moscow. pp. 5-26. (*In Russian*)
- Shieh and Taylor (1969) Shieh, Y.N. and Taylor, H P. Jr. 1969 Oxygen and carbon isotope studies of contact metamorphism of carbonate rocks. *J Petrol*. 10, p. 307-331.
- Shock and Helgeson (1988) Shock, E.L. and Helgeson, H.C. 1988 Calculation of the thermodynamic and transport properties of aqueous species at high pressures and temperatures: Correlation algorithms for ionic species and equation of state predictions to 5 kb and 1000 °C. *Geochim et Cosmochim Acta* 52, pp. 2009-2036.
- Shock et al. (1997) Shock, E.L., Sassani, D.C., Willis, M., and Sverjensky, D.A. 1997 Inorganic species in geologic fluids: correlations among standard molal thermodynamic properties of aqueous ions and hydroxide complexes. *Geochim et Cosmochim. Acta*. 61, 5, pp.

- 907-950.
- Sholkovitz et al. (1994) Sholkovitz, E., Landing, W.M., Lewis, B.L. 1994. Ocean particle chemistry the fractionation of rare-earth elements between suspended particles and seawater. *Geochim. Cosmochim Acta*, **58**, pp. 1567-1580.
- Shvarov (1999) Shvarov, Y.V. 1999 Algorithmization of numeric equilibrium modeling of the dynamic geochemical processes. *Geochemistry* **6**, pp. 646-652. (*In Russian*)
- Sibson et al. (1975) Sibson, R.H., Moore, J.M., and Rankin, A.H. 1975 Seismic Pumping - a Hydrothermal Fluid Transport Mechanism *Journal Geological Society of London*, **131**.
- Slate et al. (1999) Slate, J. L., Berry, M. E , Rowley, P. D., Fridrich, C. J., Morgan, K. S., Workman, J. B., Young, O. D., Dixon, G. L., William, s. V. S., McKee, E. H., Ponce, D. A., Hildenbrand, T. G., Swadley, W. C., Lundstrom, S. C., Ekren, E. B., Warren, R. G., Cole, J. C., Fleck, R. J., Lanphere, M. A., Sawyer, D. A., Minor, S. A., Grunwald, D. J., Laczniak, R. J., Menges, C. M., Yount, J. C. and Jayko, A. S. 1999 Digital geologic map of the Nevada Test Site and vicinity, Nye, Lincoln, and Clark Counties, Nevada, and Inyo County, California. *USGS, Open-File Report 99-554-A*, 56 p.
- Smirnov (1969) Smirnov, V.I. 1969 Velocity of coagulation and condensation growth of the aerosol particles. *Gidrometeoizdat, Moscow. (In Russian)*
- Smirnov and Dublyansky (2000) Smirnov, S. and Dublyansky, Y. 2000 Secondary mineral assemblages in fractures and lithophysal cavities at Yucca Mountain, Nevada, USA. *GSA Abstracts with Program*. **32**, 7. p. A-260.
- Smirnov and Dublyansky (2001-a) Smirnov, S.Z. and Dublyansky, Y.V. 2001-a Ontogenetic mineralogy of secondary minerals from the vadose zone of Yucca Mountain, Nevada. Report Submitted to the Agency for Nuclear Projects, State of Nevada, May 2001. Part I. 114 p + Appendices
- Smirnov and Dublyansky (2001-b) Smirnov, S. and Dublyansky, Y., 2001-b Ontogenetic Mineralogy of Secondary Minerals at Yucca Mountain, Nevada. *Proc Int Con , Amer. Nucl Soc "High-Level Radioactive Waste Management"*, Las Vegas, Nevada.
- Smirnov et al. (2002) Smirnov, S., Dublyansky, Y., Mel'gunov, M., and Mel'gunova, E. 2002 REE geochemistry of the fluorite from Yucca Mountain, USA: fingerprinting multiple sources of matter in hydrothermal fluids. 2002 International Goldschmidt Conference on Geochemistry. Zurich, 14-25 August 2002.

- Smith (1991) Smith, M.R. 1991 Natural Radionuclide/Trace Element Hydrochemistry - Characterization of the Yucca Mountain Saturated (well water) and Unsaturated (pore water) Zone Ground Waters. *Pacific Northwest Laboratory*, Richland, Washington.
- Smith and Shaw (1975) Smith, R.L., and Shaw, H.R. 1975 Igneous-Related Geothermal Systems. In: D.E. White and D.L. Williams, Eds. Assessment of Geothermal Resources of the United States – 1975. U.S. Geological Survey Circular 726. pp. 58-83.
- Smith et al. (2002) Smith, E.I., Keenean, D.L., and Plank, T. 2002 Episodic Volcanism and Hot Mantle: Implications for Volcanic Hazard Studies at the Proposed Nuclear Waste Repository at Yucca Mountain, Nevada. *GSA Today*, 12, 4, pp. 4-10.
- Smolukhovski (1936) Smolukhovski, M. 1936 Three presentations on diffusion, Brownian motion and coagulation of colloidal particles. Brownian motion. Moscow. pp. 332-415. (*In Russian*)
- Smyth and Bish (1988) Smyth, J.R. and Bish, D.L. 1988 Crystal Structure and Cations Sites of the Rock Forming Minerals. Allen and Unwin.
- Smyth and Caporuscio (1981) Smyth, J.R. and Caporuscio, F.A. 1981 Review of the thermal stability and cation exchange properties of the zeolites mineral clinoptilolite, mordenite and analcime: application to radioactive waste isolation in silicic tuffs. *Los Alamos Natl Lab, Report LA-8841-MS*
- Somerville et al. (1992) Somerville M.R., Frazier, G.A., and C.B., Archambeau, 1992. Yucca Mountain Hydrothermal History. *Quarterly Report No. 1*. Submitted to the Nuclear Waste Project Office of the State of Nevada.
- Spengler et al. (1981) Spengler, R.W., Byers, F.M., Jr., and Warner, J.B. 1981 Stratigraphy and structure of volcanic rocks in drill hole USW-G1, Yucca Mountain, Nye County, Nevada. *U.S. Geological Survey Open File Report 82-1338*. 264 p.
- Stahl (1977) Stahl, W.J. 1977 Carbon and nitrogen isotopes in hydrocarbon research and exploration. *Chemical Geology*, 20, pp. 121-149.
- Stankeev (1986) Stankeev, E.A. 1986. Genetic mineralogy. Moscow, Nedra, 272. (*In Russian*)
- Strikland-Constable (1971) Strikland-Constable, R.F. 1971 Kinetics and mechanism of crystallization. Nedra, Leningrad. (*In Russian*)
- Stuckless et al. (1991) Stuckless, J.S., Peterman, Z.E., and Muchs, D.R. 1991 U and Sr isotopes in Ground Water and Calcite, Yucca Mountain, Nevada: Evidence Against Upwelling Water *Science*, 254. pp. 551-554.

- Stuckless et al. (1998) Stuckless, J.S., Marshall, B.D., Vaniman, D.T., Dudley, W.W., Peterman, Z.E., Paces, J.B., Whelan, J.F., Taylor, E.M., Forester, R.M., and O'Leary, D.W., 1998 Comments on "Overview of calcite/opal deposits at or near the proposed high-level nuclear waste site, Yucca Mountain, Nevada, USA: pedogenic, hypogene, or both" by C.A. Hill, Y.V. Dublyansky, R.S. Harmon, C.M. Schluter. *Environmental Geology*. 43(1). pp. 70-78.
- Sullivan and Pescatore (1994) Sullivan, T.M. and Pescatore, C. 1994 Release of Radon Contaminants from Yucca Mountain: The Role of Buoyancy Driven Flow. *Report to the US DOE on contract DE-AC02-79CH00016* Brookhaven National Laboratory – Environmental and Waste Technology Center. 31 p. + Appendices.
- Sun and Semkow (1998) Sun, H. and Semkow, T.M. 1998 Mobilization of thorium, radium and radon radionuclides in ground water by successive alpha-recoil. *Journ of Hydrology*, 205, pp. 126-136.
- Sunagawa (1953) Sunagawa I. 1953 Variation of crystal habit of calcite, with special reference to the relation between crystal habit and crystallization stage. *Rep Geol Surv Japan* No. 155.
- Sunagawa (1982) Sunagawa, I. 1982. Morphology of crystals in relation to growth conditions. *Estudios geol* 38, pp. 127-134.
- Sutugin et al. (1971) Sutugin, A.G., Kotsev, E.I., Fouks, N.A. 1971 Formation of the condensation highly disperse non-coagulated aerosols. *Zourn Colloid* 33, 4, pp. 585-591. (*In Russian*)
- Sutugin et al. (1978) Sutugin, A.G., Puchkov, A.S., Luchnicov, A A. 1978 Evolution of coagulation systems. *Colloid Zh* 40, p. 285.
- Sverjensky (1984) Sverjensky, D.A. 1984 Eiranium redox equilibria in aqueous solutions. *EPSL*, 67, pp. 70-78.
- Sverjensky et al. (1991) Sverjensky, D.A., Hemley, J.J., and D'Angelo, W.M. 1991 Thermodynamic assessment of hydrothermal alkali feldspar- mica-aluminosilicate equilibria. *Geochim et Cosmochim Acta*. 55, pp. 989-1004.
- Sverjensky et al. (1997) Sverjensky, D.A., Shock, E.L., and Helgeson, H.C. 1997 Prediction of the thermodynamic properties of aqueous metal complexes to 1000°C and 5 kb. *Geochim et Cosmochim Acta*. 61, 7, pp.1359-1412.
- Szabo and Kyser (1990) Szabo, B.J. and Kyser, T.K. 1990 Ages and stable-isotope compositions of secondary calcite and opal in drill cores from tertiary volcanic rocks of the Yucca Mountain, Nevada. *Geol. Soc. Amer. Bull* 102, pp. 1714-1719.

- Szabo and O'Malley (1985) Szabo, B. J. and O'Malley, P. A. 1985 Uranium-Series Dating of Secondary Carbonate and Silica Precipitates Relating to Fault Movements in the Nevada Test Site Region and of Caliche and Travertine Samples from the Amargosa Desert. *United States Geological Survey Open-File-Report 85-47*.
- Szabo et al (1981) Szabo, B. J., Carr, W. J., and W.C. Gottschall, 1981. Uranium-Thorium Dating of Quaternary Carbonate Accumulations in the Nevada Test Site Region, Southern Nevada. *United States Geological Survey Open-File-Report 81-119*.
- Szymanski (1989) Szymanski, J.S. 1989 Conceptual Considerations of the Yucca Mountain Groundwater System with Special Emphasis on the Adequacy of this System to Accommodate a High-Level Nuclear Waste Repository. Internal Report, U.S. Department of Energy, Nevada Operations Office, Las Vegas, Nevada.
- Szymanski (1992) Szymanski, J. S. 1992 The origin and history of alteration and carbonatization of the Yucca Mountain ignimbrites *U.S. Department of Energy, Internal Report*.

T

- Talma and Netterberg (1983) Talma, A. S. and Netterberg, F. 1983 Stable isotope abundances in calcretes. In: R.C.L. Wilson, Ed. Residual deposits: Surface Related Weathering Processes and Materials. Geological Society of London. pp. 221-233.
- Taylor and McLennan (1985) Taylor, S.R., and McLennan, S. M. 1985 The continental crust: its composition and evolution. Blackwell, Oxford
- Tesoriero and Pankow (1996) Tesoriero, R. J. and Pankow, J.F. 1996 Solid solution partitioning of Sr, Ba, and Cd to calcite. *Geochim et Cosmochim Acta*, 60, pp. 1053-1063
- Thompson (1998) Thompson, J. L., ed , 1998, Laboratory and field studies related to radionuclide migration at the Nevada test site: Los Alamos National Laboratories, *Report LA-13419-PR*, 31 p.
- Thorstensen et al (1989) Thorstensen, D. C., Weeks, E. P., Haas, H., and Woodward J. C. 1989 Physical and Chemical Characteristics of Topographically Affected Airflow in an Open Borehole at Yucca Mountain, Nevada. Proceedings, the Focus '89 Nuclear Waste in the Unsaturated Zone, September 18-21, Las Vegas, Nevada.
- Tikunov (1989) Tikunov, Y.V. 1989 On the mobilization of uranium in vitric volcanogenic rocks *Acta of the Institute of Geology and Geophysics, Academy of Sciences of the USSR, Novosibirsk, № 750*, pp. 122-130. (*In Russian*)
- Truesdel and Jones (1974) Truesdel, A.H. and Jones, B. F. 1974 WATEQ: A computer program for calculating chemical equilibria of natural waters: *US Geol Survey Jour Research 2* pp 233

chemical equilibria of natural waters: *US Geol Survey Jour Research*, **2**, pp. 233-248.

- Turi (1986) Turi, B. 1986 Stable Isotope Geochemistry of Travertines. In: P. Fritz and J.Ch. Fontes, Eds. *Handbook of Environmental Isotope Geochemistry 2 The terrestrial Environment*, B. Elsevier, Amsterdam. pp. 207-238.

U

- U.S. DOE (1988) U.S. DOE (U. S. Department of Energy) 1988 Site Characterization Plan, Yucca Mountain Site, Nevada Research and Development Area. U. S. Department of Energy, Office of Civilian Radioactive Waste Management, Washington, D. C.
- U.S. DOE (1993-a) U.S. DOE (U.S. Department of Energy) 1993 Report on the Origin of Calcite-Silica Deposits at Trench 14 and Busted Butte and Methodologies Used to Determine Their Origin. *Report YMP193-11-R*. U.S. Department of Energy, Yucca Mountain Site Characterization Project, 64 pp. + Appendices.
- U.S. DOE (1993-b) U.S. DOE (U. S. Department of Energy) 1993 Transmittal Letter of December 20, 1993 "Second Installment of Data Reported in U. S. Geological Survey (USGS) Monthly Reports" from Nelson, R. M. to R. R. Loux (Agency for Nuclear Projects, State of Nevada).
- U.S. DOE (1998) U.S. DOE (U. S. Department of Energy) 1998 Viability Assessment of a Repository at Yucca Mountain. Vol. 1. Introduction and Site Characterization. *DOE/RW-0508* U. S. Department of Energy, Office of Civilian Radioactive Waste Management, Washington, D. C.
- U.S. DOE (1999) U.S. DOE (U.S. Department of Energy) 1999 Draft Environmental Impact Statement for a Geologic Repository for the Disposal of Spent Nuclear Fuel and High-Level Radioactive Waste at Yucca Mountain, Nevada. *DOE/EIS-0250D*.
- U.S. DOE (2001) U.S. DOE (U. S. Department of Energy) 2001 Yucca Mountain Science and Engineering Report. Technical Information Supporting Site Recommendation Consideration. *DOE/RW-0539*.
- USGS (1993) USGS (U.S. Geological Survey) 1993 Monthly Report of Ongoing Work. January 1993.
- USGS (1997) USGS (U.S. Geological Survey) 1997 USGS Level 4 Milestone SPC23FM4; Appendix E: U-Pb dating (L.A. Neymark, main author). pp. E-1-E-11.

V

- Vaniman (1993) Vaniman, D.T. 1993 Calcite deposits in fractures at Yucca Mountain, Nevada. *Proc. Int. Con , Amer. Nucl. Soc* "High-Level Radioactive Waste Management". La Grande Park, Illinois. pp. 1935-1939.
- Vaniman and Chipera (1996) Vaniman, D.T. and Chipera, S.J. 1996 Paleotransport of lanthanides and strontium recorded in calcite compositions from tuffs at Yucca Mountain, Nevada. USA. *Geochim. et Cosmochim Acta.* **60**, pp. 4417-4433.
- Vaniman and Whelan (1994) Vaniman, D.T., and Whelan, J.F. 1994 Inferences of Paleoenvironment from Petrographic, Chemical, and Stable-Isotope Studies of Calcretes and Fracture Calcites *Proc Int Con , Amer. Nucl Soc* "High-Level Radioactive Waste Management". La Grande Park, Illinois. pp. 2730-2737.
- Vaniman et al. (1984) Vaniman, D., Bish, D., and Levy, S. 1984 Progress report: Studies of the origins of soil and fault-related mineralogy in the vicinity of Yucca Mountain. *TWS-ESS-1-11/84-22.* 6 p.
- Vaniman et al. (1988) Vaniman, D. T., Bish, D. L., and Chipera, S. 1988. A Preliminary Comparison of Mineral Deposits in Faults Near Yucca Mountain, Nevada, with Possible Analogs. *Los Alamos National Laboratory Report, LA-11289-MS.*
- Vaniman et al. (1995) Vaniman, D. T., Chipera, S., and Bish, D. L. 1995 Petrography, Mineralogy, and Chemistry of Calcite-Silica Deposits at Exile Hill, Nevada, Compared with Local Spring Deposits. *Los Alamos National Laboratory Report, LA-13096-MS* 70 p.
- Vaniman et al. (2001) Vaniman, D. T., Chipera, S. J., Bish, D. L., Carey, W. and Levy, S. S. 2001. Quantification of unsaturated-zone alteration and cation exchange in zeolitized tuffs at Yucca mountain, Nevada, USA. *Geochim et Cosmochim Acta.* **65**, 20, pp. 3409-3433.
- Veimarn (1906) Veimarn, P.P. 1906 Colloidal state as general state of the matter. *Journ Russ Phys - Chem Soc.* **38**.
- Veizer (1983) Veizer, J. 1983 Trace elements and isotopes in sedimentary carbonates. In: Carbonates: Mineralogy and Chemistry (R.J. Reeder, Ed.). *Min Soc. Amer Rev. in Mineralogy*, **11**, pp. 265-299.
- Voloschuk and Sedunov (1975) Voloschuk, V.M. and Sedunov, Y.S. 1975 Processes of coagulation in disperse systems. Gidrometeoizdat. Leningrad. (*In Russian*)
- Von Herzen and Lee (1969) Von Herzen, R.P., and Lee, H.K. 1969 Heat Flow in Oceanic Regions. In: The Earth's Crust and Upper Mantle, *Geophysical Monograph*, **13**. American

Geophysical Union.

- Vosel and Kalinin (1999) Vosel, S.V. and Kalinin D.V. 1999 Thermodynamic analysis of formation of crystal-like noble-opal structures. *Russian Geology and Geophysics*, 40, 4, pp. 606-614.

W

- Wang and Merino (1992) Wang Y. and Merino E. 1992 Dynamic model of oscillatory zoning of trace elements in calcite: Double layer, inhibition, and self-organization. *Geochim et Cosmochim. Acta* 56, pp. 587-596.
- Warren et al. (1984) Warren, R.G., Byers, F.M., and Caporuscio, F.A., 1984 Petrography and mineral chemistry of units of the Topopah Spring, Calico Hills and Crater Flat Tuffs, and some other volcanic units, with emphasis on samples from drill hole USW G-1, Yucca Mountain, Nevada Test site. Los Alamos Natl. Lab. Report LA-10003-MS.
- Wedepohl (1971) Wedepohl, K. H. 1971. *Geochemistry*. Holt, Rinehart, and Winston, Inc.
- Weeks (1991) Weeks, E.P. 1991 Does the Wind Blow through Yucca Mountain? *In*: D.D. Evans and T.J. Nicholson, (Eds.) Workshop V: Flow and Transport in Unsaturated Fractured Rock – Related to High-Level Radioactive Waste Disposal. NUREG/CR-0040. pp. 43-53.
- Weiss (1990) Weiss, S. I. 1990. Yucca Mountain Project Monthly Report Task No. 3 - August, 1990. The State of Nevada Nuclear Waste Project Office, Agency for Nuclear Projects.
- Weiss et al. (1994) Weiss, S.I., Noble, D.C., Jackson, M.R., Connors, K.A., and McKee, E.H. 1994 Multiple Episodes of Hydrothermal Activity and Epithermal Mineralization in the Southwestern Nevada Volcanic Field and Their Relations to Magmatic Activity, Volcanism and Regional Extension. Appendix A in: Evaluation of Geologic Relations and Seismotectonic Stability of the Yucca Mountain Area Nevada Nuclear Waste Site Investigations - Progress Report, Center for Neotectonic Studies, Mackay School of Mines, University of Nevada Reno. September 1994
Inconsecutive pages.
- Wells (1976) Wells, P.V. 1976 Macrofossil analysis of wood rat (*Neotoma*) middens as a key to the Quaternary vegetation history of arid America *Quaternary Research*. 6, pp. 223-248.
- Whelan and Moscati (1998) Whelan, J.F. and Moscati, R.J. 1998 9 M.Y. record of Southern Nevada climate from Yucca Mountain secondary minerals. *Proc Int Con , Amer Nucl. Soc.* "High-

- Level Radioactive Waste Management". La Grande Park, Illinois. pp. 12-15.
- Whelan and Stuckless (1991) Whelan, J.F., and Stuckless, J.S., 1991 Paleohydrologic Implications of the Stable Isotope Composition of Secondary Calcite within the Tertiary Volcanic Rocks of Yucca Mountain, Nevada. *Proc Int Con , Amer Nucl. Soc.* "High-Level Radioactive Waste Management". La Grande Park, Illinois, pp. 1572-1581.
- Whelan et al. (1994) Whelan, J.F., Vaniman, D.T., Stuckless, J.S. and Moscati, R.J. 1994 Paleoclimatic and Paleohydrologic Records from Secondary Calcite: Yucca Mountain, Nevada. *Proc. Int Con , Amer. Nucl. Soc.* "High-Level Radioactive Waste Management". La Grande Park, Illinois. pp. 2738-2745.
- Whelan et al. (1998-a) Whelan, J.F., Moscati, R.J., Roedder, E., and Marshall, B.D. 1998 Secondary Mineral Evidence of Past Water Table Changes at Yucca Mountain, Nevada. *Proc. Int Con , Amer. Nucl. Soc.* "High-Level Radioactive Waste Management". La Grande Park, Illinois. pp. 178-181.
- Whelan et al. (1998-b) Whelan, J.F., Moscati, R.J., Allerton, S.B.M., and Marshall, B.D., 1998, Applications of Isotope Geochemistry to the Reconstruction of Yucca Mountain. Nevada, Paleohydrology – Status of Investigations: June 1996. *US Geol Survey Open-File Report 98-83*. 41 p.
- Whelan et al. (1999) Whelan, J.F., Paces, J.B., Moscati, R.J., Neymark, L.A., Marshall, B.D., and Peterman, Z.E. 1999 Paragenesis and Oxygen Isotopes of Calcite in Unsaturated Zone of Yucca Mountain, Nevada: Evidence of an Early Thermal Event. *Supplement to EOS*, April 27, 1999. p. S7.
- Whelan et al. (2000) Whelan, J., Paces, J., Neymark, L., Marshall, B., Peterman, Z., Moscatti, R., and Roedder, E. 2000 Calcite fluid inclusion, paragenetic, and oxygen isotopic records of thermal event(s) at Yucca Mountain, Nevada. *GSA Abstracts with Program*. **32**, 7. p. A-259.
- Whelan et al. (2001) Whelan, J., Roedder, E., and Paces, J. 2001 Evidence for an Unsaturated-Zone Origin of Secondary Minerals in Yucca Mountain, Nevada. *Proc. Int Con , Amer. Nucl. Soc.* "High-Level Radioactive Waste Management". La Grande Park, Illinois.
- Whipple et al. (1998) Whipple, C.G., Budnitz, R.J., Ewing, R.C., Moeller, D.W., Payer, J.H., and Whitterspoon, P.A. 1998 Yucca Mountain Total System Performance Assessment Peer Review Panel Report. *Third Interim Report*. 45 p.
- Whipple et al. (1999) Whipple, C., Budnitz, R., Ewing, R., Moeller, D., Payer, J., and Whitterspoon, P. 1999 Final Report, Total System Performance Assessment Peer Review Panel. *Civilian Radioactive Waste Management and Operating Contractor*. Las Vegas,

- NV. February 11, 1999.
- White (1957) White, D.E. 1957 Thermal waters of volcanic origin. *Bull. Soc. Geol Amer.* 68, pp. 1637-1658.
- White and Chuma (1987) White, A.F., and Chuma, H.J. 1987 Carbon and Isotopic Mass Balance Models of Oasis Valley-Fortymile Canyon Groundwater Basin, Southern Nevada. *Water Resources Research*, 23, 4.
- White and Williams (1975) White, D.E. and Williams, D.L. 1975 Introduction. *In*: D.E. White and D.L. Williams, *Eds.* Assessment of Geothermal Resources of the United States – 1975. U.S. Geological Survey Circular 726. pp. 1-4.
- White et al. (1980) White, A. G., Claassen, H. C., and Benson, L. V. 1980 The Effect of Dissolution of Volcanic Glass on the Water Chemistry in a Tuffaceous Aquifer, Rainier Mesa, Nevada. *USGS Water Supply Paper WSP 1536-Q*, Washington, D. C.
- Wilson and Cline (2001) Wilson, N. and Cline, J. 2001 Paragenesis, Temperature and Timing of Secondary Minerals at Yucca Mountain. *Proc Int. Con , Amer Nucl. Soc* “High-Level Radioactive Waste Management”. La Grande Park, Illinois.
- Wilson et al. (2000) Wilson, N.S.F., Cline, J.S., Rotert, J. and Amelin Y.V. 2000 Timing and temperature of fluid movement at Yucca Mountain, NV: Fluid inclusion analyses and U-Pb and U-series dating. *GSA Abstracts with Program*, 32, 7. p. A-260.
- Wohletz and Heiken (1992) Wohletz, K. and Heiken, G. 1992 *Volcanology and Geothermal Energy*. University of California Press, Berkeley, Los Angeles, Oxford. 432 p.
- WoldeGabriel (1993) WoldeGabriel, G. 1993 K/Ar Dating of Clinoptilolite, Mordenite, and Associated Clays from Yucca Mountain, Nevada. *Proceedings, International Zeolite Conference*, Boise, Idaho, June 20-28, 1993,
- WoldeGabriel et al. (1993) WoldeGabriel, G., Broxton, D.E., Bish, D.L., and Chipera, S.J. 1993 Mineralogy and clinoptilolite K/Ar results from Yucca Mountain, Nevada., USA: A potential high-level radioactive waste repository site. *Los Alamos Natl Lab Rept. LA-12652-MS*

Y

- Yang (1992) Yang, I. C., 1992. Flow and Transport Through Unsaturated Rock - Data from Two Test Holes, Yucca Mountain, Nevada. *Proc Int Con , Amer. Nucl Soc* “High-Level Radioactive Waste Management”. La Grande Park, Illinois.

- Yang et al. (1996) Yang, I.C., Rattray, G.W., and Yu, P. 1996 Interpretation of chemical and isotopic data from boreholes in the unsaturated zone at Yucca Mountain, Nevada. *U.S Geological Survey Water-Resources Investigations Report 96-4058*. 58 p.
- Yang et al. (1998) Yang, I.C., Yu, P. Rattray, G.W., Fararese, J.S., and Ryan, J.N. 1998 Hydrochemical Investigations in characterizing the unsaturated zone at Yucca Mountain , Nevada. *USGS Water-Resources Investigation Report 98-4132*, Denver, CO, 33. p.
- Yarborough (1980) Yarborough, K.A. 1980 The National Park Service cave radiation research and monitoring program. *Proc. Natl Cave Management Symposium*, Carlsbad, New Mexico. pp. 27-40.

Z

- Zartman and Kwak (1993-a) Zartman, R. E., and Kwak, L. M. 1993 Preliminary Study of Lead Isotopes in the Carbonate-Silica Veins of Trench 14, Yucca Mountain, Nevada. *U S Geological Survey Open-File-Report 93-690*.
- Zartman and Kwak (1993-b) Zartman, R.E. and Kwak, L.M. 1993 Lead Isotopic Composition of Paleozoic and Late Proterozoic Marine Carbonate Rocks in the Vicinity of Yucca Mountain, Nevada. *Proc Int Con , Amer. Nucl Soc "High-Level Radioactive Waste Management"*. La Grande Park, Illinois. pp. 1953-1959
- Zhang and Dawe (2000) Zhang, Y. and Dawe, R. A. 2000. Influence of Mg^{2+} on the kinetics of calcite precipitation and calcite crystal morphology. *Chemical Geology*. 163, pp. 129-138.
- Zielinski (1980) Zielinski, R.A. 1980 Uranium in Secondary Silica: A Possible Exploration Guide. *Economic Geology*. 75, pp. 592-602.
- Zielinski (1982) Zielinski, R.A. 1982 Uraniferous opal, Virgin Valley, Nevada: Conditions of Formation and Implications for Uranium Exploration. *Journal of Geochemical Exploration*. 16, pp. 197-216.
- Zielinski and Rosholt (1978) Zielinski, R.A. and Rosholt, J.N. 1978 Uranium in Waters and Aquifer Rocks at the Nevada Test Site, Nye County, Nevada. *USGS Jour Res.*, 6, 489.
- Zukin et al. (1987) Zukin, J.G , Hammond, D.E., Ku, T.L., and Elders, W.E. 1987 Uranium-Thorium Series Radionuclides in Brines and Reservoir Rocks from Two Geothermal Boreholes in the Salton Sea Geothermal Field, Southeastern California. *Geochim et Cosmochim Acta*, 551.
- Zverev et al. (1975) Zverev, V.L., Dolidze, N.I., Spiridonov, A.I. 1975 Anomaly of even isotopes of uranium in groundwaters of the seismically active regions of Georgia.

Geochemistry. 11, pp. 1720-1723. (*In Russian*)

Zverev et al. (1980)

Zverev, V.L., Tokarev, A.N., Timinski, V.G., and Shvets, V.M. 1980 Radioisotope geochemistry. Moscow, Nedra. 201 p. (*In Russian*)